

2009

Theoretical and computational design of terahertz frequency quantum cascade lasers

Adam Todd Cooney
University of Dayton

Follow this and additional works at: https://ecommons.udayton.edu/graduate_theses

Recommended Citation

Cooney, Adam Todd, "Theoretical and computational design of terahertz frequency quantum cascade lasers" (2009). *Graduate Theses and Dissertations*. 2114.
https://ecommons.udayton.edu/graduate_theses/2114

This Dissertation is brought to you for free and open access by the Theses and Dissertations at eCommons. It has been accepted for inclusion in Graduate Theses and Dissertations by an authorized administrator of eCommons. For more information, please contact mschlange1@udayton.edu, ecommons@udayton.edu.

THEORETICAL AND COMPUTATIONAL
DESIGN OF TERAHERTZ FREQUENCY
QUANTUM CASCADE LASERS

Dissertation

Submitted to

The School of Engineering of the
UNIVERSITY OF DAYTON

in Partial Fulfillment of the Requirements for

The Degree

Doctor of Philosophy in Electro-Optics

by

Adam T. Cooney

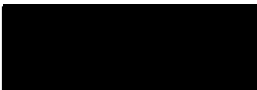
UNIVERSITY OF DAYTON

Dayton, Ohio

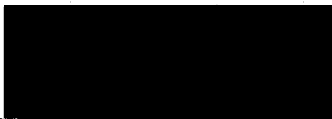
May, 2009

THEORETICAL AND COMPUTATIONAL DESIGN OF TERAHERTZ FREQUENCY
QUANTUM CASCADE LASERS


APPROVED BY:




Andrew M. Sarangan, Ph.D.
Advisory Committee Chairman
Professor, Electro-Optics
Graduate Program



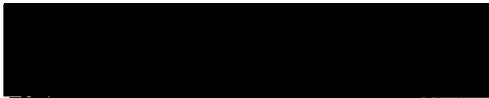
Joseph W. Haus, Ph.D.
Committee Member
Director, Electro-Optics
Graduate Program




Peter E. Powers, Ph.D.
Committee Member
Professor, Department of Physics



Lok C. Lew Yan Voon, Ph.D.
Committee Member
Chair, Department of Physics
Wright State University



Malcolm W. Daniels, Ph.D.
Associate Dean
School of Engineering



Joseph E. Saliba, Ph.D., P.E.
Dean, School of Engineering

ABSTRACT

THEORETICAL AND COMPUTATIONAL DESIGN OF TERAHERTZ FREQUENCY QUANTUM CASCADE LASERS.

Cooney, Adam, T.
University of Dayton

Advisor: Dr. A.M. Sarangan

Modeling of terahertz frequency quantum cascade lasers has become increasingly complex theoretically resulting in burdensome computational requirements. While more comprehensive treatment permits further insight and increased accuracy the modeling of these devices has, consequently, developed into a largely numerical process lacking an accessible framework. The objective of this research was simplification, both theoretically and computationally. To achieve a more analytically accessible description and to reduce time-restrictive calculations a systematic examination of the underlying theory for describing transport in quantum heterostructures was carried out. A procedure describing transport and gain was developed where all properties of a multi-quantum well system can be described as linear combinations of single well properties requiring only the input of heterostructure dimensions for immediate evaluation. The techniques developed in this research permit near real-time simulation of device operation and show excellent agreement with experimental results for terahertz frequency quantum cascade lasers.

ACKNOWLEDGEMENTS

I would like to thank my advisor Dr. Andrew Sarangan for introducing me to, and encouraging my study of, quantum cascade laser design. I hope that the results of my research will be valuable to him in both the classroom and in future projects.

I am also grateful to the Air Force Research Laboratory, Materials and Manufacturing Directorate, for providing me with the opportunity to pursue this research. Specifically, I would like to thank my supervisors in the Non-Destructive Evaluation branch for their patience as I conducted this seemingly never ending dissertation.

I also thank my entire extended family for their continued encouragement and support.

I am most appreciative of the patience of my wife Amella who has put up with the countless hours of me sitting in front of my computer nearly every night and weekend. She has been my continued support through both my master's degree and this dissertation. Finally, in nearly perfect timing, I dedicate the finality of my formal education to my expected daughter Abigail.

TABLE OF CONTENTS

CHAPTER

I. INTRODUCTION.....	1
1.1 Introduction to Quantum Wells and Heterostructures.....	2
1.2 Introduction to Quantum Cascade Lasers.....	8
1.3 Progress in QCL Technology.....	15
1.4 Theoretical and Computational Background.....	21
1.5 Dissertation Overview.....	29
II. CALCULATION OF ENERGIES AND WAVEFUNCTIONS IN QUANTUM HETEROSTRUCTURES.....	33
2.1 Introduction.....	33
2.2 Numerical Evaluation of the Time-Independent Schrödinger Equation.....	34
2.3 Analytical Single Well Solutions.....	49
2.4 Nearest-Neighbor Coupling of Single Well Solutions.....	55
III. SCATTERING RATES IN QUANTUM HETEROSTRUCTURES.....	82
3.1 Introduction.....	82
3.2 Calculation of Scattering Rates.....	83

3.3 Linear Combinations of Intrawell Scattering.....	97
3.4 Single Well Scattering Rates.....	123
IV. TRANSPORT IN QUANTUM HETEROSTRUCTURES.....	160
4.1 Introduction.....	160
4.2 Semiclassical Transport.....	161
4.3. Density Matrix Formalism.....	185
4.4 Diagonal Density Matrix.....	208
4.5 Combining Coherent and Incoherent Transport.....	221
4.6 Gain in Terahertz Quantum Cascade Lasers.....	235
V. SIMULATION OF TERAHERTZ QUANTUM CASCADE LASERS.....	243
5.1 Introduction.....	243
5.2 The 4-Well Resonant Phonon Depopulation Laser.....	247
5.3 The 3-Well Resonant Phonon Depopulation Laser.....	270
5.4 Intrawell Lasing and Potential Problems with the Simplified Model.....	277
VI. CONCLUSIONS.....	283
VII. REFERENCES.....	290

LIST OF FIGURES

1.1.1: Conduction and valence band diagrams in an arbitrary GaAs/AlGaAs heterostructure showing quantized states in the “quantum well” region.....	2
1.1.2: E-k diagram showing the 1D-confinement and 2-D in-plane dispersion of an electron in the conduction band of a quantum well.....	4
1.1.3: Conduction and valence band diagrams in an arbitrary GaAs/AlGaAs heterostructure showing intersubband and interband emission.....	4
1.1.4: An example showing the comparisons between a Hydrogen atom (left) and a quantum well (right).....	5
1.1.5: (a) Non-coupled, isolated quantum wells and (b) coupled quantum wells showing the wavefunctions splitting into symmetric (S) and anti-symmetric (AS) states. The wavefunctions are shown offset vertically to represent their respective energy levels.....	6
1.1.6: (a) A two-quantum well structure with no applied electric field and (b) the same device under an applied bias of 8kV/cm. The wavefunctions shown here are the moduli squared and are offset to their respective energies.....	7
1.2.1: The conduction band diagram in an example QCL structure showing 4 repeating periods.....	9
1.2.2: A 4-level laser diagram representing the basic operation of a QCL.....	10
1.2.3: An illustration of the kinetic energy dependence of intersubband transitions due to the emission of an LO-phonon.....	12

1.2.4: LO-phonon emission and electron-electron intersubband scattering rates vs. the subband energy separation. The phonon emission is calculated in a single GaAs well with AlAs barriers and the electron-electron rates are calculated for an interwell doublet.....	13
1.3.1: Diagram representing the original QCL proposal.....	15
1.3.2: Diagram representing the first demonstrated QCL.....	17
1.3.3: The three proven THz-QCL designs. (a) Chirped-Superlattice, (b) Bound-to-Continuum, and (c) Resonant-Phonon Depopulation.....	18
1.3.4: Diagram of the 4-well per period resonant phonon depletion QCL.....	20
1.4.1: Illustration of the evolution of QCL modeling.....	22
1.4.2: Various illustrations of transport descriptions in QCL's (a) Resonant tunneling transport description in Mid-IR QCL's. (b) The semiclassical laser rate equation approach. (c) Monte-Carlo Methods.....	25
2.2.1: Potential profile and confined states for a single 120Å GaAs well surrounded by 100Å Al _{0.15} Ga _{0.85} As barriers. The wavefunctions shown here are offset to their respective energies and are plotted as the magnitude squared.....	36
2.2.2: Confined energies vs. well width for a single GaAs well surrounded by 100Å Al _{0.15} Ga _{0.85} As barriers.....	37
2.2.3: Comparison of biased (F=20kV/cm) vs. unbiased system for a single 120Å GaAs well surrounded by 100Å Al _{0.15} Ga _{0.85} As barriers. The unbiased potential and wavefunctions are shown in bold.....	38
2.2.4: Comparison of calculations with and without Schrödinger-Poisson self-consistency for a well heavily n-type doped to produce a sheet density of $1000 \times 10^{10} \text{ cm}^{-2}$	40
2.2.5: Comparison of the ground state energy with and without Schrödinger-Poisson self-consistency for a well n-type doped producing various sheet densities.....	41

2.2.6: A 70Å and 50Å GaAs double quantum well system separated by a 60Å $\text{Al}_{0.15}\text{Ga}_{0.85}\text{As}$ barrier evaluated numerically with no applied bias.....	42
2.2.7: Wavefunctions and energies of the two ground states vs. the electric field for a 70Å and 50Å GaAs double quantum well system separated by a 60Å $\text{Al}_{0.15}\text{Ga}_{0.85}\text{As}$ barrier.....	43
2.2.8: Diagram illustrating the relationship between the spatial proximity of two wavefunctions and the probability of a transition.....	45
2.2.9: Energy of the two ground states (left) and O_{mod} vs. the electric field (right) for a 70Å and 50Å GaAs double quantum well system separated by an $\text{Al}_{0.15}\text{Ga}_{0.85}\text{As}$ barrier of various widths.....	46
2.2.10: A generic coupled well system with an arbitrary barrier width.....	47
2.2.11: Illustration of confined states in a QCL system coupling to “quasi-continuum” states.....	48
2.3.1: A single quantum well and the analytical components of a general wavefunction.....	49
2.3.2: Comparison of numerically calculated eigenvalues and empirically fit solutions for the ground and excited states in a single GaAs/ $\text{Al}_{0.15}\text{Ga}_{0.85}\text{As}$ well.....	53
2.4.1: Ground state wavefunction calculated for a 70Å GaAs well and a 50Å GaAs well separated by a 60Å $\text{Al}_{0.15}\text{Ga}_{0.85}\text{As}$ barrier.....	56
2.4.2: Diagram showing the piecewise descriptions of single well wavefunctions translated into a multi-well system.....	61
2.4.3: A comparison of the full numerical calculation (black) and the “perturbed energies” (red and blue dashed lines) calculated using Equation 2.4.42 for a 70Å GaAs well and a 50Å GaAs well separated by a 60Å $\text{Al}_{0.15}\text{Ga}_{0.85}\text{As}$ barrier.....	66

2.4.4: A comparison of the full numerical calculation (black), the “perturbed energies” (red and blue dashed lines), and the inclusion of the repelling effect (red and blue solid lines with circles) for a 70Å GaAs well and a 50Å GaAs well separated by a 60Å $\text{Al}_{0.15}\text{Ga}_{0.85}\text{As}$ barrier.....	67
2.4.5: Comparison of the energies vs. the field using the non-Hermitian (black) and forced Hermitian (red and blue) techniques for a 70Å GaAs well and a 50Å GaAs well separated by a 60Å $\text{Al}_{0.15}\text{Ga}_{0.85}\text{As}$ barrier.....	70
2.4.6: Comparison of the wavefunctions calculated numerically (black) and using the coupled single well basis (red and blue) at different biases for a 70Å GaAs well and a 50Å GaAs well separated by a 60Å $\text{Al}_{0.15}\text{Ga}_{0.85}\text{As}$ barrier.....	71
2.4.7: The coupling coefficient ratio given by Equation 2.5.58 vs the perturbed energy separation of two interwell states in units of the coupled-well interaction \tilde{V}	74
2.4.8: Eigenstates of 120Å GaAs well and a 200Å GaAs well separated by a 30Å $\text{Al}_{0.15}\text{Ga}_{0.85}\text{As}$ barrier, shown at 9kV/cm.....	75
2.4.9: Eigenstates of a 120/30/70/60/50 GaAs/ $\text{Al}_{0.15}\text{Ga}_{0.85}\text{As}$ system.....	77
2.4.10: Energies vs. the bias calculated numerically for a 120/30/70/60/50 GaAs/ $\text{Al}_{0.15}\text{Ga}_{0.85}\text{As}$ system.....	77
2.4.11: Energy separations vs. the bias calculated numerically for the three well 120/30/70/60/50 GaAs/ $\text{Al}_{0.15}\text{Ga}_{0.85}\text{As}$ system compared to the 2-state 70/60/50 GaAs/ $\text{Al}_{0.15}\text{Ga}_{0.85}\text{As}$ system.....	78
2.4.12: Numerically calculated energies (black) vs. the bias compared to the simplified expression of Equation 2.4.63 (red, blue, green) for the three well 120/30/70/60/50 GaAs/ $\text{Al}_{0.15}\text{Ga}_{0.85}\text{As}$ system.....	79

2.4.13: Numerically calculated energies (black) vs. the bias compared to the full tight-binding matrix treatment of Equation 2.4.64 (red, blue, green) for the three well 120/30/70/60/50 GaAs/Al _{0.15} Ga _{0.85} As system.....	80
3.2.1: Transformation of 2D subbands to singular objects by employing a mean subband scattering rate.....	86
3.2.2: 150Å-50Å GaAs-Al _{0.2} Ga _{0.8} As double well system. Arrows indicate the 3-1 intrawell and 2-1 interwell transitions.....	89
3.2.3: 150Å-50Å (w/b=30Å) GaAs-Al _{0.2} Ga _{0.8} As double well interface phonon dispersion.....	90
3.2.4: AlAs-like interface phonon mode potentials at $q=.025(1/\text{\AA})$ for 150Å-50Å (w/b=30Å) GaAs-Al _{0.2} Ga _{0.8} As double well.....	90
3.2.5: Confined phonon modes (order $m=1\&2$) for 150Å-50Å (w/b=30Å) GaAs-Al _{0.2} Ga _{0.8} As double well.....	91
3.2.6: Comparison of bulk-GaAs phonon, complex (confined + interface) phonon and the $g(x,b)G+a(x,b)A$ bulk-like fit for the 2-1 interwell scattering rates vs. dE 2-1 for a 150Å-50Å (w/b=30Å) GaAs-Al _{1-x} Ga _x As double well.....	94
3.2.7: Comparison of bulk-GaAs phonon, complex (confined + interface) phonon and the $g(x,b)G+a(x,b)A$ bulk-like fit for the 3-1 intrawell scattering rates vs. dE 3-1 for a 150Å-50Å (w/b=30Å) GaAs-Al _{1-x} Ga _x As double well.....	95
3.3.1: Diagram showing delocalized states and scattering represented by combinations of the localized basis.....	99
3.3.2: Eigenstates for two 155Å GaAs wells separated by a 50Å Al _{0.15} Ga _{0.85} As barrier biased at $F=21\text{kV/cm}$ calculated using the full numerical approach.....	101

3.3.3: Diagram depicting the difference between intrasubband and intersubband transitions.....	104
3.3.4: Eigenstates for two 155Å GaAs wells separated by a 50Å $\text{Al}_{0.15}\text{Ga}_{0.85}\text{As}$ barrier biased at $F=21\text{kV/cm}$ calculated using the localized basis.....	105
3.3.5: Comparison of the energies vs. the bias for two 155Å GaAs wells separated by a 50Å $\text{Al}_{0.15}\text{Ga}_{0.85}\text{As}$ barrier calculated using the full numerical approach (black lines) and the localized expansion (colored lines with circles). The energy separation for the right-ground to left-excited states in each picture is also plotted as dotted lines.....	106
3.3.6: Artificial system used to calculate the mean “basis rates” for the relevant intrawell transitions.....	108
3.3.7: Basis LO emission and absorption rates in a 155Å well at $T_e=T=77\text{K}$ and assuming $n=1\times 10^{10}\text{cm}^{-2}$ in all subbands.....	109
3.3.8: Piecewise exponential fitting functions for the gg and eg emission rates for the 155Å well.....	110
3.3.9: Intradoublet LO emission rates calculated using the full numerical simulation (solid lines) and the LCIS technique with the piecewise exponential fitting functions (dotted lines).....	111
3.3.10: Indirect LO emission rates calculated using the full numerical simulation (solid lines) and the LCIS method (dotted lines).....	113
3.3.11: Piecewise exponential fitting functions for the gg and eg emission rates for the 155Å well.....	114
3.3.12: Intradoublet LO absorption rates calculated using the full numerical simulation (solid lines) and the LCIS technique (dotted lines).....	115

3.3.13: Indirect LO absorption rates calculated using the full numerical simulation (solid lines) and the LCIS technique (dotted lines).....	116
3.3.14: The electron-electron basis rates for the gg-gg and ee-ee components.....	118
3.3.15: Comparison of the electron-electron rates calculated using the full numerical technique (solid line) and the simplified LCIS method (dotted lines). The combined 1-4 and 4-1 LCIS rates are also shown (dotted black line) for clarity.....	119
3.3.16: (a) Two arbitrary identical normalized states shifted along the z-axis ($\Delta z=4$ a.u.) and (b) their orthogonal combinations.....	120
3.3.17: Form factor comparison of the full wavefunctions vs. the LCIS expansion for the simple 2-state system with ($\Delta z=4$ a.u.).....	121
3.3.18: (a) Two arbitrary identical normalized states shifted along the z-axis ($\Delta z=2$ a.u.) and (b) their orthogonal combinations.....	122
3.3.19: Form factor comparison of the full wavefunctions vs. the LCIS expansion for the simple 2-state system with ($\Delta z=2$ a.u.).....	122
3.4.1: Wavefunctions used to determine the gg and eg mean basis rates.....	125
3.4.2: The gg and eg LO emission basis rates plotted vs. ΔE calculated at $L=100$, $L=150$, and $L=200$	125
3.4.3: The gg and eg LO emission basis rates plotted vs. ΔE calculated at $n_i=0.1 \times 10^{10} \text{ cm}^{-2}$, $1 \times 10^{10} \text{ cm}^{-2}$, and $3 \times 10^{10} \text{ cm}^{-2}$	126
3.4.4: The gg and eg LO emission basis rates plotted vs. ΔE calculated at $n_i=0.1 \times 10^{10} \text{ cm}^{-2}$, $1 \times 10^{10} \text{ cm}^{-2}$, and $3 \times 10^{10} \text{ cm}^{-2}$	127
3.4.5: The gg emission basis rates at various lattice and electron temperatures.....	129
3.4.6: The eg emission basis rates at various lattice and electron temperatures.....	130

3.4.7: The gg basis emission rates and exponential fitting functions at a lattice temperature of $T=77\text{K}$ and electron temperatures at $T_e=T+0\text{K}$, $T_e=T+100\text{K}$, and $T_e=T+200\text{K}$.	131
3.4.8: A plot of the A coefficient terms vs. the electron temperature at $T=77\text{K}$. A_1 is shown in black and A_2 in red.	132
3.4.9: A plot of the b coefficient terms vs. the electron temperature at $T=77\text{K}$. b_1 is shown in black and b_2 in red.	133
3.3.10: Comparison of the empirical fitting functions and the calculated data for the gg emission rate at $T=77\text{K}$.	133
3.3.11: Comparison of the empirical fitting functions and the calculated data for the eg emission rate at $T=77\text{K}$.	134
3.4.12: Empirical fitting functions for the gg emission rates at $T=77\text{K}$ at electron temperatures outside of the fitting points.	135
3.4.13: Corrected empirical gg-emission rates at $T=77\text{K}$ compared to the original data.	135
3.4.14: The full empirical gg-emission fit compared to the calculated data at a lattice temperature of $T=4\text{K}$.	136
3.4.15: The full empirical gg-emission fit compared to the calculated data at a lattice temperature of $T=50\text{K}$.	137
3.4.16: The full empirical gg-emission fit compared to the calculated data at a lattice temperature of $T=77\text{K}$.	137
Figure 3.4.17: The full empirical gg-emission fit compared to the calculated data at a lattice temperature of $T=150\text{K}$.	138

3.4.18: The full empirical gg-emission fit compared to the calculated data at a lattice temperature of $T=300\text{K}$	138
3.4.19: The full empirical gg-emission fit compared to the calculated data using an electron temperature of $T_e=T+100\text{K}$ at various lattice temperatures.....	139
3.4.20: The full empirical gg-emission fit compared to the calculated data at a lattice temperature of $T=77\text{K}$	140
3.4.21: The full empirical gg-emission fit compared to the calculated data at a lattice temperature of $T=300\text{K}$	140
3.4.22: Emission to absorption ratios at energy separations below the phonon resonance at $T=77\text{K}$	143
3.4.23: Emission to absorption ratios at energy separations below the phonon resonance at $T=300\text{K}$	143
3.4.24: The emission to absorption ratio fitting coefficient C , and its corresponding exponential fits at $T=77\text{K}$ and $T=300\text{K}$	144
3.4.25: Empirically fit emission and absorption rates at $T=77\text{K}$ and various electron temperatures compared to the calculated data at $T_e=T+0\text{K}$ and $T_e=T+200\text{K}$	145
3.4.26: The gg-gg mean electron-electron basis rates at 77K and a fixed $nf=1.0$, plotted for three different initial subband populations. All population units are 10^{10}cm^{-2}	146
3.4.27: The gg-gg mean electron-electron basis rates at $T_e=25\text{K}$, 77K , and 300K along with the corresponding power fitting functions.....	147
3.4.28: Localized (left) and delocalized (right) state for a system containing two 155\AA GaAs wells separated by a 50\AA $\text{Al}_{0.15}\text{Ga}_{0.85}\text{As}$ barrier.....	148
3.4.29: Comparison of the empirical LCIS predicted intradoublet emission rates (dotted lines) and the full numerical calculation (solid lines).....	149

3.4.30: Comparison of the empirical LCIS predicted indirect emission rates (dotted lines) and the full numerical calculation (solid lines).....	150
3.4.31: Comparison of the empirical LCIS predicted intradoublet absorption rates (dotted lines) and the full numerical calculation (solid lines).....	151
3.4.32: Comparison of the empirical LCIS predicted indirect absorption rates (dotted lines) and the full numerical calculation (solid lines).....	151
3.3.33: Comparison of the electron-electron rates calculated using the full numerical technique (solid line) and the empirical LCIS method (dotted lines). The combined 1-4 and 4-1 LCIS rates are also shown (dotted black line) for clarity.....	152
3.3.34: Comparison of the energies vs. the bias for two 155Å GaAs wells separated by a 20Å $\text{Al}_{0.15}\text{Ga}_{0.85}\text{As}$ barrier calculated using the full numerical approach (black lines) and the localized expansion (colored lines with circles). The energy separation for the right-ground to left-excited states in each picture is also plotted as dotted lines.....	154
3.4.35: Comparison of the empirical LCIS predicted intradoublet emission rates (dotted lines) and the full numerical calculation (solid lines) for the 20Å barrier system.....	155
3.4.36: Comparison of the empirical LCIS predicted indirect emission rates (dotted lines) and the full numerical calculation (solid lines) for the 20Å barrier system.....	156
3.4.37: Comparison of the empirical LCIS predicted intradoublet absorption rates (dotted lines) and the full numerical calculation (solid lines) for the 20Å barrier system.....	157
3.4.38: Comparison of the empirical LCIS predicted indirect absorption rates (dotted lines) and the full numerical calculation (solid lines) for the 20Å barrier system.....	157

3.4.39: Comparison of the empirical LCIS predicted intradoublet electron-electron rates (dotted lines) and the full numerical calculation (solid lines) for the 20Å barrier system.....	158
4.2.1: A generic collection of states depicting the standard rate equation model.....	161
4.2.2: Full 2-dimensional nature of the subbands and the transport.....	162
4.2.3: 3-periods of a 150Å well/50Å barrier GaAs/Al _{0.15} Ga _{0.85} As superlattice calculated using the full numerical simulation at F=6kV/cm.....	163
4.2.4: Energies vs. electric field bias for the full numerical simulation of the 150/50 GaAs/Al _{0.15} Ga _{0.85} As superlattice.....	164
4.2.5: 3-periods of a 150Å well/50Å barrier GaAs/Al _{0.15} Ga _{0.85} As superlattice calculated using the full numerical simulation at F=10kV/cm.....	165
4.2.6: 3-periods of a 150Å well/50Å barrier GaAs/Al _{0.15} Ga _{0.85} As superlattice calculated using the full numerical simulation at F=15.5kV/cm.....	166
4.2.7: 3-periods of a 150Å well/50Å barrier GaAs/Al _{0.15} Ga _{0.85} As superlattice calculated using the full numerical simulation at F=15.5kV/cm.....	166
4.2.8: Figure displaying the interface and forward current flow for the superlattice calculation.....	167
4.2.9: Current density and subband populations vs. the bias for the 150/50 GaAs/Al _{0.15} Ga _{0.85} As superlattice calculated at T _e =T=77K and assuming a total sheet density of 1x10 ¹⁰ cm ⁻²	169
4.2.10: 3-periods of a 150Å well/50Å barrier GaAs/Al _{0.15} Ga _{0.85} As superlattice calculated using the localized basis.....	171
4.2.11: Energies vs. the field for a 150/50 barrier GaAs/Al _{0.15} Ga _{0.85} As superlattice calculated using the tight-binding expansion of the localized basis.....	172

4.2.12: Diagram showing the simple implementation of repeating boundary conditions using the LCIS technique.....	173
4.2.13: 150/30 barrier GaAs/Al _{0.15} Ga _{0.85} As superlattice calculated using the localized basis expansion with the application of the repeating period conditions.....	174
4.2.14: Current density and subband populations vs. the bias for the 150/50 GaAs/Al _{0.15} Ga _{0.85} As superlattice calculated at T _e =T=77K and assuming a total sheet density of 1x10 ¹⁰ cm ⁻² using both the full simulation (solid lines and points) and the LCIS method (dotted lines with open points).....	175
4.2.15: LCIS current density calculations for a 150/b GaAs/Al _{0.15} Ga _{0.85} As superlattice system with various barrier widths.....	177
4.2.16: LCIS current density calculations for a 150/b GaAs/Al _{0.15} Ga _{0.85} As superlattice system with various barrier widths stopped at the resonance peak (the start of the NDR region). In the inset is this peak current density vs. the barrier width.....	178
4.2.17: Diagram of a generic superlattice system biased at resonance.....	179
4.2.18: Delocalized scattering components in a resonantly biased superlattice.....	180
4.2.19: Description of current flow across an arbitrary interface for a superlattice system.....	182
4.2.20: Description of current flow as interdoublet for a superlattice system.....	183
4.2.21: Localized state description of superlattice transport. R is an intrawell transition rate and Y is an undefined interwell tunneling rate.....	184
4.3.1: Two isolated quantum well states separated by a barrier.....	187
4.3.2: Time evolution of the system wavefunction for a 80/50/60 GaAs/Al _{0.15} Ga _{0.85} As system with the initial population at t=0 located in the left well.....	189

4.3.3: A plot of the coupling magnitude $2\tilde{V}$ and the $\frac{1}{2}$ period of oscillation for a 80/L/60 GaAs/Al _{0.15} Ga _{0.85} As double well system.....	191
4.3.4: The effects of pure dephasing in a generic $\tilde{V} = 4\text{meV}$ 2-state coupled well system at $T_2=0.5$ and 100ps.....	198
4.3.5: Generic 2-state system where state $ 1\rangle$ is permitted to scatter to undefined states.....	198
4.3.6: Time-dependent evolution of the distribution where state $ 1\rangle$ has a finite incoherent lifetime.....	199
4.3.7: Multiple periods of a general 2-state superlattice.....	200
4.3.8: Folding the repeating 2-state superlattice back into a 2-state system. The curved arrows represent the coherent oscillation between states $ 2\rangle$ and $ 1\rangle$ and the black lines represent incoherent scattering.....	200
Figure 4.3.9: Time-dependent evolution of the distribution in a repeating period 2-state superlattice.....	201
4.3.10: Time-dependent evolution of the distribution in a repeating period 2-state superlattice with the $ 2\rangle$ to $ 1\rangle$ rate increased.....	202
4.3.11: 2-state superlattice structure.....	202
4.3.12: Interaction of a radiation field with a two-state system.....	206
4.3.13: A plot of the susceptibilities vs. $\omega-\omega_0$, in units of T_2 , for the limiting case of $4\Omega^2\tau T_2 \ll 1$	207
4.4.1: General multi-well system with 2-states per well.....	209
4.4.2: Simple repeating two state superlattice for the diagonal density matrix description.....	215

4.4.3: The repeating superlattice in the 2-state description.....	215
4.4.4: The equivalence of the DDM and LCIS method (w/o intradoublet scattering) for the limiting case of $\Omega^2\tau_d\tau \gg 1$	218
4.4.5: The non-equivalence of the DDM and LCIS method (w/o intradoublet scattering) for the limiting case of $\Omega^2\tau_d\tau \ll 1$	219
4.4.6: A more general treatment of the 2-state superlattice with numerous interwell tunneling terms.....	219
4.4.7: A more general treatment of the 2-state superlattice with numerous interwell tunneling terms.....	221
4.5.1: Comparison of the DDM and LCIS descriptions of transport.....	222
4.5.2: The equivalence of the DDM and LCIS method for the limiting case of $\Omega^2 \gg \Gamma W$	223
4.5.3: The non-equivalence of the DDM and LCIS method for the limiting case of $\Omega^2 \ll W\Gamma$	223
4.5.4: General strategy for an intradoublet lasing THz-QCL.....	224
4.5.5: Simple picture of two states with a repeating pumping mechanism.....	226
4.5.6: Repeating 2-state system connected by a pumping mechanism in the delocalized state representation.....	226
4.5.7: The inclusion of additional (Coherent + Incoherent) current.....	228
4.5.8: The oscillation frequency for a typical doublet in a THz-QCL.....	230
4.5.9: Comparison of the normalized inversion and current densities for a doublet pumped and drained at $P=1 \times 10^{11} \text{ s}^{-1}$	231

4.5.10: Comparison of the normalized inversion and current densities for a doublet pumped and drained at $P=5 \times 10^{12} \text{s}^{-1}$	232
4.5.11: Comparison of the normalized inversion and current densities for a doublet with a constant $\tilde{V} = 1 \text{meV}$ at various pumping rates.....	233
4.5.12: Comparison of the normalized inversion and current densities for a doublet with a constant $\tilde{V} = 10 \text{meV}$ at various pumping rates.....	233
4.5.13: Locally expanded intradoublet scattering	234
5.2.1: Picture of the Monte Carlo/Tight-Binding Density Matrix hybrid model of Callebaut and Hu [102].....	244
5.2.1: Diagram of the 4-well resonant phonon depopulation QCL.....	247
5.2.2: Full numerical simulation over 3-periods of the device from Reference [34]. The system is displayed at a bias of 12kV/cm	249
5.2.3: Localized basis for device from Reference [34].	249
5.2.4: Comparison of the energies vs. the bias for the coupled-well expansion in the localized basis and the full numerical model.....	250
5.2.5: Localized basis calculation of the lasing state energy separation and the phonon depletion mechanism compared to reported results.....	250
5.2.6: Localized basis calculation of wavefunctions compared to the full simulation at $F=12 \text{kV/cm}$	251
5.2.7: Emperical LCIS (I-V and V-I) calculations using a semiclassical rate equation model.....	252
5.2.8: Emperical LCIS gain and electron temperature calculations using a semiclassical rate equation model.....	253

5.2.9: DDM picture of transport using the localized basis and assuming intrawell scattering only.....	254
5.2.10: DDM picture of transport using the localized basis with a pseudo or “hybrid-doublet” used as the active region.....	257
5.2.11: DDM picture of energies vs. bias with the “hybrid doublet”.....	258
5.2.12: Depiction of subband heating and cooling due to kinetic energy redistributions for phonon emission.....	259
5.2.13: Current-Voltage curves for the 4-well QCL of Reference [34] calculated using the simple DDM technique at various lattice and electron temperatures.....	260
5.2.14: Gain vs. bias curves for the 4-well QCL of Reference [34] calculated using the simple DDM technique at various lattice and electron temperatures.....	261
5.2.15: Peak gain vs. lattice temperature curves for the 4-well QCL Reference [34] calculated using the simple DDM technique at various electron temperatures.....	261
5.2.16: Current-Voltage for the 4-well QCL Reference [34] for various T_2 values.....	262
5.2.17: Gain vs. the bias for the 4-well QCL Reference [34] for various T_2 values.....	263
5.2.18: Normalized plots of the tunneling terms Φ as well as the current density and inversion vs. the bias.....	264
5.2.19: The tunneling terms Φ vs. the bias.....	265
5.2.20: Simulated Voltage and gain vs. Current and at various lattice temperatures for the device of Reference [34].....	266
5.2.21: Normalized tunneling terms and current for the three variations of the 4-well QCL described in the text.....	267
5.2.22: Threshold current densities and peak gain vs. lattice temperature for the three variations of the 3-well resonant phonon design.....	268

5.2.23: Peak gain and peak inversion vs. the lattice temperature.....	269
5.2.24: Peak gain (red dots) vs. temperature and the value $\Delta N/\Gamma$ (black dotted line) normalized at T=5K.....	270
5.3.1: Diagram of the 3-well resonant phonon depopulation THz-QCL.....	271
5.3.2: Comparison of the energies vs. the bias for the coupled-well expansion in the localized basis and the full numerical model.....	272
5.3.3: Localized basis calculation of the lasing state energy separation and the phonon depletion mechanism compared to reported results.....	272
5.3.4: DDM picture of transport using the localized basis with a pseudo or “hybrid-doublet” used as the active region.....	273
5.3.5: Figure 5.2.18: Simulated voltage and gain vs. current at various lattice temperatures for the device of References [42,43].....	275
5.3.6: Normalized tunneling terms for the two variations of the 4-well QCL described in the text.....	276
5.3.7: Threshold current densities and peak gain vs. lattice temperature for the two variations of the 3-well resonant phonon design.....	277
5.4.1: 2-well QCL laser design.....	278
5.4.2: 4-well resonant phonon laser design.....	280
5.4.3: The 4-well resonant phonon design depicted as repeating “quintuplets”.....	280
5.4.4: Diagram showing 2 nd order tunneling effects.....	282

LIST OF TABLES

2.3.1: Coefficients for single well energy fits in a GaAs/ $\text{Al}_{0.15}\text{Ga}_{0.85}\text{As}$ system.....	52
2.3.3: Table of numerical eigenvalues, empirical fits, and the magnitude of their difference for a single GaAs/ $\text{Al}_{0.15}\text{Ga}_{0.85}\text{As}$ well.....	53
2.4.1: Comparison between the localized basis eigenvalues (labeled E(70) and E(5) and the numerical approach (E1 and E2) for a 70Å GaAs well and a 50Å GaAs well separated by a 60Å $\text{Al}_{0.15}\text{Ga}_{0.85}\text{As}$ barrier.....	56
2.4.2: Table of values for the coupled well interaction terms \tilde{V} for the two state system shown in Figure 2.4.1.....	64
2.4.3: Comparison of the original localized energies (E(70) and E(50)) with both the numerical calculation (E1 and E2) and the new perturbed values (E(L) and E(R)).....	65
2.4.4: Interaction terms \tilde{V} for the 120Å/200Å double GaAs well system separated by a 30Å $\text{Al}_{0.15}\text{Ga}_{0.85}\text{As}$ barrier biased at 9kV/cm.....	75
3.4.1: Coefficients for the mean LO-emission gg basis rates.....	141
3.4.2: Coefficients for the mean LO-emission eg basis rates.....	141
3.4.3: Ratios of the $W_{21\text{-em}}$ to the $W_{12\text{-ab}}$ rates at various ΔE_{21} subband separations for both the gg and eg basis rates.....	142
3.4.4: Coefficients required for determining the basis absorption rates.....	145
3.4.5: Coefficients required for determining the basis electron-electron rates.....	148

CHAPTER 1

INTRODUCTION

The transmission and spectral “fingerprinting” capabilities of electromagnetic waves with terahertz (THz) frequencies has fashioned a rapidly expanding community of THz researchers and engineers exploring a wide range of scientific and practical applications. The promise of a compact and low cost THz source, emitting in a region of the electromagnetic spectrum plagued by expensive and inefficient generation techniques, could be the enabling technology which permits THz research to emerge from the laboratory and be implemented in a multitude of industrial, medical, & defense applications currently being proposed. Advancement in the engineering of multi-quantum well heterostructures lasers, known as quantum cascade lasers or QCL’s, offers the potential to design miniature, efficient, high power, and direct terahertz emitters using standard semiconductor materials and fabrication techniques.

While steady advancement has been made in the design and fabrication of THz-QCL’s and the progression towards longer wavelengths and higher operating temperatures is in motion, there exists fundamental aspects of electron transport in these devices which remain active areas of research. The goal of achieving continuous-wave operation efficiently using thermoelectric cooled or ideally, room temperature operation, will likely require further technological improvements in fabrication methods,

electromagnetic mode confinement, heat-sinking capabilities, and the design and control of these electron transport characteristics. The focus of this research will be the latter, i.e. the engineering through computational and analytical descriptions of transport which permit population inversion and gain by the design of multi-quantum well heterostructures.

1.1 Introduction to Quantum Wells and Heterostructures

The basic building block of the QCL is the heterostructure quantum well. A quantum well is a semiconductor “sandwich” made by fabricating one material with a lower bandgap surrounded by materials with a larger bandgap (see Figure 1.1.1).

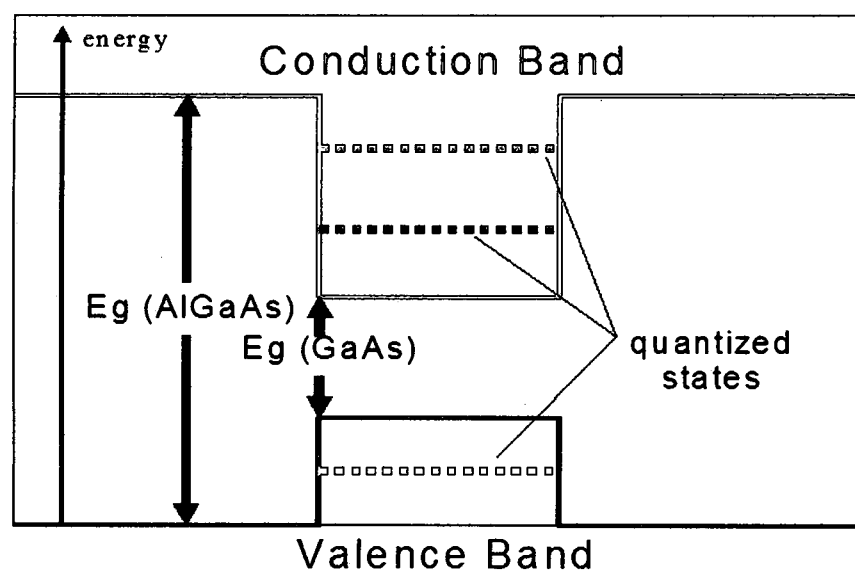


Figure 1.1.1: Conduction and valence band diagrams in an arbitrary GaAs/AlGaAs heterostructure showing quantized states in the “quantum well” region.

This mismatch of semiconductor materials leads to discontinuities in both the valence and conduction bands creating a “quantum well” where the potential energy in the

central region is lower for electrons in the conduction band and for holes in the valence band. If the central region is made on a small enough scale, typically a few monolayers to hundreds of angstroms, quantized states become apparent in the well region where electrons(holes) are confined along the growth direction in the conduction(valence) bands. This is, in many respects, the first engineering implementation of the 'particle-in-a-box' problem often illustrated in introductory quantum mechanics.

While commonly depicted, as in Figure 1.1.1, as discrete states (single lines) the one-dimensional structure of a quantum well, logically, provides confinement in only one dimension. To illustrate this consider the time-independent Schrödinger's equation

$$-\frac{\hbar^2}{2m^*} \left(\frac{\partial^2}{\partial x^2} + \frac{\partial^2}{\partial y^2} + \frac{\partial^2}{\partial z^2} \right) \psi + V(z)\psi = E\psi \quad (1.1.1)$$

where m^* is the effective mass of the electron and $V(z)$ represents the potential along the growth axis (z). This equation can be separated into parts

$$\begin{aligned} -\frac{\hbar^2}{2m^*} \frac{\partial^2}{\partial x^2} \psi_x &= E_x \psi_x \\ -\frac{\hbar^2}{2m^*} \frac{\partial^2}{\partial y^2} \psi_y &= E_y \psi_y \\ -\frac{\hbar^2}{2m^*} \frac{\partial^2}{\partial z^2} \psi_z + V(z)\psi_z &= E_z \psi_z \end{aligned} \quad (1.1.2)$$

The solution to these equations leads to quantized energy states in the z -direction, due to the quantum well potential, while still allowing for freedom of in-plane motion in the x and y -directions. For example, a state in the conduction band of the well region can be described as a subband with a minimum energy of E_z and in-plane kinetic energy, assumed to be parabolic, E_k . Thus the total energy forms a parabola in k -space such as shown in Figure 1.1.2.

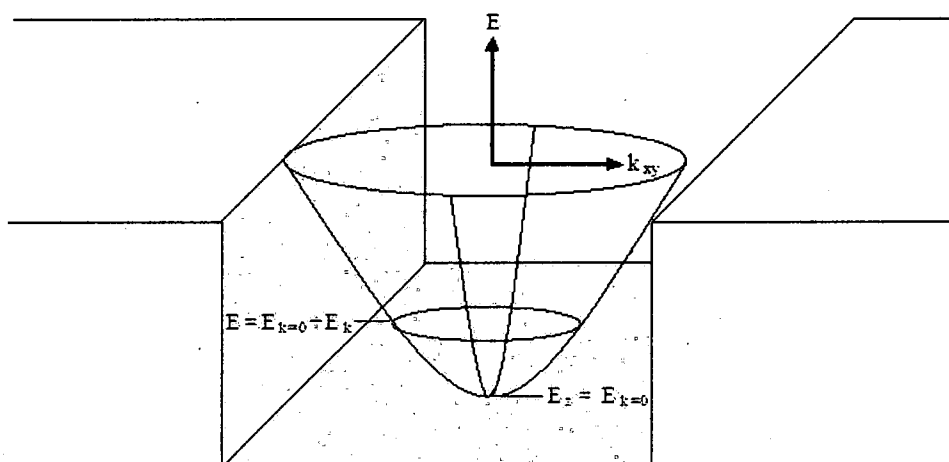


Figure 1.1.2: E-k diagram showing the 1D-confinement and 2-D in-plane dispersion of an electron in the conduction band of a quantum well.

Radiative emission in quantum wells can occur between bands, known as interband transitions, or between states in a single band, termed intersubband transitions (see Figure 1.1.3).

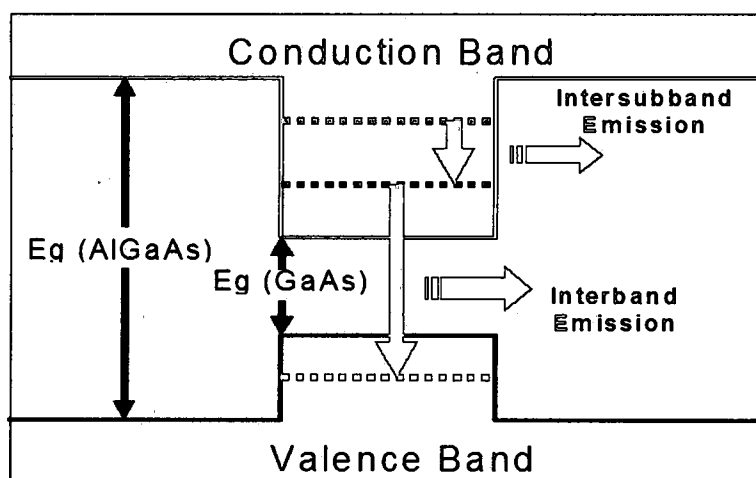


Figure 1.1.3: Conduction and valence band diagrams in an arbitrary GaAs/AlGaAs heterostructure showing intersubband and interband emission.

While the emission frequency from an interband transition is largely dependent upon the natural bandgap of the semiconductor material the emission frequency, or subband energy separation, of an intersubband transition can be controlled by the width of the well and composition of the well and barrier materials. Because of the ability to engineer the energy separation between confined states in a quantum well, intersubband devices can be exploited to create radiative emission at low energies, or long wavelengths, which are not available in standard semiconductor materials due to the limitations of the natural bandgaps.

The flexibility for engineering the subband energy separations has lead to the analogy of the quantum well as an “artificial atom”. A general diagram of this comparison is shown in Figure 1.1.4. In this figure the conduction band of a quantum well and three confined states (labeled E1-E3) are shown on the right while a generic potential of a hydrogen atom and its associated states is depicted on the left.

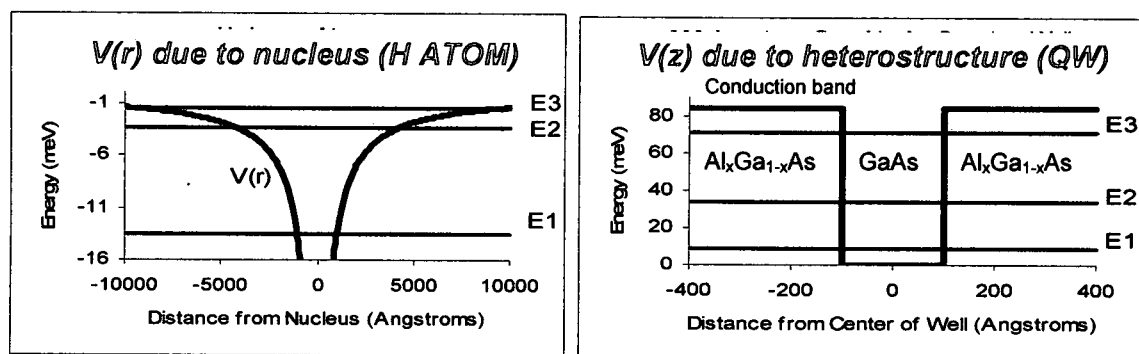


Figure 1.1.4: An example showing the comparisons between a Hydrogen atom (left) and a quantum well (right).

While nature has provided a limited variety of potentials, as represented by the periodic table, the artificial atoms (quantum wells), and their associated electron energy states, can be engineered over a nearly boundless range using different combinations of semiconductor materials and quantum well dimensions.

Extending this “atomic” analogy into artificial molecules and materials whose electronic properties can be engineered provides a basis for understanding the design of quantum cascade lasers. Consider two quantum wells separated from one another such that there is no interwell interaction (Figure 1.1.5a). Here both wells contain their own respective energy states and corresponding wavefunctions which are dependent on the potential of the individual systems. If the individual wells are combined such that they share a common barrier, typically on the order of or less than the width of the wells themselves, the systems are no longer isolated and the wells are considered coupled (Fig 1.1.5b).

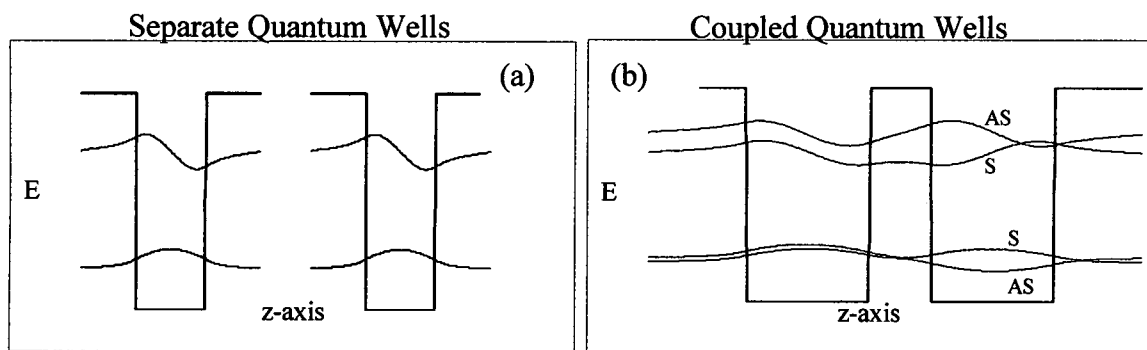


Figure 1.1.5: (a) Non-coupled, isolated quantum wells and (b) coupled quantum wells showing the wavefunctions splitting into symmetric (S) and anti-symmetric (AS) states. The wavefunctions are shown offset vertically to represent their respective energy levels.

In this coupled-well case the energies and wavefunctions are now a function of the potentials of both wells. In keeping with the atomic analogy there is now an “artificial molecule”. In fact the splitting of the wavefunctions into symmetric (S) and anti-symmetric (AS) states is often referred to in atomic physics as the bonding and anti-bonding states of a molecule.

Now with the coupled-well interaction there is a system where the electron energies and the wavefunctions are controlled by the widths and compositions of the individual wells, as well as the width and composition of the barrier material. In addition to the flexibility permitted by the choice of material and the dimensions of the layers, application of an electric field across the growth direction permits an addition to the potential $V(z)$ which can be described as

$$V(z) = V_{\text{material}} + V_{\text{electric field}} \quad (1.1.3)$$

Consider two GaAs wells, one 150Å and the other 100Å, separated by an $\text{Al}_{0.15}\text{Ga}_{0.85}\text{As}$ barrier of 25Å shown in Figure 1.1.6a.

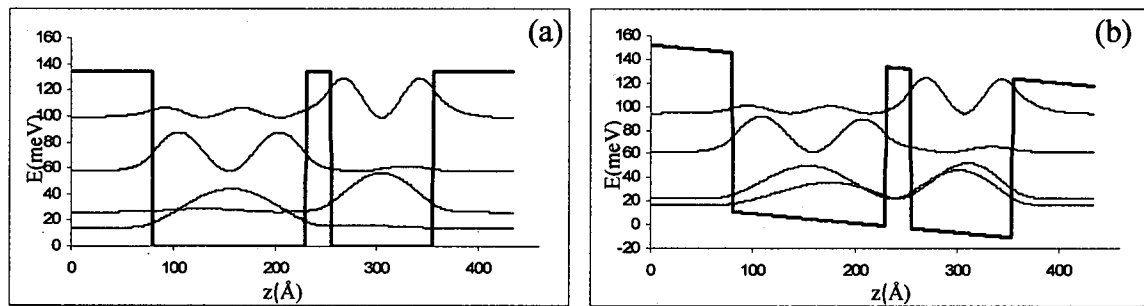


Figure 1.1.6: (a) A two-quantum well structure with no applied electric field and (b) the same device under an applied bias of 8kV/cm. The wavefunctions shown here are the moduli squared and are offset to their respective energies.

Here it is observed that, since the leftmost well is wider than the neighboring well, the energy separation between the ground state of each is sufficient enough that the coupled well interaction is minimal and the wavefunctions appear primarily isolated in their respective wells. If a voltage is applied across the growth-axis of 8kV/cm , which for the current system corresponds to approximately 4mV , the result is a slope to the potential of the system resulting in the wavefunctions shown in Fig. 1.1.6b. This example clearly illustrates that the combined variability of material choice, layer thickness, and applied voltage allows for manipulation of not only the subband energies but also the respective wavefunctions. This energy and wavefunction engineering is what enables the design of quantum cascade lasers.

1.2 Introduction to Quantum Cascade Lasers

QCL's are intersubband unipolar devices meaning that the radiative transitions occur between discrete states entirely within the conduction band and involve only electrons (i.e. electron-hole recombination and other intraband transitions are negligible compared to intersubband transitions). The devices are typically constructed of multiple quantum wells arranged in some periodic fashion which repeats several to hundreds of times. Returning to the previous atomic analogy a QCL can be envisioned as truly representing an "artificial material" where, through designed manipulation of subband energies and wavefunctions, the electrical characteristics can be tailored to a desired operation. To illustrate this effect of using multiple quantum-well structures to engineer a QCL observe the diagram in Fig. 1.2.1.

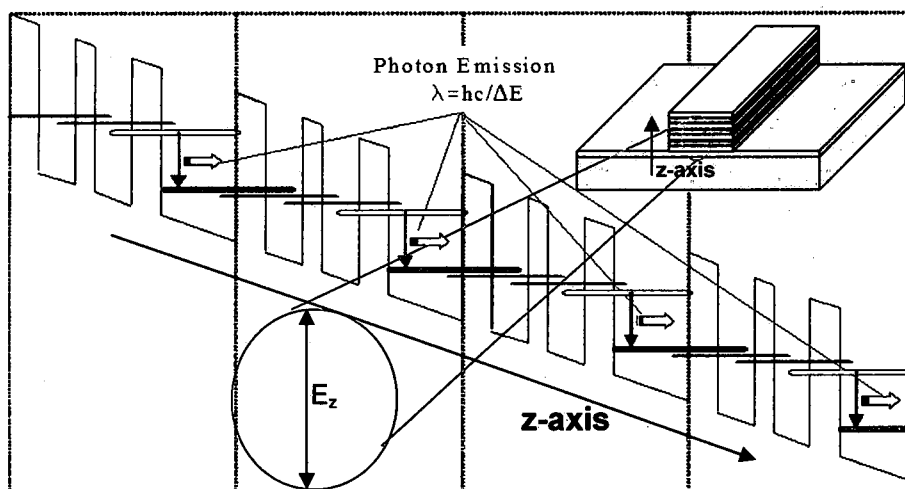


Figure 1.2.1: The conduction band diagram in an example QCL structure showing 4 repeating periods.

This example QCL structure shows 4 identical periods of 3 quantum wells per period with a bias applied across the growth direction. Due to selection rules for radiative emission these devices operate as an edge emitters. In this theoretical structure electrons from the two narrower wells are injected into the upper lasing state (shown in red) of the larger well. Radiative intrawell emission is allowed to occur within the larger well followed by a depopulation of the lower lasing state (shown in blue) to the states in the narrower wells of the next stage. This process continues through the subsequent periods of the extended structure thus creating a “cascading” effect where a single electron traveling through the conduction band has the ability to emit a photon during each period. Theoretically, an electron could emit as many photons as there are stages leading to greater than 100% quantum efficiency. In reality there are much faster non-radiative scattering mechanisms, especially at the lower subband energy separations required for terahertz frequency emission, which makes even the creation of a population inversion a difficult task.

in the treatment of “ideal” 4-level lasers, such as τ_{43} and τ_{21} being much faster than τ_{32} , similar conclusions cannot be made *a priori* in these quantum cascade structures. This critical fact is especially important for THz QCL’s as the energy spacing between lasing levels is small (roughly 4 to 40meV) and therefore states in the active region are subject to similar intersubband scattering effects as the injection and collection processes.

Since typical approximations concerning the lifetime of states cannot be made with adequate confidence, the intersubband scattering processes must be calculated explicitly for all relevant transport phenomena. The typical approach to this problem is through the use of Fermi’s Golden rule

$$\frac{1}{\tau_i} = \frac{2\pi}{\hbar} \sum_f \left| \langle f | \tilde{H} | i \rangle \right|^2 \delta(E_f - E_i) \quad (1.2.1)$$

which describes the lifetime of a particle in initial state $|i\rangle$ scattering out to all states $|f\rangle$ due to a perturbation \tilde{H} . The primary component of this equation is the matrix element

$$\langle f | \tilde{H} | i \rangle = \int_{-\infty}^{+\infty} \psi_f^* \tilde{H} \psi_i dz \quad (1.2.2)$$

which indicates that the scattering rate is largely due to the spatial overlap between the respective initial and final state wavefunctions with the specific perturbation. Since the ability to modify the wavefunctions using coupled quantum wells and applied electric fields was already established it becomes evident that this can be exploited for the flexibility to engineer scattering rates in quantum cascade lasers. Therefore, as shown in figure 1.2.2, once transitions to be allowed, maximized, or minimized, have been identified the examination of system parameters required for the proper “wavefunction engineering”, which will produce the desired laser operation, can be initiated.

While this capability to tailor the electron transport through multiple quantum well structures is remarkable it is noteworthy to point out some complicating factors specific to THz-frequency QCL's that clearly indicates the colossal scope of the design process. To start, the single particle expression of equation (1.2.1) represents scattering from a specific state $|i, k_{\parallel}\rangle$ to specific states $|f, k_{\parallel}\rangle$ and thus is not sufficient to represent the lifetime of a singular subband unless one intends to track each individual particle traversing the system. In fact, intersubband scattering processes between two states can vary dramatically for small energy separations depending on the in-plane kinetic energy k_{\parallel} . This effect is most easily illustrated by considering that in many THz-QCL designs the subband energies are separated by less than the longitudinal-optical (LO) phonon energy (see figure 1.2.3).

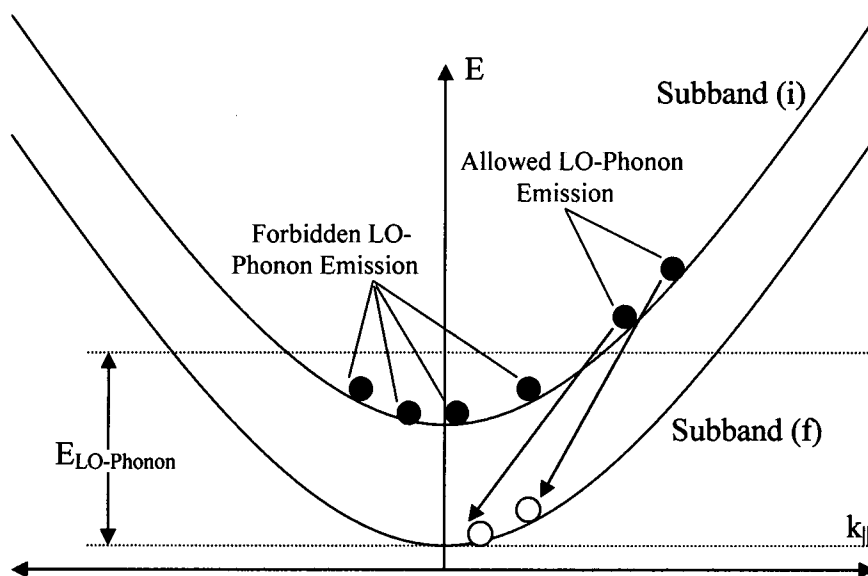


Figure 1.2.3: An illustration of the kinetic energy dependence of intersubband transitions due to the emission of an LO-phonon.

In this diagram it is observed that electrons near the minima of the initial subband (i) are forbidden from transitioning to the lower subband (f) through LO-phonon emission whereas electrons with sufficient in-plane kinetic energy can emit a phonon. This effect demonstrates the unequal scattering due to a specific mechanism even within a particular subband. In fact, these thermally activated scattering mechanisms are a leading cause of the difficulties in high temperature THz-QCL operation which were not apparent in mid-IR devices. These THz specific complications are further illustrated in Figure 1.2.4 where the mean (i.e. integrated over the Fermi-Dirac distributions in both initial and final states) LO-phonon and electron-electron scattering rates are plotted vs. the subband energy separation.

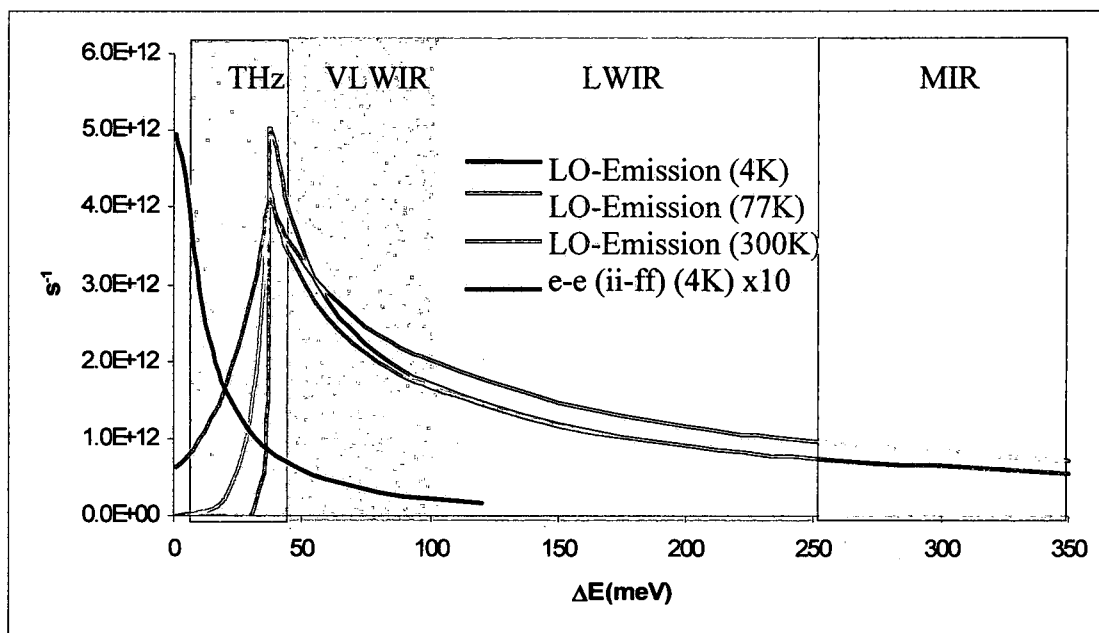


Figure 1.2.4: LO-phonon emission and electron-electron intersubband scattering rates vs. the subband energy separation. The phonon emission is calculated in a single GaAs well with AlAs barriers and the electron-electron rates are calculated for an interwell doublet.

Figure 1.2.4 shows that at large energy separations, corresponding to mid-IR devices, the LO-phonon scattering rate is nearly constant with respect to energy. At the smaller energy separations required for THz devices, the phonon scattering rate becomes a strong function of both the energy and the temperature. Additionally, at these THz energies, electron-electron scattering is not only significant but also a strong function of the subband separation. To further complicate the design of THz frequency lasers, in the typical rate equation picture as depicted by Figure 1.2.2, these scattering rates are, in some circumstances, shown to be functions of not only the energy separation and temperature, but also of the electron concentrations themselves, i.e. a scattering rate $W_{if}(\Delta E_{if}, T)$ becomes $W_{if}(\Delta E_{if}, T, n_i, n_j)$. Further, as electrons flow through a multi-well structure, the possibility of many scattering mechanisms between (intersubband) and within (intrasubband) states can lead to a redistribution of the kinetic energy introducing an electron temperature T_e distinct from that of the lattice. This further complicates the determination of scattering rates where $W_{if}(\Delta E_{if}, T, n_i, n_j) \rightarrow W_{if}(\Delta E_{if}, T, n_i, n_j, T_e)$.

Additionally, the use of Fermi's Golden Rule to describe electron transport is routinely treated as a representation of electrons "hopping" from spatially extended stationary-state to stationary-state and does not normally consider a coherent time-evolution of the states involved. On the contrary, an attempt to model QCL transport based solely on resonant tunneling does not fully characterize the effects of incoherent scattering on the tunneling processes. These effects and ambiguities are a subject of current and future research and thus will be treated in detail in subsequent chapters.

1.3 Progress in QCL Technology

Quantum cascade lasers were conceived alongside early work involving the optical and electrical confinement properties of semiconductor heterostructures [1]. Following the prediction of the influential 1970 paper by Esaki and Tsu [2], which described negative differential conductivity in a quantum well superlattice, Kazirinov and Suris predicted light amplification by photon-assisted resonant tunneling in a superlattice design [3]. In this proposed device a repeating lattice of quantum wells was envisioned where the application of a voltage across the structure would permit electrons to tunnel across a barrier, assisted by the emission of a photon, and then continue to the next well allowing for the process to repeat for a many periods as the “superlattice” contained (see Figure 1.3.1).

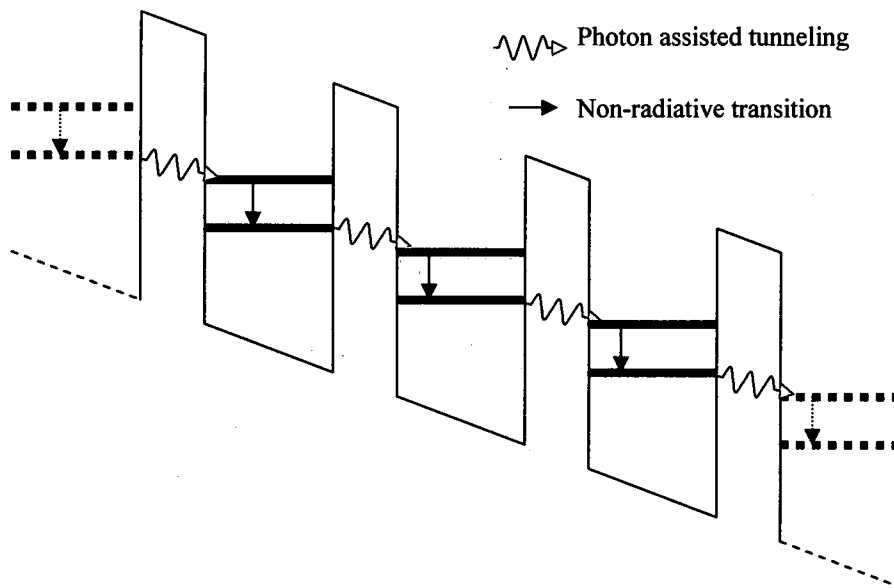


Figure 1.3.1: Diagram representing the original QCL proposal.

Experimental verification of quantized states in heterostructures containing a lower potential middle layer, on the order of hundreds of angstroms, was reported in 1974 [4]. Concepts of "bandstructure engineering" [5] started to emerge where the notion of tailoring electronic and optical properties of semiconductors by creating artificial materials was realized. Throughout the 1970's and 1980's many devices based on quantum well structures were proposed and confirmed leading to tangential technologies but the demonstration of a quantum cascade laser remained elusive. In-depth historical reviews of the technology preceding the development of QCL's can be found in references 6-8.

Evolution of designs and the maturation of crystal growth technologies and procedures eventually lead to the first confirmed device, operating in the Mid-IR and at cryogenic temperatures, to be demonstrated in 1994 by Faist et. al. at Bell Labs [9]. The key design aspect which permitted operation of this laser came from a more in-depth understanding of non-radiative transitions due to mechanisms such as electron-electron and longitudinal-optical (LO) phonon scattering. These extremely fast non-radiative transitions, which can be in the sub-picosecond range, make achieving an intersubband population inversion very difficult while attempting to permit radiative transitions necessary for gain. Recognizing these impediments to achieving inversion Faist and colleagues developed the concept of utilizing injector regions which separate the active regions where lasing is to occur (Figure 1.3.2). In this type of design intermediate injector wells are used to create "minibands" separated by "minigaps" that form the active regions.

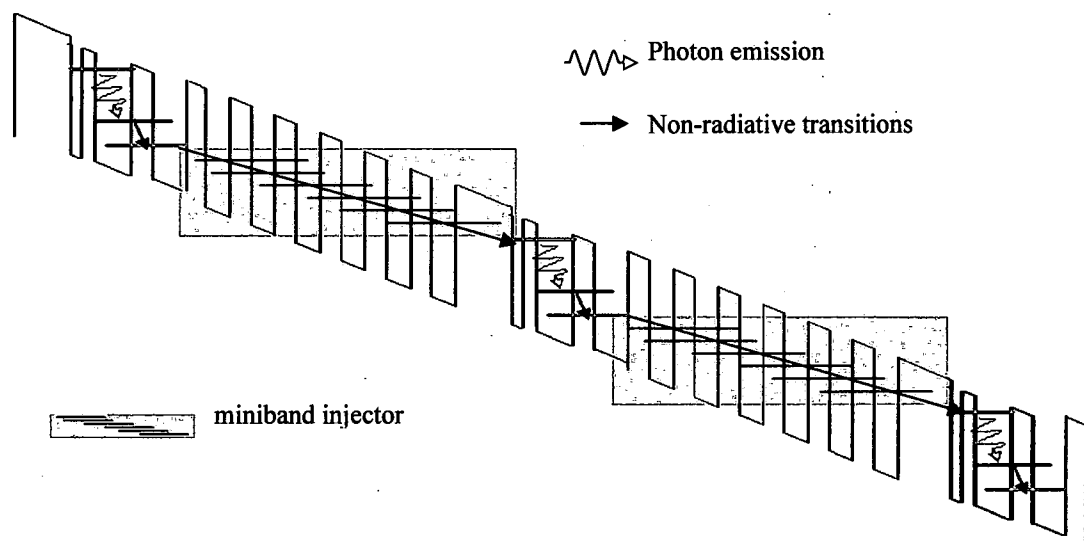


Figure 1.3.2: Diagram representing the first demonstrated QCL.

Since this initial breakthrough mid-IR QCL technology has advanced rapidly, permitting high power and continuous-wave (CW) operation at and above room temperature [10,11]. The emergence of the QCL as a dominant source for mid-IR applications, where natural solid-state sources are lacking, inevitably guided research further into the far-infrared and THz regions of the spectrum which have been historically plagued by an absence of efficient and high-power sources.

Early proposals for THz-QCL's were based upon trying to selectively inject and depopulate the active regions, where the lasing transition occurs, by chirped-superlattice designs (Figure 1.3.3a) similar to the successful mid-IR devices [12-15]. While THz-electroluminescence was observed in several cases [16-18] these designs could not achieve lasing in part due to the poor radiative confinement of the long wavelength THz frequencies. In 1998 the idea of a surface plasmon waveguide was proposed [19] and first implemented in 1999 by Ulrich et. al. [20]. Although evidence of spontaneous emission was observed, lasing at THz-frequencies remained unconfirmed. During this same time

period an alternative, non-miniband injector, design based on a phonon-depopulation (Figure 1.3.3c) of the lower lasing state was being pursued by researchers at MIT, under the direction of Qing Hu, where THz-emission was again verified without lasing [21,22].

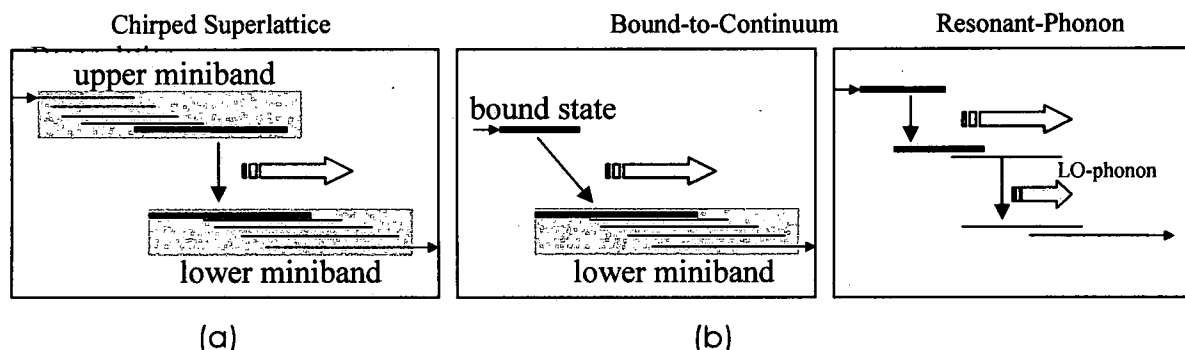


Figure 1.3.3: The three proven THz-QCL designs. (a) Chirped-Superlattice, (b) Bound-to-Continuum, and (c) Resonant-Phonon Depopulation.

The first successful demonstration of a THz-QCL operating at 4.4THz in pulsed mode at a temperature of 50K was reported in 2002 by Kohler et. al. [23] using a chirped superlattice design with a surface plasmon waveguide. In these devices (Figure 1.3.3.a) lasing takes place between bands of many coupled-well states spaced closely in energy such that the radiative transition can be considered as taking place between two “minibands” separated by a “minigap”. The concept in these devices is essentially that intra-miniband transport is much faster than the interminiband processes permitting a population inversion between the lowest state in the upper miniband and the highest state in the lower miniband. Soon after the initial demonstration Rochat et. al. [24] described lasing in a similar structure at 4.5THz and later in the same year CW THz-QCL operation was reported [25,26].

In 2003 two alternative THz-QCL designs were reported to have achieved lasing. A bound-to-continuum design created by Scalari et. al. [27] (Figure 1.3.3b) achieved THz lasing above liquid Nitrogen temperature for the first time and displayed pulsed operation up to 100K and 50mW CW power at 10K. These bound-to-continuum designs typically consist of a more localized upper lasing state while still employing a miniband in the lower portion of the active region. The second successful alternative design, based on a resonant-phonon depopulation mechanism (Figure 1.3.3c), was also verified by Williams et. al. [28].

With the direction towards longer wavelengths and higher operational temperatures being pursued, problems of confinement and free-carrier absorption in the heavily doped outer layers were becoming more problematic [29]. To combat these unfavorable long-wavelength conditions Williams et. al. [30] introduced a metal-metal waveguide in 2003 providing near unity confinement and combined with further design and fabrication improvements reached above liquid Nitrogen temperature at 3.0THz and later pulsed operation up to 137K at 3.8THz [31]. Recognizing the potential for depletion of the lower lasing state using resonant LO-phonon transitions the inclusion of an additional miniband stage in the superlattice designs to produce alternating photon-phonon cascades also permitted these devices to reach lasing at 80K in 2004 [32].

With the problem of confinement being solved by the metal-metal waveguides much of the recent progress has been in optimizing previously established designs. In particular, the resonant phonon depopulation QCL, which contains limited injector states between active regions minimizing THz absorption compared to the densely packed states of the minibands designs, has emerged as the leading candidate for high temperature operation. The initial design for these resonant phonon lasers, based on a

four-well per period scheme (figure 1.3.4), have undergone extensive optimization in recent years.

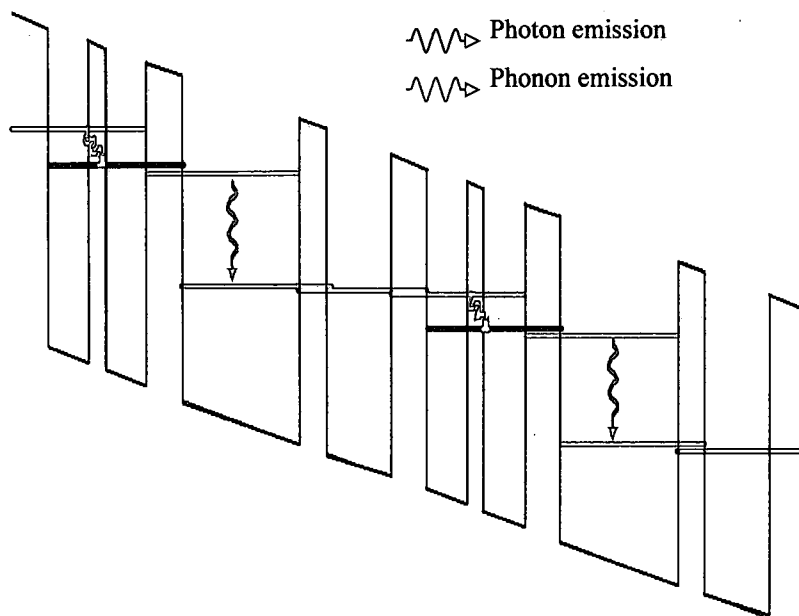


Figure 1.3.4: Diagram of the 4-well per period resonant phonon depletion QCL.

Improvements in the metal-metal waveguide [33,34], studies of optimal doping levels [35-37], and investigations of injection and collection barrier widths [38,39] continue to improve the original design. To date, this 4-well resonant phonon depletion QCL has operated up to 164K pulsed and 117K cw at 3.0 THz [34]. High power operation up to 248mW pulsed and 138mW cw has also been demonstrated [40] in these devices at low, 10K, temperatures, and adjustments to the injector have lead to frequencies as low as 1.9THz [41]. Recently three-well per period designs, grown without the intermediate injector well between the phonon stage and the active region, were demonstrated [42] and currently hold the THz high temperature operation record of 178K in pulsed mode at 3 THz [43].

1.4 Theoretical and Computational Background

The theoretical foundation for QCL's, namely the quantization of states in a quantum well, is based on established foundations of quantum and wave mechanics and has become standard textbook physics. While basic concepts of confined states, tunneling phenomena, and the scattering of electrons in semiconductors are theoretically mature, the implementation of well known principles to the design of modern day heterostructures is still being actively researched and debated. Since the analytical groundwork can be traced back to the beginning of quantum mechanics and solid-state theory, and have been developed over an extensive range of disciplines, a precise timeline of the various theory and computational techniques necessary for modeling QCL's is difficult to portray in a linear manner.

Starting with the original proposals and explanations of quantum cascade laser operation this evolution of the theoretical and computational development can be portrayed by considering the perpetually linked, yet distinct, motivations of the physics and engineering communities. In this manner the background of the modeling for quantum cascade lasers can be roughly illustrated as shown in Figure 1.4.1. Although the true development of various theoretical and computational approaches have been ongoing for decades, and thus does not truly fit into the ordered timeline displayed in Figure 1.4.1, the basic trend of the engineers desire for employable computational models and the physicists continued curiosity into the nature of QCL phenomena have combined to create an large web of theories and simulation techniques which can be extremely difficult to unravel. Current trends however, as illustrated in the figure, seem to be recombining the assortment of approximations into comprehensive, fully quantum

mechanical, descriptions. In what follows will be a general outline, certainly not all-inclusive, of the theoretical and computational evolution of QCL modeling.

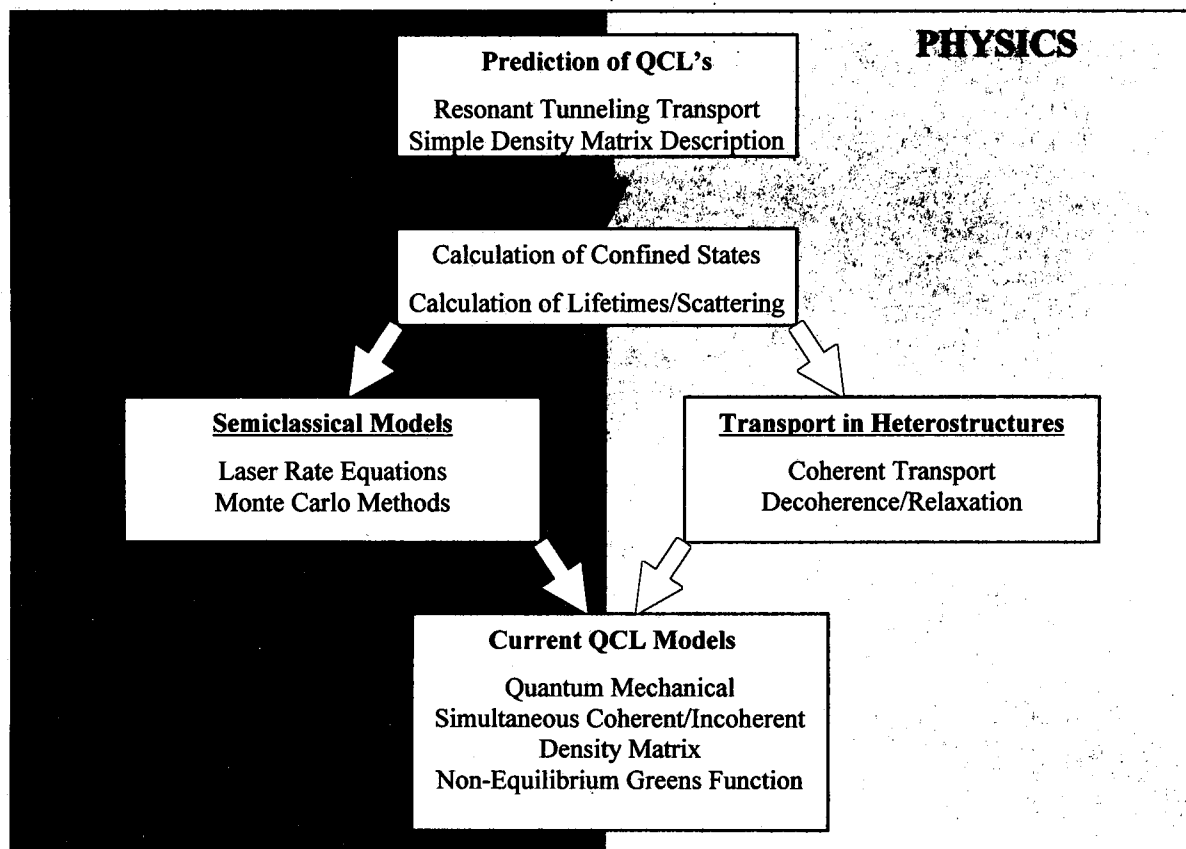


Figure 1.4.1: Illustration of the evolution of QCL modeling.

Investigations into the electronic properties of 2-D systems [44], i.e. devices where electrons are confined and quantized in a single dimension, go back several decades to the original papers by Tsu[2] and Kazarinov and Suris[3]. Theoretical considerations of the altered bandstructure, including determination of quantized energy states and their corresponding wavefunctions, have been rigorously treated using a wide variety of techniques. While atomic level approaches have been examined [45-49] more

accessible and computationally simpler approaches, using the envelope and effective mass approximations have traditionally shown, in most cases [50,51], to be suitable in describing quantization effects in quantum wells, coupled wells, and superlattice structures [52-63].

Essential for laser design is the knowledge of the lifetimes of particular states, leading directly, in the traditional semiclassical sense, to the determination of potential population inversion and thus gain. As a result, active modeling of the scattering rates for intersubband and intrasubband transitions began concurrently with the modeling of 2-D electron states. Similar to the precise description of the electronic states, determination of scattering rates has been treated in a variety of approaches. Most procedures invoke Fermi's Golden Rule and differ primarily in the portrayal of the subbands, wavefunctions, and the perturbation, specific to the 2-D systems. The multitude of potential scattering phenomena considered has included: phonon scattering [68-71], electron-electron scattering [72-75], impurity scattering [70,76,77], and interface roughness scattering [70,78].

In the original prediction [3] and first demonstration [9] of QCL operation, electron transport was explained using simplified, somewhat qualitative, descriptions of sequential resonant tunneling. In the original mid-IR QCL's the numerous states of the minibands were essentially treated as a single entity and the injection mechanism was analyzed in terms of a 2-state density matrix description of transport between the lowest miniband state and the upper lasing level [79]. By assuming intraminiband transport effectively carries the electrons quickly to the lowest states, the system is basically a 4-level laser, driven by resonant tunneling (figure 1.4.2a). Although the lifetime of the states is employed in the tunneling description, usually by considering phonon scattering

from states within the active region, explicit calculation of the numerous scattering transitions previously mentioned was typically not involved [79].

Using scattering rate calculations based on Fermi's Golden Rule, Harrison and colleagues developed a model to treat transport in a manner more similar to the standard rate equation approaches to laser operation [80]. As discussed previously in section 1.1., the quantized states, typically depicted as singular objects, are truly subbands containing states distributed in a two dimensional k-space (Figure 1.1.2). By considering that the population distributed in these subbands are thermalized and can be described by Fermi Dirac statistics [81], a mean scattering rate [50] for electron-phonon and electron-electron transitions was implemented allowing the QCL system to be treated as an N-level laser (Figure 1.4.2b).

With the transition rates themselves dependant on the subband populations $W_{if}(n_i, n_f)$ these models were solved using a self-consistent rate/population iteration. Simulation of the mid-IR QCLs using this approach showed qualitative and sufficient quantitative agreement with experimental results [82-84]. Improvements to this approach were made by developing a technique to account for the non-equilibrium electron distributions [85], where the electron temperatures must be described separately from that of the lattice. Implementation of another level of self-consistency (scattering rate/population/kinetic energy balance) displayed improved results in the modeling of both Mid-IR and THz-QCL's [86-87]. Calculation of electron-ionized impurity and interface roughness scattering was also been implemented showing enhanced simulation capabilities [88].

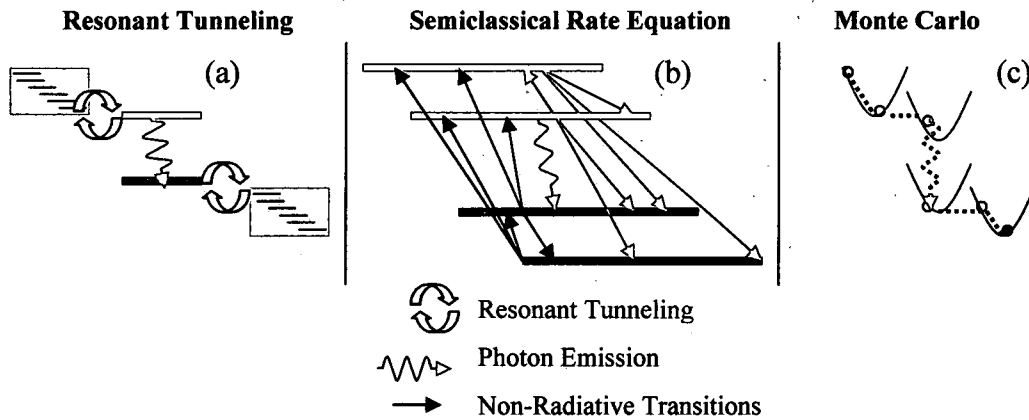


Figure 1.4.2: Various illustrations of transport descriptions in QCL's (a) Resonant tunneling transport description in Mid-IR QCL's. (b) The semiclassical laser rate equation approach. (c) Monte-Carlo Methods.

Another simulation strategy which emerged into the design of QCL's is the Monte Carlo method. Unlike the rate equation models described above, these calculations statistically track the transitions of an electron in both energy and momentum space traversing through the subbands of a QCL system (Figure 1.4.2c). These types of simulations [89-92] follow a single particle, or an ensemble of particles, through a heterostructure in time subjected to probabilistic transitions due to interactions with other particles or scattering mechanisms. Application of these methods to THz-QCLs has and continues to be implemented for the simulation and design of THz-QCL's [93-101].

Representation of transport as due to resonant tunneling injection in mid-QCL's [79], and in the initially proposed devices [3], was derived by considering the wavefunctions of the states as localized on opposite sides of a barrier. This description of tunneling transport was derived using a tight-binding/coupled-mode scheme using a simple 2-state density matrix calculation. In the semiclassical rate equation and Monte

Carlo methods the eigenstates of the system are calculated using a Hamiltonian which describes the repeating QCL structure usually over a few periods of the system. Unlike the resonant tunneling picture, these eigenstates are defined over the entire calculated system and have the ability to couple to all other states producing delocalized wavefunctions across, sometimes, many wells. This phenomenon, which is a direct result of the time independent Schrödinger's Equation, can result in large current spikes being predicted at certain biases where "parasitic current channels" are predicted to materialize via a state becoming extended across the system. These simulated current spikes, which are not observed experimentally, are many times omitted [96,97], and have been attributed to unrealistic wavefunction delocalization [93,94] which cannot be accounted for using a picture of scattering between unbounded envelope wavefunctions.

As an alternative to omitting the predictions at certain biases, Callebaut and Hu returned to a calculation similar to the resonant tunneling description [79] of separating the injector and upper lasing state. In their "hybrid simulation" [102] the repeating periods of a QCL were separated. Intraperiod transport using delocalized wavefunctions were treated using the semiclassical Monte Carlo method. The inter-period transport was described by breaking up the system and using a density-matrix/tight-binding approach to tunneling between states localized in their respective periods [102]. In this simulation they found that the treatment of coherent inter-period transport displayed superior prediction of current voltage characteristics, without unreasonable current spikes. This model also demonstrated that a proper description of incoherent scattering, which not only transfers electron between and within subbands, but also leads to dephasing of the coherent interaction, allows for a more accurate prediction of gain, which the semiclassical/delocalized methods tend to over-predict [93,94,102]. While the usefulness

of these semiclassical methods has not been entirely negated by these results further examination of the physics concerning coherent and incoherent transport, and their interplay, has been recognized as important for accurate modeling and prediction.

Questions regarding the physics of the transport in quantum heterostructures have been actively pursued since the conception of these devices. Transport has been described in numerous ways such as hopping between localized states [103-105], sequential resonant tunneling [79, 106], and scattering between delocalized states, as in the semiclassical models previously discussed. While results of some simulations treating both coherent and incoherent transport simultaneously have lead to the argument that quantum(coherent) effects are negligible in QCL's [107,108] due to semiclassical agreement with current voltage characteristics, experimentally observed gain oscillations [109,110] suggest that these descriptions may not fully represent QCL operation. Indeed, as pointed out previously in the work of Callebaut and Hu [102], it may be possible to reasonably simulate I-V curves while overestimating the gain.

The arguments for and against treating transport as coherent or incoherent are likely a result of the either/or choice which permits simplification of a model. In depth treatments of even 2-state systems [111] have shown that collisions/scattering events lead to relaxation of the coherent resonant tunneling between states initially treated as localized [112, 113]. In this picture a coherent oscillation between localized interwell states is eventually disrupted by incoherent scattering mechanisms. Other analysis has shown that full quantum mechanical treatment permits "scattering induced coherence" [114-116] where incoherent phenomena (electron-phonon interactions etc.) can be the cause, in addition to the disrupter, of coherences. The potential confusion which can occur due to these varying pictures is clarified by the reality that the multitude of

modeling approaches are truly approximations to the same comprehensive physical models [116, 117] and under various limiting situations, dictated by the device structure, each model may have validity.

With current progress in THz-QCLs approaching a technological phase largely consisting of improving already established designs, the validity of models which may or may not predict all important aspects of device performance has become increasingly important. As a result highly quantum mechanical models are becoming more prevalent. Among these approaches are the Density Matrix Formalism [116,118], the Non-Equilibrium Greens Function NEGF [119-126], and other many-body techniques [127]. Although the “fully-quantum mechanical” models should be theoretically equivalent, divergence can still occur due to approximations, such as the choice of truncated basis sets [121], which must be made for implementation. Results from these models have been promising in comparison to experimental results [120-122] and have shed light on some of the breakdown of conventional models. In particular, calculations of gain in various QCL designs has reconfirmed the suggestion that traditional approaches may be reasonable in certain Mid-IR devices yet insufficient in many THz-QCL designs [123]. In fact, recent simulations [126] suggest that the gain can be reduced substantially at increasing temperatures due to scattering induced level broadening even while a significant population inversion exists. This result indicates the usual emphasis on calculating populations cannot fully describe a systems ability to achieve above threshold gain. Further contrasting semiclassical models, simulation using the NEGF approach have implied that interwell transport is fully a coherent process while scattering redistributes particles locally in energy and momentum [124,125]. While these more comprehensive models are invaluable to understanding the fundamental mechanisms of

QCL operation, and can lead to further improvements in established designs, the analytical complexity and computational demands may limit their application in the exploration of new and novel heterostructures unrevealed in a nearly limitless design space.

1.5 Dissertation Overview

This research is a methodical examination of fundamental theory and required calculations in an effort to reduce theoretical complexity and computational demands. This dissertation is not an attempt to establish or further a comprehensive theory of transport in quantum heterostructures nor is it an application of previous models towards simulating new designs or investigating parameters within quantum cascade lasers. Presently, the most commonly applied techniques to the modeling of THz-QCL's are the semiclassical approaches, such as the Monte Carlo simulation, or the quantum-mechanical techniques, for example, the Non-Equilibrium Green's Function method. The semiclassical techniques typically require many hours for the simulation of a single device at a single operating temperature. These models are not only restricted in their ability for iterative design, or implementation into algorithms, but have the flaw of predicting unphysical operation due to the unbounded delocalization of static wavefunctions. The fully quantum mechanical models correct these semiclassical deficiencies by treating coherent and incoherent phenomena simultaneously, however, at the expense of even greater computational demands. Due largely to the recognition of the constraining computational requirements, and the highly numerical implementation for the modeling of laser operation, a direction of simplicity was chosen. Through a systematic analysis of theoretical framework and numerical procedures a description of

transport and gain in THz-QCL's is developed where all properties of a multi-quantum well system can be described as linear combinations of single well properties requiring only the input of heterostructure dimensions for immediate evaluation. The result is a simple model which incorporates both coherent and incoherent effects in an analytically accessible manner and is capable of near real-time THz-QCL simulation in excellent agreement with experimental data, without the unphysical predictions of the semiclassical models.

In Chapter 2 approaches for the calculation of eigenstates (i.e. electron energies and wavefunctions) are discussed. While these calculations, in general, are not computationally limiting the conventionally used numerical techniques immediately stray, at these preliminary stages, from an intuitive analytical description. As a result, potential unphysical phenomena, such as unconstrained wavefunction delocalization, become difficult to interpret without significant familiarity observing numerically generated data. To overcome the obstacles present in these approaches an analytical construction for the eigenstates in single quantum wells is chosen as a basis. Coupled well interactions are then described using a tight-binding analysis of the local single well basis. While these general procedures are not unique, the specific description of the analytical basis in an automatically normalized form, simplifications to the standard tight-binding analysis, and the pre-evaluation of all necessary matrix elements (integrals) to an indefinite form, is offered. This presentation allows for the immediate analytical description of eigenstates for arbitrary multi-well systems requiring only the designation of the heterostructure interface locations for evaluation.

The most considerable obstacle to efficient calculation of transport in quantum heterostructures is the evaluation of scattering rates, or lifetimes. In the context of

Fermi's Golden Rule, these scattering events include the fundamental matrix element (integral) of the initial and final state wavefunctions with the specific perturbing potential. Since the confined electronic states are in fact two-dimensional "subbands" these calculations require the integration over all initial and final state wavevectors and the perturbing wavevectors weighted over thermal kinetic energy distributions. In addition, the traditional numerical techniques produce wavefunctions which vary at each separate bias (voltage). These complications generate enormous computational requirements and can take many hours to simulate a single current-voltage (I-V) relationship for a specific device.

In Chapter 3 these scattering rate complications are investigated and techniques to limit computation are presented. Specifically, using the unbiased single well eigenstates as a basis combined with the approximated tight-binding procedure for representing coupled-well states, a technique is given to reduce this computational time to nearly zero. To accomplish this Fermi's Golden Rule is expanded in the single-well basis with the hypothesis that all scattering occurs locally (intrawell). Using mean scattering rates, where the 2D nature of the subbands is averaged out, an approximation is presented where transitions in multi-well systems can be described by linear combinations of intrawell scattering rates. Under this assumption, empirical fitting functions for the limited transitions occurring between single well basis states are found permitting all lifetimes in arbitrary systems to be immediately evaluated by the designation of the interface locations and the temperature.

In Chapter 4 the developed procedures are incorporated into descriptions of transport in simple quantum heterostructures. The comparison of a full numerical approach with the presented simplified method is demonstrated in the context of the

semiclassical “laser rate equations” clearly establishing the tremendous computational advantage of the prescribed technique. The validity of the semiclassical transport models applied to terahertz quantum cascade lasers are then called into question. Treatment of the interplay between coherent and incoherent phenomena, and resulting dephasing effects, is illustrated using the Density Matrix Formalism. Using simple approximations the full density matrix treatment is then reduced to a diagonal form resembling the familiar “laser rate equations” while maintaining a description of decoherence. A description of the gain is also derived where, contrary to the semiclassical models, dephasing effects play a crucial role. With all the necessary parameters for evaluating the diagonal density matrix coming from the analytical basis, the tight-binding procedure, and the empirical scattering rate expansion, the simplified description of transport allows for subband populations, current densities, and gain to be presented in an analytical form which can be evaluated in near real-time.

In Chapter 5 the culmination of all the presented techniques, simplifications, and approximations is demonstrated by simulating realistic terahertz quantum cascade lasers. Calculations are compared with reported measurements available in the literature. The procedures outlined in this research are shown to permit near-real time simulation of laser operation, compared to hours or days for more heavily numerical techniques, while predicting measurable quantities in excellent agreement with experimental results. The accessibility and speed of the procedures implemented, their accuracy compared to other models and experimental results, as well as their potential limitations are summarized.

CHAPTER 2

CALCULATION OF ENERGIES AND WAVEFUNCTIONS IN QUANTUM HETEROSTRUCTURES

2.1 Introduction

Calculation of electron energies and wavefunctions in quantum heterostructures is central to the design of quantum cascade lasers and, as eluded to in the introduction, has been thoroughly investigated using an assortment of established procedures [44-63]. With the advent of modern computers the customary practice is to simply use brute-force numerical methods to determine the eigenstates of an arbitrary Hamiltonian used in the time-independent Schrödinger's equation. These numerical calculations, while typically not burdensome, lack the intuitive nature of a more analytical description and have the potential to predict unphysical phenomena, such as unconstrained wavefunction delocalization. In the first section of this chapter these fully numerical calculations will be presented and used as a secondary introduction to quantum well eigenstates, illustrating common coupled quantum well behavior.

After this numerical introduction the description of an analytical single well basis is developed. While analytical solutions for the eigenstates in a single finite-barrier height quantum well can be solved using a variety of established methods, this approach formulates a manner where wavefunctions are described analytically over all space for

arbitrary wells without the need for any eigenvalue search or renormalization procedure. Following the description of the localized analytical basis coupled-well behavior is then reconstructed using a tight-binding analysis. In this development the traditional tight-binding procedure is simplified, based on assumptions and observations of typical THz-QCL properties, to a condensed expression which quickly estimates the new, perturbed, eigenstates based on combinations of two-state interactions. In addition, using the analytical form of the basis states, all matrix element integrals are reduced to an indefinite form requiring only the designation of the heterostructures interface locations to be evaluated. A comparison of this localized basis expansion to the full numerical approach is then illustrated and discussed.

2.2 Numerical Evaluation of the Time-Independent Schrödinger Equation

The Hamiltonian for a variable effective mass heterostructure is [128-131]

$$H = -\frac{\hbar^2}{2} \frac{\partial}{\partial z} \frac{1}{m^*(z)} \frac{\partial}{\partial z} + V(z) \quad (2.2.1)$$

where $m^*(z)$ and $V(z)$ are the effective mass and potential profiles along the growth axis, respectively. Using this operator in Schrödinger's equation and expanding the derivatives into their finite-difference form produces the following expression [50]

$$\frac{\psi(z+\Delta z)}{m^*(z+\Delta z/2)} = \left[\frac{2(\Delta z)^2}{\hbar^2} (V(z) - E) + \frac{1}{m^*(z+\Delta z/2)} + \frac{1}{m^*(z-\Delta z/2)} \right] \psi(z) - \frac{\psi(z-\Delta z)}{m^*(z-\Delta z/2)} \quad (2.2.2)$$

The method of solving equation (2.2.2) can then accomplished numerically using the "shooting method" [50,59,131]. In this technique the potential energy $V(z)$ and the effective mass $m^*(z)$ are known from the description of the well and barrier widths of the

heterostructure in question. Since the boundary conditions for the envelope wavefunctions $\psi(z)$ require that [128]

$$\psi(z) \rightarrow 0 \text{ and } \frac{\partial}{\partial z}\psi(z) \rightarrow 0 \text{ as } z \rightarrow \pm\infty \quad (2.2.3)$$

the numerical algorithm can be implemented by choosing the starting conditions of the wavefunction as

$$\psi(z - \Delta z) = 0 \text{ and } \psi(z) = 1 \quad (2.2.4)$$

The search for the eigenvalues corresponding to the confined states in the system is then accomplished by searching for the energy values E which satisfy the boundary conditions at the other end of the system, i.e. $\psi(\infty, E) = 0$. Due to the somewhat arbitrary starting conditions the wavefunctions are not automatically normalized and thus, once the eigenvalues are found, must be scaled such that

$$\langle \psi_i | \psi_i \rangle = \int_{-\infty}^{+\infty} \psi_i \psi_i dz = 1 \quad (2.2.5)$$

The boundary conditions stated in (Equation 2.2.3) are valid for confined states in quantum well structures where the lower potential layers are always bounded by higher energy barriers at the ends of the system. The numerical wavefunctions for these states are always real-valued, hence the neglect of the complex conjugate in Equation 2.2.5. The simplest example of this type of system is a single quantum well (Figure 2.2.1). For this plot a single 120Å GaAs well surrounded by 100Å $\text{Al}_{0.15}\text{Ga}_{0.85}\text{As}$ barriers was evaluated using Equation 2.2.2. The conduction band potential energy profile is displayed by the bold black line. In this simulation, and throughout this document, the conduction band offset parameter is set at 0.67, which is the standard value for GaAs/AlGaAs. The blue and red lines are the ground and first excited state

wavefunctions, respectively, and are offset to their corresponding energies. They are also plotted as the magnitude squared of the wavefunction, and with arbitrary magnitudes suitable for viewing, which is commonly observed in the display of confined quantum well states.

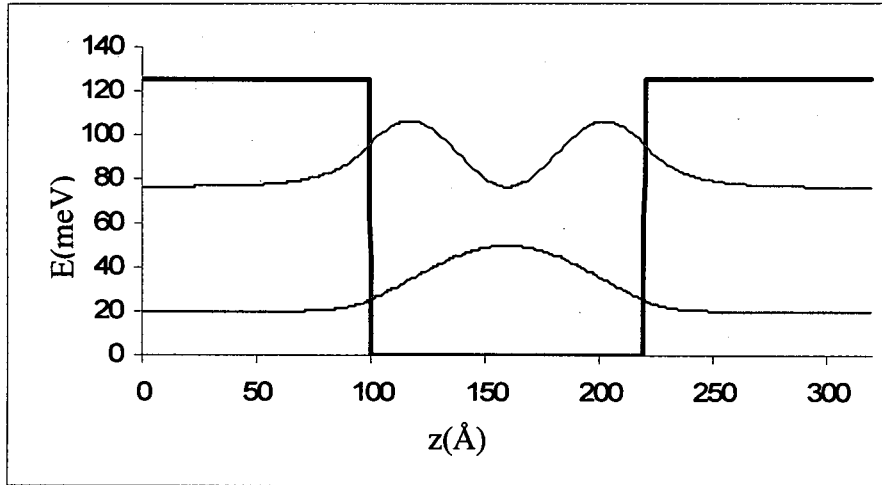


Figure 2.2.1: Potential profile and confined states for a single 120Å GaAs well surrounded by 100Å $\text{Al}_{0.15}\text{Ga}_{0.85}\text{As}$ barriers. The wavefunctions shown here are offset to their respective energies and are plotted as the magnitude squared.

In quantum well structures a critical design factor is the energy of the confined subbands. As illustrated previously in Figure 1.1.2, electrons in a quantum well remain unconfined in the plane of the well. This results in a two-dimensional dispersion of energy with respect to the in-plane momentum $k_{||}$. In the subsequent discussions, unless otherwise noted, the “energy” of a confined state is taken as the subband minima ($k_{||}=0$). In a particular material system, such as $\text{Al}_x\text{Ga}_{1-x}\text{As}$ where the composition x is fixed, the dominant factor in determining these energies, and the intersubband energy

separations, is the width of the well. A plot of the energies vs. the well width for the ($x=0.15$) GaAs/ $\text{Al}_x\text{Ga}_{1-x}\text{As}$ single well is shown in Figure 2.2.2.

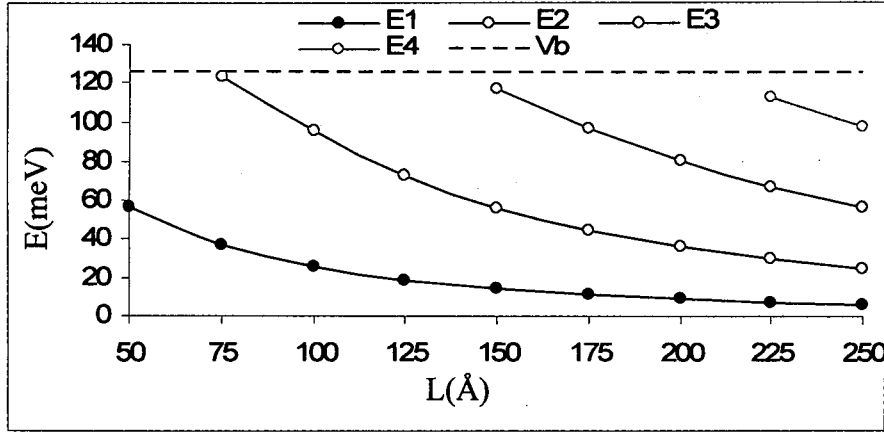


Figure 2.2.2: Confined energies vs. well width for a single GaAs well surrounded by 100\AA $\text{Al}_{0.15}\text{Ga}_{0.85}\text{As}$ barriers.

In this figure it can be observed that the energies and the energy separations are reduced as the well width is increased. The potential energy of the barrier is also included (dashed line) to indicate when the additional states can truly be considered as being “confined” to the quantum well.

As discussed in Chapter 1, another parameter that can be introduced into the design of quantum heterostructures is an applied bias. The inclusion of a linear electric field across a system is easily implemented into the numerical approach simply by changing the potential energy term in the Hamiltonian from

$$V(z) \rightarrow V(z) + F(z - z_0) \quad (2.2.6)$$

where F is the magnitude of the field and z_0 is the origin, usually chosen at the center of the system to prevent absolute offsets. A constant electric field applied across the system

simply introduces a position dependent tilt to the potential. This effect is illustrated in Figure 2.2.3 where the same single 120Å GaAs well surrounded by 100Å $\text{Al}_{0.15}\text{Ga}_{0.85}\text{As}$ barriers is biased at $F=20\text{kV/cm}$. In this figure the unbiased potential and wavefunctions are shown in bold for comparison. The shape of the wavefunctions biased at this level display only minor shifts toward the lower potential direction. The energies also experience a slight reduction, known as the “quantum confined Stark effect” [132-134], which is barely noticeable from the plot.

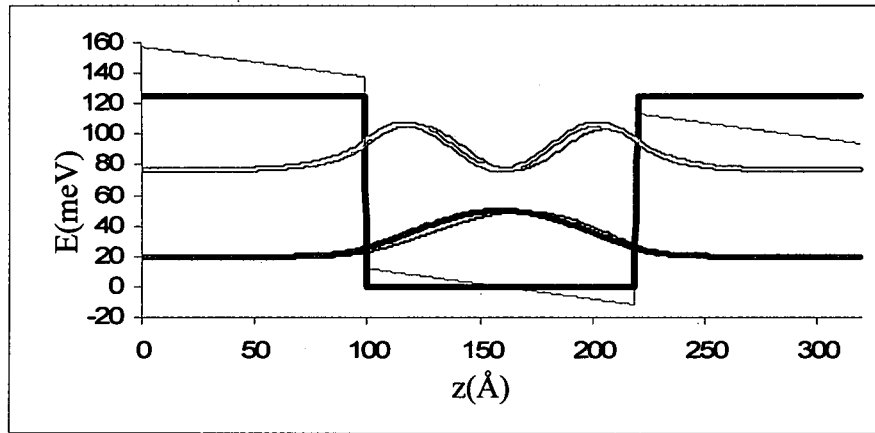


Figure 2.2.3: Comparison of biased ($F=20\text{kV/cm}$) vs. unbiased system for a single 120Å GaAs well surrounded by 100Å $\text{Al}_{0.15}\text{Ga}_{0.85}\text{As}$ barriers. The unbiased potential and wavefunctions are shown in bold.

In addition to external fields contributing to the potential energy, internal electric fields can influence the Hamiltonian. These additional charges can be calculated using Poisson’s equation

$$\nabla^2 V_p = -\frac{\rho}{\epsilon} \quad (2.2.7)$$

where V_p is the additional potential, ρ is the charge distribution, and ϵ is the permittivity of the material. The potential in Schrödinger's equation then takes on another term

$$V(z) \rightarrow V(z) + F(z - z_0) + V_p(z) \quad (2.2.8)$$

These internal charges are due to the presence of ionized donors as well as the concentration of electrons populating various eigenstates. Since the electron distributions are determined by the wavefunctions themselves, a self-consistent solution of both the Schrödinger and Poisson equations must be solved. The details of these calculations can be found elsewhere [50,135-137]

Demonstration of these internal charge effects can be observed by simulating a 100Å GaAs well with $Al_{0.2}Ga_{0.8}As$ barriers. In this example the well is n-type doped producing a sheet density of $1000 \times 10^{10} \text{ cm}^{-2}$. This level is several orders of magnitude above most of the THz-QCL structures of interest in later chapters. The effect caused by this extreme case on both the quantum well potential and the energy is simulated using a self-consistent iteration (see Figure 2.2.4). In this calculation the donors in the well were assumed to supply only the ground state with electrons. In this figure a slight downward bending of the potential at the barrier edges and the edges at the bottom of the well is observed due to the charge of the ionized donors. The upward bend of the potential in the center of the well can be observed to closely follow the wavefunction, representing the distribution of the electrons. Examination of the self-consistently calculated with the single-particle wavefunctions, offset to their respective energies, shows that the change in potential results only in the slight upward shift of the energy. The overall shape of the wavefunction remains visibly unchanged.

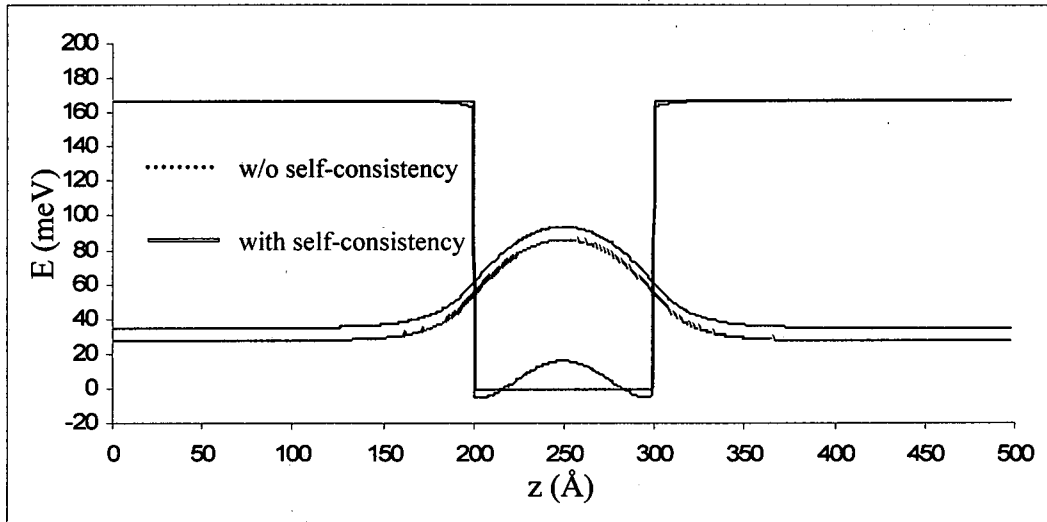


Figure 2.2.4: Comparison of calculations with and without Schrödinger-Poisson self-consistency for a well heavily n-type doped to produce a sheet density of $1000 \times 10^{10} \text{ cm}^{-2}$.

Sheet densities near the level used for the calculation displayed in Figure 2.2.4 are again, generally not implemented in the THz-QCL devices to be modeled. To investigate the extent that these internal fields have for more realistic doping levels a plot of the energy change of this ground state vs. various sheet density concentrations is shown in Figure 2.2.5. In this plot it is shown that the consequence of considering the internal fields becomes noticeable only at concentrations approaching 10^{12} cm^{-2} . The devices to be considering in later chapters have per-period concentrations in the 10^{10} cm^{-2} range. These doping levels can clearly be seen to produce negligible changes to the eigenstates calculated without self-consistency.

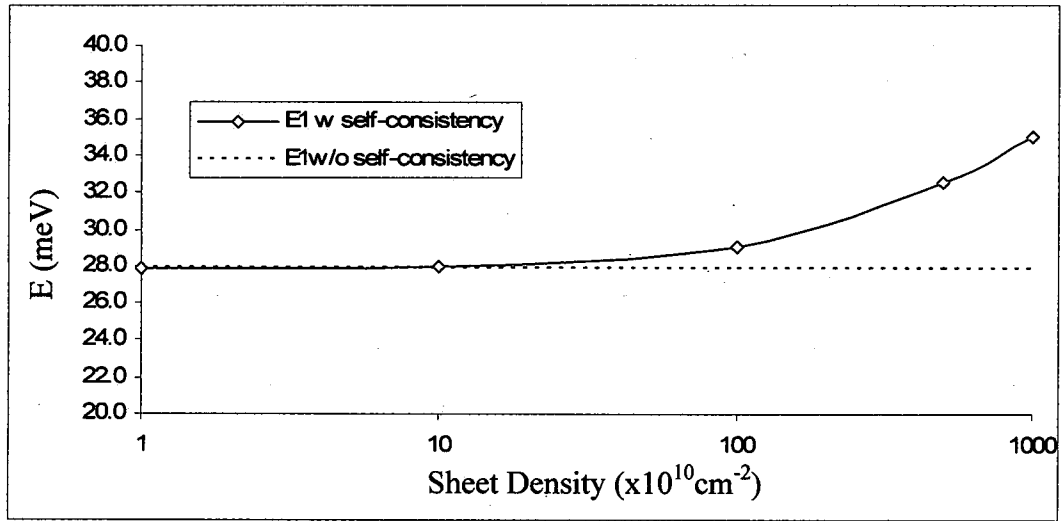


Figure 2.2.5: Comparison of the ground state energy with and without Schrödinger-Poisson self-consistency for a well n-type doped producing various sheet densities.

As mentioned in the previous chapter, quantum cascade lasers are constructed using multiple quantum wells, where the combination of material system, well widths, barrier widths, and applied biases, are used to tailor the quantum states for the purpose of controlling the electronic properties. While the application of the electric field to the single quantum well, shown in Figure 2.2.3, produced negligible effects, a more illustrative example of the control of electronic states can be observed by evaluating a multi-quantum well system. Consider, for example, a 70\AA GaAs well and another 50\AA GaAs well separated by a 60\AA $\text{Al}_{0.15}\text{Ga}_{0.85}\text{As}$ barrier. Evaluating this system using Equation 2.2.2 produces the plot shown in Figure 2.2.6. Here it is observed that the wavefunctions for each well appear to resemble what would be expected for the ground state in each respective well, had they been evaluated separately.

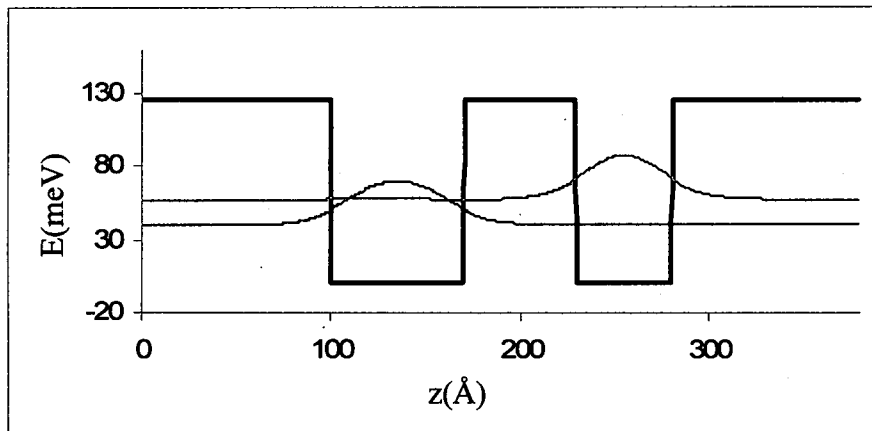


Figure 2.2.6: A 70Å and 50Å GaAs double quantum well system separated by a 60Å $\text{Al}_{0.15}\text{Ga}_{0.85}\text{As}$ barrier evaluated numerically with no applied bias.

Application of a bias across the system at different electric field strengths, is shown in Figure 2.2.7. In this figure the wavefunctions are plotted as the magnitude squared and the lowest energy solution is always depicted as blue, while the higher energy is shown in red. As the bias is increased from 6kV/cm, and the states move closer in energy, the wavefunctions start to become delocalized across the barrier and the magnitude of their profiles appear more and more alike. At 12kV/cm the wavefunctions almost appear equivalent where the lower energy state (blue) is just slightly more localized in the leftmost well. As the bias is increased to 15kV/cm the states still appear very similar only now the lower energy state (blue) appears to be more localized in the right well. This trend continues with increasing bias and, as the energy separation again increases, the wavefunctions appear more like single well solutions. This behavior is also illustrated in the central diagram of Figure 2.2.7 where the energy vs. the field is plotted. Here the blue line represents the lower energy state and the red line is the higher energy state.

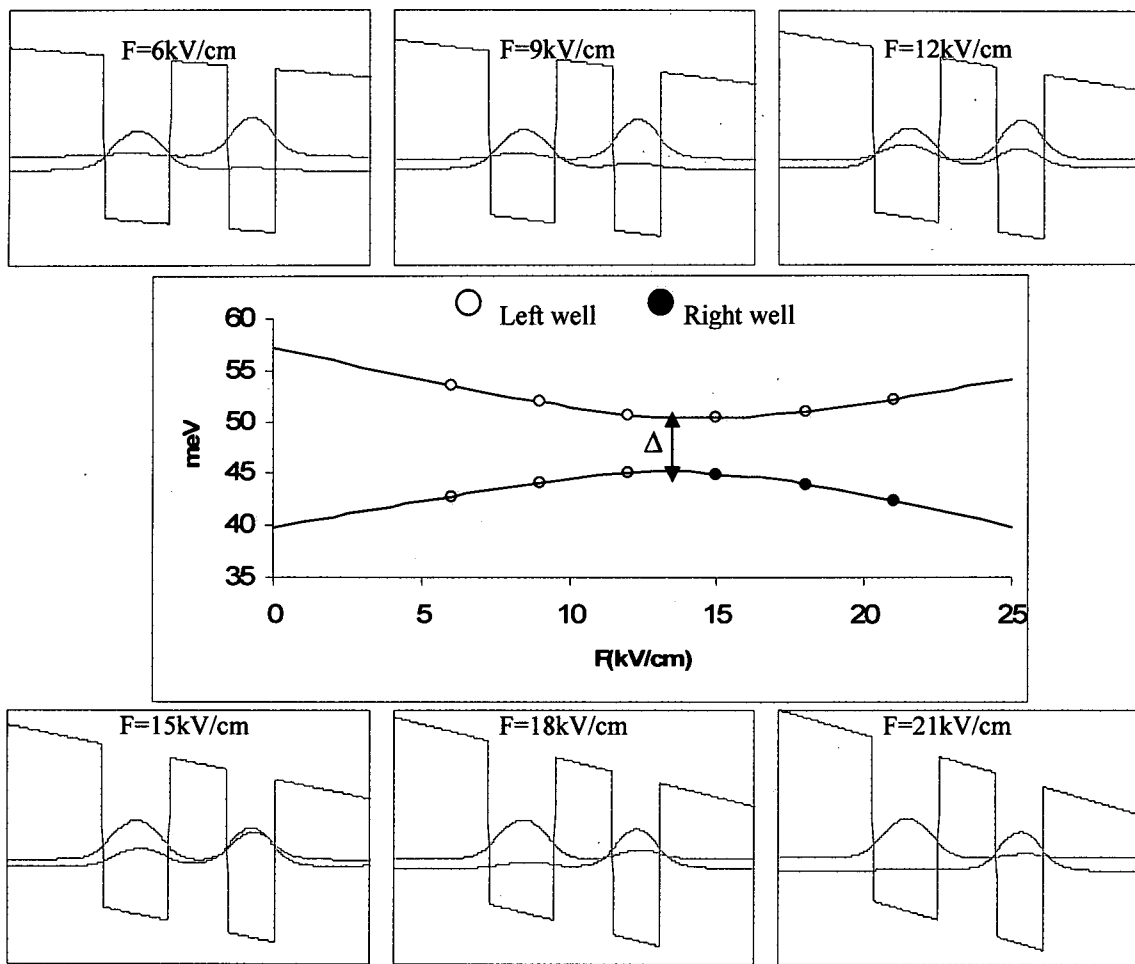


Figure 2.2.7: Wavefunctions and energies of the two ground states vs. the electric field for a 70Å and 50Å GaAs double quantum well system separated by a 60Å $\text{Al}_{0.15}\text{Ga}_{0.85}\text{As}$ barrier.

Viewing of only the solid lines depicts a phenomenon where the energies move closer together, reach a minimum, and then move apart. This behavior is known as an anti-crossing. At the minimum energy separation Δ the wavefunction magnitudes would be equivalent across the structure and would form what is known as a “doublet”. The open and closed circles in the diagram correspond to the bias points shown in the surrounding figures and represent the states which appear mainly localized in the left and right well,

respectively. This figure concludes that increasing the electric field causes the energies to repel (anti-cross) yet the designation of which state belongs the which well switches after the anti-crossing.

The ability to tailor the shape of the wavefunctions, as demonstrated in Figure 2.2.7, is directly associated with the ability to control the electrical and optical properties in quantum heterostructures. While a more detailed discussion of transition rates and electron transport will be presented in chapters 3 and 4 it is important here to point out how the shape of the calculated wavefunction affects the electrical properties to be investigated in the design of quantum cascade lasers. Specifically, a very simple view of transport due to columbic interaction can be approximated by considering the value of the overlap integral between two wavefunctions. A simple overlap integral can be expressed as

$$O_{ij,mod} = \langle \psi_j | \psi_i \rangle = \int_{-\infty}^{+\infty} \psi_j^* \psi_i dz \quad (2.2.9)$$

where again the complex conjugate is omitted due to our entirely real-valued, numerically evaluated, envelope wavefunctions. This quantity is a measure of the spatial proximity of the confined, resonant, states. The relationship between this quantity and electron transport is straightforward since the wavefunctions represent the probability of finding an electron. Therefore, the spatial proximity of two states must be related to the electrons ability to transition from one state to another. This basic concept is illustrated below in Figure 2.2.8.

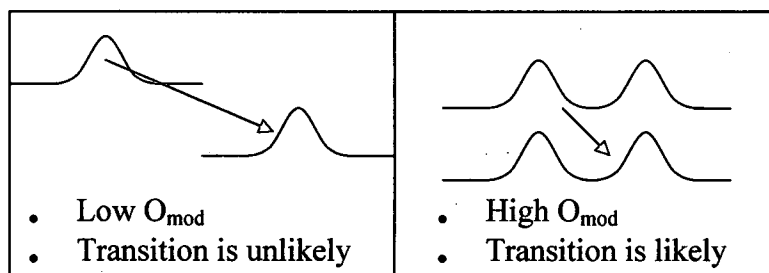


Figure 2.2.8: Diagram illustrating the relationship between the spatial proximity of two wavefunctions and the probability of a transition.

The simple diagram shown in Figure 2.2.8, combined with the wavefunction delocalization phenomena observed in Figure 2.2.7, depicts the fundamental process which is involved in the design of quantum cascade lasers. The ability to alter, or engineer, the shape of the wavefunctions will inevitably change the transport processes through a system. Using the overlap integral defined by Equation 2.2.9 the design combinations of layer widths and electric field biases contributing to the electrical and optical properties of heterostructures can be analyzed. This simple examination will also lead to a fundamental problem with the numerical evaluation of the time-independent Schrödinger's equations used for the design of quantum cascade lasers.

Consider the same 70Å and 50Å GaAs double quantum well system separated by an $\text{Al}_{0.15}\text{Ga}_{0.85}\text{As}$ barrier which was evaluated and shown in Figure 2.2.7. Recalculation of the same system, as well as the overlap integral, can now be carried out while varying the barrier width. The results of these calculations are displayed in Figure 2.2.9. Observation of the energy vs. the electric field (left figure) shows that as the barrier width is increased from 30Å to 120Å the anti-crossing energy separation Δ is reduced. As observed in Figure 2.2.7, near the anti-crossing position the wavefunctions form a “doublet” and

thus the value of O_{mod} approaches unity (right figure). Although the width of O_{mod} vs. the field narrows as the barrier width increases there is always a bias that will lead to a strong delocalization of the states.

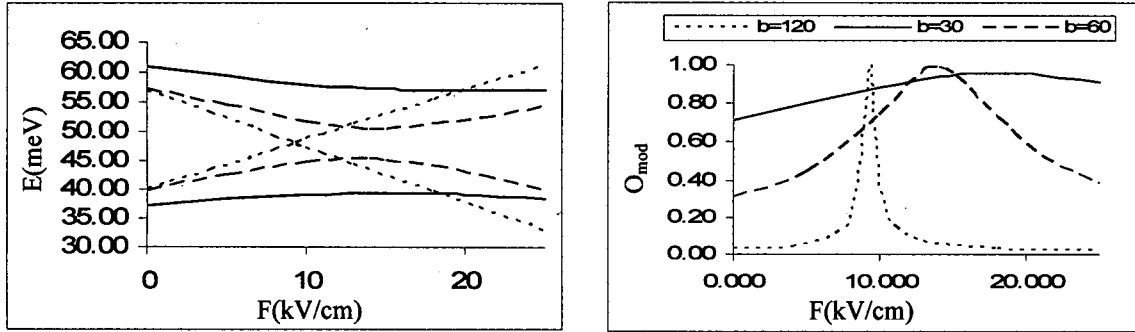


Figure 2.2.9: Energy of the two ground states (left) and O_{mod} vs. the electric field (right) for a 70Å and 50Å GaAs double quantum well system separated by an $\text{Al}_{0.15}\text{Ga}_{0.85}\text{As}$ barrier of various widths.

In practice, using the numerical “shooting method” approach, this anti-crossing energy separation Δ could become so small that, at a certain bias, the search for the eigenvalues of the system actually misses both the coupled states. This potential error could be corrected by simply reducing the stepsize search in energy ΔE . Theoretically if a small enough energy step is chosen this wavefunction delocalization between two states could be calculated regardless of the barrier width. Further examination is then required to determine physical reality of the states being calculating. Consider the generic coupled well system shown in Figure 2.2.10. If the wavefunctions are meant to represent the probability of finding an electron, and the bias is such that the calculated wavefunctions are delocalized across both wells for any arbitrary separation L , any electron injected into the left well would be considered as instantaneously having a probability of being found

in the right well. Certainly the envelope wavefunctions do not represent the entire description of the electronic state. However, even a more thorough description in the form of $\psi(z)u(z)$, where $u(z)$ is the rapidly varying portion on the atomic scale, will produce a delocalized state with the “slowly varying envelope” function following this behavior.

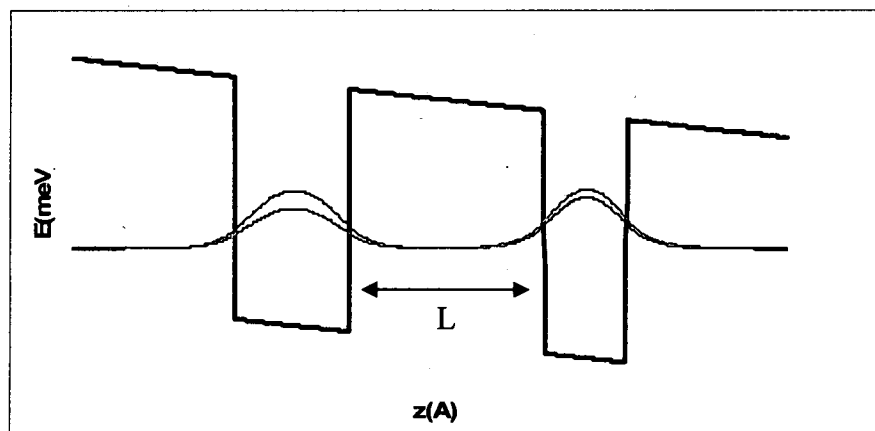


Figure 2.2.10: A generic coupled well system with an arbitrary barrier width.

In addition to this possibility of wavefunction delocalization over arbitrary distances to other confined states the likelihood of coupling to continuum or “quasi-continuum” states above the potential of the barriers leads to further numerical abnormalities. This situation is illustrated in Figure 2.2.11. While numerically these “continuum” states are generally found as artifacts due to hard “infinite” barriers surrounding the calculated system they do, in fact, exist and leakage of current into these states should be considered for energies near the barrier height [138,139]. The problem which arises numerically is that, for certain biases, any state in an extended system could couple to a generic “numerical artifact” continuum state. In Figure 2.2.11 for example, it can be reasoned that an excited state (shown in blue) may couple to the continuum since

it is near the top of the barrier. Does this logic also extend to the ground state (shown in green), which must travel through four barriers before reaching the continuum?

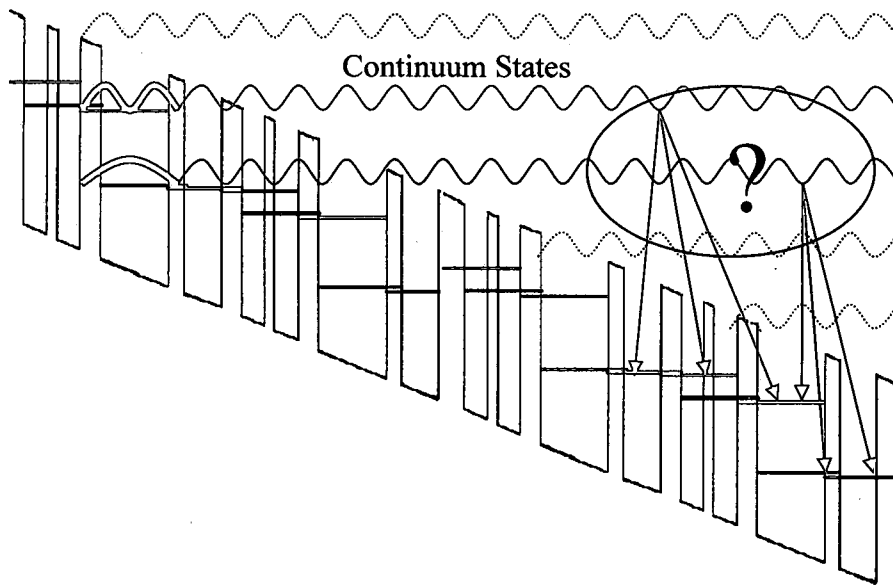


Figure 2.2.11: Illustration of confined states in a QCL system coupling to “quasi-continuum” states.

These artificial “quasi-confined” states in the typical calculation could be adjusted by changing the boundary conditions but this does not alter their physical reality. Therefore, if it is concluded that these couplings can occur without limits than they must occur for all states in a biased QCL. Numerically, this can result in a supposed confined state becoming delocalized across the entire range of the system being calculated and would thus open up transport paths allowing transitions across multiple periods. Similar to the example with an arbitrary barrier width, this would imply an electron injected into a state as being instantaneously transported across the entire device. Clearly then there must exist a limit to this wavefunction delocalization which

cannot be appropriately treated using a full numerical evaluation of the time-independent Schrödinger's equation over an arbitrary heterostructure. While a detailed discussion of time-dependant phenomena will be discussed in subsequent chapters it is important to realize that standard, full numerical evaluations can result in these extended states. These delocalized states can then predict unrealistically large current spikes as mentioned in Chapter 1 as being primary criticism of the semiclassical transport models.

2.3 Analytical Single Well Solutions

With suspected unrealistic wavefunction delocalization being a likely problem with the full numerical evaluation technique outlined in Section 2.2, some means to control the localization of states is sought. To start, reconsider the single quantum well. General analytical solutions can be written for the wavefunctions of a single well in a piecewise manner. The bound portion inside the well can be written as a combination of sine and cosine functions and the evanescent (decaying) portions can be written as exponentials in the barriers (Figure 2.3.1).

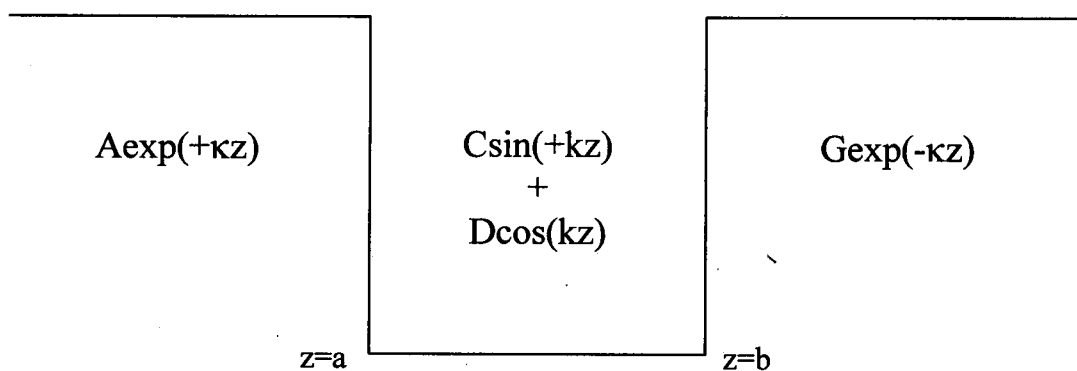


Figure 2.3.1: A single quantum well and the analytical components of a general wavefunction.

The wavevectors can be expressed as

$$k = \frac{\sqrt{2m_w^* E}}{\hbar} \text{ and } \kappa = \frac{\sqrt{2m_b^* (V - E)}}{\hbar} \quad (2.3.1)$$

where m_w^* and m_b^* is the effective mass in the well and barrier regions respectively.

Since the solutions must be continuous across the barrier a parameter can be defined

$$|Y_a| = |Y_b| \quad (2.3.2)$$

representing the magnitude of the normalized wavefunction at the interface $z=a$ or $z=b$.

The following two expressions can then be written

$$A \exp(\kappa a) = C \sin(ka) + D \cos(ka) = Y_a \quad (2.3.3)$$

$$C \sin(kb) + D \cos(kb) = G \exp(-\kappa b) = \pm Y_a$$

where the sign $+Y_a$ is used for the symmetric ground state and $-Y_a$ for the first excited state. This allows for the coefficients in the barriers to be written as

$$A = \frac{Y_a}{\exp(\kappa a)} \text{ and } G = \frac{\pm Y_a}{\exp(-\kappa b)} \quad (2.3.4)$$

leaving the following system of equations

$$C \sin(ka) + D \cos(ka) = Y_a \quad (2.3.5)$$

$$C \sin(kb) + D \cos(kb) = \pm Y_a$$

For a ground state the solutions are

$$C = \frac{Y_a [\cos(kb) - \cos(ka)]}{\cos(kb) \sin(ka) - \sin(kb) \cos(ka)} \quad (2.3.6)$$

$$D = \frac{Y_a [\sin(ka) - \sin(kb)]}{\cos(kb) \sin(ka) - \sin(kb) \cos(ka)}$$

and for an excited state

$$C = \frac{Y_a [\cos(kb) + \cos(ka)]}{\cos(kb)\sin(ka) - \sin(kb)\cos(ka)} \quad (2.3.7)$$

$$D = \frac{-Y_a [\sin(ka) + \sin(kb)]}{\cos(kb)\sin(ka) - \sin(kb)\cos(ka)}$$

With these expressions for the coefficients the ground state wavefunction can be written as

$$\begin{aligned} \psi_{LB} &= \frac{Y_a}{e^{\kappa a}} e^{\kappa z} \\ \psi_w &= \left[\frac{Y_a [\cos(kb) - \cos(ka)]}{\cos(kb)\sin(ka) - \sin(kb)\cos(ka)} \right] \sin(kz) \\ &+ \frac{Y_a [\sin(ka) - \sin(kb)]}{\cos(kb)\sin(ka) - \sin(kb)\cos(ka)} \cos(kz) \end{aligned} \quad (2.3.8)$$

$$\psi_{RB} = \frac{Y_a}{e^{-\kappa b}} e^{-\kappa z}$$

where LB, W, and RB correspond to the left barrier, well, and right barrier regions, respectively. The normalization condition requires that

$$\int_{-\infty}^a \psi_{LB}^2 dz + \int_a^b \psi_w^2 dz + \int_b^{+\infty} \psi_{RB}^2 dz = 1 \quad (2.3.9)$$

which allows the parameter Y_a to be written as

$$Y_a = \pm \frac{\sqrt{\kappa k (S_a S_b + C_a C_b + 1) (k [S_a S_b + C_a C_b + \kappa b + 1 - \kappa a] + \kappa [S_b C_a - C_b S_a])}}{k [S_a S_b + C_a C_b + \kappa b + 1 - \kappa a] + \kappa [S_b C_a - C_b S_a]} \quad (2.3.10)$$

where the notation

$$S_i = \sin(ki) \text{ and } C_i = \cos(ki) \quad (2.3.11)$$

has been used for convenience. Similarly, for the excited state

$$Y_a = \pm \frac{\sqrt{\kappa k (S_a S_b + C_a C_b - 1) (k [S_a S_b + C_a C_b - \kappa b - 1 + \kappa a] + \kappa [S_b C_a - C_b S_a])}}{k [S_a S_b + C_a C_b - \kappa b - 1 + \kappa a] + \kappa [S_b C_a - C_b S_a]} \quad (2.3.12)$$

With k and κ described by Equation 2.3.1 there is now a description of the wavefunction in the form of

$$\psi(k(m_w^*, E), \kappa(m_b^*, V, E), a, b) \quad (2.3.13)$$

Since m_w^* , m_b^* , and V are functions of the material system, and the interface position b , is $b=a+L$, concern need only to be given to the parameters: a (the preceding interface location), L (the well width), and E (the energy of the state). As was observed in the previous section (Figure 2.2.2), the energy is a function of the well width and thus the entire description of the normalized wavefunction is reduced to $\psi(L, a)$.

While the standard approach to calculating the energies, i.e. searching for eigenvalues, is not computationally restrictive, the fact that the normalized wavefunctions can be analytically reduced to a function dependant only on the energy and interface location makes a simple empirical fit of the energies attractive. Fitting single energies vs. the well width $e(L)$ for any given material system is accomplished by simply using a polynomial fit over the given range of interest. For example, in GaAs wells with $Al_{0.15}Ga_{0.85}As$ barriers for a fit is chosen for well widths between 75Å and 200Å to write the ground and excited state energies as

$$E_g(L) = C_{1g}L^4 + C_{2g}L^3 + C_{3g}L^2 + C_{4g}L + C_{5g} \quad (2.3.14)$$

$$E_e(L) = C_{1e}L^4 + C_{2e}L^3 + C_{3e}L^2 + C_{4e}L + C_{5e}$$

where the coefficients are displayed in Table 2.3.1.

	C1	C2	C3	C4	C5
Ground	7.73492786E-8	-5.46226584E-5	1.51529058E-2	-2.04817479E+0	1.25962796E+2
Excited	-1.81926075E-7	9.07876026E-5	-1.19608341E-2	-6.28901063E-1	2.05410246E+2

Table 2.3.1: Coefficients for single well energy fits in a GaAs/ $Al_{0.15}Ga_{0.85}As$ system.

The accuracy of this polynomial expression is compared to a numerical simulation using Equation 2.2.2 and is displayed in Figure 2.3.2. The energies calculated using the fourth order polynomial fits of Equation 2.3.14 were evaluated using double-point precision. A direct comparison of the calculated values using both expressions, as well as the magnitude of their difference, is shown in Table 2.3.3.

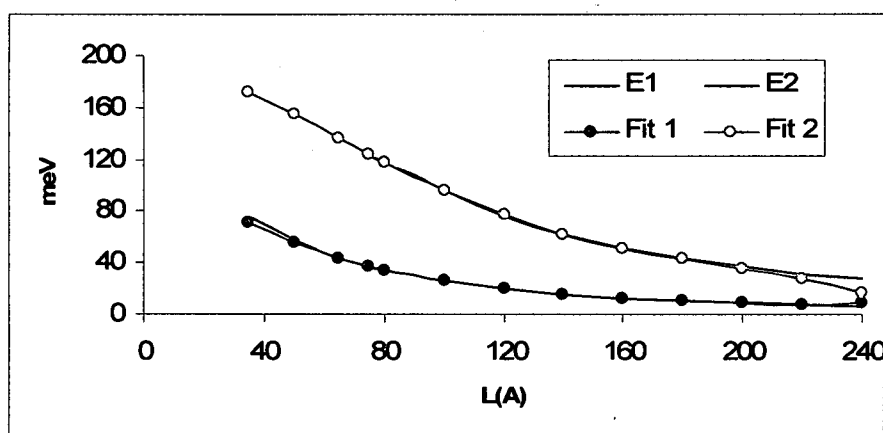


Figure 2.3.2: Comparison of numerically calculated eigenvalues and empirically fit solutions for the ground and excited states in a single GaAs/Al_{0.15}Ga_{0.85}As well.

L(Å)	E1	E2	Fit 1	Fit 2	E1-F1	E2-F2
35	75.850000		70.613114	172.366203	5.236886	X
50	56.787500		55.091922	154.274521	1.695578	X
65	43.543750		43.232447	135.682205	0.311303	X
75	37.010352	123.200000	36.988227	123.507740	0.022124	0.307740
80	34.260938	118.000000	34.288835	117.580384	0.027898	0.419616
100	25.781641	95.450000	25.786645	95.506794	0.005004	0.056794
120	20.060547	76.664063	20.034858	76.862894	0.025689	0.198831
140	16.036230	62.287695	16.045204	62.164209	0.008973	0.123486
160	13.104752	51.372754	13.126433	51.227671	0.021682	0.145083
180	10.905975	42.995959	10.884318	43.171611	0.021658	0.175652
200	9.215736	36.466602	9.221650	36.415770	0.005914	0.050832
220	7.889062	31.295565	8.338244	28.681287	0.449182	2.614278
240	6.828956	27.138468	8.730935	16.990709	1.901980	10.147758

Table 2.3.3: Table of numerical eigenvalues, empirical fits, and the magnitude of their difference for a single GaAs/Al_{0.15}Ga_{0.85}As well.

The fit over the desired range, from 75Å to 200Å, is shown to be sufficiently agreeable with a mean error of approximately 0.017meV for the ground state and 0.18meV for the excited state. Below approximately 75Å the excited state is above the barrier potential and is not considered bound. The ground state energy fit for the narrower wells remains within 1meV of error until approximately 50Å. For the larger wells the error for the excited state polynomial fit begins to deviate from the full calculation near 220Å. The suitable range for these fitting functions is appropriate for the QCL systems to be considered in later chapters.

The sufficiency of the energy fit $\epsilon(L)$ over the desired range now permits the instant calculation of normalized wavefunctions for any single quantum well of the GaAs/Al_{0.15}Ga_{0.85}As system simply by using Equation 2.3.8 with the chosen values of L and the designation of the leading interface $z=a$. This analytical form of the wavefunction can then be expressed without the need to locate and refine the eigenvalues and vectors as required by the numerical technique outlined in section 2.2. As will become evident in later chapters, the primary benefit of describing the single well eigenstates using this procedure is to permit an immediate description of the wavefunctions in an analytical manner based solely on the designation of the interface locations, without any need of an iterative eigenvalue search.

2.4 Nearest-Neighbor Coupling of Single Well Solutions

With the localized single well basis detailed in Section 2.3 a description for multi-well structures can now be examined. Recalling that the motivation is to limit the unphysical delocalization of the numerical technique of Section 2.2, reconstruction of coupled well interactions is now presented. While the use of single-well eigenstates in a multi-well structure do not form an orthogonal basis set, since they represent solutions to separate Hamiltonians, the established success of solid-state physics models utilizing Linear Combinations of Atomic Orbitals (LCAO) techniques [140-144] suggests that this obstacle can be overlooked. Indeed, the ability to even approximately describe complex multi-quantum well heterostructures using constituent single-well eigenstates is not only favorable analytically, but as shall be seen in later discussion of transport, offer techniques capable of extremely fast computation.

The extension of the single well analytical solution method of the previous section to a multi-well system is initiated simply by defining the location and width of any number of wells and translating the single well solutions from $z \rightarrow z'$, where z' represents the multi-well structure. Take, for example, the double well system that was evaluated in section 2.2. This was a 70Å GaAs well and 50Å GaAs well separated by a 60Å $\text{Al}_{0.15}\text{Ga}_{0.85}\text{As}$ barrier (Figure 2.4.1). In this figure both the analytical wavefunctions for the ground states, calculated using the single well analytical wavefunctions of (Equation 2.3.8), and the numerical approach of Section 2.2, are displayed for comparison. In this plot, since the 50Å well is pushing the range of the polynomial energy fits $\epsilon(L)$, the full eigenvalue is used for the localized basis.

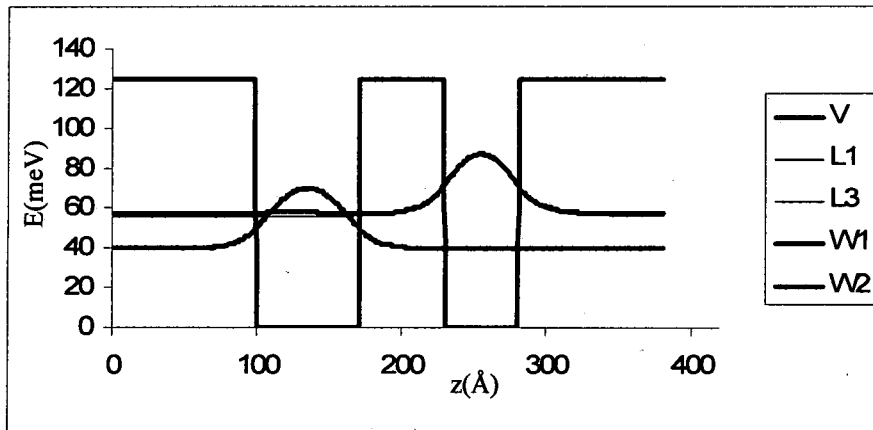


Figure 2.4.1: Ground state wavefunction calculated for a 70Å GaAs well and a 50Å GaAs well separated by a 60Å $\text{Al}_{0.15}\text{Ga}_{0.85}\text{As}$ barrier.

Here the numerical wavefunctions, shown in black, and the translated single well functions (red and blue), are shown to be practically identical within their respective wells. A very small coupling of the numerical wavefunctions across the barrier is noticeable while the single well states, of course, are not affected by the neighboring well. The calculated energies for each technique are displayed in Table 2.4.1.

E(70)	E(50)	E1	E2
40.08828	56.7875	39.80352	57.2561

Table 2.4.1: Comparison between the localized basis eigenvalues (labeled E(70) and E(50) and the numerical approach (E1 and E2) for a 70Å GaAs well and a 50Å GaAs well separated by a 60Å $\text{Al}_{0.15}\text{Ga}_{0.85}\text{As}$ barrier.

In this table the numerical calculation of the ground state energies for a single well are labeled as E(L) and the numerical calculation of the coupled system as E1, E2. The first thing which can be noticed is that in the numerical solution, once the wells are

combined, the lower state E1 is pushed down relative to the E(50) eigenvalue. The higher state E2 has similarly been pushed up in the calculation relative to E(50). This is the repelling phenomenon observed previously in Section 2.2. In order to make use of the analytical/empirical single well solutions this repelling effect as well as the effect of an additional electric field bias must be accounted for.

Consider a set of Hamiltonians H^m corresponding to the individual wells where Schrödinger's equation for each well (m) is

$$H^m \Psi_n^m = \epsilon_n^m \Psi_n^m \quad (2.4.1)$$

The operator consists of kinetic (K) and potential (P) energy components allowing for this expression to be rewritten as

$$(K + P^m(z)) \Psi_n^m = \epsilon_n^m \Psi_n^m \quad (2.4.2)$$

where E_n^m and Ψ_n^m are the energy and wavefunction, respectively, for state (n) in well (m).

The Hamiltonian then, for a system made up of multiple wells, will be a combination of the potential energies translated into a new space z'

$$H = K + \sum_j (P^j(z') - |V|) + |V| \quad (2.4.3)$$

where K is the kinetic energy operator assumed to be unchanged by the new system, P^j is the appropriately translated potential energy of well (j) and $|V|$ is the magnitude of barrier potential. Assuming the new coupled wavefunctions can be described by a linear combination of the localized basis provided by equation (2.4.1), Schrödinger's equation can be rewritten as

$$H \left| \sum_b \sum_a c_{na}^{mb} \Psi_a^b \right\rangle = E_n^m \left| \sum_b \sum_a c_{na}^{mb} \Psi_a^b \right\rangle \quad (2.4.4)$$

where c_{na}^{mb} is the coefficient describing the coupling between state (n) in well (m) and state (a) in well (b).

Inserting equation (2.4.3) into equation (2.4.4) gives

$$\left[K + \sum_j (P^j - |V|) + |V| \right] \left| \sum_b \sum_a c_{na}^{mb} \Psi_a^b \right\rangle = E_n^m \left| \sum_b \sum_a c_{na}^{mb} \Psi_a^b \right\rangle \quad (2.4.5)$$

which can then be expanded to

$$K \left| \sum_b \sum_a c_{na}^{mb} \Psi_a^b \right\rangle + \sum_j (P^j - |V|) \left| \sum_b \sum_a c_{na}^{mb} \Psi_a^b \right\rangle + |V| \left| \sum_b \sum_a c_{na}^{mb} \Psi_a^b \right\rangle = E_n^m \left| \sum_b \sum_a c_{na}^{mb} \Psi_a^b \right\rangle \quad (2.4.6)$$

The operator $(P^j - |V|)$ can be separated into intrawell ($j=b$) and interwell ($j \neq b$) components.

$$\begin{aligned} & K \left| \sum_b \sum_a c_{na}^{mb} \Psi_a^b \right\rangle + (P^b - |V|) \left| \sum_b \sum_a c_{na}^{mb} \Psi_a^b \right\rangle + \sum_{j \neq b} (P^j - |V|) \left| \sum_b \sum_a c_{na}^{mb} \Psi_a^b \right\rangle + |V| \left| \sum_b \sum_a c_{na}^{mb} \Psi_a^b \right\rangle \\ & = E_n^m \left| \sum_b \sum_a c_{na}^{mb} \Psi_a^b \right\rangle \end{aligned} \quad (2.4.7)$$

This expression can be simplified to

$$K \left| \sum_b \sum_a c_{na}^{mb} \Psi_a^b \right\rangle + (P^b) \left| \sum_b \sum_a c_{na}^{mb} \Psi_a^b \right\rangle + \sum_{j \neq b} (P^j - |V|) \left| \sum_b \sum_a c_{na}^{mb} \Psi_a^b \right\rangle = E_n^m \left| \sum_b \sum_a c_{na}^{mb} \Psi_a^b \right\rangle \quad (2.4.8)$$

The first two operators then combine to form the original, localized Hamiltonians, weighted by the coefficients, i.e.

$$\sum_b \sum_a c_{na}^{mb} (K + P^b) \left| \Psi_a^b \right\rangle = \sum_b \sum_a c_{na}^{mb} \epsilon_a^b \left| \Psi_a^b \right\rangle \quad (2.4.9)$$

Using this Equation 2.4.8 simplifies to

$$\sum_b \sum_a \epsilon_a^b \left| c_{na}^{mb} \Psi_a^b \right\rangle + \sum_b \sum_a \tilde{V} \left| c_{na}^{mb} \Psi_a^b \right\rangle = E_n^m \sum_b \sum_a \left| c_{na}^{mb} \Psi_a^b \right\rangle \quad (2.4.10)$$

where the perturbing potential operator \tilde{V} is

$$\tilde{V} = \sum_{j \neq b} (P^j - |V|) \quad (2.4.11)$$

Multiplying both sides of Equation 2.4.10 by $\langle \Psi_s^w |$ gives

$$\sum_b \sum_a c_{na}^{mb} \epsilon_a^b \langle \Psi_s^w | \Psi_a^b \rangle + \sum_b \sum_a c_{na}^{mb} \langle \Psi_s^w | \tilde{V} | \Psi_a^b \rangle = \sum_b \sum_a c_{na}^{mb} E_n^m \langle \Psi_s^w | \Psi_a^b \rangle \quad (2.4.12)$$

Now, assuming that the localized basis states Ψ_n^m are close to orthogonal, gives

$$c_{ns}^{mw} E_n^m = c_{ns}^{mw} \epsilon_s^w + \sum_b \sum_a c_{na}^{mb} \tilde{V}_{sa}^{wb} \quad (2.4.13)$$

where

$$\tilde{V}_{sa}^{wb} = \langle \Psi_s^w | \tilde{V} | \Psi_a^b \rangle \quad (2.4.14)$$

Now, removing the (s,w)th element from the summation leaves

$$E_n^m = \tilde{\epsilon}_s^w + \sum_b \sum_a \frac{c_{na}^{mb}}{c_{ns}^{mw}} \tilde{V}_{sa}^{wb} (1 - \delta_{as}^{bw}) \quad (2.4.15)$$

where a new "perturbed energy" is defined as

$$\tilde{\epsilon}_s^w = \epsilon_s^w + \tilde{V}_{ss}^{ww} \quad (2.4.16)$$

Note that the diagonal element \tilde{V}_{ss}^{ww} , which is written as

$$\tilde{V}_{ss}^{ww} = \langle \Psi_s^w | \sum_{j \neq w} (P^j - |V|) | \Psi_s^w \rangle \quad (2.4.17)$$

includes the potential energy operator $(P^j - |V|)$ from all wells (j) except for well (w).

This operation is analogous to one which can be derived using standard perturbation, or coupled-mode theory. The full diagonal matrix element \tilde{V}_{ss}^{ww} essentially describes the energy change seen by the isolated basis state (s) in well (m) due to the presence of the additional potentials introduced by the multi-well system.

The expression for E_n^m given by Equation 2.4.15 describes the energy of a state (n) in well (m) in terms of the "perturbed energy" of a state (s) in well (w) with the

addition of the scaled potential perturbations \tilde{V} of state (s,w) with all other states in the system. Since the designation of the state (s,w) is arbitrary, the case where (s,w)=(n,m) and (s,w)≠(n,m) can be set equal

$$\tilde{\epsilon}_n^m + \sum_b \sum_a \frac{c_{na}^{mb}}{c_{nn}^{mm}} \tilde{V}_{na}^{mb} (1 - \delta_{an}^{bm}) = \tilde{\epsilon}_s^w + \sum_b \sum_a \frac{c_{na}^{mb}}{c_{ns}^{mw}} \tilde{V}_{sa}^{wb} (1 - \delta_{as}^{bw}) \quad (2.4.18)$$

Defining the perturbed energy difference as $\Delta \tilde{\epsilon}_{ns}^{mw} = \tilde{\epsilon}_n^m - \tilde{\epsilon}_s^w$, removing the remaining (s,w) and (n,m) terms from the summations, and rearranging allows for a quadratic equation for the coefficient c_{ns}^{mw}

$$\frac{\tilde{V}_{ns}^{mw}}{c_{nn}^{mm}} (c_{ns}^{mw})^2 + \left(\Delta \tilde{\epsilon}_{ns}^{mw} + \sum_b \sum_a \frac{c_{na}^{mb}}{c_{nn}^{mm}} \tilde{V}_{na}^{mb} \Theta_{ns}^{mw} \right) c_{ns}^{mw} - \left(c_{nn}^{mm} \tilde{V}_{sn}^{wm} + \sum_b \sum_a c_{na}^{mb} \tilde{V}_{sa}^{wb} \Theta_{ns}^{mw} \right) = 0 \quad (2.4.19)$$

where $\Theta_{ns}^{mw} = (1 - \delta_{an}^{bm})(1 - \delta_{as}^{bw})$. The solution can then be written as the ratio between the diagonal and off-diagonal coefficients

$$\frac{c_{ns}^{mw}}{c_{nn}^{mm}} = - \frac{[\Delta \tilde{\epsilon}_{ns}^{mw} + \Sigma_n^m]}{2 \tilde{V}_{ns}^{mw}} \pm \frac{\sqrt{[\Delta \tilde{\epsilon}_{ns}^{mw} + \Sigma_n^m]^2 + 4 \tilde{V}_{ns}^{mw} [\tilde{V}_{sn}^{wm} + \Sigma_s^w]}}{2 \tilde{V}_{ns}^{mw}} \quad (2.4.20)$$

where

$$\Sigma_n^m = \sum_b \sum_a \frac{c_{na}^{mb}}{c_{nn}^{mm}} \tilde{V}_{na}^{mb} \Theta_{ns}^{mw} \text{ and } \Sigma_s^w = \sum_b \sum_a \frac{c_{na}^{mb}}{c_{nn}^{mm}} \tilde{V}_{sa}^{wb} \Theta_{ns}^{mw} \quad (2.4.21)$$

Recalling the description of \tilde{V} by Equations 2.4.11 and 2.4.14 gives

$$\tilde{V}_{if}^{jg} = \langle \Psi_f^g | \tilde{V} | \Psi_i^j \rangle = \int_{-\infty}^{+\infty} \Psi_f^g \sum_{w \neq j} (P^w - |V|) \Psi_i^j dz \quad (2.4.22)$$

and using the fact that all of the localized wavefunctions Ψ can be described using the analytical form outlined in Section 2.3 the evaluation of the matrix elements for any possible coupled well system can be expanded analytically. To evaluate these integrals the states of a general coupled well system (Figure 2.4.2) can be written in a piecewise form

$$\Psi_i^n = A_i^n e^{+\kappa_i^n z} \Big|_{-\infty}^{z_n} + [C_i^n \sin(k_i^n z) + D_i^n \cos(k_i^n z)] \Big|_{z_n}^{z_n+L_n} + G_i^n e^{-\kappa_i^n z} \Big|_{z_n+L_n}^{+\infty} \quad (2.4.23)$$

where the bar $\Big|_a^b$ denotes the limits where the function is nonzero.

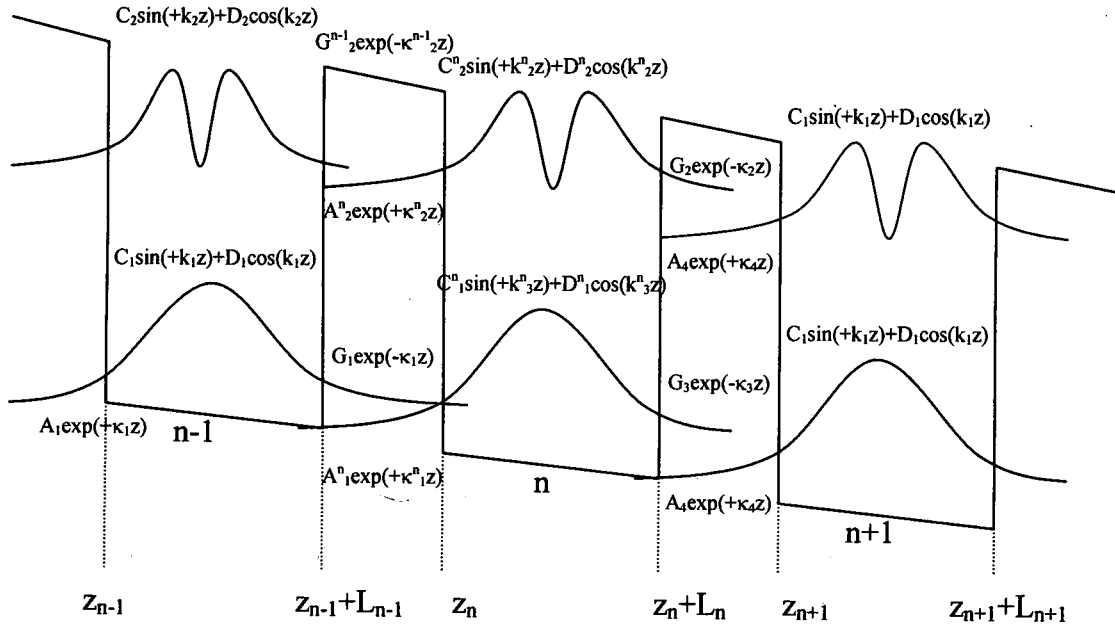


Figure 2.4.2: Diagram showing the piecewise descriptions of single well wavefunctions translated into a multi-well system.

The operator \tilde{V} for a state in well (n) will be nonzero in all wells of an extended system, except for well (n). Choosing a nearest-neighbor interaction only reduces this operator to only having significance for the wells $n \pm 1$. The matrix elements coupling interwell localized states through the additional potential can then be written as

$$\tilde{V}_{ij}^{nm} = \left\langle a_j^m \Big|_{-\infty}^{z_m} + c d_j^m \Big|_{z_m}^{z_m+L_m} + g_j^m \Big|_{z_m+L_m}^{+\infty} \left| -|V_{z_{n-1}}^{z_{n-1}+L_{n-1}} - |V_{z_{n+1}}^{z_{n+1}+L_{n+1}} \right| a_i^n \Big|_{-\infty}^{z_n} + c d_i^n \Big|_{z_n}^{z_n+L_n} + g_i^n \Big|_{z_n+L_n}^{+\infty} \right\rangle \quad (2.4.24)$$

where the notation has been condensed using

$$\begin{aligned}
a_i^n &= A_i^n e^{\kappa_i^n z} \\
cd_i^n &= C_i^n \sin(k_i^n z) + D_i^n \cos(k_i^n z) \\
g_i^n &= G_i^n e^{-\kappa_i^n z}
\end{aligned} \tag{2.4.25}$$

Now, the coupled well interaction for a state (i) in well (n) to another state (j) in well (m) can be written depending on the location of the final state. For example,

$$\underline{m=n-1}$$

$$\tilde{V}_{ij}^{nn-1} = \left\langle cd_j^{n-1} \left| (-|V|) a_i^n \right. \right\rangle_{z_{n-1}}^{z_{n-1}+L_{n-1}} + \left\langle g_j^{n-1} \left| (-|V|) g_i^n \right. \right\rangle_{z_{n+1}}^{z_{n+1}+L_{n+1}} \tag{2.4.26}$$

$$\underline{m=n}$$

$$\tilde{V}_{ij}^{nn} = \left\langle a_j^n \left| (-|V|) a_i^n \right. \right\rangle_{z_{n-1}}^{z_{n-1}+L_{n-1}} + \left\langle g_j^n \left| (-|V|) g_i^n \right. \right\rangle_{z_{n+1}}^{z_{n+1}+L_{n+1}} \tag{2.4.27}$$

$$\underline{m=n+1}$$

$$\tilde{V}_{ij}^{nn+1} = \left\langle a_j^{n+1} \left| (-|V|) a_i^n \right. \right\rangle_{z_{n-1}}^{z_{n-1}+L_{n-1}} + \left\langle cd_j^{n+1} \left| (-|V|) g_i^n \right. \right\rangle_{z_{n+1}}^{z_{n+1}+L_{n+1}} \tag{2.4.28}$$

It can therefore be concluded that there are actually only four unique integrals which need to be evaluated to be applicable for any state in an arbitrary multi-well system. These elements can then be evaluated to indefinite integrals for each elements as

$$\left\langle cd_j^m \left| (-|V|) a_i^n \right. \right\rangle_{z_a}^{z_b} = \left(\frac{A_i^n (-|V|)}{\alpha_1} \right) \left[(D_j^m \kappa_i^n - C_j^m k_j^m) \cos(k_j^m z) + (D_j^m k_j^m + C_j^m \kappa_i^n) \sin(k_j^m z) \right] e^{\kappa_i^n z} \Big|_{z_a}^{z_b} \tag{2.4.29}$$

$$\left\langle g_j^m \left| (-|V|) g_i^n \right. \right\rangle_{z_a}^{z_b} = \frac{-G_i^n G_j^m (-|V|)}{\xi} e^{-\xi z} \Big|_{z_a}^{z_b} \tag{2.4.30}$$

$$\left\langle a_j^m \left| (-|V|) a_i^n \right. \right\rangle_{z_a}^{z_b} = \frac{A_i^n A_j^m (-|V|)}{\xi} e^{\xi z} \Big|_{z_a}^{z_b} \tag{2.4.31}$$

$$\langle \text{cd}_j^m | (-|V|) | \xi_i^n \rangle_{z_1}^{z_2} = \left(\frac{-G_i^n(-|V|)}{\alpha_1} \right) \left[(D_j^m \kappa_i^n + C_j^m k_j^m) \cos(k_j^m z) + (C_j^m \kappa_i^n - D_j^m k_j^m) \sin(k_j^m z) \right] e^{-\kappa_i^n z} \Big|_{z_1}^{z_2} \quad (2.4.32)$$

where $\xi = (\kappa_i^n + \kappa_j^m)$ and $\alpha = (\kappa_i^n)^2 + (k_j^m)^2$. There are now analytical expressions that describe all \tilde{V} terms which can be evaluated simply by inserting the predetermined single-well energy $\epsilon(L)$ and the location of the interfaces for any multi-well system.

Now that there are expressions for the \tilde{V} terms the two state example, depicted in Figure 2.4.1., can be revisited. Assuming the ground states in the left and right well are the only states in the system and are labeled as (g,L) and (g,R), respectively, Equation 2.4.20 can be used to write

$$\frac{c_{gg}^{LR}}{c_{gg}^{LL}} = -\frac{\Delta \tilde{\epsilon}_{gg}^{LR}}{2\tilde{V}_{gg}^{LR}} \pm \frac{\sqrt{(\Delta \tilde{\epsilon}_{gg}^{LR})^2 + 4\tilde{V}_{gg}^{LR}\tilde{V}_{gg}^{RL}}}{2\tilde{V}_{gg}^{LR}} \quad \text{and} \quad \frac{c_{gg}^{RL}}{c_{gg}^{RR}} = -\frac{\Delta \tilde{\epsilon}_{gg}^{RL}}{2\tilde{V}_{gg}^{RL}} \pm \frac{\sqrt{(\Delta \tilde{\epsilon}_{gg}^{RL})^2 + 4\tilde{V}_{gg}^{RL}\tilde{V}_{gg}^{LR}}}{2\tilde{V}_{gg}^{RL}} \quad (2.4.33)$$

and using the left-hand side of Equation 2.4.18 the energies can be written as

$$E_g^L = \tilde{\epsilon}_g^L + \frac{c_{gg}^{LR}}{c_{gg}^{LL}} \tilde{V}_{gg}^{LR} \quad \text{and} \quad E_g^R = \tilde{\epsilon}_g^R + \frac{c_{gg}^{RL}}{c_{gg}^{RR}} \tilde{V}_{gg}^{RL} \quad (2.4.34)$$

Substituting in the coefficient ratios of Equation (2.4.33) into the energy expressions of Equation 2.4.34 results

$$E_g^L = \frac{\tilde{\epsilon}_g^L + \tilde{\epsilon}_g^R}{2} \pm \frac{\sqrt{(\Delta \tilde{\epsilon}_{gg}^{LR})^2 + (\Delta_{gg}^{LR})^2}}{2} \quad \text{and} \quad E_g^R = \frac{\tilde{\epsilon}_g^R + \tilde{\epsilon}_g^L}{2} \pm \frac{\sqrt{(\Delta \tilde{\epsilon}_{gg}^{RL})^2 + (\Delta_{gg}^{LR})^2}}{2} \quad (2.4.35)$$

where $\Delta_{gg}^{LR} = \Delta_{gg}^{RL} = 2\sqrt{\tilde{V}_{gg}^{LR}\tilde{V}_{gg}^{RL}}$.

These expressions can then be applied to the evaluation of the double well system shown in Figure 2.4.1. With the knowledge of the single well energies and the designation of the interfaces the \tilde{V} terms can be calculated and displayed as in Table 2.4.2

V(meV)	L	R
L	-0.054106	-1.914919
R	-3.251829	-0.162259

Table 2.4.2: Table of values for the coupled well interaction terms \tilde{V} for the two state system shown in Figure 2.4.1.

Inserting these values into Equation 2.4.35 gives

$$E_g^L \approx 48.546 \pm 8.766 \quad \text{and} \quad E_g^R \approx 48.546 \pm 8.766 \quad (2.4.36)$$

Therefore, the new solutions for both the state in the left and the state in the right well is the average of their perturbed energies plus or minus a repelling term. Since there is *a priori* knowledge that the lower state will be pushed downward and the higher state will be pushed upward the correct \pm term can be selected by rewriting Equation 2.4.35 as

$$E_g^L = \frac{\tilde{\epsilon}_g^L + \tilde{\epsilon}_g^R}{2} + \sigma_{gg}^{LR} \frac{\sqrt{(\Delta\tilde{\epsilon}_{gg}^{LR})^2 + (\Delta_{gg}^{LR})^2}}{2} \quad \text{and} \quad E_g^R = \frac{\tilde{\epsilon}_g^R + \tilde{\epsilon}_g^L}{2} + \sigma_{gg}^{RL} \frac{\sqrt{(\Delta\tilde{\epsilon}_{gg}^{RL})^2 + (\Delta_{gg}^{LR})^2}}{2} \quad (2.4.37)$$

where

$$\sigma_{ij}^{nm} = \begin{cases} 1, & \Delta\epsilon_{ij}^{nm} > 0 \\ -1, & \Delta\epsilon_{ij}^{nm} < 0 \end{cases} \quad (2.4.38)$$

Using this formulation for the designated \pm term for each energy a comparison of these values with the original, numerically calculated, values of Table 2.4.1. can be made This comparison is shown below in Table 2.4.3.

E(70)	E(50)	E1	E2	E[L]	E[R]
40.09	56.79	39.80	57.26	39.67	56.99

Table 2.4.3: Comparison of the original localized energies (E(70) and E(50)) with both the numerical calculation (E1 and E2) and the new perturbed values (E(L) and E(R)).

From Table 2.4.3 it is seen that this method of describing the coupled well repelling effect analytically using the localized single well basis agrees well with the full numerical calculation. While the values of the numerical results are not exactly predicted the behavior of the lowest state being pushed downward and the higher state upward is reproduced.

The next step is to account for a linear bias across the coupled well system. In this case, unlike the coupled well effect outlined above, the additional bias is treated as a position dependent shift of the localized energy ϵ . With this single well energy being

$$\epsilon_n^m = \langle \Psi_n^m | H^m | \Psi_n^m \rangle \quad (2.4.39)$$

the effect of the electric field can be described using the Hellmann-Feynman Theorem [145]

$$\epsilon_n^m(F) = \langle \Psi_n^m | H_F' | \Psi_n^m \rangle = \tilde{F}_{nn}^{mm} \quad (2.4.40)$$

Due to the symmetry of localized wavefunctions Ψ , with respect to their respective single wells, the evaluation of the matrix element reduces to

$$\tilde{F}_{nn}^{mm} = \langle \Psi_n^m | F(z - z_o) | \Psi_n^m \rangle = F(z - z_o)_{z=m_c} \quad (2.4.41)$$

where $|_{z=m_c}$ implies the evaluation of the field at the center of well m . With these terms acting on the isolated states themselves this effect can be inserted into the “perturbed energy” term previously defined in Equation 2.4.16. The new definition will then be

$$\tilde{\epsilon}_s^w = \epsilon_s^w + \tilde{V}_{ss}^{ww} + \tilde{F}_{ss}^{ww} \quad (2.4.42)$$

A direct comparison of only this perturbed energy value to the full numerical calculation originally presented in Figure 2.2.7. is displayed in Figure 2.4.3. In this figure the numerical calculation for the ground state in each well is displayed using black lines. The value of the perturbed energy, as given by Equation 2.2.42, for the ground state in the left and right well are displayed as dotted blue and red lines, respectively.

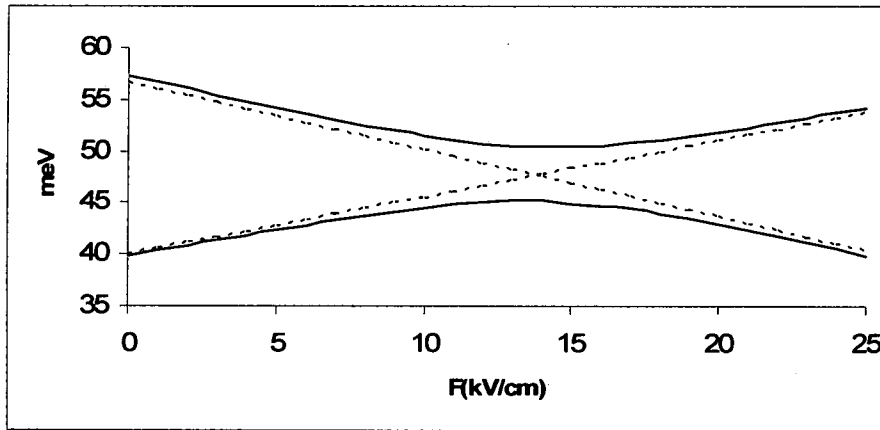


Figure 2.4.3: A comparison of the full numerical calculation (black) and the “perturbed energies” (red and blue dashed lines) calculated using Equation 2.4.42 for a 70Å GaAs well and a 50Å GaAs well separated by a 60Å $\text{Al}_{0.15}\text{Ga}_{0.85}\text{As}$ barrier.

Examination of the perturbed energy values vs. the field shows that the localized states follow closely the numerical calculation until the states approach the anti-crossing field. Clearly the change in energy due to the application of the field is linear

in this case without the inclusion of the repelling effect. Including the repelling effect via Equation 2.4.37 using the new $\tilde{\epsilon}$ terms provided by Equation 2.4.42 produces the behavior depicted in Figure 2.4.4.

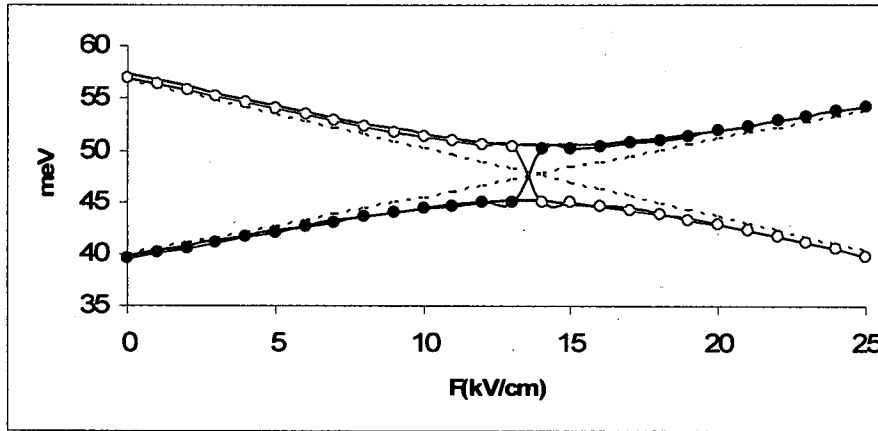


Figure 2.4.4: A comparison of the full numerical calculation (black), the “perturbed energies” (red and blue dashed lines), and the inclusion of the repelling effect (red and blue solid lines with circles) for a 70\AA GaAs well and a 50\AA GaAs well separated by a 60\AA $\text{Al}_{0.15}\text{Ga}_{0.85}\text{As}$ barrier.

In this figure the full numerical result is shown in black, the perturbed energies are red and blue dashed lines, and the energies including the repelling effect are shown as full red and blue lines with circles. As is shown in the figure, including the repelling effect causes the energies to deviate from the linear behavior of the perturbed energies. As these perturbed energies cross, the repelling effect produces a discontinuous jump. As discussed and displayed previously in Figure 2.2.7 this “jump” is where the numerical solution produces an anticrossing of the 1st and 2nd states, yet the designation of which state belongs in which well changes. Using the description of a localized basis the designation of which state belongs to which well is not ambiguous. Thus the behavior of

the energies produces a crossing instead of an anticrossing. Regardless of the designation of states Figure 2.4.4 shows that this method agrees very well therefore validating the calculation of energies using the localized basis coupling method outlined above for a two-state system.

Returning to the description of the wavefunction coefficients, given by Equation 2.4.33, with the inclusion of the proper \pm choice as described above for the energy calculation, i.e.

$$\frac{c_{gg}^{LR}}{c_{gg}^{LL}} = -\frac{\Delta \tilde{\epsilon}_{gg}^{LR}}{2\tilde{V}_{gg}^{LR}} + \sigma_{gg}^{LR} \frac{\sqrt{(\Delta \tilde{\epsilon}_{gg}^{LR})^2 + (\Delta_{gg}^{LR})^2}}{2\tilde{V}_{gg}^{LR}} \quad \text{and} \quad \frac{c_{gg}^{RL}}{c_{gg}^{RR}} = -\frac{\Delta \tilde{\epsilon}_{gg}^{RL}}{2\tilde{V}_{gg}^{RL}} + \sigma_{gg}^{RL} \frac{\sqrt{(\Delta \tilde{\epsilon}_{gg}^{RL})^2 + (\Delta_{gg}^{RL})^2}}{2\tilde{V}_{gg}^{RL}} \quad (2.4.43)$$

Since these are expressions describing the ratios of the off-diagonal to the diagonal wavefunction coefficients the respective values can be solved by considering the new wavefunctions must be normalized. Therefore, a new delocalized wavefunction ψ for a state (n) in well (m), created by the coupled well system, is

$$\psi_n^m = \sum_b \sum_a c_{na}^{mb} \Psi_a^b \quad (2.4.44)$$

which must be normalized such that $\langle \psi_n^m | \psi_n^m \rangle = 1$. Expanding this normalization condition using the localized basis gives

$$\left\langle \sum_j \sum_i c_{ni}^{mj} \Psi_i^j \right\| \sum_b \sum_a c_{na}^{mb} \Psi_a^b \rangle = \sum_j \sum_i \sum_b \sum_a c_{ni}^{mj} c_{na}^{mb} \langle \Psi_i^j | \Psi_a^b \rangle = 1 \quad (2.4.45)$$

Assuming orthogonality of the basis, the above reduces to

$$\sum_b \sum_a (c_{na}^{mb})^2 = 1 \quad (2.4.46)$$

The two-state system can then be written as

$$(c_{gg}^{LR})^2 + (c_{gg}^{LL})^2 = 1 \quad \text{and} \quad (c_{gg}^{RL})^2 + (c_{gg}^{RR})^2 = 1 \quad (2.4.47)$$

The diagonal component for the state (g,L) is

$$c_{gg}^{LL} = \frac{1}{\sqrt{1 + \left(-\frac{\Delta \tilde{\epsilon}_{gg}^{LR}}{2\tilde{V}_{gg}^{LR}} + \sigma_{gg}^{LR} \frac{\sqrt{(\Delta \tilde{\epsilon}_{gg}^{LR})^2 + (\Delta_{gg}^{LR})^2}}{2\tilde{V}_{gg}^{LR}} \right)^2}} \quad (2.4.48)$$

and the off-diagonal is

$$c_{gg}^{LR} = \frac{-\frac{\Delta \tilde{\epsilon}_{gg}^{LR}}{2\tilde{V}_{gg}^{LR}} + \sigma_{gg}^{LR} \frac{\sqrt{(\Delta \tilde{\epsilon}_{gg}^{LR})^2 + (\Delta_{gg}^{LR})^2}}{2\tilde{V}_{gg}^{LR}}}{\sqrt{1 + \left(-\frac{\Delta \tilde{\epsilon}_{gg}^{LR}}{2\tilde{V}_{gg}^{LR}} + \sigma_{gg}^{LR} \frac{\sqrt{(\Delta \tilde{\epsilon}_{gg}^{LR})^2 + (\Delta_{gg}^{LR})^2}}{2\tilde{V}_{gg}^{LR}} \right)^2}} \quad (2.4.49)$$

Similar expression can also be derived for the state (g,R).

The first thing to examine is the value of the coefficients when the states are at resonance, i.e. $\Delta \tilde{\epsilon} = 0$. The above equations reduce to

$$c_{gg}^{LL} = \frac{1}{\sqrt{1 + \frac{(\Delta_{gg}^{LR})^2}{(2\tilde{V}_{gg}^{LR})^2}}} \quad \text{and} \quad c_{gg}^{LR} = \frac{\frac{\Delta_{gg}^{LR}}{2\tilde{V}_{gg}^{LR}}}{\sqrt{1 + \frac{(\Delta_{gg}^{LR})^2}{(2\tilde{V}_{gg}^{LR})^2}}} \quad (2.4.50)$$

It is expected, in the case of 2 states at resonance, that the normalized coefficient magnitudes would both have the value $\frac{1}{\sqrt{2}}$. From the previous definition of

$\Delta_{gg}^{LR} = \Delta_{gg}^{RL} = 2\sqrt{\tilde{V}_{gg}^{LR}\tilde{V}_{gg}^{RL}}$ it can be noted that Equation 2.4.50 reduces to this value only

if $\tilde{V}_{gg}^{LR} = \tilde{V}_{gg}^{RL}$. This is essentially a statement that the matrix elements \tilde{V} should be

Hermitian. Unfortunately, calculation of these terms using the method outlined in this section will not automatically satisfy this condition unless the localized wavefunctions

have the same wavevector κ . However, in the repelling term the value of

$$\left(\Delta_{gg}^{LR}\right)^2 = 4\tilde{V}_{gg}^{LR}\tilde{V}_{gg}^{RL} \approx 4\left(\frac{\tilde{V}_{gg}^{LR} + \tilde{V}_{gg}^{RL}}{2}\right)^2 \quad (2.4.51)$$

when $\tilde{V}_{gg}^{LR} \approx \tilde{V}_{gg}^{RL}$. The hermiticity of \tilde{V} can then be implemented by averaging the value of the off-diagonal terms without significantly changing the calculation of the energy (see Figure 2.4.5). In this plot the energy calculated using the non-Hermitian form of \tilde{V} is shown in black and the forced Hermitian form is plotted in red and blue. As is obvious from the plot, averaging the off-diagonal terms can be used to force Hermiticity while producing a negligible effect on the energy calculation.

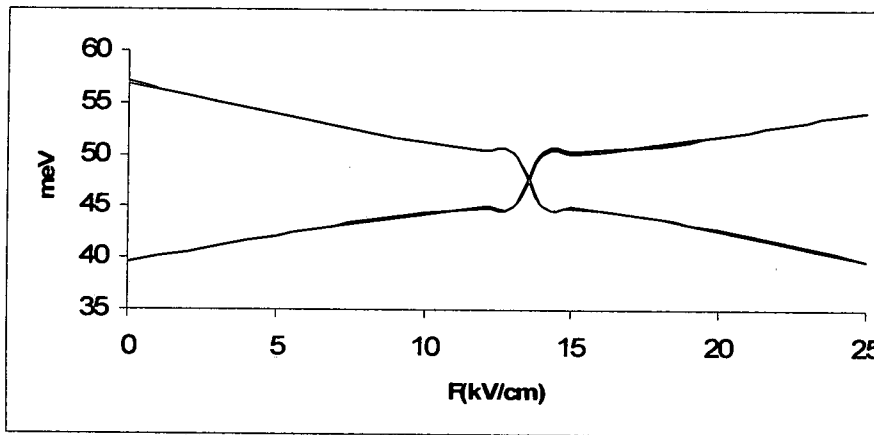


Figure 2.4.5: Comparison of the energies vs. the field using the non-Hermitian (black) and forced Hermitian (red and blue) techniques for a 70Å GaAs well and a 50Å GaAs well separated by a 60Å $\text{Al}_{0.15}\text{Ga}_{0.85}\text{As}$ barrier.

With this form of \tilde{V} the calculation of the wavefunction coefficients can be carried out and a comparison of the new coupled wavefunctions to those calculated using the full numerical simulation can be made. A plot of this wavefunction comparison is shown in Figure 2.4.6 for biases before, near, and after the anti-crossing. In these plots

the full numerical calculations are plotted in black and the coupled states calculated using the single well basis is shown in red and blue. All wavefunctions are plotted as the magnitude squared.

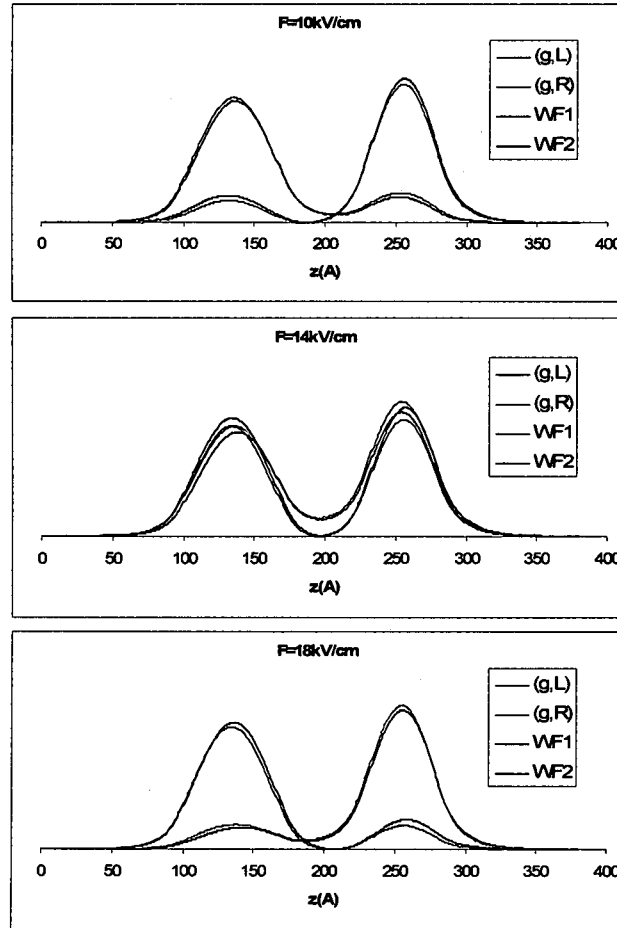


Figure 2.4.6: Comparison of the wavefunctions calculated numerically (black) and using the coupled single well basis (red and blue) at different biases for a 70Å GaAs well and a 50Å GaAs well separated by a 60Å $\text{Al}_{0.15}\text{Ga}_{0.85}\text{As}$ barrier.

From these plots it is observed that the wavefunctions calculated using the expansions of the isolated single well basis agree very well with the full numerical simulation. This result, combined with the agreement of the energy calculation displayed in Figure 2.4.4 prove that the simulation of a coupled well system constructed from isolated single well

states, in the manner outlined above, matches very closely with numerical simulations of the complete Hamiltonian for a 2-state system.

Extending this method to the calculation of a system containing more than two states requires further scrutiny of the result derived previously in Equation 2.4.20 shown again below.

$$\frac{c_{ns}^{mw}}{c_{nn}^{mm}} = - \frac{[\Delta \tilde{\epsilon}_{ns}^{mw} + \Sigma_n^m]}{2 \tilde{V}_{ns}^{mw}} \pm \frac{\sqrt{[\Delta \tilde{\epsilon}_{ns}^{mw} + \Sigma_n^m]^2 + 4 \tilde{V}_{ns}^{mw} [\tilde{V}_{sn}^{wm} + \Sigma_s^w]}}{2 \tilde{V}_{ns}^{mw}} \quad (2.4.52)$$

In this expression for a general multi-state system the coefficient ratio takes the same form as the two-state example, with the addition of some extra quantities. These extra quantities are, as shown previously,

$$\Sigma_n^m = \sum_b \sum_a \frac{c_{na}^{mb}}{c_{nn}^{mm}} \tilde{V}_{na}^{mb} \Theta_{ns}^{mw} \text{ and } \Sigma_s^w = \sum_b \sum_a \frac{c_{na}^{mb}}{c_{nn}^{mm}} \tilde{V}_{sa}^{wb} \Theta_{ns}^{mw} \quad (2.4.53)$$

First consider the second term Σ_s^w and how it differs from the 2-state expression.

When there were only two states the energies described by Equation (2.4.37) can be rewritten as the magnitude of the energy difference

$$|E_g^L - E_g^R| = \sqrt{(\Delta \tilde{\epsilon}_{gg}^{LR})^2 + (\Delta_{gg}^{LR})^2} \quad (2.4.54)$$

At resonance this reduces to

$$|E_g^L - E_g^R| = \Delta_{gg}^{LR} = 2\sqrt{\tilde{V}_{gg}^{LR} \tilde{V}_{gg}^{RL}} \quad (2.4.55)$$

or simply $\Delta E_o = 2\Delta V$, where $\Delta V = \tilde{V}_{gg}^{LR} = \tilde{V}_{gg}^{RL}$, assuming the elements of \tilde{V} are Hermitian. It can therefore be concluded that this second term in the sqrt of Equation 2.4.52 leads directly to the anti-crossing gap of the coupled-well system. Consider then the inclusion of the additional term $4\tilde{V}_{ns}^{mw} \tilde{V}_{sn}^{wm} \rightarrow 4\tilde{V}_{ns}^{mw} [\tilde{V}_{sn}^{wm} + \Sigma_s^w]$ as a correction to

this anti-crossing gap induced by other states in the system. Each element in this correction takes the form

$$\frac{c_{na}^{mb}}{c_{nn}^{mm}} \tilde{V}_{sa}^{wb} \quad (2.5.56)$$

where the state $(a,b) \neq (n,m)$ or (s,w) . In the description of nearest neighbor coupling the location of the well (b) can only be $(m-1)$, m , or $(m+1)$, otherwise $c_{na}^{mb} = 0$. In addition, well (b) must be $(w-1)$, w , or $(w+1)$ otherwise $\tilde{V}_{sa}^{wb} = 0$. Therefore, in describing the coupling between a state (n,m) and, for example, a state (s,w) where $w=m+1$, the only possibilities for a nonzero element of Σ_s^w are in the form

$$\frac{c_{na}^{mm}}{c_{nn}^{mm}} \tilde{V}_{sa}^{m+1m} \text{ or } \frac{c_{na}^{mm+1}}{c_{nn}^{mm}} \tilde{V}_{sa}^{m+1m+1} \quad (2.5.57)$$

Assuming that in the description of the new coupled wavefunction that a state in well (m) will not have a contribution from another intrawell state, first term $c_{na}^{mm} = 0$ can be neglected. This assumption essentially restricts the basis wavefunctions Ψ to always be in the form of unbiased single well states, a condition assumed anyhow for simplicity. In fact, this assumption was already implemented by considering the effect of the electric field to only "perturb" the localized energy based on the location of the state in a multi-well system. Using this approximation the "quantum confined Stark effect" and the wavefunction shift toward the lower potential side of a well cannot be accounted for. However, as previously shown numerically in Figure 2.2.3 this effect is practically negligible for lower biases.

The second term in Equation 2.5.57 suggests that the anti-crossing gap between the (n,m) and (s,w) states is perturbed by the other state in well w . In this case it cannot

be immediately assumed that either c_{na}^{mm+1} or \tilde{V}_{sa}^{m+lm+1} are insignificant. However, since the coefficient will be a function of the field (i.e. $c_{ni}^{mj}(F)$) the general behavior of the 2-state coefficient ratio expression can be observed

$$R(F) = -\frac{\Delta\tilde{\epsilon}(F)}{2\tilde{V}} + \sigma(\Delta\tilde{\epsilon}) \frac{\sqrt{(\Delta\tilde{\epsilon}(F))^2 + 4\tilde{V}}}{2\tilde{V}} \quad (2.5.58)$$

to be a function of the perturbed energy difference $\Delta\tilde{\epsilon}(F)$. A plot of the magnitude of this ratio vs. $\Delta\tilde{\epsilon}$, in units of \tilde{V} , is shown below in Figure 2.4.7.

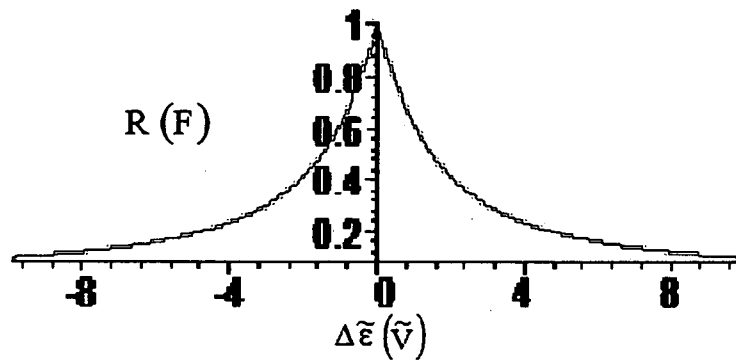


Figure 2.4.7: The coupling coefficient ratio given by Equation 2.5.58 vs the perturbed energy separation of two interwell states in units of the coupled-well interaction \tilde{V} .

Since the value of the coefficient reduces quickly with increasing $|\Delta\tilde{\epsilon}|$ the assumption can be made that, in describing the coupling between two interwell states which are near resonance such that their interaction is non-negligible, interaction with another state in the same neighboring well will be negligible due to the energy separation. For example, consider a double well structure with a 120Å GaAs well and a 200Å GaAs well separated by a 30Å $Al_{0.15}Ga_{0.85}As$ barrier (shown in Figure 2.4.8). In this case consider the coupling of the ground state in the left well (labeled state $|1\rangle$) and either state in the right well (labeled $|3\rangle$ and $|4\rangle$).

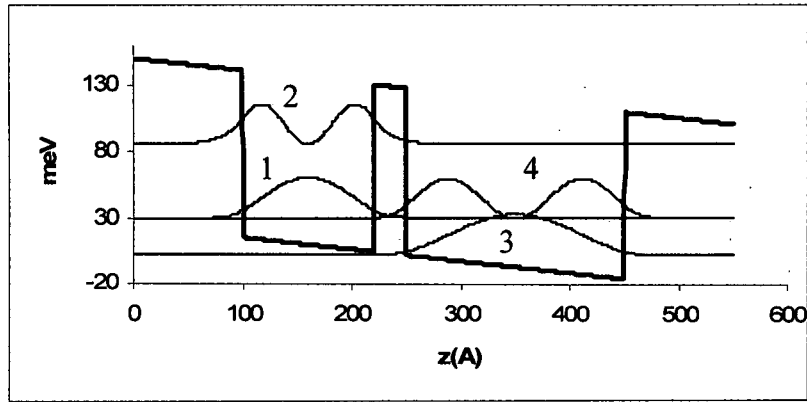


Figure 2.4.8: Eigenstates of 120Å GaAs well and a 200Å GaAs well separated by a 30Å $\text{Al}_{0.15}\text{Ga}_{0.85}\text{As}$ barrier, shown at 9kV/cm.

The calculated \tilde{V} terms for this system are shown in Table 2.4.4

(meV)	1	2	3	4
1	-0.176	0.586	-1.273	-2.609
2	0.586	-2.031	3.950	5.830
3	-1.273	3.950	-0.046	-0.115
4	-2.609	5.830	-0.115	-0.287

Table 2.4.4: Interaction terms \tilde{V} for the 120Å/200Å double GaAs well system separated by a 30Å $\text{Al}_{0.15}\text{Ga}_{0.85}\text{As}$ barrier biased at 9kV/cm.

Here the magnitudes of the terms for the 1-3 coupling and the 1-4 coupling are 1.273 and 2.609 meV, respectively. For this 200Å well the energy separation between the intrawell states is approximately 27meV. Therefore, if the ground state in the left well is near resonant with either state in the right well the other state in the right well is close to

27meV away. This energy separation is roughly 20 times the 1-3 \tilde{V} term and 10 times the 1-4 value. By again observing the plot in Figure 2.4.7 it is shown that the value of the coefficient at this $\Delta\epsilon/\tilde{V}$ ratio will be nearly zero. It is therefore concluded that, except for the case of very large wells with small intrawell energy separations, the Σ_s^w describing a correction to the 2-state anti-crossing gap can be neglected.

Consider now the other additional term Σ_n^m , which accompanies the description of the perturbed energy difference $\Delta\tilde{\epsilon}_{ns}^{mw}$. Here the terms take the form

$$\frac{c_{na}^{mb}}{c_{nn}^{mm}} \tilde{V}_{na}^{mb} \quad (2.4.59)$$

thereby describing the coupling to other states, besides the primary $(s,w)^{th}$, or the $(n,m)^{th}$ state. The same arguments presented previously for neglecting the Σ_s^w term can be applied here to remove from consideration the coupling to another intrawell state as well as another state in well (w). This leaves one term which cannot be logically neglected. This would be a state near resonant with (n,m) in the other neighboring well, not (w). Thus if (s,w) is in well $(m+1)$ there could be a non-negligible interaction from a state (a) in well $(m-1)$

$$\frac{c_{na}^{mm-1}}{c_{nn}^{mm}} \tilde{V}_{na}^{mm-1} \quad (2.4.60)$$

To observe this effect take the two-well system previously analyzed and introduce another well on the left. Consider a 120/**30**/70/**60**/50 GaAs/ $Al_{0.15}Ga_{0.85}As$ structure where the barriers are listed in boldface. A plot of this structure is shown in Figure 2.4.9.

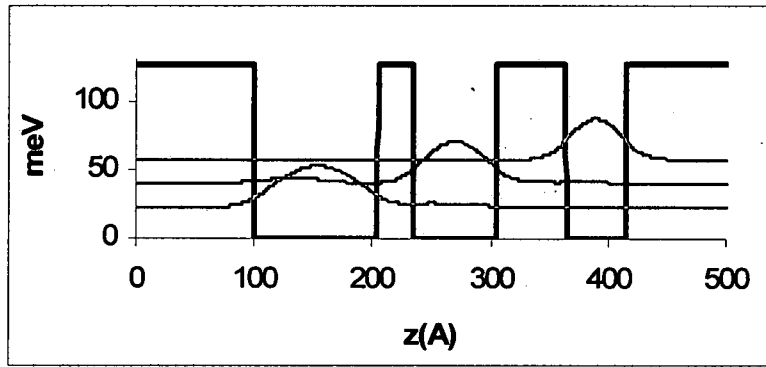


Figure 2.4.9: Eigenstates of a 120/30/70/60/50 GaAs/ $\text{Al}_{0.15}\text{Ga}_{0.85}\text{As}$ system.

Consider first the numerical technique of Section 2.2. The simulation of the energies vs the field is shown in Figure 2.4.10. The energy separations for this 3-state system are plotted in Figure 2.4.11 along with the 2-state energy separation calculated previously for the 70/60/50 GaAs/ $\text{Al}_{0.15}\text{Ga}_{0.85}\text{As}$ system.

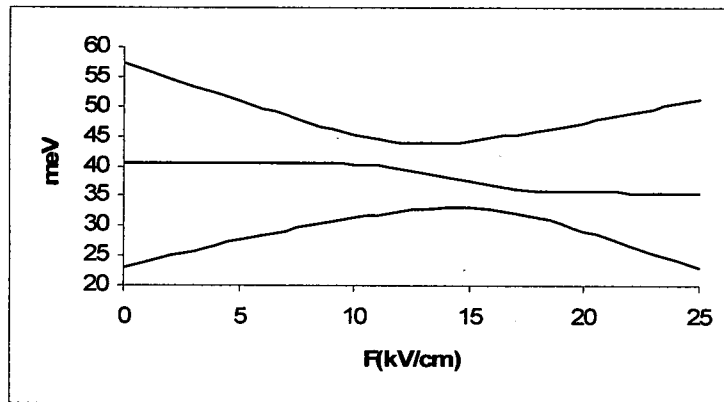


Figure 2.4.10: Energies vs. the bias calculated numerically for a 120/30/70/60/50 GaAs/ $\text{Al}_{0.15}\text{Ga}_{0.85}\text{As}$ system.

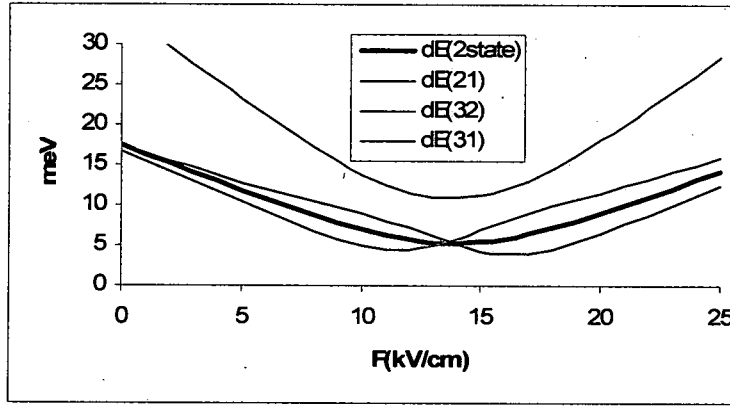


Figure 2.4.11: Energy separations vs. the bias calculated numerically for the three well 120/30/70/60/50 GaAs/Al_{0.15}Ga_{0.85}As system compared to the 2-state 70/60/50 GaAs/Al_{0.15}Ga_{0.85}As system.

Now assume a simulation of the above system where the correcting terms Σ_n^m are considered small such that

$$\frac{c_{ns}^{mw}}{c_{nn}^{mm}} = -\frac{\Delta \tilde{\epsilon}_{ns}^{mw}}{2 \tilde{V}_{ns}^{mw}} + \sigma_{ns}^{mw} \frac{\sqrt{(\Delta \tilde{\epsilon}_{ns}^{mw})^2 + (\Delta_{ns}^{mw})^2}}{2 \tilde{V}_{ns}^{mw}} \quad (2.4.61)$$

This expression for the ratio of the components essentially assumes all interwell couplings are independent of one another. The new energy of a state (n) in well (m) can then be written as the combination of all interwell couplings

$$E_n^m = \tilde{\epsilon}_n^m + \sum_w \sum_s \frac{c_{ns}^{mw}}{c_{nn}^{mm}} \tilde{V}_{ns}^{mw} (1 - \delta_{sn}^{wm}) \quad (2.4.62)$$

Substituting (2.4.61) into this gives

$$E_n^m = \tilde{\epsilon}_n^m + \sum_w \sum_s \left[-\frac{\Delta \tilde{\epsilon}_{ns}^{mw}}{2} + \sigma_{ns}^{mw} \frac{\sqrt{(\Delta \tilde{\epsilon}_{ns}^{mw})^2 + (\Delta_{ns}^{mw})^2}}{2} \right] (1 - \delta_{sn}^{wm}) \quad (2.4.63)$$

Evaluation of the energies using this analytical approach produces the energy vs. field plot displayed in Figure 2.4.12. In this plot it is clearly observed that the new energies for the previously localized state (1 in green), (2 in blue), and (3 in red) follow the numerical calculation (black) fairly well until the common anti-crossing point is approached. Near this common field the strong coupling of state $|2\rangle$ in the middle well to state $|1\rangle$ in the left well combines with the $|2\rangle$ to $|3\rangle$ repelling and causes both states $|2\rangle$ and $|1\rangle$ to overshoot the fully numerical simulations of the gaps. After this point however, the analytical simulation tends back toward the full numerical results.

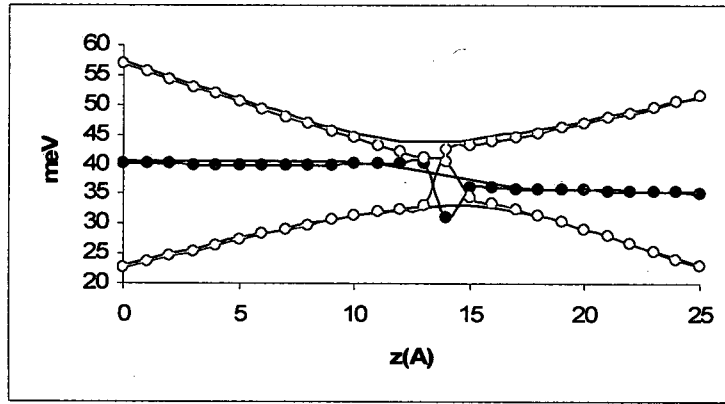


Figure 2.4.12: Numerically calculated energies (black) vs. the bias compared to the simplified expression of Equation 2.4.63 (red, blue, green) for the three well 120/30/70/60/50 GaAs/ $\text{Al}_{0.15}\text{Ga}_{0.85}\text{As}$ system.

It is worth noting here that the error shown above in Figure 2.4.12 is due to the approximation used in writing Equations 2.4.61 and 2.4.62, namely the assumption that the interwell couplings can be treated as independent of each other. The error is not due to the use of localized single-well eigenstates, or the nearest-neighbor approximation, as the problem could have been stated in the full tight-binding matrix form

$$H = \begin{bmatrix} \tilde{\epsilon}_1 & \tilde{V}_{12} & 0 \\ \tilde{V}_{12} & \tilde{\epsilon}_2 & \tilde{V}_{23} \\ 0 & \tilde{V}_{23} & \tilde{\epsilon}_3 \end{bmatrix} \quad (2.4.64)$$

and solved for the eigenvalues of H . This full tight-binding treatment of the eigenvalues is compared to the full numerical evaluation in Figure 2.4.13.

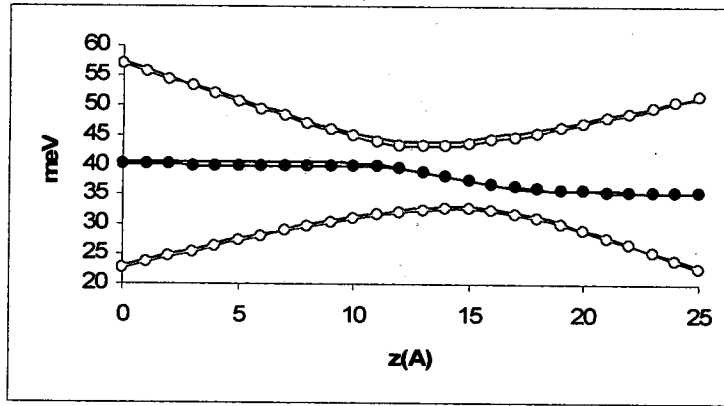


Figure 2.4.13: Numerically calculated energies (black) vs. the bias compared to the full tight-binding matrix treatment of Equation 2.4.64 (red, blue, green) for the three well 120/30/70/60/50 GaAs/ $\text{Al}_{0.15}\text{Ga}_{0.85}\text{As}$ system.

In this plot the full numerical simulation is plotted using black lines and the eigenvalues of Equation (2.6.64) are displayed as green, blue, and red lines with circles. The agreement between the results indicates that the full tight-binding solutions are valid as they follow almost exactly the full numerical simulation. As the construction of the matrix for this method used the single-well basis and assumed nearest-neighbor only interactions, these assumptions are still proven sufficient. The downside to this approach however, is the lack of an analytical expression such as Equation 2.4.63. Because this

approach would require solving the eigenvalues of a matrix it differs little, in its use as an analytical tool, from the full numerical simulation.

In summary, what was derived in a rather lengthy manner is an analytical expression which approximates the eigenvalues and vectors of a multi-well Hamiltonian expanded in a localized single well basis under the assumption of nearest-neighbor only interactions. While the full treatment, as shown in Figure 2.4.13, validates this expansion method by comparison to the full numerical simulation, the simplified treatment (Figure 2.4.12) shows acceptable results while maintaining an analytical form. Further, the expressions given by Equation 2.4.63 and Equation 2.4.61 not only permits an analytical means of reproducing coupled well wavefunction delocalization but maintains the designation of which state "belongs" to which well. This distinction can not easily be made using either the numerical approach or the full tight-binding matrix expansion. In addition, due to the analytical form of the single-well basis wavefunctions, perturbed energies, coupled well repelling effects, and nearest neighbor delocalization can now be described for any arbitrary heterostructure simply by the designation of the interface locations and the applied bias.

CHAPTER 3

SCATTERING RATES IN QUANTUM HETEROSTRUCTURES

3.1 Introduction

Calculation of scattering rates which lead to the determination of the lifetime of states is essential for subsequent predictions of electron transport. Since the scattering rates are highly dependent on both the wavefunctions and energies of the states involved, which can be engineered through the heterostructure design; the manipulation of lifetimes to achieve the desired performance is the fundamental problem to be solved in the design of QCL's. The accurate description of scattering rates becomes increasingly important at THz frequencies where a multitude of transition mechanisms are highly energy and temperature dependent. As a result, the computational requirements for modeling THz-QCL's have become very restraining.

In this chapter two primary scattering mechanisms, electron-longitudinal optical (LO) phonon and electron-electron interactions, are investigated and techniques to limit the computational requirements of these calculations are presented. An expansion of Fermi's Golden Rule in the localized single well basis is demonstrated to result in an extraordinary reduction of computing time. This procedure utilizes two primary simplifying assumptions: (1) scattering between the basis states occur intrawell only, and (2) an approximation to mean coupled-well scattering rates can be directly written as a

linear combination of intrawell mean scattering rates. These approximations are validated by direct comparison to full numerical calculations. Once demonstrated in principle the fundamental time saving aspect of this research is realized; properties of multi-quantum well systems can be written as linear combinations of intrawell properties. With this in mind, LO-phonon and electron-electron scattering is examined over a wide range of parameters for the limited available transitions which occur within a single well. Empirical fitting functions are then introduced to permit instant mean scattering rates for the localized basis. With the analytical basis and pre-simplified tight-binding coupling parameters, scattering rates in multi-well systems are then constructed and immediately evaluated by the designation of the interface locations and the temperature.

3.2 Calculation of Scattering Rates

In most descriptions of quantum mechanical scattering a time-dependent perturbation \tilde{H} , which enables a transition from an initial state $|i\rangle$ to a final state $|f\rangle$, is treated using Fermi's Golden Rule

$$W_{if} = \frac{1}{\tau_{if}} = \frac{2\pi}{\hbar} |\langle f | \tilde{H} | i \rangle|^2 \delta(E_f - E_i) \quad (3.2.1)$$

where W_{if} is the transition rate and τ_{if}^{-1} is the lifetime. In quantum heterostructures there are many potential mechanisms for electron scattering including: longitudinal acoustic (LA) phonon scattering, longitudinal optic (LO) phonon scattering, electron-electron scattering, electron-ionized impurity scattering, and interface disorder. Rigorous derivations and detailed discussions of these numerous mechanism and their relative significance have been extensively treated elsewhere [68-78]. In this section the general

procedures for calculating scattering rates for two primary mechanisms (LO-phonon and electron-electron scattering) will be introduced.

For the calculation of electron-LO phonon scattering it can first be assumed that the phonons in a heterostructure follow the usual bulk material phonon modes. The perturbing Hamiltonian for these bulk modes can be written as

$$\tilde{H} = e \sum_{\mathbf{K}} \left(\frac{\hbar \omega P}{2|\mathbf{K}|^2} \right)^{1/2} \frac{e^{-i\mathbf{K} \cdot \mathbf{r}}}{V^{1/2}} \quad (3.2.2)$$

where \mathbf{K} is the phonon wavevector, $\hbar \omega$ is the energy of the phonon mode which is assumed dispersionless, $P = \frac{1}{\epsilon_\infty} - \frac{1}{\epsilon_s}$ where ϵ_∞ and ϵ_s describe the high and low frequency permittivities of the material, and V is the crystal volume. Following the method of Harrison [50] the following expressions can be derived describing the lifetime of a state in subband (i) with an in-plane wavevector k_i scattering to all final states k_f in subband (f)

$$\frac{1}{\tau_{if}} = \frac{Y''}{2} \Theta \left(k_i^2 - \frac{2m^* \Delta}{\hbar^2} \right) \int_{-\infty}^{+\infty} \frac{\pi |G_{if}(\mathbf{K}_z)|^2}{\sqrt{K_z^4 + 2K_z^2 \left(2k_i^2 - \frac{2m^* \Delta}{\hbar^2} \right) + \left(\frac{2m^* \Delta}{\hbar^2} \right)^2}} \quad (3.2.3)$$

where Θ is a Heaviside step function of the argument $\Delta = E_f - E_i \pm \hbar \omega$ and the $+$ ($-$) represents phonon emission(absorption). The term Y'' is

$$Y'' = \frac{2m^* e^2 \omega P}{(2\pi)^2 \hbar^2} \left(N_0 + \frac{1}{2} \pm \frac{1}{2} \right) \quad (3.2.4)$$

where N_0 is the Bose-Einstein factor describing the number of phonons per unit volume, i.e.

$$N_o = \frac{1}{e^{(\hbar\omega/kT)} - 1} \quad (3.2.5)$$

The term $|G_{if}(K_z)|^2$ is commonly referred to as the form factor

$$G_{if} = \langle \psi_f | e^{-iK_z z} | \psi_i \rangle \quad (3.2.6)$$

where ψ_i, ψ_f are the electron envelope wavefunctions along the growth axis (z) and the central term represents the component of the phonon along this axis.

The expression given by Equation 3.2.3 describes the lifetime of state in subband (i) with a specific in-plane kinetic energy k_i scattering to all final states in subband (f). While this expression would be useful if the intention was to track individual particles, a manner of assigning some "effective lifetime" of the entire subband is highly favorable. To accomplish this a definition is defined for a mean subband rate [50], which accounts for the electron distributions in both subbands as well as incorporates final state blocking effects, as

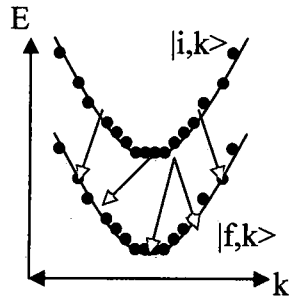
$$W_{if} = \frac{\int \frac{1}{\tau_i} f_i(E) f_f(E - \hbar\omega) dE}{\int \frac{1}{\tau_i} f_i(E) dE} \quad (3.2.7)$$

The terms f_i and f_f describe the Fermi-Dirac distributions in the initial and final subbands

$$f_i = \frac{1}{\exp[(E - E_f)/kT] + 1} \quad (3.2.8)$$

where E_f is the "quasi" Fermi energy. Utilizing these mean scattering rates results in a dramatic simplification of intersubband transport as the 2-dimensional nature of the electronic states are averaged out. This is illustrated in Figure 3.2.1 as this procedure is shown to allow the description of subbands as truly singular entities.

Full Subband Treatment



Mean Subband Rate

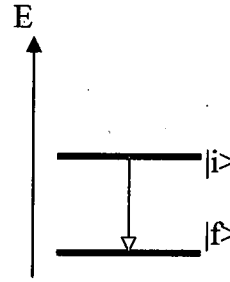


Figure 3.2.1: Transformation of 2D subbands to singular objects by employing a mean subband scattering rate.

Treatment of the electron/LO-phonon interaction in the approach outlined above assumed that the phonons in a heterostructure take the form of bulk LO modes. In this approach the interaction in a $\text{GaAs}/\text{Al}_x\text{Ga}_{1-x}\text{As}$ system is assumed to occur between confined electrons and bulk-GaAs phonons. The inclusion of the complex phonon spectra, i.e. where the phonon modes are also altered by the heterostructure, in the calculation of scattering rates has lead to conflicting results. Prior simulations have claimed that electron-phonon interactions with certain complex phonon modes can produce scattering much faster than traditional bulk-mode transitions [146-150]. Other calculations have shown that scattering due to the complex phonon spectrum in $\text{GaAs}/\text{Al}_x\text{Ga}_{1-x}\text{As}$ systems are bounded by the bulk GaAs and AlAs rates [151,152]. While determination of these altered phonon modes has been approached microscopically [151,153], a simpler macroscopic model known as the dielectric continuum model [154-156] has been shown to provide a close approximation to the microscopic approaches [157,158]. Using this approach the necessity for including these complex modes will be scrutinized.

In the dielectric continuum model the phonon modes are obtained using the electrostatic equations [150]

$$\nabla \cdot \mathbf{D}(\vec{r}) = 0$$

$$\mathbf{D}(\vec{r}) = \epsilon \mathbf{E}(\vec{r}) = \epsilon_0 \mathbf{E}(\vec{r}) + \mathbf{P}(\vec{r}) \quad (3.2.9)$$

$$\mathbf{E}(\vec{r}) = -\nabla \phi(\vec{r})$$

In quantum well structures phonons, like electrons, are confined in only one direction along the growth axis (z-axis). The phonon potential can therefore be written as

$$\Phi(\mathbf{r}) = \sum_{\mathbf{q}} \phi(\mathbf{q}, z) e^{-\vec{q} \cdot \vec{p}} \quad (3.2.10)$$

where \vec{q} and \vec{p} are the in-plane wave and position vectors, respectively, and $q = |\vec{q}|$.

From equations (3.2.9) and (3.2.10) it is found that $\phi(\mathbf{q}, z)$ must satisfy

$$\epsilon(\omega) \left(\frac{\partial^2}{\partial z^2} - q^2 \right) \phi(\mathbf{q}, z) = 0 \quad (3.2.11)$$

Equation (3.2.11) permits two types of solutions and correspondingly, two distinct types of phonon modes. Confined phonon modes satisfy $\epsilon(\omega) = 0$ while interface phonon modes occur for $\epsilon(\omega) \neq 0$. These are solutions to $\left[\partial^2 / \partial z^2 - q^2 \right] \phi(\mathbf{q}, z) = 0$. All modes must be normalized in accordance with orthonormality and completeness conditions which require [156]

$$\frac{\hbar}{2\omega} = \sum_i \frac{\epsilon_0}{2\omega} \frac{\partial \epsilon_i(\omega)}{\partial \omega} \int \left(q^2 |\phi_i(\mathbf{q}, z)|^2 + \left| \frac{\partial \phi_i(\mathbf{q}, z)}{\partial z} \right|^2 \right) dz \quad (3.2.12)$$

where the subscript i refers to a particular layer of the heterostructure. The dielectric function $\epsilon_i(\omega)$ is described, for ternary semiconductors, by

$$\epsilon_i(\omega) = \epsilon_i(\infty) \frac{(\omega^2 - \omega_{LOA}^2)}{(\omega^2 - \omega_{TOA}^2)} \frac{(\omega^2 - \omega_{LOB}^2)}{(\omega^2 - \omega_{TOB}^2)} \quad (3.2.13)$$

where ω_{LO} and ω_{TO} are the longitudinal and transverse optical phonon frequencies for materials A and B. For confined phonon modes the normalized potential can be written as [152]

$$\phi_i(q, z) = \left(\frac{\hbar}{\epsilon_0} \frac{1}{\partial \epsilon_i(\omega)/\partial \omega} \right)^{1/2} \left(\frac{1}{q^2 + (m\pi/a_i)^2} \right)^{1/2} \left(\frac{2}{a_i} \right)^{1/2} \sin \left(\frac{m\pi}{a_i} [z - z_i] \right) \quad (3.2.14)$$

The potential in each layer of width a_i , and order m , is treated as a separate mode in electron-phonon interactions. For the interface phonon modes a transfer matrix method [156] is used to find the allowed frequencies and corresponding potentials.

The rate of transition for an electron initially in state i with in-plane wave vector k_i to a final state f with in-plane wave vector k_f is calculated using Fermi's golden rule with the electron-phonon interaction Hamiltonian expressed as

$$H_{e-ph} = -e \sum_q \phi(q, z) e^{-i\vec{q} \cdot \vec{p}} (a_{-q}^\dagger + a_q) \quad (3.2.15)$$

where a_{-q}^\dagger and a_q are the phonon creation and annihilation operators. The transition rate for phonon emission is then [152]

$$W_{if}(k_i, k_f) = \frac{2\pi}{\hbar} (N_0 + 1) \left| \langle \psi_f(z) | -e\phi(q, z) | \psi_i(z) \rangle \right|^2 \times \delta(E_i + E_{ki} - \hbar\omega - [E_f + E_{kf}]) \quad (3.2.16)$$

which is specific to a transition between an electron in a state $|i, k_i\rangle$ to a state $|f, k_f\rangle$. To convert this general expression to the mean subband rate it must be first integrated over all final states k_f before using Equation 3.2.7.

To demonstrate these altered phonon modes consider a simple two-well system containing a 100Å and a 50Å GaAs well separated by a single Al_xGa_{1-x}As barrier of 30Å

(Figure 3.2.2). This simple structure will permit the examination of the effect of the complex phonon spectrum on both intrawell and interwell transitions. The energies of the IF phonon modes for this double well structure were calculated as previously described and are plotted vs. the phonon wavevector, for an Al composition of $x=0.2$ and a barrier width of 30\AA in figure 3.2.3. From this figure the existence of two GaAs-like bands are observed, one corresponding to the GaAs well regions and the other to the GaAs component of the $\text{Al}_{0.2}\text{Ga}_{0.8}\text{As}$ barriers. There is also a higher energy single AlAs-like band which corresponds to the AlAs component of the barrier.

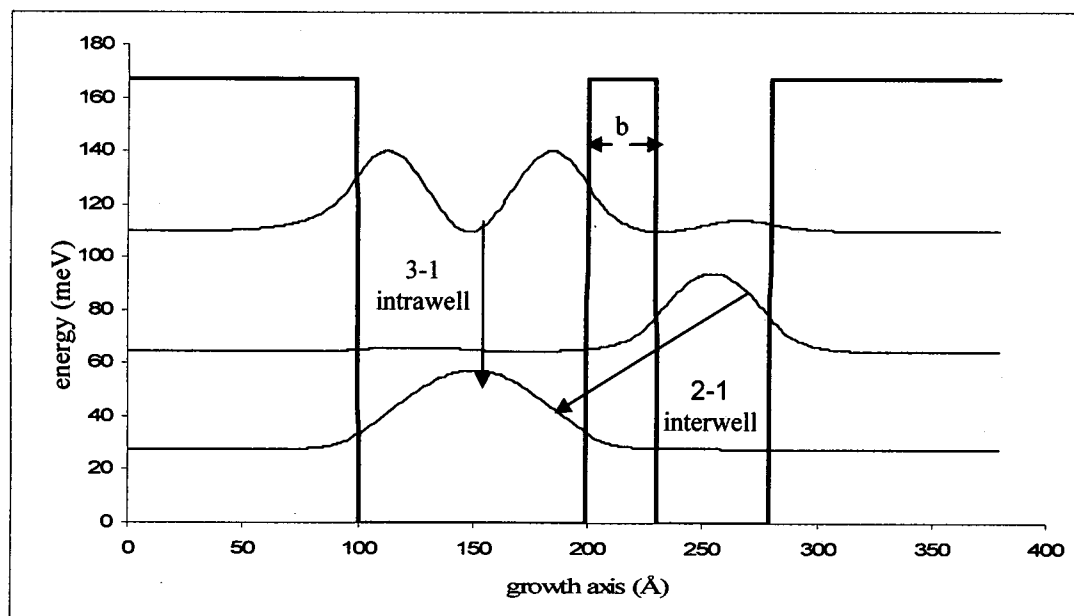


Figure 3.2.2: 150\AA - 50\AA GaAs- $\text{Al}_{0.2}\text{Ga}_{0.8}\text{As}$ double well system. Arrows indicate the 3-1 intrawell and 2-1 interwell transitions.

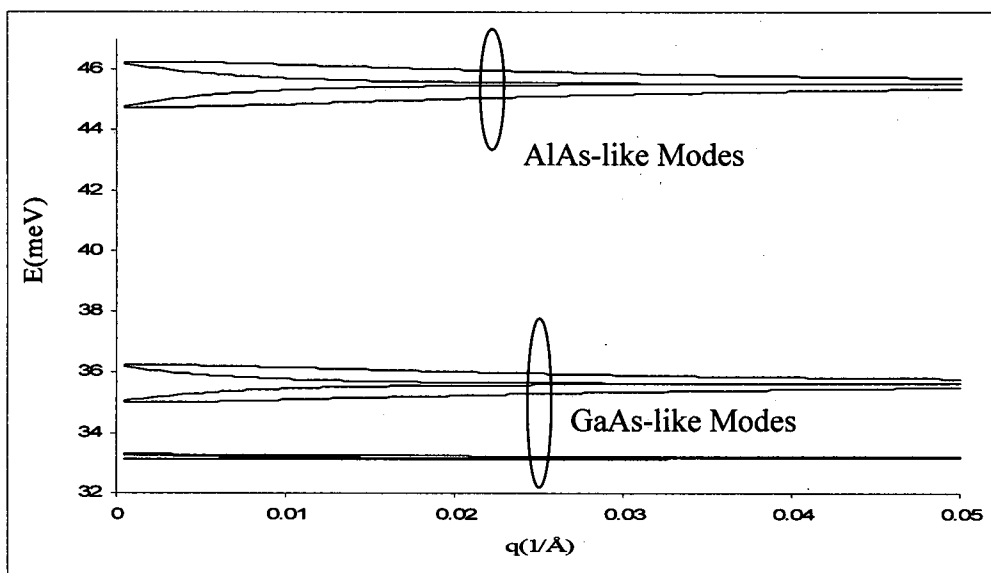


Figure 3.2.3: 150 \AA -50 \AA ($w/b=30\text{\AA}$) GaAs- $\text{Al}_{0.2}\text{Ga}_{0.8}\text{As}$ double well interface phonon dispersion.

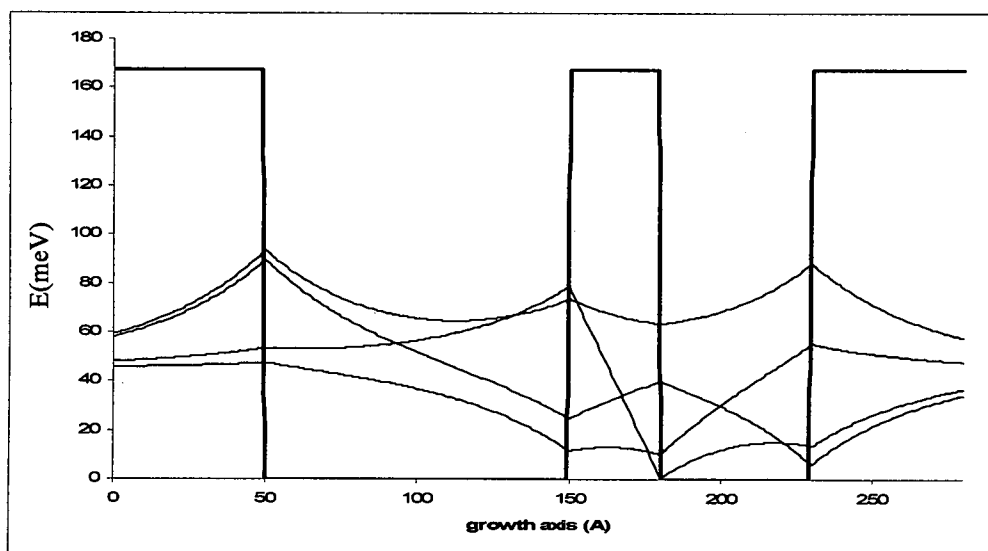


Figure 3.2.4: AlAs-like interface phonon mode potentials at $q=.025(1/\text{\AA})$ for 150 \AA -50 \AA ($w/b=30\text{\AA}$) GaAs- $\text{Al}_{0.2}\text{Ga}_{0.8}\text{As}$ double well.

The phonon potentials for these AlAs-like modes are shown in Figure 3.2.4 at $q=0.025(1/\text{\AA})$. The confined phonon modes of order $m=1$ and $m=2$ are shown in Figure 3.2.5. Half-space modes, which exist in the outer barriers, have negligible effect on the electron-phonon transition rates and are not plotted or considered in subsequent calculations.

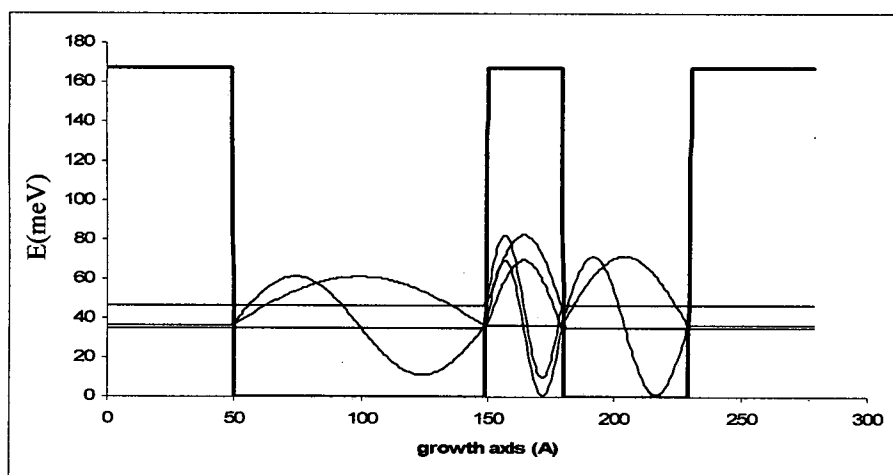


Figure 3.2.5: Confined phonon modes (order $m=1\&2$) for $150\text{\AA}-50\text{\AA}$ ($w/b=30\text{\AA}$) GaAs- $\text{Al}_{0.2}\text{Ga}_{0.8}\text{As}$ double well.

Due to the large number of complex phonon modes to consider, $6w$ for interface modes and $3w-2$ per order m for confined modes (w being the number of wells), the numerical evaluation of the electron-phonon scattering rates quickly becomes a computational nightmare. Since previous reports have indicated that the complex phonon interactions are bounded by the bulk GaAs and AlAs rates [151,152] the possibility of using a combination of GaAs and AlAs-like bulk rates to approximate this full treatment is examined.

To isolate the effects of the complex phonon modes, and their dependence on the barrier composition, the electron wavefunctions were kept fixed at a constant composition ($x=0.2$). The width of the barrier was varied from 20-50 Å and the composition from $x=0.1$ to $x=0.4$. Both intrawell (3-1) and interwell (2-1) intersubband transitions were calculated at manually varied energy separations between 30 and 56 meV. For each case, the interface and confined phonon modes were found along with the respective interwell and intrawell scattering rates. The mean scattering rates were then calculated at room temperature ($T=300\text{K}$). For this mean rate, the electron temperature used for the Fermi-Dirac distribution is assumed to be equal to the lattice temperature and the population of all subbands is set at $1 \times 10^{10} \text{cm}^{-2}$.

Bulk phonon-electron transition rates were also calculated at each variation for both a GaAs ($\hbar\omega_{\text{GaAs}} = 36\text{meV}$) and an AlAs-like ($\hbar\omega_{\text{AlAs-like}}(x) = 44.63 + 8.78x - 3.32x^2$) phonon energy. This bulk-AlAs energy was fit to the energy where the AlAs-like IF modes converge, thus neglecting the dispersion which is only noticeable at small phonon wavevectors (see Figure 3.2.3). The strength of the bulk phonon interaction is calculated using the composition dependant values

$$\begin{aligned}\epsilon_s(x) &= 12.90 - 2.84x \\ \epsilon_\infty(x) &= 10.89 - 2.73x\end{aligned}\tag{3.2.17}$$

For the bulk fit to the complex phonon scattering rates we assume a combination of bulk-GaAs and AlAs phonons of the form

$$B = g(x, b)W_{\text{if}}^{\text{GaAs}} + a(x, b)W_{\text{if}}^{\text{AlAs}}\tag{3.2.18}$$

To obtain the coefficients $g(x, b)$ and $a(x, b)$ for both the intrawell (3-1) and interwell (2-1) transitions, the value of $B(\Delta E) - C(\Delta E)$, C being the total (interface + confined) phonon rates, was minimized over $\Delta E = 30..56$ for each variation of the double well

structure. The resulting fits, linear in composition and 2nd order in barrier width for the interwell rates and linear in composition for the intrawell rates) were found to be

Intrawell:

$$\begin{aligned} g(x) &= 1 - .1395x \\ a(x) &= .2009x \end{aligned} \quad (3.2.19)$$

Interwell:

$$\begin{aligned} g(x, b) &= 1 - (.2826 + .0137b - .0001b^2)x \\ a(x, b) &= (.3383 + .0135b - .0001b^2)x \end{aligned} \quad (3.2.20)$$

A comparison of the mean rates obtained using the total complex (interface and confined) calculation, a single bulk-GaAs approximation, and the above GaAs/AlAs fitting parameters are shown for the interwell (2-1) transition in (Figure 3.2.6) and the intrawell (3-1) transition in (Figure 3.2.7) for a double well structure with $b=30\text{\AA}$ at various compositions. The interwell transitions shown in Figure 3.2.6 show the deviation of the complex rates from the bulk-GaAs rate being a strong function of the AlAs composition of the barriers. This is a logical conclusion noted by previous authors [151,152]. It is also observed that the GaAs/AlAs fit is a more appropriate approximation to the full calculation at higher AlAs compositions with minimal computation expense, compared to the simple bulk-GaAs simplification. The intrawell transitions of Figure 3.2.7 show a similar dependence on barrier composition, although a less pronounced contribution from AlAs-like modes is observed due to less interaction with IF and confined modes near and inside the barrier.

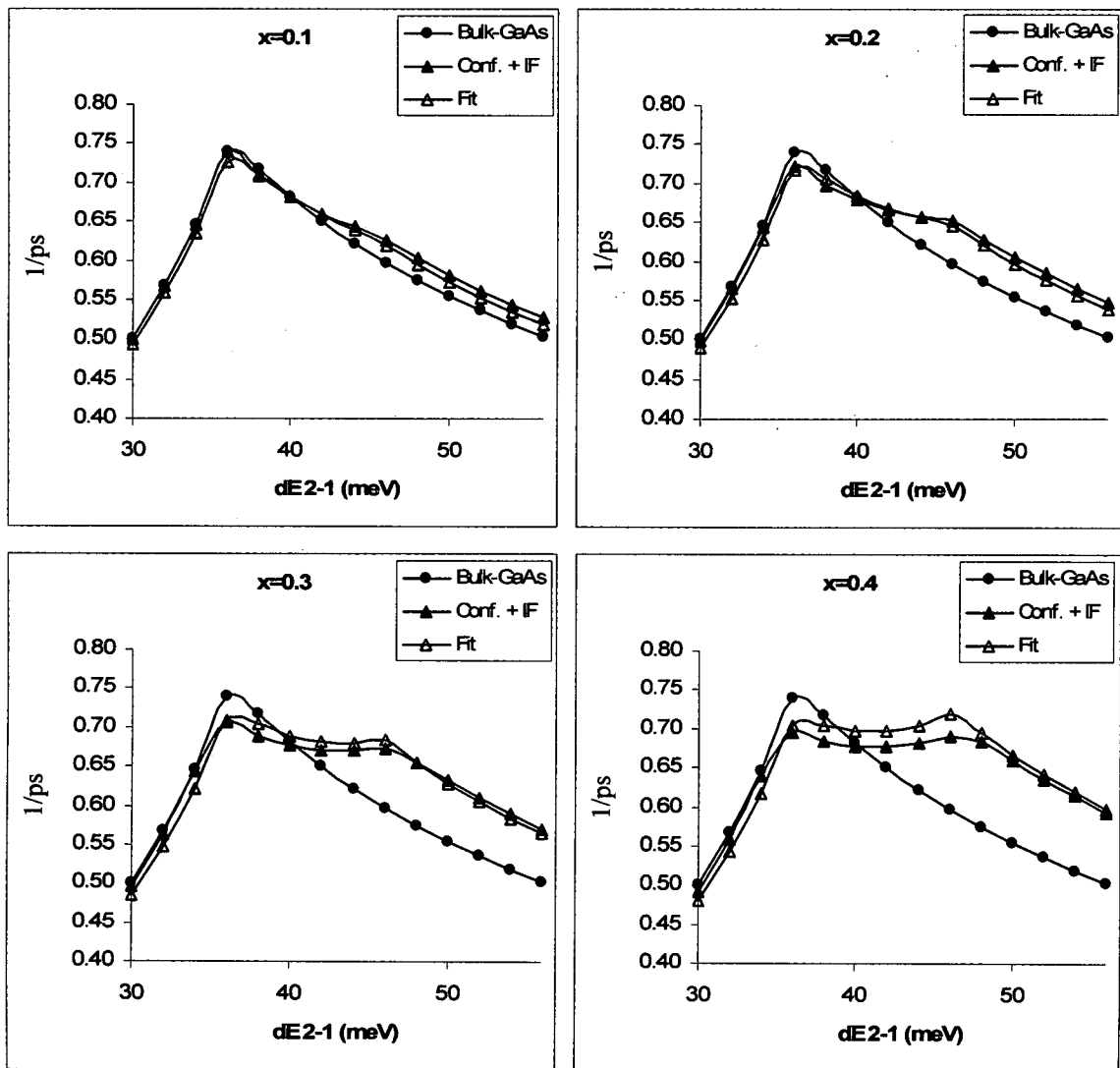


Figure 3.2.6: Comparison of bulk-GaAs phonon, complex (confined + interface) phonon and the $g(x,b)G+a(x,b)A$ bulk-like fit for the 2-1 interwell scattering rates vs. dE_{2-1} for a $150\text{\AA}-50\text{\AA}$ ($w/b=30\text{\AA}$) GaAs- $\text{Al}_{1-x}\text{Ga}_x\text{As}$ double well.

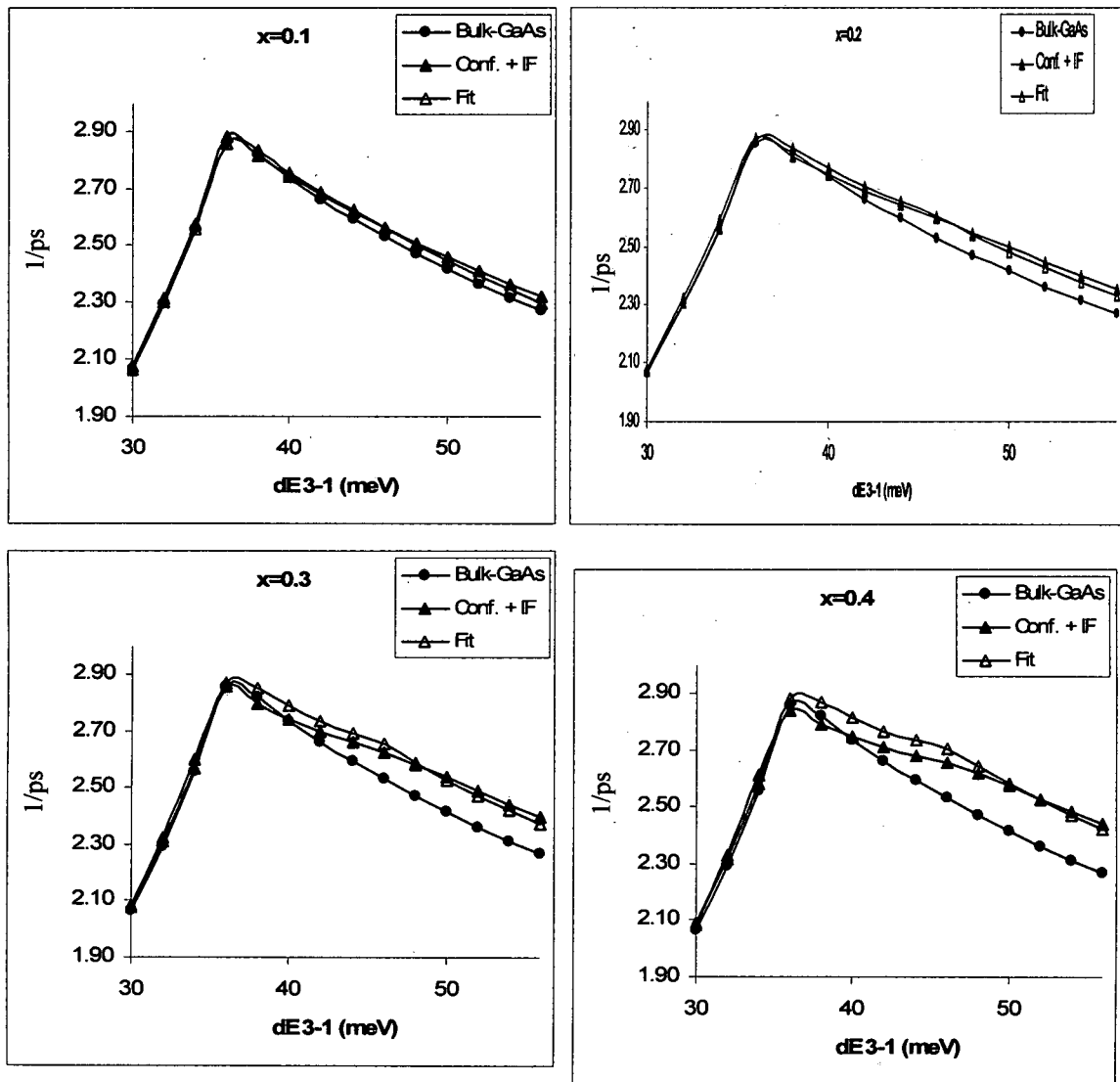


Figure 3.2.7: Comparison of bulk-GaAs phonon, complex (confined + interface) phonon and the $g(x,b)G+a(x,b)A$ bulk-like fit for the 3-1 intrawell scattering rates vs. dE 3-1 for a $150\text{\AA}-50\text{\AA}$ ($w/b=30\text{\AA}$) GaAs- $\text{Al}_{1-x}\text{Ga}_x$ double well.

From these two plots (Figure 3.2.6 and Figure 3.2.7) it is observed that no extremely large scattering rates, relative to the bulk GaAs-modes, are calculated as suggested by References [146-150]. Instead, like the simulations of References [151,152], observing the rates at low Al concentrations show results very similar to the bulk GaAs

rate. In the QCL structures to be simulated in later chapters the typical Al composition is in the ($x=0.15$) range and thus simply considering the bulk-GaAs rates is sufficient. As demonstrated above, even for increasing Al composition in the interwell transition case, where interaction with AlAs-like interface modes is more pronounced, a simple linear fit of GaAs and AlAs bulk phonon modes approximates the full calculation quite well and can be implemented with little additional computational requirements.

In addition to electron/LO-phonon scattering consideration must also be given to electron-electron interactions. While the use of phonon interactions using Fermi's Golden Rule is logical, as the phonon wave creates the time-varying perturbation, to treat electrons interacting through the Coulomb potential the Born Approximation [159] is usually invoked. This method allows the perturbation in Fermi's Golden Rule to be a function of the spatial separation of charges as opposed to a time-varying potential. In this approach the perturbing Hamiltonian is

$$\tilde{H} = \frac{e^2}{4\pi\epsilon r} \quad (3.2.21)$$

where r is the separation of the electrons. The matrix element can be written as [50]

$$\left\langle \psi_f(z) \frac{e^{-ik_f \cdot r_{xy}}}{\sqrt{A}} \psi_g(z') \frac{e^{-ik_g \cdot r_{xy}}}{\sqrt{A}} \left| \frac{e^2}{4\pi\epsilon r} \right| \psi_i(z) \frac{e^{-ik_i \cdot r_{xy}}}{\sqrt{A}} \psi_j(z') \frac{e^{-ik_j \cdot r_{xy}}}{\sqrt{A}} \right\rangle \quad (3.2.22)$$

where there is now the case of two initial electrons $|i, k_i\rangle$ and $|j, k_j\rangle$ which scatter to two final states $|f, k_f\rangle$ and $|g, k_g\rangle$.

In-depth treatments of electron-electron scattering have been reported elsewhere [71-75] and for brevity the detailed derivation will not be given here. The method used for the calculation of electron-electron scattering rates throughout the rest of this research can be found in Harrison [50]. In this treatment the effects of electron spin are

neglected and a single subband screening model is utilized. This screening effect is a result of the Coulombic repulsions changing the internal static fields and as a consequence the dielectric constant ϵ becomes a function of the relative wavevector $\epsilon(q_{xy})$ of a given 4-state transition where

$$q_{xy} = \frac{(k_f - k_i) + (k_j - k_g)}{2} \quad (3.2.23)$$

While again details of this can be found elsewhere [50,71-75] the result of the screening effect essentially complicates the already complex four-subband matrix element of Equation 3.2.22 by making the perturbation itself a many-body problem. Further, since these rates are in the form W_{ijfg} there are potentially 4^n types of scattering events for a system with n subbands. Therefore, as demonstrated above for the case of simplifying numerous complex phonon mode interactions, a manner will be sought to lessen the computational complexity of these, and all scattering rate calculations. To accomplish this the localized single well basis will again be exploited.

3.3 Linear Combinations of Intrawell Scattering

Consider Fermi's Golden Rule describing a single transitions from a state $|i\rangle$ to a state $|f\rangle$

$$W_{if} = \frac{2\pi}{\hbar} \left| \langle \psi_f | \tilde{H} | \psi_i \rangle \right|^2 \delta(E_f - E_i) \quad (3.3.1)$$

Here the recognition can be made that the scattering rate is proportional to the magnitude squared of the matrix element

$$W_{if} \propto \left| \langle \psi_f | \tilde{H} | \psi_i \rangle \right|^2 \quad (3.3.2)$$

Returning to the description of multi-well states ψ expanded in the localized basis Ψ such that

$$\psi_i^j = \sum_w \sum_s c_{is}^{jw} \Psi_s^w \quad (3.3.3)$$

where again, ψ_i^j represents a multi-well state (i) designated to well (j), Ψ_s^w is a localized basis state (s) in well (w), and c_{is}^{jw} is the coupling coefficient derived in Section 2.4.

Expanding the matrix element in this basis gives

$$W_{if}^{jg} \propto \left\langle \sum_m \sum_n c_{fn}^{gm} \Psi_n^m \left| \tilde{H} \right| \sum_w \sum_s c_{is}^{jw} \Psi_s^w \right\rangle^2 \quad (3.3.4)$$

Implementing the "nearest-neighbor only" approximation in the coupling coefficients simplifies this expression to

$$W_{if}^{jg} \propto \left\langle \sum_{m=g-1}^{g+1} \sum_n c_{fn}^{gm} \Psi_n^m \left| \tilde{H} \right| \sum_{w=j-1}^{j+1} \sum_s c_{is}^{jw} \Psi_s^w \right\rangle^2 \quad (3.3.5)$$

which can then be separated into distinct components

$$\begin{aligned} W_{if}^{jg} \propto & \left| \sum_n \sum_s c_{is}^{jj-1} c_{fn}^{gg-1} \tilde{H}_{sn}^{j-1g-1} + \sum_n \sum_s c_{is}^{jj} c_{fn}^{gg-1} \tilde{H}_{sn}^{jg-1} + \sum_n \sum_s c_{is}^{jj+1} c_{fn}^{gg-1} \tilde{H}_{sn}^{j+1g-1} \right. \\ & + \sum_n \sum_s c_{is}^{jj-1} c_{fn}^{gg} \tilde{H}_{sn}^{j-1g} + \sum_n \sum_s c_{is}^{jj} c_{fn}^{gg} \tilde{H}_{sn}^{jg} + \sum_n \sum_s c_{is}^{jj+1} c_{fn}^{gg} \tilde{H}_{sn}^{j+1g} \\ & \left. + \sum_n \sum_s c_{is}^{jj-1} c_{fn}^{gg+1} \tilde{H}_{sn}^{j-1g+1} + \sum_n \sum_s c_{is}^{jj} c_{fn}^{gg+1} \tilde{H}_{sn}^{jg+1} + \sum_n \sum_s c_{is}^{jj+1} c_{fn}^{gg+1} \tilde{H}_{sn}^{j+1g+1} \right|^2 \end{aligned} \quad (3.3.6)$$

where the notation has been simplified by writing

$$\tilde{H}_{ax}^{by} = \langle \Psi_x^y | \tilde{H} | \Psi_a^b \rangle \quad (3.3.7)$$

Assuming that the localized single well basis states Ψ are limited to intrawell scattering only a description of all delocalized wavefunction transitions, in an extended multi-well system, can be made using linear combinations of intrawell scattering. In Section 2.4 the technique to describe delocalized states using the localized basis was

shown to accurately represent the wavefunctions over the nearest-neighbor wells (Figure 2.4.6). In light of this representation consider the diagram shown in Figure 3.3.1.

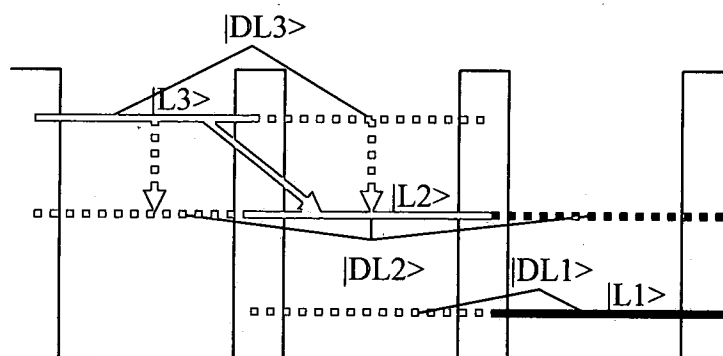


Figure 3.3.1: Diagram showing delocalized states and scattering represented by combinations of the localized basis.

In this figure, localized and delocalized states are labeled $|L\rangle$ and $|DL\rangle$, respectively. In the coupled well system the extended states are described as combinations of the localized basis, shown using the dotted lines. For instance, the extended state $|DL3\rangle$ has a wavefunction component comprised of the $|L3\rangle$ state and another which contains the $|L2\rangle$ state. Since it is assumed that the localized states $|L3\rangle$ and $|L2\rangle$ will not directly scatter to each other, it is hypothesized that scattering between the extended states $|DL3\rangle \rightarrow |DL2\rangle$ (shown by the full red line) can be described by combinations of the component scattering $|L3\rangle \rightarrow |L3\rangle$ and $|L2\rangle \rightarrow |L2\rangle$ (shown by the dotted red lines). Clearly the weighting factors for these combinations are given by the coupling coefficients c_{is}^{jw} . From this figure it is also noticed that although the expansion in the local basis was nearest-neighbor only, the fact that both $|DL3\rangle$ and $|DL1\rangle$ have $|L2\rangle$ components in the central well that 2nd nearest-neighbor transitions are permitted.

Considering that scattering can occur intrawell, nearest-neighbor, and 2nd nearest-neighbor, an examination of these separate cases can be made. First, for intrawell transitions take Equation 3.3.6 and let $g=j$.

$$\begin{aligned}
 W_{if}^{jj} \propto & \left| \sum_n \sum_s c_{is}^{jj-1} c_{fn}^{jj-1} \tilde{H}_{sn}^{j-1j-1} + \sum_n \sum_s c_{is}^{jj} c_{fn}^{jj-1} \tilde{H}_{sn}^{jj-1} + \sum_n \sum_s c_{is}^{jj+1} c_{fn}^{jj-1} \tilde{H}_{sn}^{j+1j-1} \right. \\
 & + \sum_n \sum_s c_{is}^{jj-1} c_{fn}^{jj} \tilde{H}_{sn}^{j-1j} + \sum_n \sum_s c_{is}^{jj} c_{fn}^{jj} \tilde{H}_{sn}^{jj} + \sum_n \sum_s c_{is}^{jj+1} c_{fn}^{jj} \tilde{H}_{sn}^{j+1j} \\
 & \left. + \sum_n \sum_s c_{is}^{jj-1} c_{fn}^{jj+1} \tilde{H}_{sn}^{j-1j+1} + \sum_n \sum_s c_{is}^{jj} c_{fn}^{jj+1} \tilde{H}_{sn}^{jj+1} + \sum_n \sum_s c_{is}^{jj+1} c_{fn}^{jj+1} \tilde{H}_{sn}^{j+1j+1} \right|^2
 \end{aligned} \quad (3.3.8)$$

Now, the intrawell scattering condition is

$$\tilde{H}_{ax}^{by} = \delta_{by} \tilde{H}_{ax}^{by} \quad (3.3.9)$$

which simplifies the expression to

$$W_{if}^{jj} \propto \left| \sum_n \sum_s \left(c_{is}^{jj-1} c_{fn}^{jj-1} \tilde{H}_{sn}^{j-1j-1} + c_{is}^{jj} c_{fn}^{jj} \tilde{H}_{sn}^{jj} + c_{is}^{jj+1} c_{fn}^{jj+1} \tilde{H}_{sn}^{j+1j+1} \right) \right|^2 \quad (3.3.10)$$

Similarly, for nearest neighbor interwell scattering ($g=j\pm 1$)

$$W_{if}^{jj\pm 1} \propto \left| \sum_n \sum_s \left(c_{is}^{jj} c_{fn}^{j\pm 1j} \tilde{H}_{sn}^{jj} + c_{is}^{jj\pm 1} c_{fn}^{j\pm 1j\pm 1} \tilde{H}_{sn}^{j\pm 1j\pm 1} \right) \right|^2 \quad (3.3.11)$$

and for 2nd nearest neighbor ($g=j\pm 2$)

$$W_{if}^{jj\pm 2} \propto \left| \sum_n \sum_s \left(c_{is}^{jj\pm 1} c_{fn}^{j\pm 2j\pm 1} \tilde{H}_{sn}^{j\pm 1j\pm 1} \right) \right|^2 \quad (3.3.12)$$

In the initial development of the localized basis (Section 2.3) expressions were derived for a ground and first excited state for single wells. This 2-state per well restriction is not only sufficient for the QCL designs to be analyze but, additionally, the assumption of equal states in each well makes the expressions easy to cast into a simple matrix form. To accomplish this define the matrix element of the delocalized scattering as

$$M_{ax}^{by} = \langle \psi_x^y | \tilde{H} | \psi_a^b \rangle \quad (3.3.13)$$

Expanding the new wavefunctions in terms of the localized basis gives

$$M = bmb^T \quad (3.3.14)$$

where (m) represents the matrix elements of the localized states and b is the coupling coefficient matrix where $b_{ij} = |c_{ij}|$. For example, for a three well system with two states in each well

$$M = \begin{bmatrix} b_{11}^{j-1,j-1} & b_{12}^{j-1,j-1} & b_{11}^{j-1,j} & b_{12}^{j-1,j} & 0 & 0 \\ b_{21}^{j-1,j-1} & b_{22}^{j-1,j-1} & b_{21}^{j-1,j} & b_{22}^{j-1,j} & 0 & 0 \\ b_{11}^{j,j-1} & b_{12}^{j,j-1} & b_{11}^{j,j} & b_{12}^{j,j} & b_{11}^{j,j+1} & b_{12}^{j,j+1} \\ b_{21}^{j,j-1} & b_{22}^{j,j-1} & b_{21}^{j,j} & b_{22}^{j,j} & b_{21}^{j,j+1} & b_{22}^{j,j+1} \\ 0 & 0 & b_{11}^{j+1,j} & b_{12}^{j+1,j} & b_{11}^{j+1,j+1} & b_{12}^{j+1,j+1} \\ 0 & 0 & b_{21}^{j+1,j} & b_{22}^{j+1,j} & b_{21}^{j+1,j+1} & b_{22}^{j+1,j+1} \end{bmatrix} \begin{bmatrix} \tilde{H}_{11}^{j-1,j-1} & \tilde{H}_{12}^{j-1,j-1} & 0 & 0 & 0 & 0 \\ \tilde{H}_{21}^{j-1,j-1} & \tilde{H}_{22}^{j-1,j-1} & 0 & 0 & 0 & 0 \\ 0 & 0 & \tilde{H}_{11}^{j,j} & \tilde{H}_{12}^{j,j} & 0 & 0 \\ 0 & 0 & \tilde{H}_{21}^{j,j} & \tilde{H}_{22}^{j,j} & 0 & 0 \\ 0 & 0 & 0 & 0 & \tilde{H}_{11}^{j+1,j+1} & \tilde{H}_{12}^{j+1,j+1} \\ 0 & 0 & 0 & 0 & \tilde{H}_{21}^{j+1,j+1} & \tilde{H}_{22}^{j+1,j+1} \end{bmatrix} \begin{bmatrix} b_{11}^{j-1,j-1} & b_{21}^{j-1,j-1} & b_{11}^{j,j-1} & b_{21}^{j,j-1} & 0 & 0 \\ b_{12}^{j-1,j-1} & b_{22}^{j-1,j-1} & b_{12}^{j,j-1} & b_{22}^{j,j-1} & 0 & 0 \\ b_{11}^{j,j-1} & b_{21}^{j,j-1} & b_{11}^{j,j} & b_{21}^{j,j} & b_{11}^{j+1,j} & b_{21}^{j+1,j} \\ b_{12}^{j,j-1} & b_{22}^{j,j-1} & b_{12}^{j,j} & b_{22}^{j,j} & b_{12}^{j+1,j} & b_{22}^{j+1,j} \\ 0 & 0 & b_{11}^{j+1,j} & b_{21}^{j+1,j} & b_{11}^{j+1,j+1} & b_{21}^{j+1,j+1} \\ 0 & 0 & b_{12}^{j+1,j} & b_{22}^{j+1,j} & b_{12}^{j+1,j+1} & b_{22}^{j+1,j+1} \end{bmatrix} \quad (3.3.15)$$

After evaluation of the matrix M, the rates are then assumed to be the magnitude

squared of each element (i.e.) $W = |M|^2$.

As an example consider two 155Å GaAs wells separated by a 50Å $Al_{0.15}Ga_{0.85}As$ barrier, shown in figure (3.3.2.) at $F=21kV/cm$.

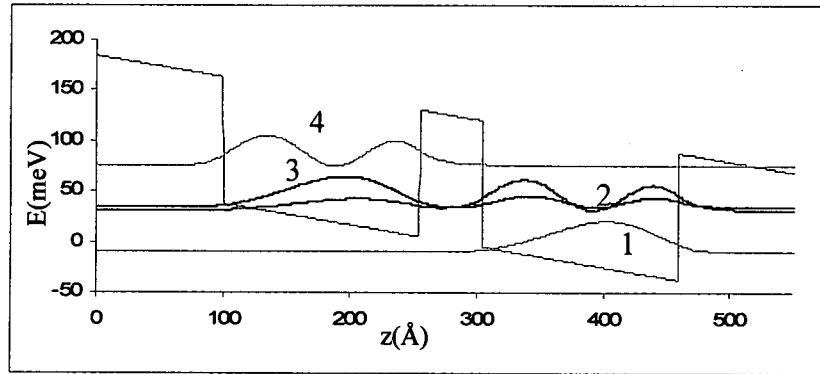


Figure 3.3.2: Eigenstates for two 155Å GaAs wells separated by a 50Å $Al_{0.15}Ga_{0.85}As$ barrier biased at $F=21kV/cm$ calculated using the full numerical approach.

First, consider the ground state in the left well scattering to the excited state in the right well. In Figure 3.3.2., this scattering rate is labeled as the $3 \rightarrow 2$ transition. As observed previously using the delocalized, full-Hamiltonian, system the designation of the states $|3\rangle$ and $|2\rangle$ will change when these states anticross. Consideration must then be made simultaneously for both the 3-2 and the 2-3 rates. Assume, for now, that the localized states are labeled as observed above, i.e. (1)=ground state in the right well, (2)=excited state in right well, (3)=ground state in left well, and (4)=excited state in left well. In this system the matrix expression can be written, ignoring any intrawell coupling, as

$$M = \begin{bmatrix} b_{11} & 0 & b_{13} & b_{14} \\ 0 & b_{22} & b_{23} & b_{24} \\ b_{31} & b_{32} & b_{33} & 0 \\ b_{41} & b_{42} & 0 & b_{44} \end{bmatrix} \begin{bmatrix} m_{11} & m_{12} & 0 & 0 \\ m_{21} & m_{22} & 0 & 0 \\ 0 & 0 & m_{33} & m_{34} \\ 0 & 0 & m_{43} & m_{44} \end{bmatrix} \begin{bmatrix} b_{11} & 0 & b_{31} & b_{41} \\ 0 & b_{22} & b_{32} & b_{42} \\ b_{13} & b_{23} & b_{33} & 0 \\ b_{14} & b_{24} & 0 & b_{44} \end{bmatrix} \quad (3.3.16)$$

where the m_{if} terms represent the matrix elements in the localized basis. Evaluating the M_{32} component gives

$$W_{32} = |b_{31}b_{22}m_{12} + b_{32}b_{22}m_{22} + b_{33}b_{23}m_{33} + b_{33}b_{24}m_{34}|^2 \quad (3.3.17)$$

which, of course, is equivalent to Equation (3.3.11) applied to this system. Now, in the expansion of the delocalized wavefunction in the localized basis, described by the coefficient (b) terms, the way to interpret the new rate expression is very logical. Since the new delocalized wavefunctions ψ are written in terms of the localized basis Ψ the terms describing the ψ_3 to ψ_2 scattering can be explained as:

$b_{31}b_{22}m_{12}$: ψ_3 has a Ψ_1 component. ψ_2 has a Ψ_2 component. Ψ_1 scatters to Ψ_2 .

$b_{32}b_{22}m_{22}$: ψ_3 has a Ψ_2 component. ψ_2 has a Ψ_2 component. Ψ_2 scatters to Ψ_2 .

$b_{33}b_{23}m_{33}$: ψ_3 has a Ψ_3 component. ψ_2 has a Ψ_3 component. Ψ_3 scatters to Ψ_3 .

$b_{33}b_{24}m_{34}$: ψ_3 has a Ψ_3 component. ψ_2 has a Ψ_4 component. Ψ_3 scatters to Ψ_4 .

For simplicity, consider just the single term $b_{32}b_{22}m_{22}$. Observing the full numerical wavefunctions shown in Figure 3.3.2., it is clearly seen that the state labeled $|3\rangle$ has a wavefunction which extends into the right well which resembles state $|2\rangle$. It is therefore logical to assume that a component of the scattering from state $|3\rangle$ to state $|2\rangle$ should resemble a $|2\rangle$ to $|2\rangle$ scattering rate in that it has a component $m_{22} = \langle \Psi_2 | \tilde{H} | \Psi_2 \rangle$. Using elements in this form inside the full description of Fermi's Golden Rule could be implemented but with little computational advantage. This expression would still need to be integrated over all initial and final subband transitions and then again integrated over the Fermi-Dirac statistics of both subbands to arrive at an "effective" or mean scattering rate. True computational simplicity can be found if the assumption is made that the internal localized basis matrix elements are in the form $m = \sqrt{W_L}$, where W_L is the mean scattering rate of the local transition. Under this assumption the new coupled well scattering rates $W = |M|^2$ would automatically represent the mean subband rate and, if this rate were predetermined, all mean scattering rates at any bias could be easily found regardless of the change in the coupled wavefunctions since they are described by the coupling coefficients.

To implement this approximation an account for the true energy separations of the new coupled states must be made. Surely the component of the $|3\rangle$ to $|2\rangle$ scattering in Figure 3.3.2. cannot be represented by a component $b_{32}b_{22}m_{22}$, where $m_{22} = \sqrt{W_{22}}$ and W_{22} is the mean rate for an intrasubband (i.e. $\Delta E=0$) transition. Instead there must be $W_{32} \propto W_{22}(\Delta E_{32})$. Equation 3.3.17 should then be written as

$$\begin{aligned}
W_{32} &= |b_{31}b_{22}M_{12} + b_{32}b_{22}M_{22} + b_{33}b_{23}M_{33} + b_{33}b_{24}M_{34}|^2 \\
&= |b_{31}b_{22}\sqrt{W_{12}(\Delta E_{32})} + b_{32}b_{22}\sqrt{W_{22}(\Delta E_{32})} + b_{33}b_{23}\sqrt{W_{33}(\Delta E_{32})} + b_{33}b_{24}\sqrt{W_{34}(\Delta E_{32})}|^2
\end{aligned}
\tag{3.3.18}$$

Therefore, even though the localized scattering components are written in a form which implies an intrasubband transition, i.e. $W(i \rightarrow i)$, the finite energy separation due to the repelling effect suggests that these elements should be considered as intersubband events between identical wavefunctions components (Figure 3.3.3).

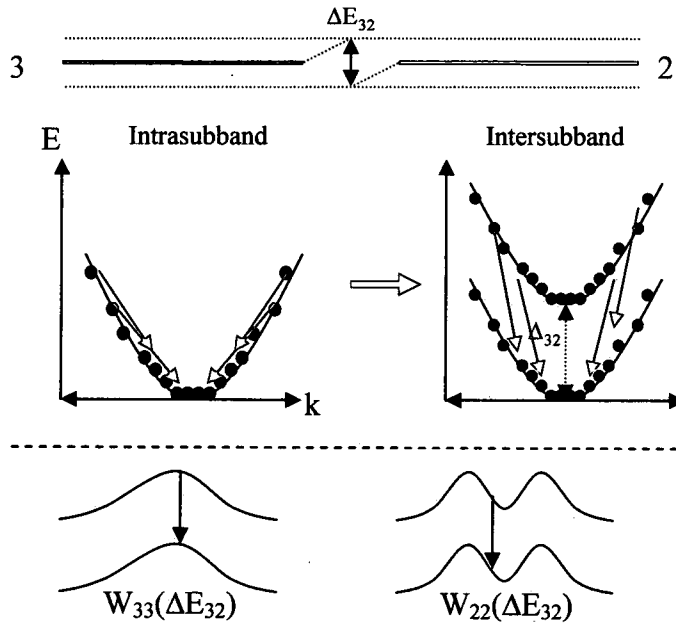


Figure 3.3.3: Diagram depicting the difference between intrasubband and intersubband transitions.

To examine the feasibility and demonstrate the implementations of this approximation consider the same two well system shown previously in Figure 3.3.2., only now in the localized basis as shown in Figure (3.3.4).

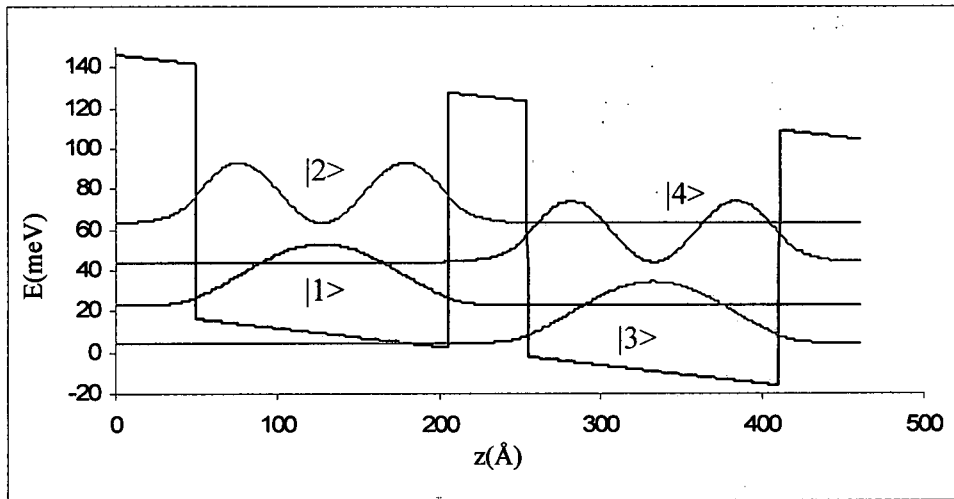


Figure 3.3.4: Eigenstates for two 155Å GaAs wells separated by a 50Å $\text{Al}_{0.15}\text{Ga}_{0.85}\text{As}$ barrier biased at $F=21\text{kV/cm}$ calculated using the localized basis.

In this figure, and throughout the remainder of this work, the states in the localized basis are labeled from left to right as $|1\rangle$ =ground state in leftmost well, $|2\rangle$ =excited state in leftmost well, $|3\rangle$ =ground state in next well, $|4\rangle$ =excited state in next well, etc. The first thing to compare is energies vs. the bias using both the full numerical simulation and the coupling of the local basis using the method of Section 2.4. This comparison is shown in Figure 3.3.5. In this plot the localized basis calculation is shown to very closely match the full numerical calculation of the eigenvalues over the entire range of biases. A slight deviation can be seen between the localized state $|2\rangle$ and the full numerical calculation at electric field approaching 30kV/cm. At these higher biases the high energy state in the full simulation starts to couple with “quasi-confined” or “quasi-continuum” states and is shown to be repelled downward. In the localized system states are restricted to coupling only with the defined “confined states”.

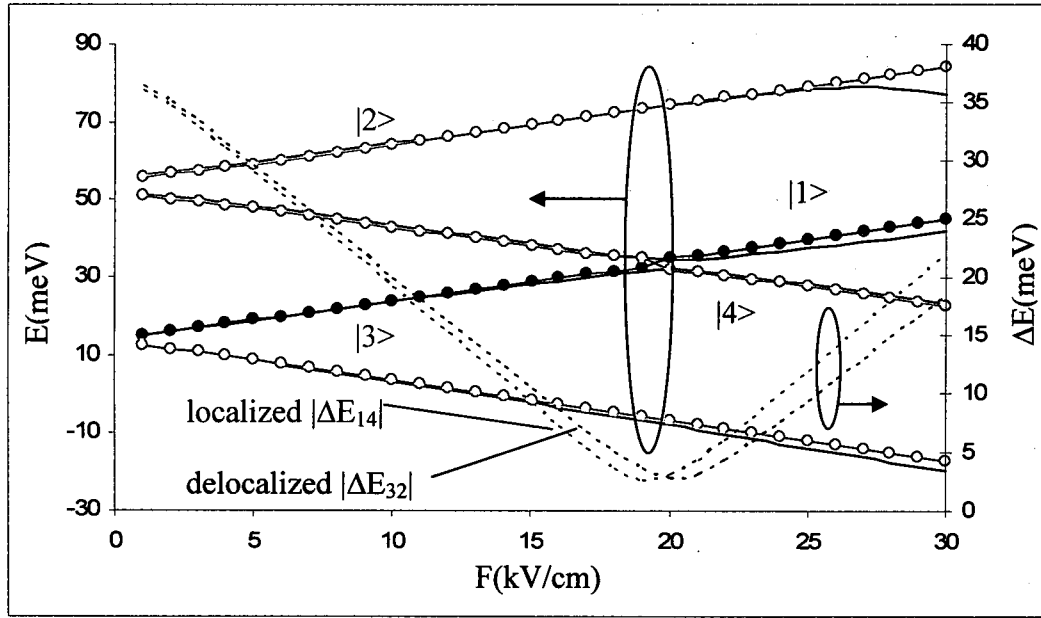


Figure 3.3.5: Comparison of the energies vs. the bias for two 155\AA GaAs wells separated by a 50\AA $\text{Al}_{0.15}\text{Ga}_{0.85}\text{As}$ barrier calculated using the full numerical approach (black lines) and the localized expansion (colored lines with circles). The energy separation for the right-ground to left-excited states in each picture is also plotted as dotted lines.

For the scattering rate calculations first consider the $|1\rangle$ to $|4\rangle$ interaction. The expanded matrix elements are then

$$M_{14} = b_{11}b_{41}m_{11} + b_{11}b_{42}m_{12} + b_{13}b_{44}m_{34} + b_{14}b_{44}m_{44} \quad (3.3.19)$$

$$M_{41} = b_{44}b_{14}m_{44} + b_{44}b_{13}m_{43} + b_{41}b_{11}m_{11} + b_{42}b_{11}m_{21}$$

To describe these new, coupled-well, wavefunction transitions there is only a need to determine the localized values of m_{11} , m_{12} , m_{34} , m_{44} , m_{43} , and m_{21} . Since the wells in this system are identical, the corresponding ground and excited state wavefunctions are also identical and thus actually only determination of m_{gg} , m_{ge} , m_{eg} , and m_{ee} is necessary. In this notation gg represents a ground-to-ground transitions, ge is a ground-to-excited

transition, etc. As mentioned previously, these "basis rates" need to be calculated at the appropriate coupled state energy separation. Equation 3.3.19 is then rewritten as

$$\begin{aligned}
 M_{14} &= b_{11}b_{41}\sqrt{W_{gg}(\pm\Delta_{14})} + b_{11}b_{42}\sqrt{W_{eg}(\pm\Delta_{14})} \\
 &+ b_{13}b_{44}\sqrt{W_{eg}(\pm\Delta_{14})} + b_{14}b_{44}\sqrt{W_{ee}(\pm\Delta_{14})} \\
 M_{41} &= b_{44}b_{14}\sqrt{W_{ee}(\pm\Delta_{14})} + b_{44}b_{13}\sqrt{W_{eg}(\pm\Delta_{14})} \\
 &+ b_{42}b_{11}\sqrt{W_{eg}(\pm\Delta_{14})} + b_{41}b_{11}\sqrt{W_{gg}(\pm\Delta_{14})}
 \end{aligned}
 \tag{3.3.20}$$

At this point it is not immediately clear where the computational benefit comes from. If these basis rates must be calculated at every new coupled state energy separation it is not much different then simply calculating the full numerical eigenstate scattering. However, in the localized basis these wavefunctions never change and thus their intrawell scattering rates vs. any arbitrary energy separation are fixed. These unchanging quantities, once determined, can be used to reconstruct the coupled well properties through the changing coefficient terms for any given system. This procedure then is analogous to the concept of the established Linear Combinations of Atomic Orbitals (LCAO) method in solid-state physics. Once the determination of single atom or quantum well properties are calculated, molecules and solids, or in this case multi-well systems, can be described based on precalculated single atom or well quantities. With this in mind a technique is then needed for determining these intrawell basis rates and then recombining them using the Linear Combinations of Intrawell Scattering (LCIS) method previously outlined.

Continuing with this specific example a predetermination of all possible intrawell scattering rates can be carried out. To simulate these mean basis rates consider using the single 155Å well and repeating this 4 times in the localized basis (Figure 3.3.6). Since various combinations of ground-ground (gg), ground-excited (ge) etc. types of transitions are wanted at various energy separations a simple copying of the appropriate wavefunctions is used. The energies are artificially changed without altering their form (i.e. the wavevectors are not changed by the artificial energies).

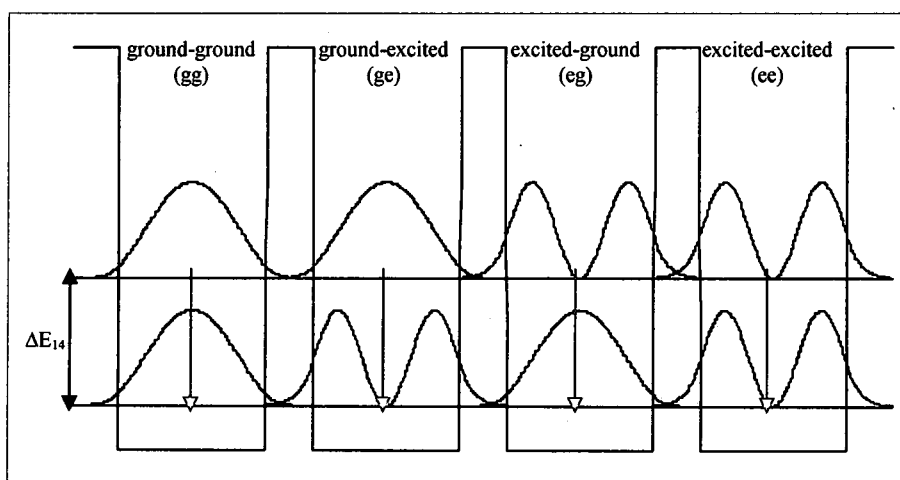


Figure 3.3.6: Artificial system used to calculate the mean "basis rates" for the relevant intrawell transitions.

First, a plot of the mean LO-emission and absorption rates over a wide range of energy separations is shown in Figure 3.3.7. These rates are simulated using identical electronic and lattice temperatures $T_e = T = 77\text{K}$ and assuming $n = 1 \times 10^{10} \text{ cm}^{-2}$ in all subbands.

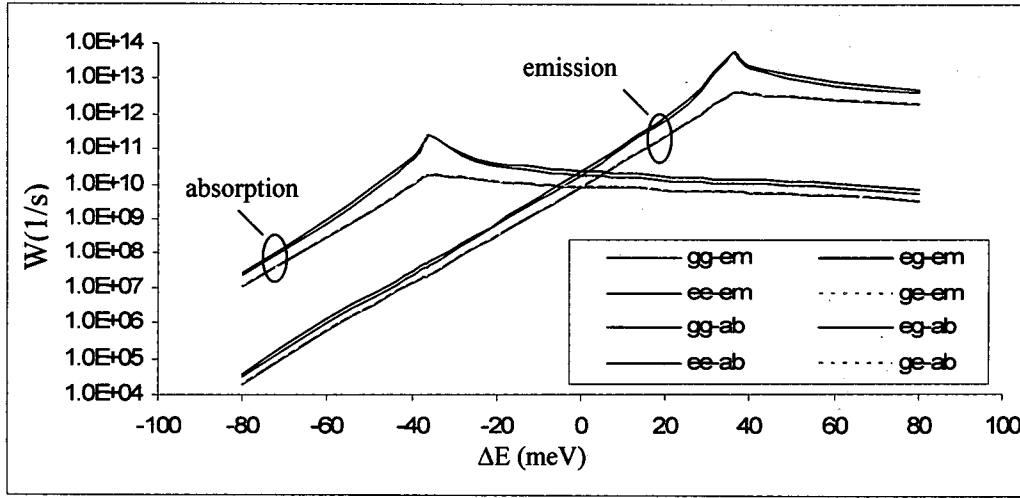


Figure 3.3.7: Basis LO emission and absorption rates in a 155Å well at $T_e=T=77K$ and assuming $n=1 \times 10^{10} \text{ cm}^{-2}$ in all subbands.

From this plot it is immediately seen that the ge and eg rates are identical, which is logical as the wavefunctions are just flipped in the integration of the matrix element. It is also noticed that, although not identical, the gg and ee rates are very close to the same values. Assuming they are essentially the same the previous expressions simplify to

$$M_{14} = (b_{11}b_{41} + b_{14}b_{44})\sqrt{W_{gg}(\pm \Delta E_{14})} + (b_{11}b_{42} + b_{13}b_{44})\sqrt{W_{eg}(\pm \Delta E_{14})} \quad (3.3.21)$$

$$M_{41} = (b_{44}b_{14} + b_{41}b_{11})\sqrt{W_{gg}(\mp \Delta E_{14})} + (b_{44}b_{13} + b_{42}b_{11})\sqrt{W_{eg}(\mp \Delta E_{14})}$$

These expressions, representing the $|1\rangle$ to $|4\rangle$ and $|4\rangle$ to $|1\rangle$ transitions have been reduced to an identical form, only differing in the designation of the sign of the energy separation. Further examination of the rates in Figure (3.3.7) shows the emission rate follows a linear slope (on the logarithmic scale) until it reaches the LO-phonon resonance at 36meV. After this peak it appears to turn downward, again following a nearly linear slope. Near the peak there appears to be some deviation from this linear behavior but nonetheless it appears as though 2-piecewise exponential functions on each

side of the resonance should provide a sufficient fit. Further, as noted above, it is only necessary to find a suitable fit for gg and eg transitions. Application of a least squares fitting procedure for exponential functions on each side of the phonon peak for the emission rates is shown in Figure 3.3.8.

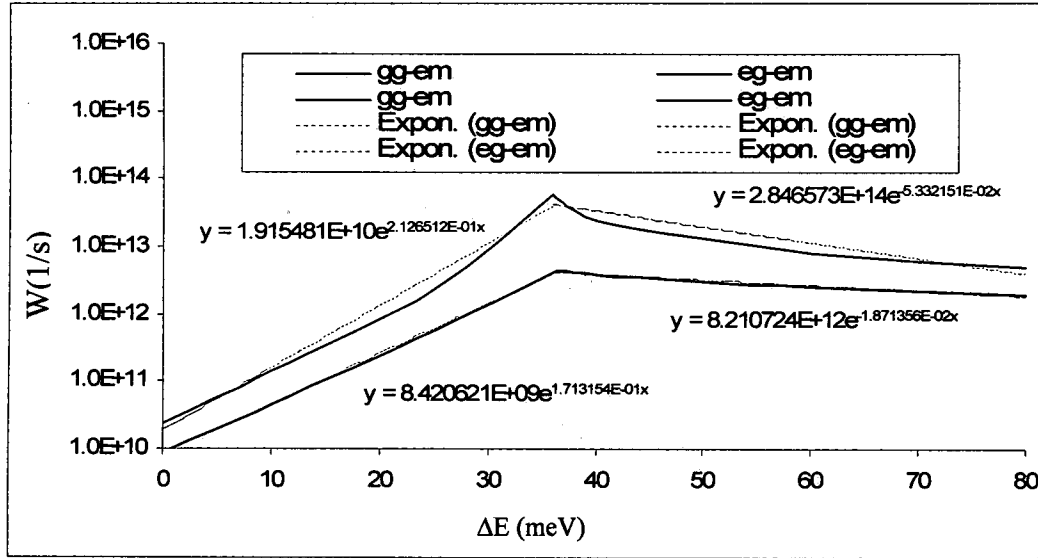


Figure 3.3.8: Piecewise exponential fitting functions for the gg and eg emission rates for the 155Å well.

Now there are exponential fits to the scattering rates $W_{gg-em}(\Delta E)$ and $W_{eg-em}(\Delta E)$ which can be easily inserted into the expression

$$M_{14_em} = (b_{11}b_{41} + b_{14}b_{44})\sqrt{W_{gg-em}(\Delta E_{14})} + (b_{11}b_{42} + b_{13}b_{44})\sqrt{W_{eg-em}(\Delta E_{14})} \quad (3.3.22)$$

$$M_{41_em} = (b_{44}b_{14} + b_{41}b_{11})\sqrt{W_{gg-em}(\Delta E_{41})} + (b_{44}b_{13} + b_{42}b_{11})\sqrt{W_{eg-em}(\Delta E_{41})}$$

This approach is compared directly to the LO-emission rates using the fully-numerical/delocalized wavefunctions. This comparison is shown in Figure 3.3.9. In this figure the fully numerical delocalized scattering is between the states designated 3 and 2 as shown in Figure 3.3.2. These states of course undergo an anti-crossing where the wavefunctions switch wells. In the localized picture (Figure 3.3.4) the states are the ground in the left well $|1\rangle$ and the excited in the right well $|4\rangle$. These types of transitions will be referred to as intradoublet as the coupling between the states themselves is what directly permits the interwell scattering.

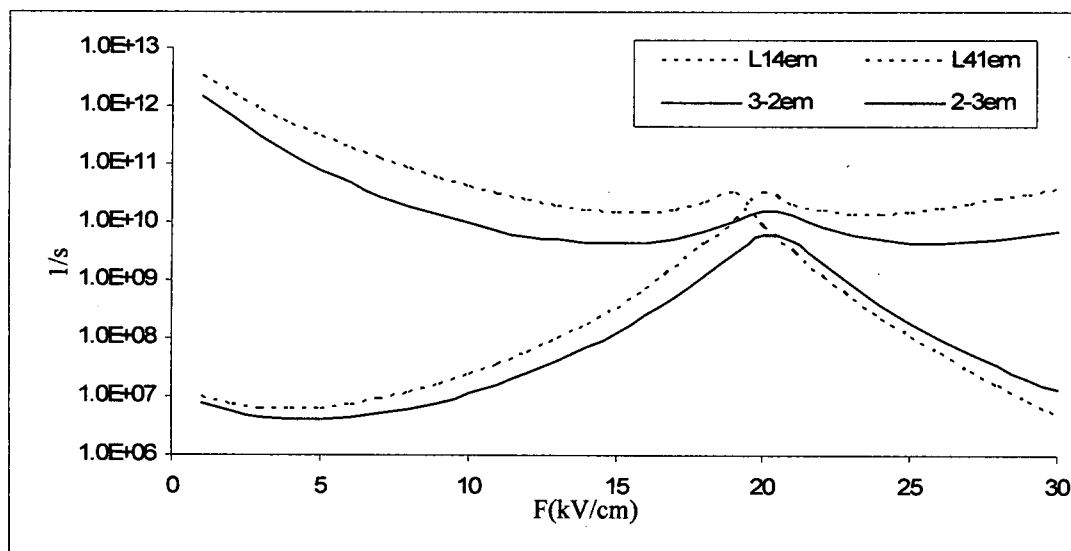


Figure 3.3.9: Intradoublet LO emission rates calculated using the full numerical simulation (solid lines) and the LCIS technique with the piecewise exponential fitting functions (dotted lines).

Observing the rates vs the field it is observed that the localized $1 \rightarrow 4$ rate (dotted red line) starts by following the $(2 \rightarrow 3)$ delocalized rate. This is logical as the excited state in the right well is initially the higher energy state. After the crossing/anti-crossing this

1→4 localized rate jumps across and starts to follow the behavior of the delocalized 3→2 rate. Likewise the localized 4→1 transition follows this similar crossing pattern. This behavior is just like the energies themselves where the localized states cross while the delocalized designation of states displays and anticrossing. Surprisingly, with all the approximations and a simple piecewise exponential fit of the mean LO-emission rates, the behavior of the scattering rates vs. the field is captured quite well.

Due to this agreement in the very simplified form the limited basis rates can be used to rewrite the general expressions using the simplified 2-state per well matrix system

$$M = \begin{bmatrix} b_{11}^{j-1,j-1} & b_{12}^{j-1,j-1} & b_{11}^{j-1,j} & b_{12}^{j-1,j} & 0 & 0 \\ b_{21}^{j-1,j-1} & b_{22}^{j-1,j-1} & b_{21}^{j-1,j} & b_{22}^{j-1,j} & 0 & 0 \\ b_{11}^{j,j-1} & b_{12}^{j,j-1} & b_{11}^{j,j} & b_{12}^{j,j} & b_{11}^{j,j+1} & b_{12}^{j,j+1} \\ b_{21}^{j,j-1} & b_{22}^{j,j-1} & b_{21}^{j,j} & b_{22}^{j,j} & b_{21}^{j,j+1} & b_{22}^{j,j+1} \\ 0 & 0 & b_{11}^{j+1,j} & b_{12}^{j+1,j} & b_{11}^{j+1,j+1} & b_{12}^{j+1,j+1} \\ 0 & 0 & b_{21}^{j+1,j} & b_{22}^{j+1,j} & b_{21}^{j+1,j+1} & b_{22}^{j+1,j+1} \end{bmatrix} \begin{bmatrix} m_{gg} & m_{eg} & 0 & 0 & 0 & 0 \\ m_{eg} & m_{gg} & 0 & 0 & 0 & 0 \\ 0 & 0 & m_{gg} & m_{eg} & 0 & 0 \\ 0 & 0 & m_{eg} & m_{gg} & 0 & 0 \\ 0 & 0 & 0 & 0 & m_{gg} & m_{eg} \\ 0 & 0 & 0 & 0 & m_{eg} & m_{gg} \end{bmatrix} \begin{bmatrix} b_{11}^{j-1,j-1} & b_{21}^{j-1,j-1} & b_{11}^{j,j-1} & b_{21}^{j,j-1} & 0 & 0 \\ b_{12}^{j-1,j-1} & b_{22}^{j-1,j-1} & b_{12}^{j,j-1} & b_{22}^{j,j-1} & 0 & 0 \\ b_{11}^{j,j-1} & b_{21}^{j,j-1} & b_{11}^{j,j} & b_{21}^{j,j} & b_{11}^{j+1,j} & b_{21}^{j+1,j} \\ b_{12}^{j,j-1} & b_{22}^{j,j-1} & b_{12}^{j,j} & b_{22}^{j,j} & b_{12}^{j+1,j} & b_{22}^{j+1,j} \\ 0 & 0 & b_{11}^{j+1,j} & b_{21}^{j+1,j} & b_{11}^{j+1,j+1} & b_{21}^{j+1,j+1} \\ 0 & 0 & b_{12}^{j+1,j} & b_{22}^{j+1,j} & b_{12}^{j+1,j+1} & b_{22}^{j+1,j+1} \end{bmatrix} \quad (3.3.23)$$

The general equations can then be rewritten for the various transitions. The new intrawell rates for coupled states is

Intrawell

$$M_{if}^{nn} = b_{ii}^{nn} b_{ff}^{nn} \hat{m}_{if} + \sum_{x=1}^2 \sum_{y=1}^2 b_{ix}^{nn-1} b_{fy}^{nn-1} \hat{m}_{xy} + \sum_{x=1}^2 \sum_{y=1}^2 b_{ix}^{nn+1} b_{fy}^{nn+1} \hat{m}_{xy} \quad (3.3.24)$$

where

$$\hat{m}_{ab} = \begin{cases} m_{gg} & \text{for } a = b \\ m_{eg} & \text{otherwise} \end{cases} \quad (3.3.25)$$

For the nearest neighbor transitions

Interwell(m±1)

$$M_{if}^{nn\pm 1} = \sum_{x=1}^2 b_{ii}^{nn} b_{fx}^{n\pm 1n} \hat{m}_{ix} + \sum_{x=1}^2 b_{ix}^{nn\pm 1} b_{ff}^{n\pm 1n\pm 1} \hat{m}_{xf} \quad (3.3.26)$$

and for 2nd nearest neighbor

Interwell(m±2)

$$M_{if}^{nn\pm 2} = \sum_{x=1}^2 \sum_{y=1}^2 b_{ix}^{nn\pm 1} b_{fy}^{n\pm 2n\pm 1} \hat{m}_{xy} \quad (3.3.27)$$

Using these new simplified equations other transitions can be simulated in the example system. Consider the $|1\rangle \rightarrow |3\rangle$ scattering in the localized picture. Here this scattering channel opens up as the ground state $|1\rangle$ couples with the excited state $|4\rangle$ in the right well permitting transitions to the ground state in the right well $|3\rangle$. These types of transitions will be referred to as indirect interwell scattering as the initial state $|i\rangle$ scatters to the interwell state $|f\rangle$ assisted indirectly by the coupling to another state $|j\rangle$ in the same well as $|f\rangle$. In the delocalized picture this would be the 3-1 and 2-1 scattering (depending on when the states anticross). This comparison is shown in Figure 3.3.10:

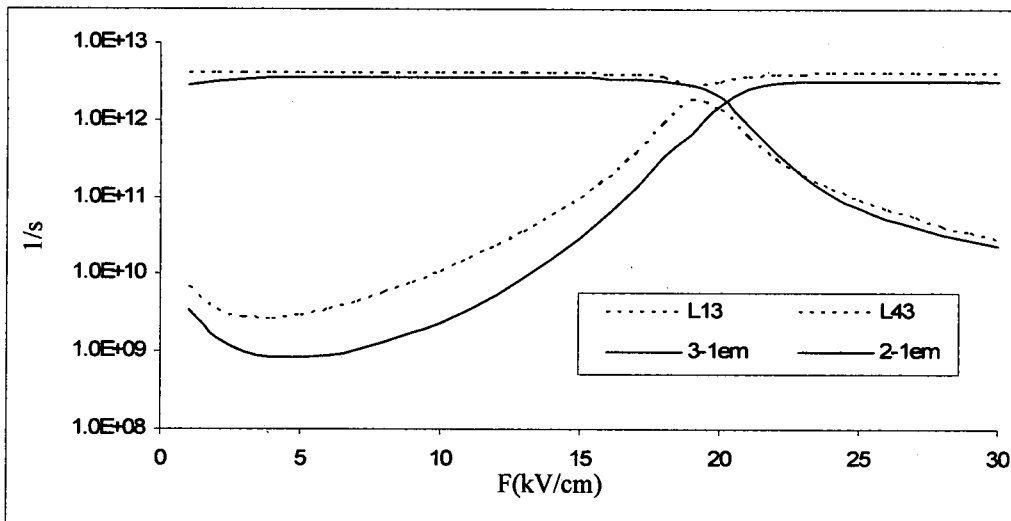


Figure 3.3.10: Indirect LO emission rates calculated using the full numerical simulation (solid lines) and the LCIS method (dotted lines).

For this indirect scattering the opposite crossing/anticrossing behavior witnessed previously in Figure 3.3.9. is observed. Here the delocalized transitions ($3 \rightarrow 1$ and $2 \rightarrow 1$) display a crossing of their scattering rates while the LCIS method (L13 and L43) show anti-crossing behavior. Again this is a logical result. In the delocalized picture state 1 is always the ground state in the right well. State 2 is initially the ground state in the left well. As the states anticross in energy the excited state in the right well and the ground state in the left well switch, thus change their respective ability to scatter into state 1. On the contrary, in the localized picture $|1\rangle$ is always the ground state in the left well. It becomes maximally coupled with the excited state $|4\rangle$, experiencing its largest scattering to the ground state $|3\rangle$, followed by a drop as the states cross and begin to decouple. As in the previous example, although the rates are not identical, the behavior is reproduced very well.

The same procedure can then be applied to the LO-phonon absorption. The absorption data and exponential fits are shown in Figure 3.3.11.

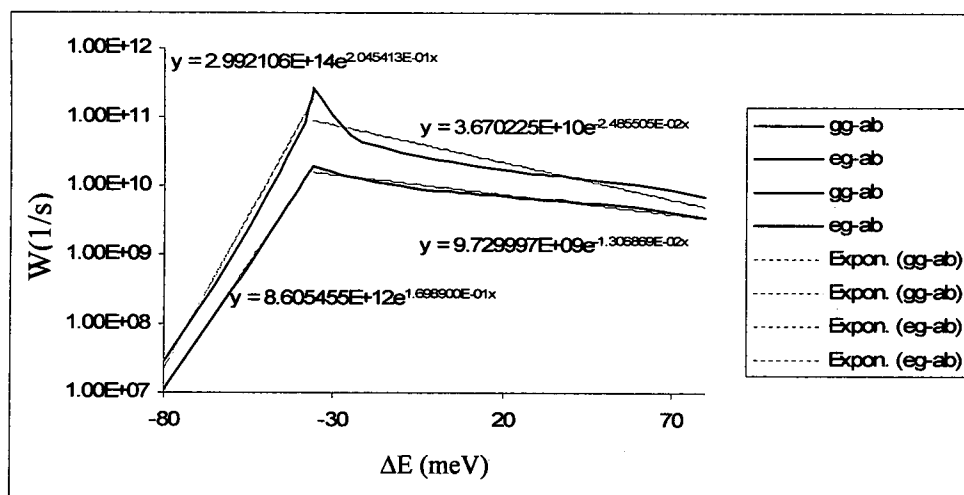


Figure 3.3.11: Piecewise exponential fitting functions for the gg and eg emission rates for the 155Å well.

The intradoublet LO absorption rates calculated using this LCIS method are plotted along with the full calculation in Figure 3.3.12 and the indirect absorption is shown in Figure 3.3.13. For the intradoublet rates it is again observed that the manner in which the rates changes with the bias is reproduced well using the LCIS technique. The crossing vs. anticrossing behavior is also seen for the localized and delocalized calculations, respectively.

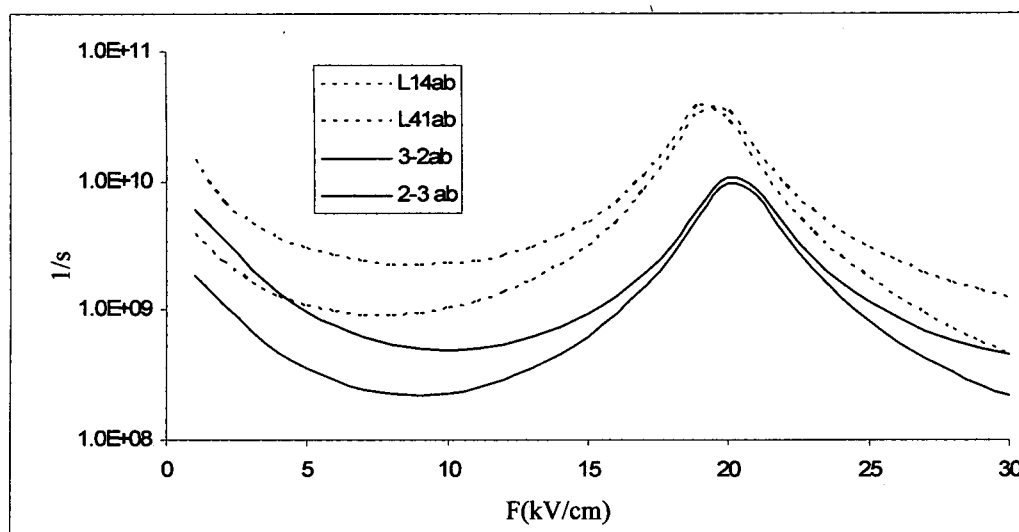


Figure 3.3.12: Intradoublet LO absorption rates calculated using the full numerical simulation (solid lines) and the LCIS technique (dotted lines).

The indirect absorption rates (Figure 3.3.13) show, similar to the emission rates, the opposite crossing/anticrossing behavior. The LCIS rates are again observed to follow the full calculation closely, especially near the crossing/anticrossing bias. These examples justify the approximations used in the presented LCIS method and, although the magnitude of the rates is not precisely reproduced, the form of the rates vs. the bias is predicted very well for the LO phonon emission and absorption transitions.

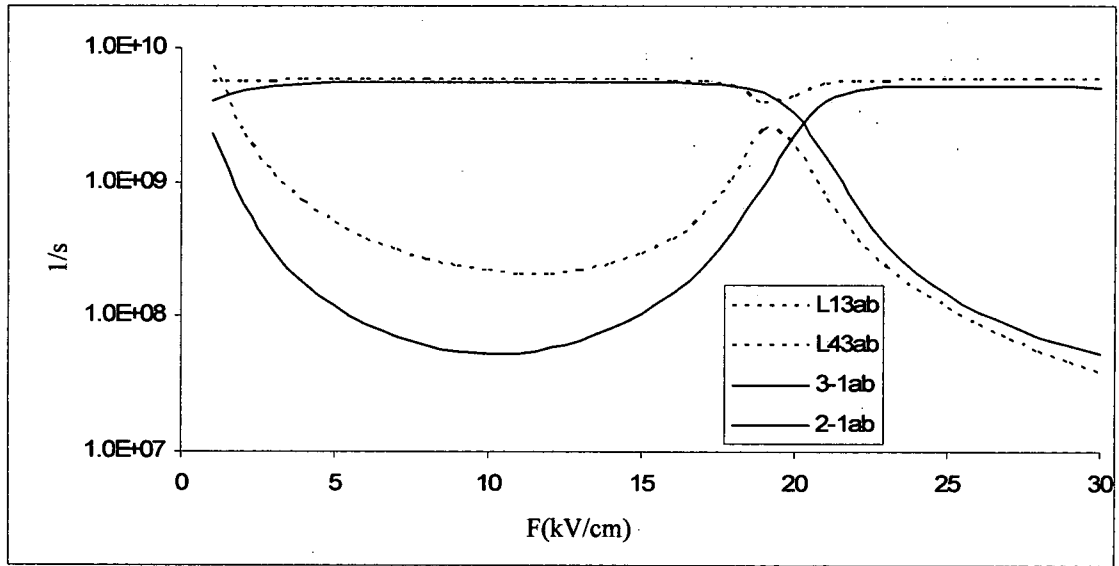


Figure 3.3.13: Indirect LO absorption rates calculated using the full numerical simulation (solid lines) and the LCIS technique (dotted lines).

Now that it has been justified, in principle, that the electron-phonon behavior can be described using an expansion of Fermi's Golden Rule in a localized, mean rate approximation, consider now the electron-electron scattering. For this procedure, as indicated by Equation 3.2.22 in Section 3.2, the same simple, two-wavefunction, matrix element as presented for the phonon transitions cannot be used. For these rates the 4-wavefunction matrix element must be considered

$$M_{ijfg} = \langle \psi_i \psi_j | \tilde{H} | \psi_f \psi_g \rangle \quad (3.3.28)$$

Seeking as simplified a description as possible a few assumptions are made. First, assume that all intrawell electron-electron scattering is small compared to the phonon scattering at the typical well widths to be considered. This should be valid as it was shown that the rates fall off quickly with increasing energy separation (Figure 1.2.4). The concern can

then be limited to the interwell, intradoublet types of transitions. The rates can then be limited to those containing the 2 interwell states involved in the transition.

Consider simply 2-states $|i\rangle$ and $|f\rangle$

$$\psi_i = b_{ii}\Psi_i + b_{if}\Psi_f \quad (3.3.29)$$

$$\psi_f = b_{fi}\Psi_i + b_{ff}\Psi_f$$

These expressions do not necessarily mean these are the only states in the system. If there are other contributing states to the wavefunction expansion the coupling coefficients above will simply not be normalized over these two specific states. Inserting this into (3.2.28) gives the matrix element for an ii-ff transition as

$$M_{iiff} = \langle b_{fi}^2\Psi_i\Psi_i + b_{fi}b_{ff}\Psi_i\Psi_f + b_{ff}b_{fi}\Psi_f\Psi_i + b_{ff}^2\Psi_f\Psi_f | \tilde{H} | b_{ii}^2\Psi_i\Psi_i + b_{ii}b_{if}\Psi_i\Psi_f + b_{if}b_{ii}\Psi_f\Psi_i + b_{if}^2\Psi_f\Psi_f \rangle \quad (3.3.30)$$

Considering that the only nonzero elements are intrawell, i.e.,

$$\langle \Psi_i\Psi_i | \tilde{H} | \Psi_i\Psi_i \rangle \text{ and } \langle \Psi_f\Psi_f | \tilde{H} | \Psi_f\Psi_f \rangle \quad (3.3.31)$$

simplifies Equation 3.3.30 to

$$M_{iiff} = b_{fi}^2 b_{ii}^2 m_{iiii} + b_{if}^2 b_{ff}^2 m_{ffff} \quad (3.3.32)$$

Similarly, for the 2-state ii-fi and if-ff transitions

$$M_{iifi} = b_{fi} b_{ii}^3 m_{iiii} + b_{if}^3 b_{ff} m_{ffff} \quad (3.3.33)$$

and

$$M_{ifff} = b_{fi}^3 b_{ii} m_{iiii} + b_{if} b_{ff}^3 m_{ffff} \quad (3.3.34)$$

In these expressions all the localized matrix elements are of the form m_{gggg} or m_{eeee} , depending on the states i or f . In the LO-phonon rates previously observed there was little difference in these two elements. Just to be sure plots of these are shown below in Figure 3.3.14.

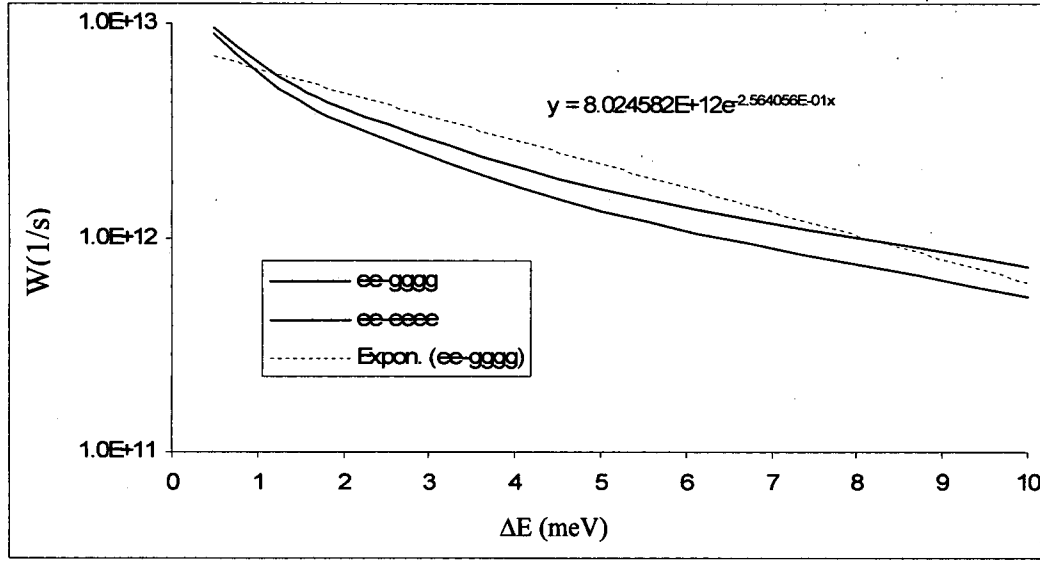


Figure 3.3.14: The electron-electron basis rates for the gg-gg and ee-ee components.

In this picture, as in the LO phonon case, the difference between the ground-ground and excited-excited basis transitions is fairly small. Again choosing a single fit to the gggg type to simplify the description to

$$\begin{aligned}
 M_{iiff} &= b_{fi}^2 b_{ii}^2 m_{gggg}(\Delta E_{if}) + b_{if}^2 b_{ff}^2 m_{gggg}(\Delta E_{if}) \\
 M_{iifi} &= b_{fi}^3 b_{ii}^3 m_{gggg}(\Delta E_{if}) + b_{if}^3 b_{ff}^3 m_{gggg}(\Delta E_{if}) \\
 M_{iiff} &= b_{fi}^3 b_{ii}^3 m_{gggg}(\Delta E_{if}) + b_{if}^3 b_{ff}^3 m_{gggg}(\Delta E_{if})
 \end{aligned} \tag{3.3.34}$$

The total electron-electron scattering will then be written as

$$W_{ee} = 2W_{iiff} + W_{iifi} + W_{iiff} \tag{3.35}$$

where the 2 is inserted for the W_{iiff} rate since 2-electrons are transferred from $|i\rangle$ to $|f\rangle$.

The interdoublet $|1\rangle \rightarrow |4\rangle$ and $|4\rangle \rightarrow |1\rangle$ rates for the localized picture can then be compared to the 3-2 rate for the delocalized picture. This comparison is shown in Figure 3.3.15. In this figure the delocalized e-e rates are calculated using all permutations of the form W_{ijfg} where $E_i > E_f$ and $E_j > E_g$.

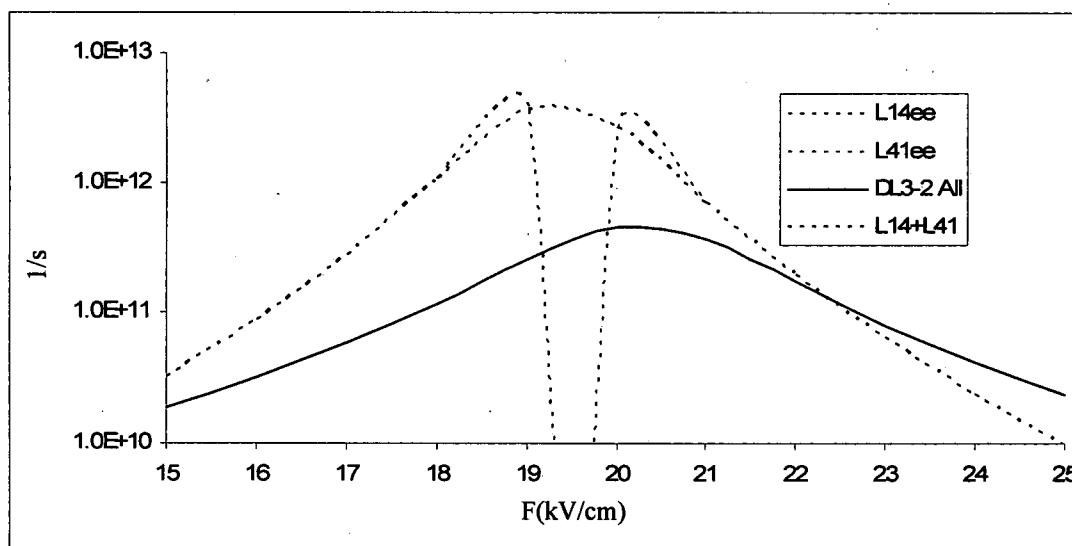


Figure 3.3.15: Comparison of the electron-electron rates calculated using the full numerical technique (solid line) and the simplified LCIS method (dotted lines). The combined 1-4 and 4-1 LCIS rates are also shown (dotted black line) for clarity.

In these plots, where the focus is on the crossing/anti-crossing point, there is the observed crossing of the localized rates (red and blue dotted lines). The combination of these rates (dotted black line) is shown to follow the behavior of the delocalized rate but is overestimated by almost an order of magnitude.

This error can be attribute to the actual value of the rates to the “magnitude squared” portion of the matrix element in Fermi’s Golden Rule and the approximation of inserting the localized basis elements as the sqrt of the mean rates. Consider two localized functions (Figure 3.3.16.a) separated by some distance along the z-axis and their two orthogonal combinations (Figure 3.3.16.b).

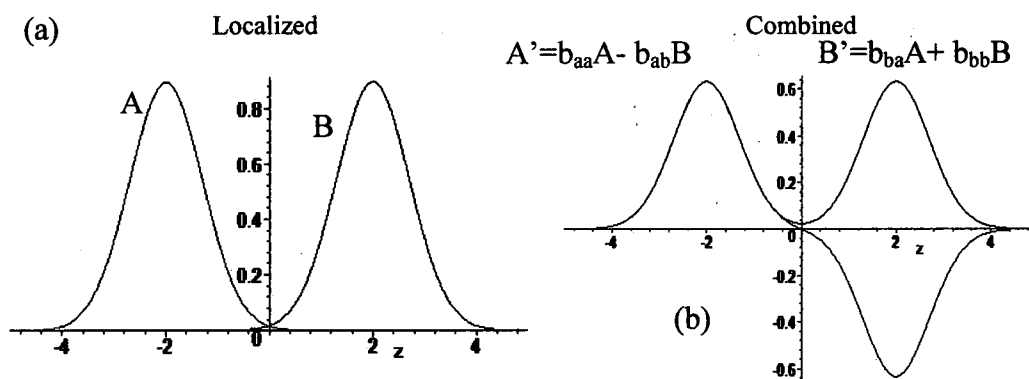


Figure 3.3.16: (a) Two arbitrary identical normalized states shifted along the z-axis ($\Delta z=4$ a.u.) and (b) their orthogonal combinations.

In this case the localized functions (A & B) are, for simplicity, chosen to be normalized Gaussians and the orthogonal combinations are

$$\begin{aligned} A' &= \frac{1}{\sqrt{2}} A - \frac{1}{\sqrt{2}} B \\ B' &= \frac{1}{\sqrt{2}} A + \frac{1}{\sqrt{2}} B \end{aligned} \quad (3.3.36)$$

In Section 2.4 it was shown that the descriptions of the delocalized combinations of the single-well basis were very accurately described using the tight-binding coupling parameters. Thus, in the above picture assume that the localized states (Figure 3.3.16a) are combined to perfectly describe the delocalized states (Figure 3.3.16b). Under this assumption consider the delocalized rates expanded in the local basis

$$W'_{AB} = |b_{AA} b_{BA} m_{AA} + b_{AB} b_{BB} m_{AA}|^2 \quad (3.3.37)$$

In this simple 2-state example it becomes clear why the “absolute value of the coefficients” is used as this expression would always go to zero if this was not implemented. Using this expression take the localized matrix elements to be

$$m_{AA} = \langle A | \tilde{H} | A \rangle = \sqrt{W_{AA}} \quad (3.3.38)$$

Now if a comparison is made between this scattering rate and one calculated using the combined form (A' & B') i.e.,

$$W_{A'B'} \propto \left| \langle A' | \tilde{H} | B' \rangle \right|^2 \quad (3.3.39)$$

and, assuming a phonon-like perturbation in the form

$$\tilde{H} = \exp(-iqz)$$

the form factors for these two descriptions can be evaluated (Figure 3.3.17).

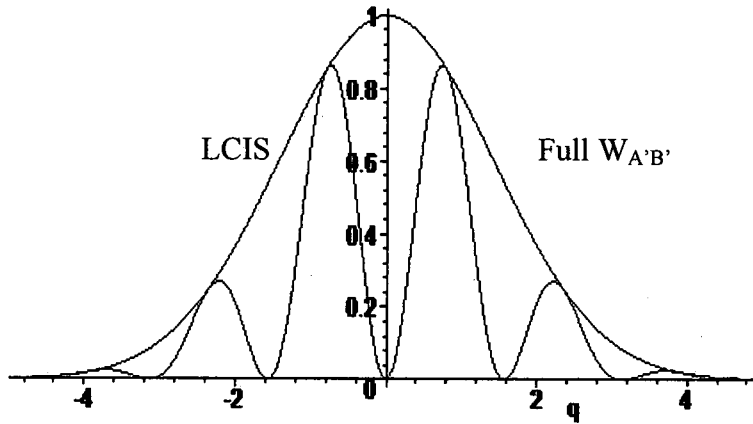


Figure 3.3.17: Form factor comparison of the full wavefunctions vs. the LCIS expansion for the simple 2-state system with ($\Delta z=4$ a.u.).

In this figure it can be seen that the LCIS form factor appears to follow the envelope of the full expression. Since scattering rates for transitions such as this phonon type would be integrated over all phonon wavevectors q , it is clear that the LCIS technique will always have some inherent error in the actual magnitude. In addition, this calculation was performed for a single z -axis separation of $\Delta z=4$ (a.u.). Consider the shifting of the initial functions closer together $\Delta z=2$ (a.u.), displayed in Figure 3.3.18.

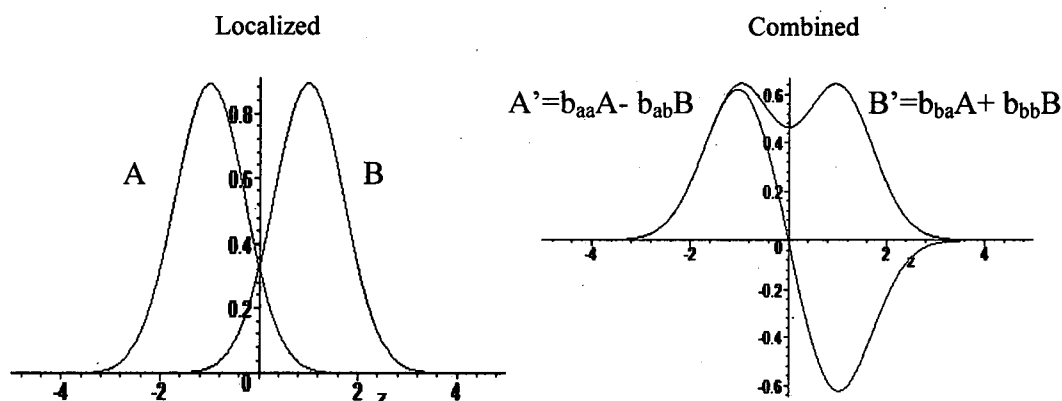


Figure 3.3.18: (a) Two arbitrary identical normalized states shifted along the z-axis ($\Delta z=2$ a.u.) and (b) their orthogonal combinations.

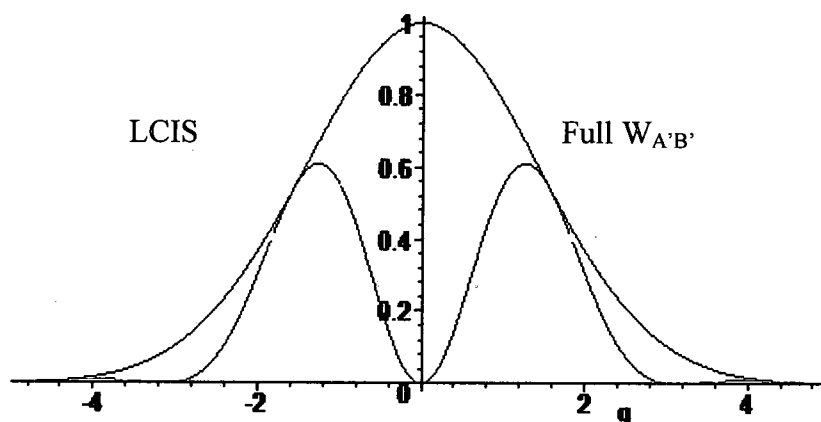


Figure 3.3.19: Form factor comparison of the full wavefunctions vs. the LCIS expansion for the simple 2-state system with ($\Delta z=2$ a.u.).

The comparison of the form factors for this example (Figure 3.3.19) still shows the LCIS method to be the envelope of the full calculation but now the internal oscillations of the full calculation differ dramatically from the previous calculation. These peaks and valleys inside the full form factor are highly dependent on the changing overlap between the states (thus their position and wavevectors) as well as the specific perturbation. Since

these form factors must be integrated, in this case over q , it becomes clear that the LCIS technique will be always have error in the magnitude yet should follow the general rate effect due to the changing wavefunctions in the full calculation.

These potential errors could be corrected by actually using combinations of the localized matrix elements $m_{AA} = \langle A | \tilde{H} | A \rangle$ inside of the expanded Fermi's Golden Rule instead of assuming their description as $m_{AA} = \sqrt{W_{AA}}$, where W_{AA} describes the mean localized scattering. This approach, as previously mentioned, would not however, permit the extraordinary computational advantage of assuming the mean rate expansion. Taking into account the fact that this LCIS technique being employed has the ability to reproduce the behavior quite well, while being off in the magnitude; a method to compensate for this error could be found using "best fit" empirical factors.

3.4 Single Well Scattering Rates

In Section 3.3 a simple linear combinations of intrawell scattering (LCIS) technique demonstrated that the behavior of transition rates in a coupled well system can be reproduced quite well by using the tight-binding coupling coefficients of Section 2.4 along with easily obtainable fits of the mean subband scattering rates between single-well wavefunctions. While the exact magnitude of the delocalized scattering rates cannot be reconstructed using this approach the computational benefits could be enormous if sufficient empirical "best fits" can be made. In the previous section the use of simple piecewise exponential functions was used to represent the basis rates for a single lattice temperature, electron temperature, subband population, and well width. To truly exploit

the computational advantage of the LCIS method, applied to any arbitrary system, the use of more comprehensive fitting functions is required. In this section the effects of varying potentially relevant parameters is examined and determination of what needs to be taken into consideration and what can be neglected is made. After finding suitable empirical fits for the localized basis rate comparisons with the delocalized fully numerical calculations will again be presented.

To start, a further scrutiny of the LO-phonon emission rates can be made. In the previous section it was found that the delocalized scattering can be approximated simply by fitting two-types of localized scattering transitions, namely the ground-to-ground (gg) and the excited-to-ground (eg) types (Figure 3.4.1). In the previous examples all parameters were held constant except for the energy separation which varied with the electric field bias of the extended system. The piecewise functions $W(\Delta E)$ were then implemented. Since the interwell scattering to be reproduced was between 2-wells of identical width the same wavefunctions could be used on each side of the barrier. In a general system this would not be the case and thus the dependence of the mean basis rates on the well width must be determined.

To investigate this well width dependence the wavefunctions are again translated into the single wells as shown in Figure 3.4.1. With the subband populations fixed at $1 \times 10^{10} \text{ cm}^{-2}$ and the temperature at $T_e = T = 77 \text{ K}$ these calculated rates are plotted vs. the energy separation at well widths of 100, 150, and 200 \AA , as shown in figure 3.4.2.

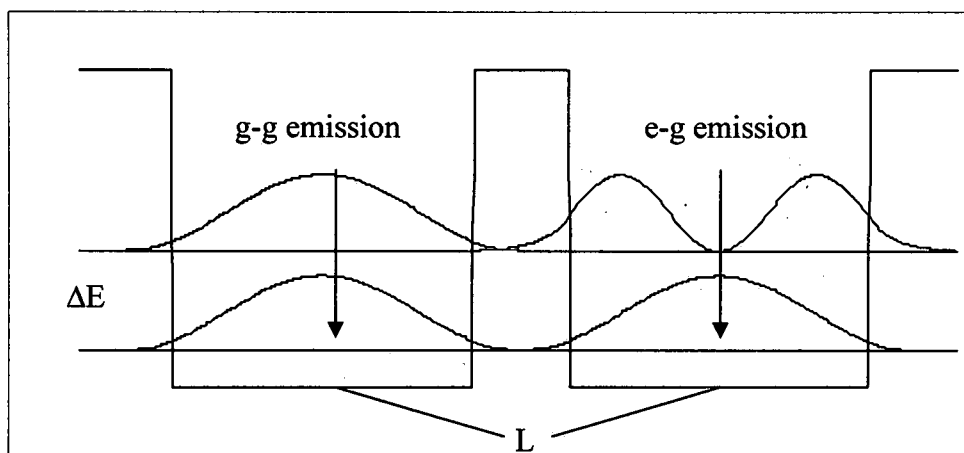


Figure 3.4.1: Wavefunctions used to determine the gg and eg mean basis rates.

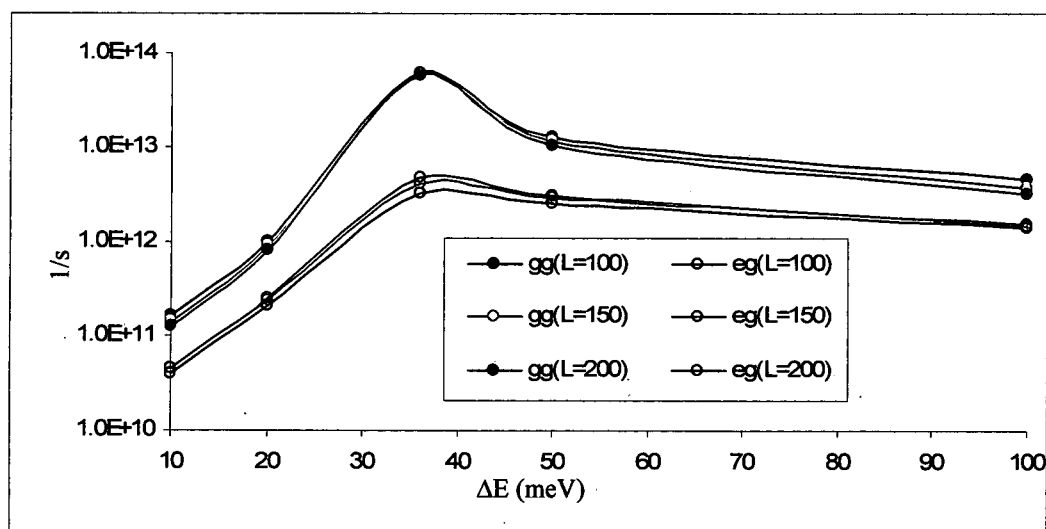


Figure 3.4.2: The gg and eg LO emission basis rates plotted vs. ΔE calculated at $L=100$, $L=150$, and $L=200$.

Using this plot it is concluded that the difference in the form of the wavefunctions, for well widths between 100 and 200Å has little effect on the calculated rates for these components. This will allow the calculations to proceed with fitting general component functions that are suitable for any size well, within a reasonable range. It is therefore

considered it safe to neglect the well width effects for these basis transitions. With this assumption of negligible well width effects a nominal well width of 150\AA will be used for future calculations.

Next an examination can be made as to the effects of the subband populations. Since the QCL systems to be modeled have low ($1\text{--}10 \times 10^{10} \text{ cm}^{-2}$) per period, assume that the maximum population in a given state is near $3 \times 10^{10} \text{ cm}^{-2}$. Under this assumption a simulation of these rates at $T_e = T = 77\text{K}$ for populations in the initial state of $0.1 \times 10^{10} \text{ cm}^{-2}$, $1 \times 10^{10} \text{ cm}^{-2}$, and $3 \times 10^{10} \text{ cm}^{-2}$ is calculated while keeping the final state population fixed at $1 \times 10^{10} \text{ cm}^{-2}$, as shown in Figure 3.4.3.

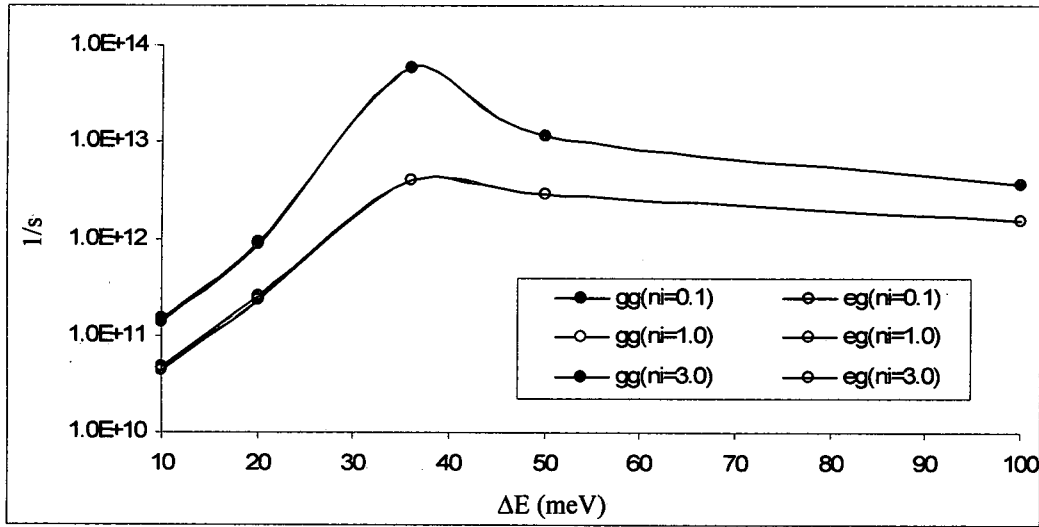


Figure 3.4.3: The gg and eg LO emission basis rates plotted vs. ΔE calculated at $n_i = 0.1 \times 10^{10} \text{ cm}^{-2}$, $1 \times 10^{10} \text{ cm}^{-2}$, and $3 \times 10^{10} \text{ cm}^{-2}$.

Here the variance with the subband population of an initial state, over this given range ($1\text{--}3 \times 10^{10} \text{ cm}^{-2}$), has a negligible effect on the rates. Similarly, the rates calculated for

various final subband population while fixing the initial at $1 \times 10^{10} \text{ cm}^{-2}$ is shown in (Figure 3.4.4).

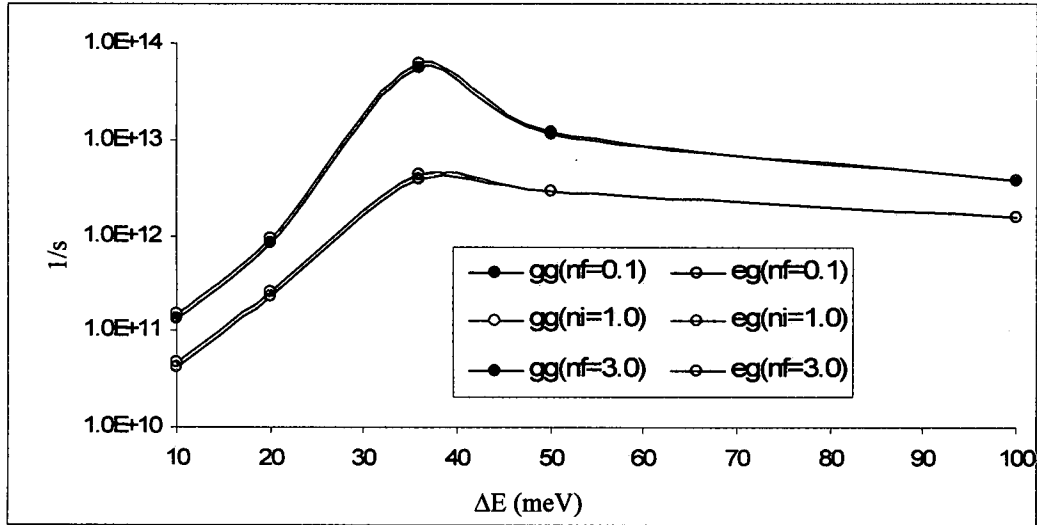


Figure 3.4.4: The gg and eg LO emission basis rates plotted vs. ΔE calculated at $n_i = 0.1 \times 10^{10} \text{ cm}^{-2}$, $1 \times 10^{10} \text{ cm}^{-2}$, and $3 \times 10^{10} \text{ cm}^{-2}$.

From this plot it is again observed that the final state blocking effects are negligible at these low carrier concentrations. These two realizations will have additional significant computational advantages moving on to transport calculations. In a typical rate equation model, one would calculate the total electrons coming into a given state (f) from a state (i) as $n_i W_{if}$. In previous modeling efforts [82-88] of more heavily doped mid-infrared QCL's a self-consistent rate equation was employed to account for the population dependent rates (i.e. $n_i W_{if}(n_i, n_f)$). In these calculations iterative solutions must be found for the populations and the scattering rates based on the populations. From the results above these self-consistent methods will be entirely dismissed and the calculations will proceed with fixed populations $n_i = n_f = 1 \times 10^{10} \text{ cm}^{-2}$.

Moving on to temperature it must now be assumed, for these phonon assisted transitions, that these are non-negligible effects. Since the phonons themselves are Bosons and behave according to temperature dependent Bose-Einstein statistics, the phonon rates are likely very dependent on the lattice temperature (as was shown previously in Figure 1.2.4.), especially at THz energy separations. In addition, the mean subband rates are calculated by integrating over the subband distributions using Fermi-Dirac statistics. These kinetic energy distributions will be highly dependent on the electron temperature. To observe these temperature effects the rates are plotted in Figure 3.4.5 (for the g-g rate) and 3.4.6 (for the e-g rate) at lattice temperatures of 4K, 77K, and 300K, and at electron temperatures of $T_e = T + 0K$, $T + 100K$, and $T + 200K$. In both plots it is clearly seen that these emission rates vary considerably vs. the electron temperature, especially before the phonon resonance. This is due to electrons near the subband minima not having sufficient in-plane kinetic energy to emit a phonon and transition to the lower subband. As the electron temperature is increased the distribution moves towards higher kinetic energy allowing for previously forbidden transitions.

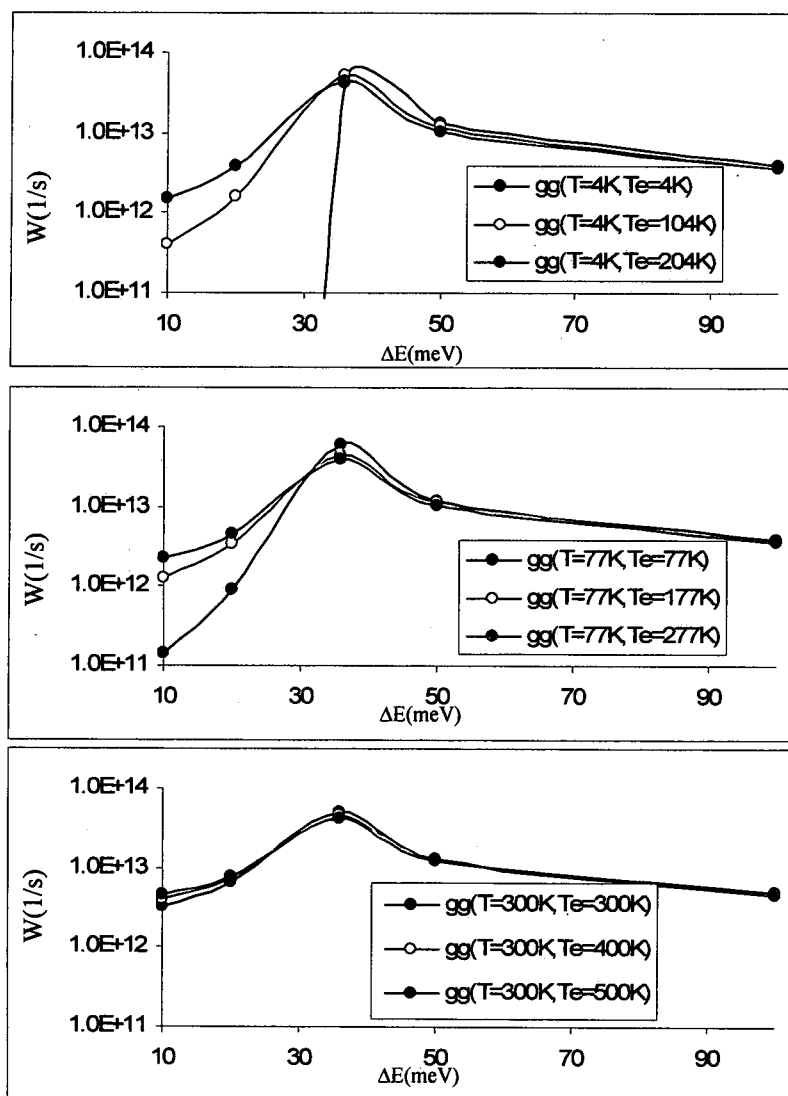


Figure 3.4.5: The gg emission basis rates at various lattice and electron temperatures.

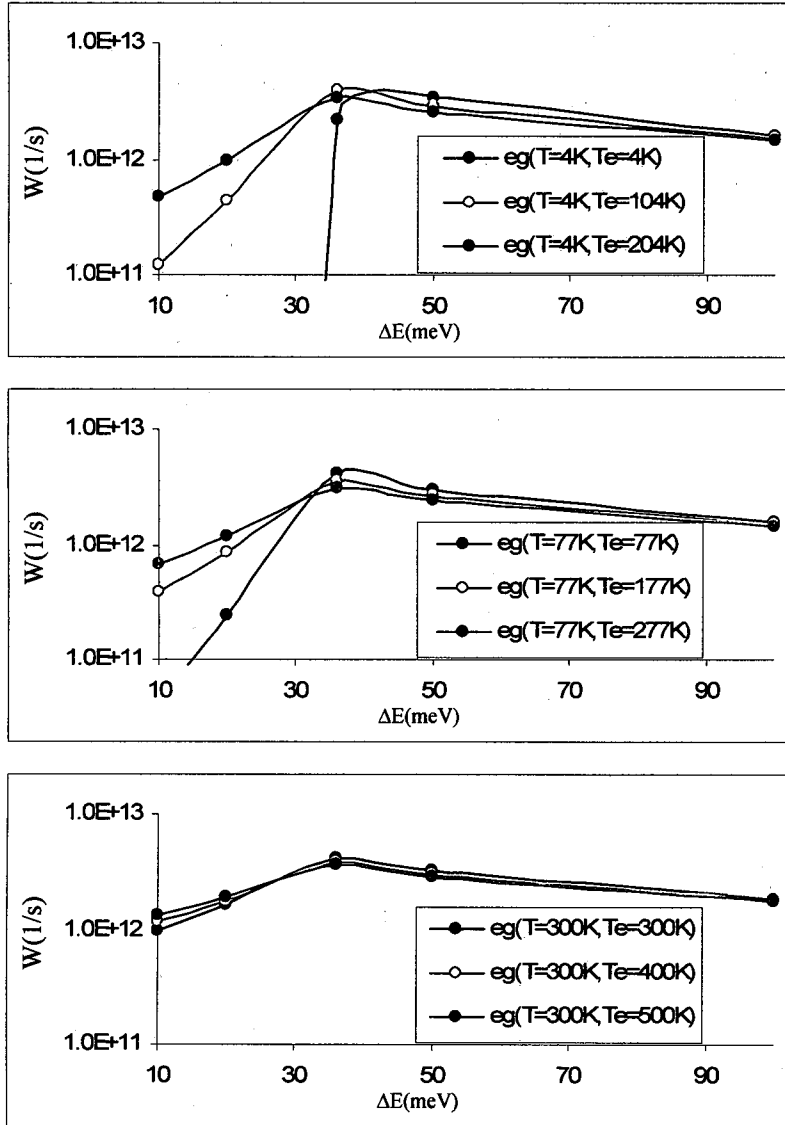


Figure 3.4.6: The eg emission basis rates at various lattice and electron temperatures.

To reasonably fit a function which can be used for a range of electron temperatures a 2nd order polynomial fit is considered for the coefficients of the already established exponential fits vs. the energy separation. For example, consider the g-g emission rates at 77K (shown in Figure 3.4.7).

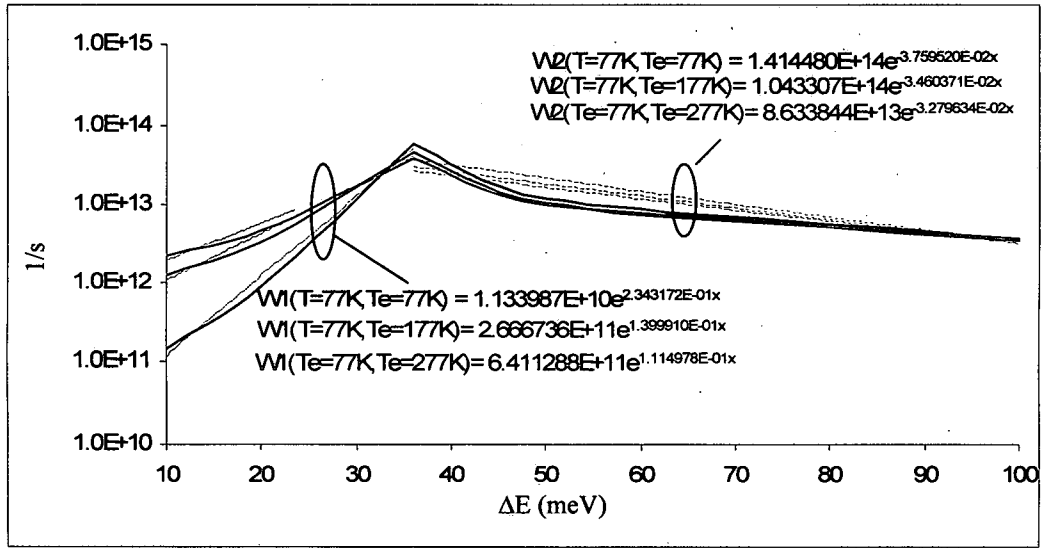


Figure 3.4.7: The gg basis emission rates and exponential fitting functions at a lattice temperature of $T=77\text{K}$ and electron temperatures at $T_e=T+0\text{K}$, $T_e=T+100\text{K}$, and $T_e=T+200\text{K}$.

The least squares exponential fits shown in Figure 3.4.7 are of the form

$$W_1(\Delta E \leq 36\text{meV}) = A_1 e^{b_1 \Delta E} \quad (3.4.1)$$

$$W_2(\Delta E \geq 36\text{meV}) = A_2 e^{b_2 \Delta E}$$

This fitting approach does not automatically set the functions to equal at the phonon resonance ($\Delta E=36\text{meV}$). To force this condition the following expression is used

$$A_1 e^{b_1 36} = A_2 e^{b_2 36} \quad (3.4.2)$$

which implies

$$\frac{A_1}{A_2} = \frac{e^{b_2 36}}{e^{b_1 36}} \quad (3.4.3)$$

After the initial fit the A coefficients are then altered by writing

$$A'_1 = A_1 - \Delta \quad A'_2 = A_2 + \Delta \quad (3.4.4)$$

The matching condition is then

$$(A_1 - \Delta)e^{b_1 36} = (A_2 + \Delta)e^{b_2 36} \quad (3.4.5)$$

Solving this for Δ gives

$$\Delta = \frac{A_1 e^{b_1 36} - A_2 e^{b_2 36}}{e^{b_1 36} + e^{b_2 36}} \quad (3.4.6)$$

After resetting the A terms a fit for both the A and the b coefficients vs. Te using 2nd order polynomials is found. A plot of the coefficients and the fitting functions are shown in Figure 3.4.8 and Figure 3.4.9 for the A and b terms, respectively.

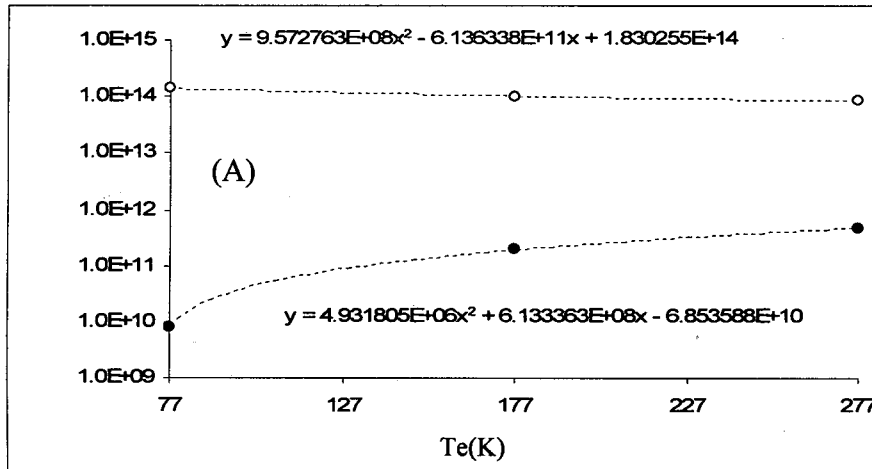


Figure 3.4.8: A plot of the A coefficient terms vs. the electron temperature at T=77K. A₁ is shown in black and A₂ in red.

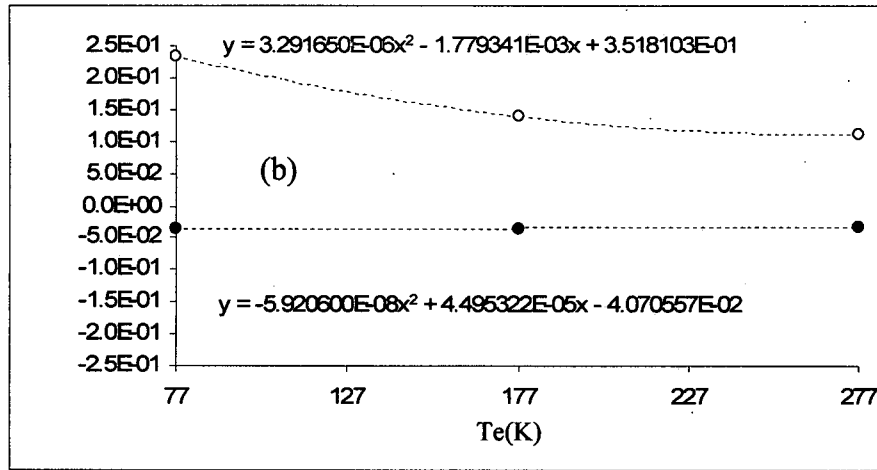


Figure 3.4.9: A plot of the b coefficient terms vs. the electron temperature at T=77K. b_1 is shown in black and b_2 in red.

Now using these fits for the coefficients the empirical rates can be written as

$$W_{gg,em}^{T=77K} = \begin{cases} (x_{a1} + y_{a1}T_e + z_{a1}T_e^2) \exp((x_{b1} + y_{b1}T_e + z_{b1}T_e^2)\Delta E) & \text{for } \Delta E < 36 \\ (x_{a2} + y_{a2}T_e + z_{a2}T_e^2) \exp((x_{b2} + y_{b2}T_e + z_{b2}T_e^2)\Delta E) & \text{otherwise} \end{cases} \quad (3.4.7)$$

A comparison of these fits to the original data is shown below in Figure 3.4.10.

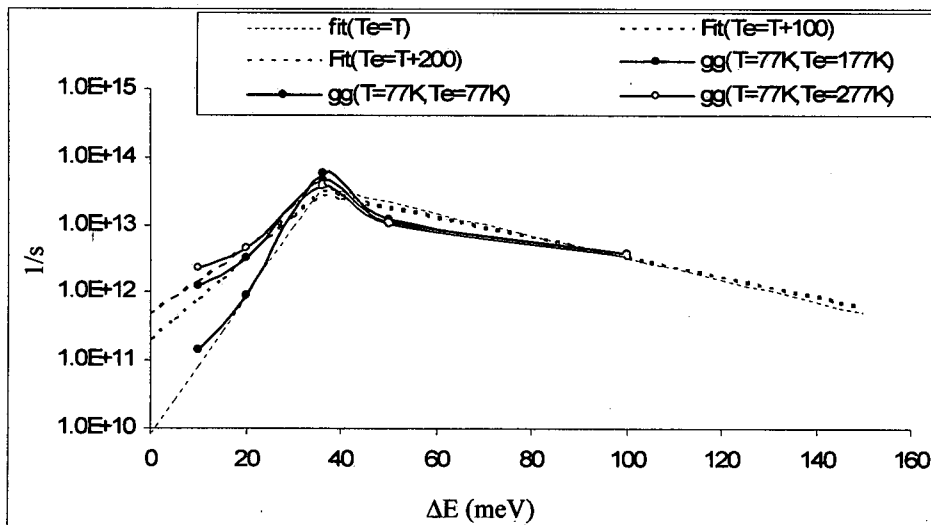


Figure 3.3.10: Comparison of the empirical fitting functions and the calculated data for the gg emission rate at T=77K.

Carrying out the same procedure for the e-g emission rates produces the fit shown in Figure 3.4.11.

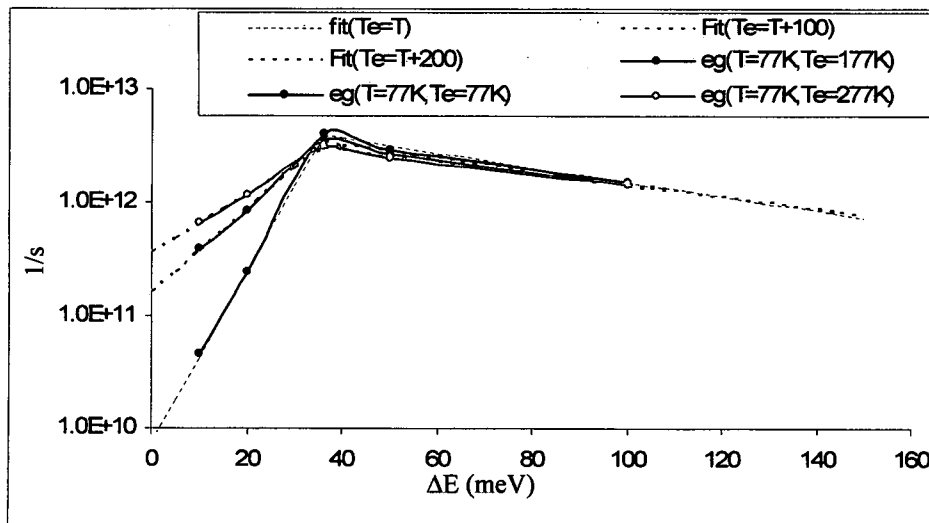


Figure 3.3.11: Comparison of the empirical fitting functions and the calculated data for the eg emission rate at $T=77\text{K}$.

The fits shown in Figures 3.3.10 and 3.3.11 show, as expected, good agreement with the data points ($T_e=T$, $T_e=T+100$, and $T_e=T+200\text{K}$) used to create the polynomials. It is important though to check the points outside of those used for the fits. Looking at several of these temperatures for the gg emission rate (Figure 3.4.12) it is seen that although the behavior is still well represented the mismatch at the phonon resonance is again observed. To correct this, application of the same procedure described by Equations 3.4.4 and 3.4.6., is used.

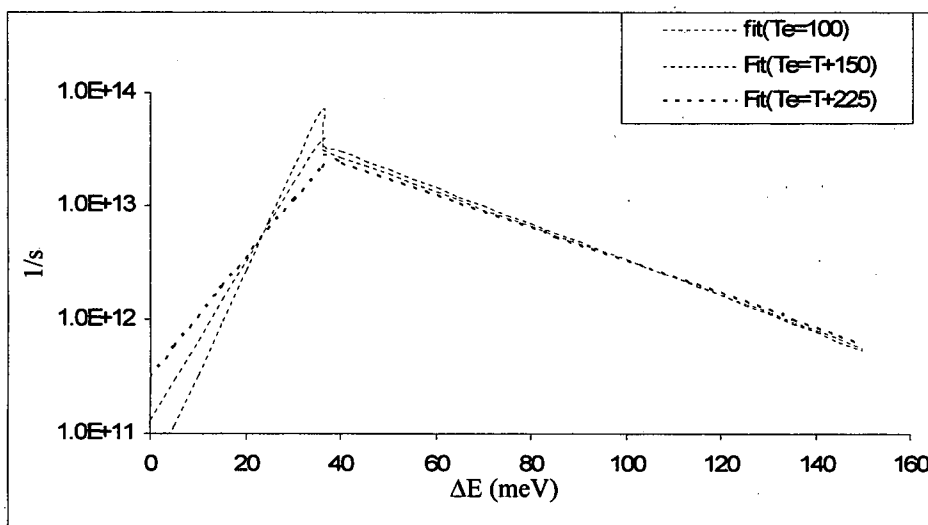


Figure 3.4.12: Empirical fitting functions for the gg emission rates at $T=77\text{K}$ at electron temperatures outside of the fitting points.

After correcting the resonance peak a plot of various T_e values between the limits (for the 77K example this is between $T_e=77$ and $T_e=277$) is displayed. A comparison of these values to the original data is shown in Figure 3.4.13.

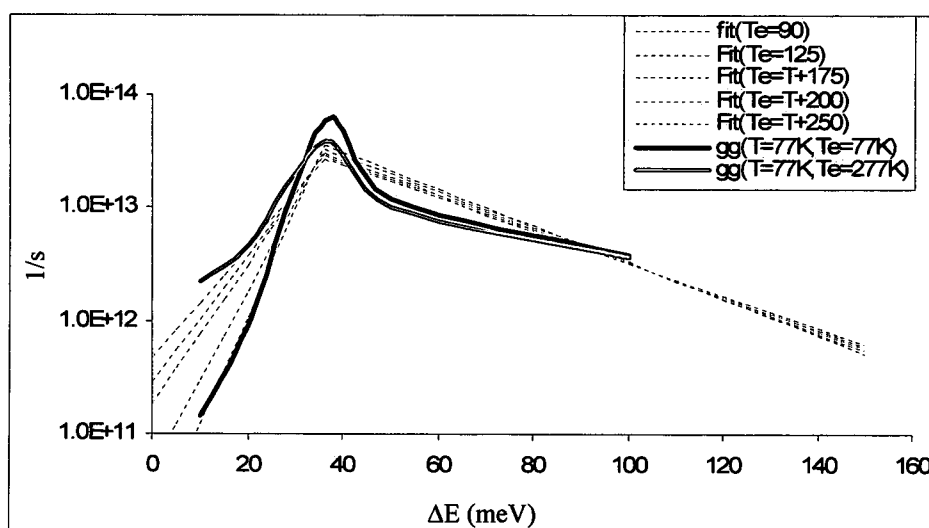


Figure 3.4.13: Corrected empirical gg-emission rates at $T=77\text{K}$ compared to the original data.

Now there is an empirical fit which works reasonably well for all electron temperatures at this specific lattice temperature of $T=77\text{K}$. In Figure 3.4.13 the behavior of the increasing rate with T_e below the peak is accurately portrayed and the opposite, decreasing rate with T_e is shown immediately on other side of the peak.

To extend this fitting function to account for all lattice temperatures a linear fit is applied to all coefficients in the form

$$x, y, z = w + vT \quad (3.4.8)$$

For this determination the linear fit was performed between $T=77\text{K}$ and $T=300\text{K}$. The accuracy of this fit extended to lattice temperatures between 4K and 300K is displayed, along with the calculated data, for this gg-emission rate in Figures 3.4.14 through 3.4.18.

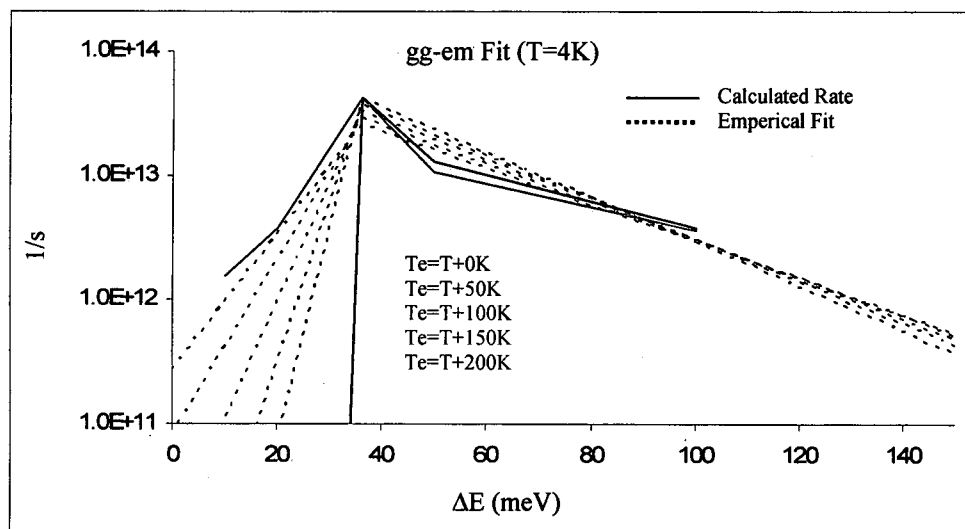


Figure 3.4.14: The full empirical gg-emission fit compared to the calculated data at a lattice temperature of $T=4\text{K}$.

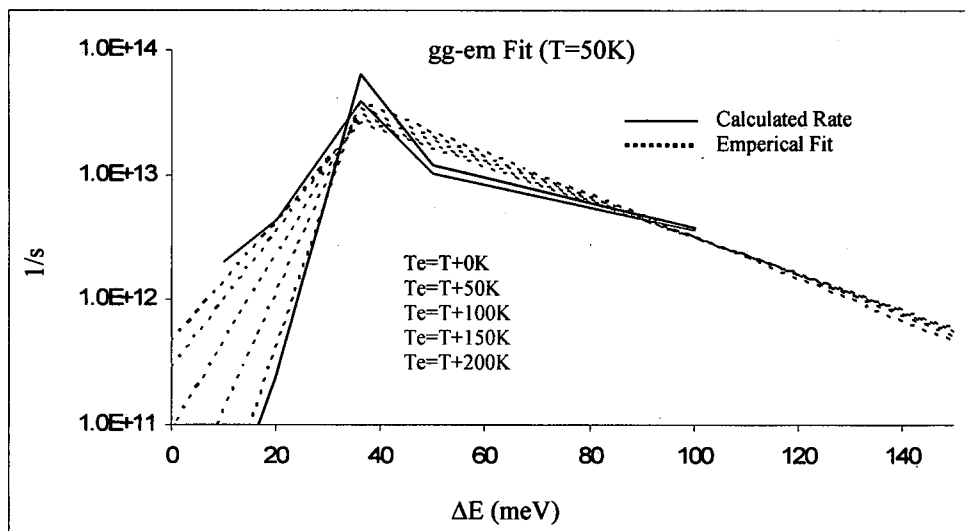


Figure 3.4.15: The full empirical gg-emission fit compared to the calculated data at a lattice temperature of $T=50K$.

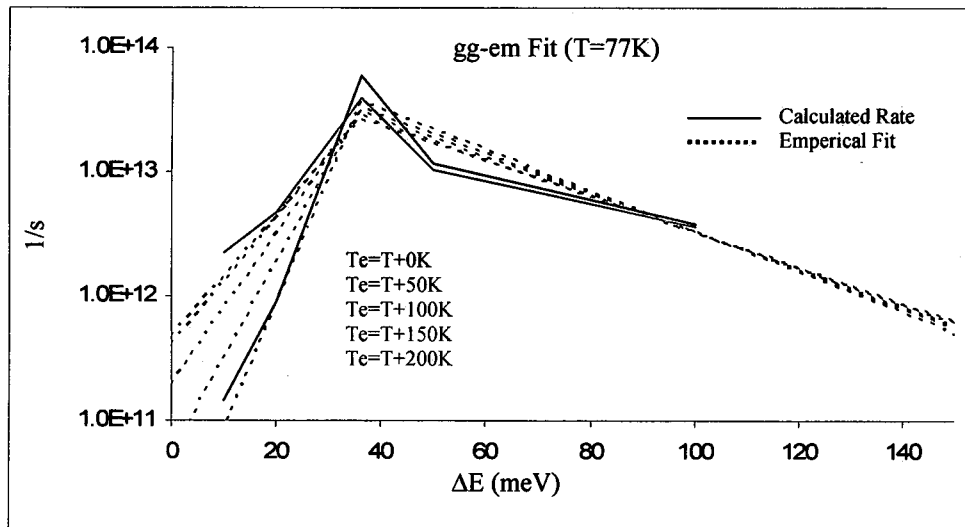


Figure 3.4.16: The full empirical gg-emission fit compared to the calculated data at a lattice temperature of $T=77K$.

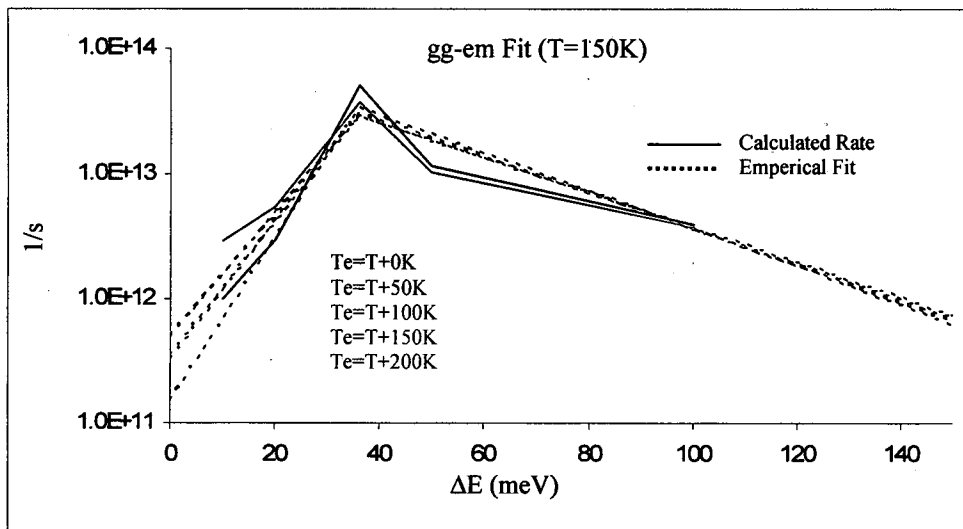


Figure 3.4.17: The full empirical gg-emission fit compared to the calculated data at a lattice temperature of $T=150K$.

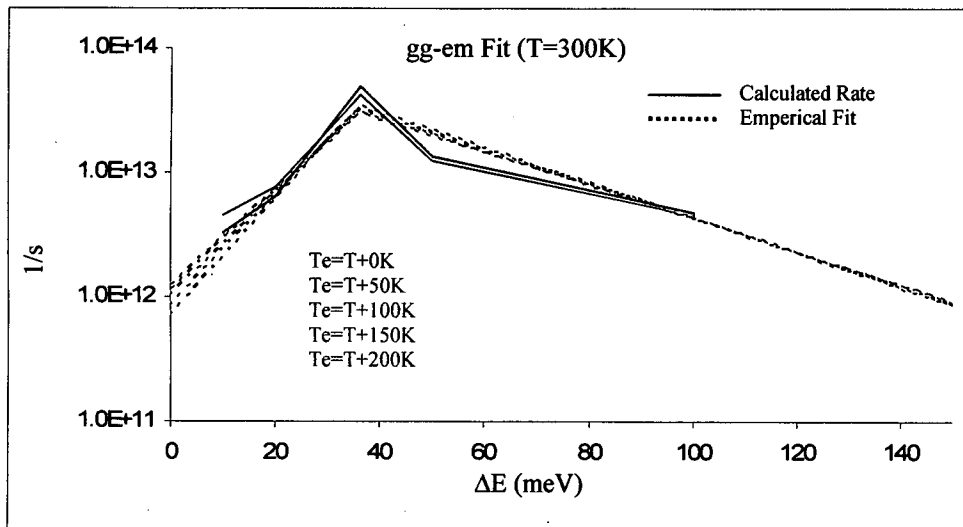


Figure 3.4.18: The full empirical gg-emission fit compared to the calculated data at a lattice temperature of $T=300K$.

In these figure the full gg-emission rate is shown to agree surprisingly well over the entire range of lattice and electron temperatures. The behavior of an increasing rate with T_e (below the resonance peak) and a decrease (above the peak) is captured quite well. In addition, the above plots clearly shown the decrease in this T_e rate spread with increasing lattice temperatures.

To observe if the correct lattice temperature dependence is captures the electron temperature is then fixed at $T_e = T + 100K$ and plotted in Figure 3.4.19.

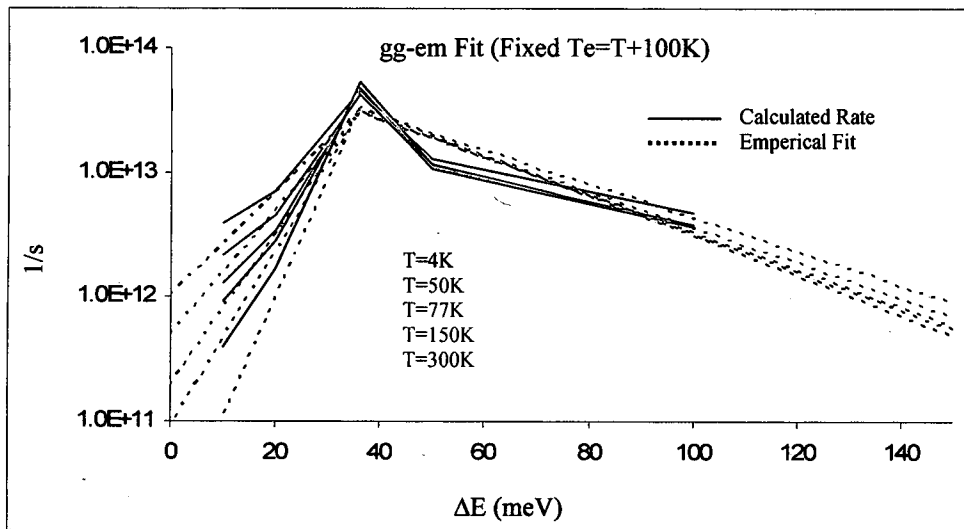


Figure 3.4.19: The full empirical gg-emission fit compared to the calculated data using an electron temperature of $T_e = T + 100K$ at various lattice temperatures.

In this plot the fitting function again predicts the correct increasing rate behavior with increasing lattice temperatures below the phonon resonance. At energy separations greater than the resonance the fit also agrees with the data in that the $T=4K$ is the largest resonance but then decays faster than the higher temperatures. At larger separations the trend is flipped where the 300K lattice temperature has the highest rate, followed by the 150K, and so on.

These empirical rates are therefore shown to sufficiently predict the behavior of this specific LO emission rate vs. ΔE , T , and T_e , using simplified to fitting functions in the method outlined above. This same method can then be repeated for the e-g emission rate. The calculated rates and the fits for this type of transition are plotted at 77K (Figure 3.3.20) and 300K (Figure 3.3.21).

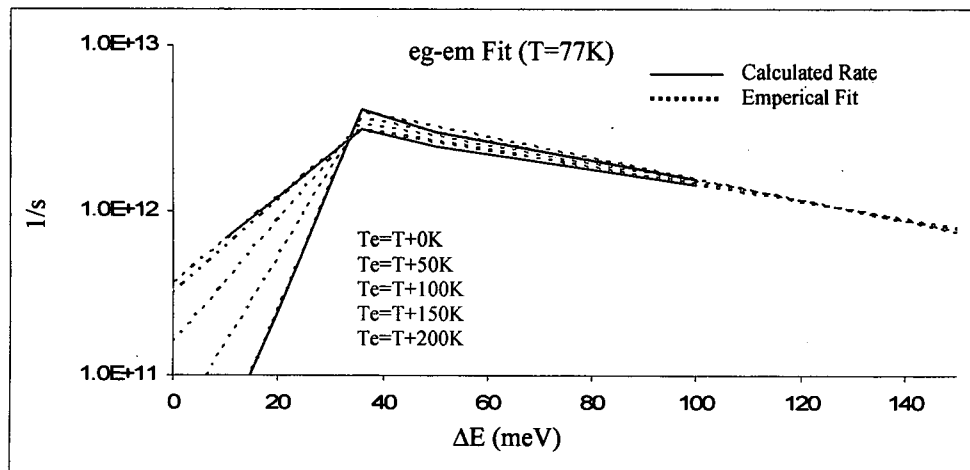


Figure 3.4.20: The full empirical gg-emission fit compared to the calculated data at a lattice temperature of $T=77K$.

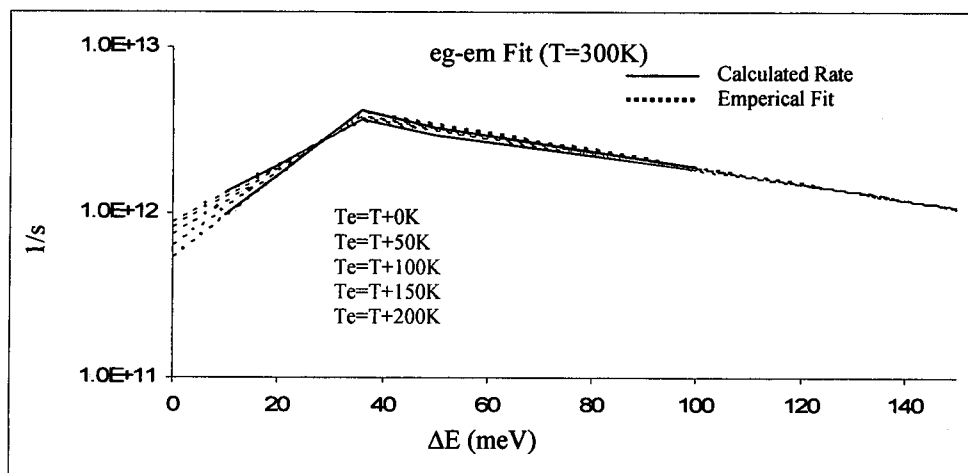


Figure 3.4.21: The full empirical gg-emission fit compared to the calculated data at a lattice temperature of $T=300K$.

These plots again show the fit working very well for these excited-to-ground (eg) emission rates. In fact, the behavior and magnitude is captured even more accurately than the gg rates as these transitions seem to follow the exponential decay more consistently near the phonon resonance.

The method and examples shown above now permits a reasonable fit to the basis mean LO-emission rates at any ΔE , T , and T_e using the coefficients given in Tables 3.4.1 and 3.4.2.

gg	A1(x)	A1(y)	A1(z)
v	-2.588183E+09	2.238128E+07	-3.805705E+04
w	1.307542E+11	-1.110022E+09	7.862198E+06
	b1(x)	b1(y)	b1(z)
v	-8.019354E-04	6.676715E-06	-1.368197E-08
w	4.135593E-01	-2.293448E-03	4.345161E-06
	A2(x)	A2(y)	A2(z)
v	-4.233857E+10	1.514230E+09	-3.313434E+06
w	1.862856E+14	-7.302295E+11	1.212411E+09
	b2(x)	b2(y)	b2(z)
v	1.315103E-05	-1.006295E-07	1.929484E-10
w	-4.171820E-02	5.270169E-05	-7.406303E-08

Table 3.4.1: Coefficients for the mean LO-emission gg basis rates.

eg	A1(x)	A1(y)	A1(z)
v	-1.426324E+09	1.378704E+07	-2.426273E+04
w	3.572537E+10	-2.042768E+08	4.489698E+06
	b1(x)	b1(y)	b1(z)
v	-7.743417E-04	6.461018E-06	-1.326098E-08
w	3.454832E-01	-2.194798E-03	4.193766E-06
	A2(x)	A2(y)	A2(z)
v	3.329466E+09	3.397121E+07	-7.854904E+04
w	7.673798E+12	-2.152029E+10	3.224013E+07
	b2(x)	b2(y)	b2(z)
v	6.318475E-06	-4.681054E-08	8.725112E-11
w	-1.681282E-02	2.768276E-05	-3.591934E-08

Table 3.4.2: Coefficients for the mean LO-emission eg basis rates.

Determination of suitable absorption rate fits can be accomplished in a much simpler manner by using the well known relationship between the ratio of emission to absorption, i.e.,[50]

$$\frac{W_{21}(\text{em})}{W_{12}(\text{ab})} \propto \exp\left(\frac{\Delta E_{21}}{kT}\right) \quad (3.4.9)$$

As an example consider the ratios of the $W_{21-\text{em}}$ and $W_{12-\text{ab}}$ rates calculated $T_e=T=77\text{K}$ for both basis transitions (gg & eg). These ratios are shown in (Table 3.4.3).

DE(2-1)	Rgg(77/77)	Reg(77/77)
10	4.5034E+00	4.5030E+00
20	2.0229E+01	2.0226E+01
36	2.1986E+02	2.2048E+02
50	1.8310E+03	1.8304E+03
100	3.5742E+06	3.5697E+06

Table 3.4.3: Ratios of the $W_{21-\text{em}}$ to the $W_{12-\text{ab}}$ rates at various ΔE_{21} subband separations for both the gg and eg basis rates.

Here it is observed that this ratio agrees very well for either type of transition. To incorporate a fit for any T and T_e we will focus on the region below $\Delta E=36\text{meV}$. From the table above it is clearly seen that beyond this peak the emission clearly dominates and absorption will have a minimal effect on transport. A plot of the ratios of emission to absorption at energy separations less than the LO phonon energy are shown in Figure 3.4.22 at 77K and figure (3.4.23) at 300K.

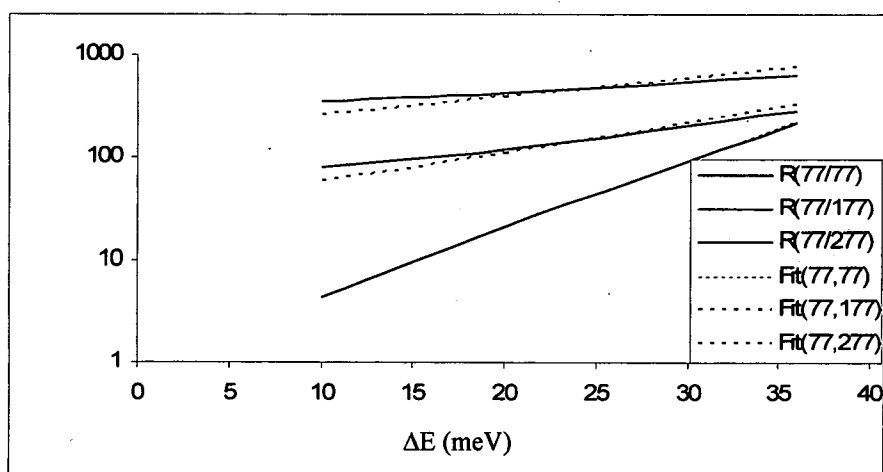


Figure 3.4.22: Emission to absorption ratios at energy separations below the phonon resonance at $T=77\text{K}$.

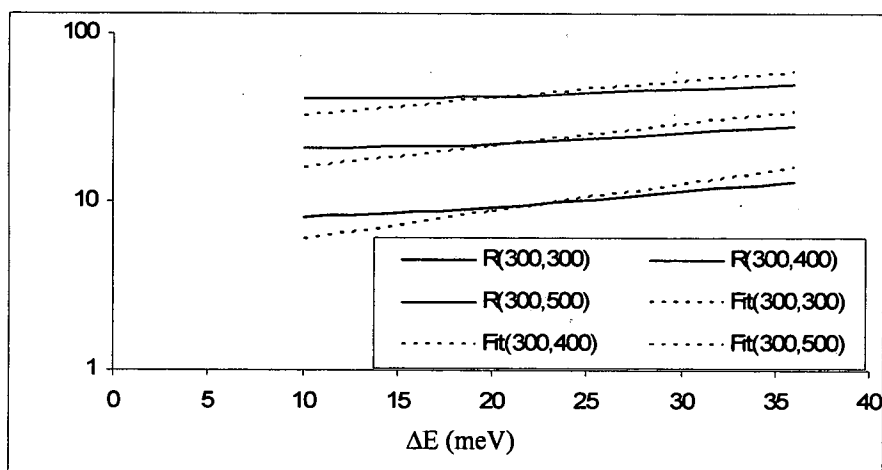


Figure 3.4.23: Emission to absorption ratios at energy separations below the phonon resonance at $T=300\text{K}$.

In these plots the fitting functions in the form

$$R = \frac{W_{21}(\text{em})}{W_{12}(\text{ab})} = C(T_e, T) \exp\left(\frac{\Delta E_{21}}{kT_e}\right) \quad (3.4.10)$$

are used where the coefficient C is then fit exponentially to $T_e - T$ (Figure 3.4.24) and then linearly with T .

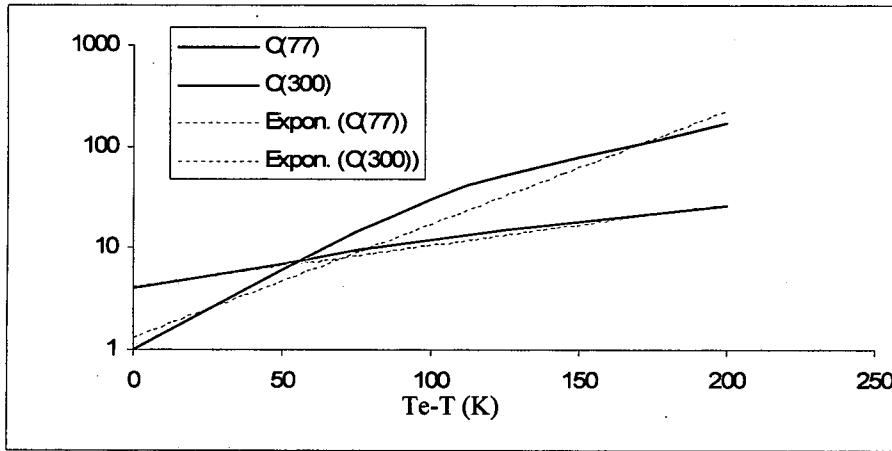


Figure 3.4.24: The emission to absorption ratio fitting coefficient C , and its corresponding exponential fits at $T=77\text{K}$ and $T=300\text{K}$.

Therefore the coefficient C is written as

$$C(T_e, T) = A \exp(b(T_e - T)) \quad (3.4.11)$$

where A & b are linearly fit to the lattice temperature

$$A, b = y + xT \quad (3.4.12)$$

The necessary coefficients for these absorption rates are displayed in Table 3.4.4.

	A	b
x	1.301687E-02	-7.318376E-05
y	3.178780E-01	3.131414E-02

Table 3.4.4: Coefficients required for determining the basis absorption rates.

These coefficients can then be used to calculate the absorption rates $W_{fi,abs}$ for any ΔE , T , and T_e , based on the previous fitting functions used for the emission $W_{if,em}$. The energy dependence in this case must be flipped from $\Delta E_{fi} = -\Delta E_{if}$. An example of this fit along with the emission rates is shown in Figure 3.4.25.

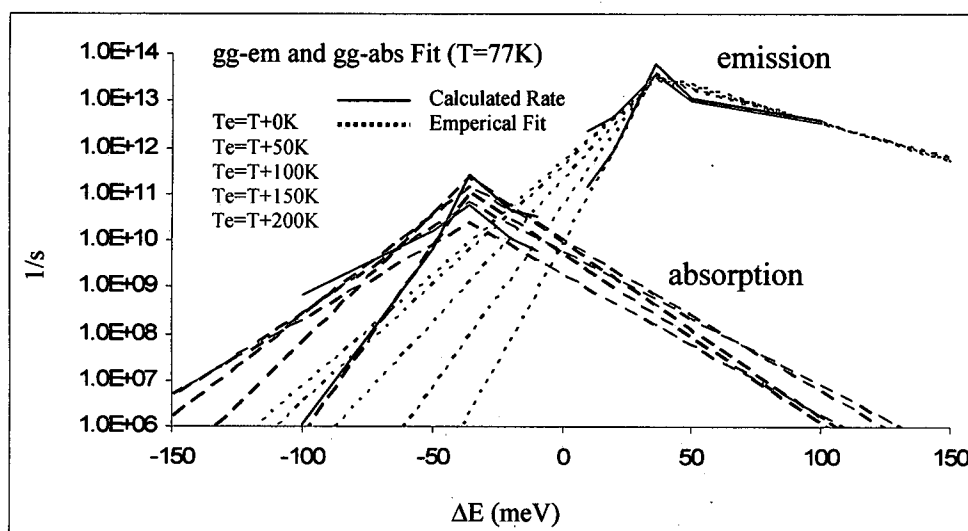


Figure 3.4.25: Empirically fit emission and absorption rates at $T=77K$ and various electron temperatures compared to the calculated data at $T_e=T+0K$ and $T_e=T+200K$.

Using this simple fit agreement is again found with the absorption rate vs. energy separation behavior. This is expected as the emission and absorption rates are closely linked. Now that sufficient fitting functions have been found describing the LO phonon basis rates the same procedure can be applied to the electron-electron scattering.

As was shown in Section 3.3 reasonable fits for the electron-electron scattering rates can be found using combinations of intrawell scattering between ground state wavefunctions. In this procedure then, all that is required is a fit to the gg-gg rate. Since these rates are significantly different than the phonon transitions some initial considerations must again be examined. For example, a plot of these basis rates vs. the energy separation at various initial state populations is shown in Figure 3.4.26.

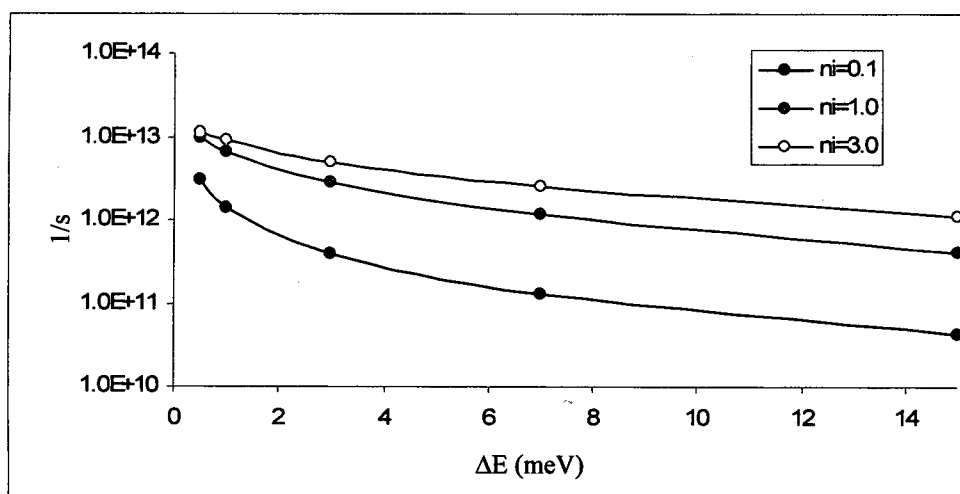


Figure 3.4.26: The gg-gg mean electron-electron basis rates at 77K and a fixed $nf=1.0$, plotted for three different initial subband populations. All population units are 10^{10} cm^{-2} .

In these simulations the concentration of electron produces, as one might expect, a non-negligible change in the electron-electron scattering rates. Inclusion of these population dependent scattering mechanisms would require self-consistent iterative methods. With

the goal of avoiding these complications this dependency will be ignored with the realization that there is the potential for error in the e-e calculations without self-consistency.

The effects of temperature for the electron-electron rates will only be dependent on a single temperature (T_e). Unlike the phonon transitions, where the lattice temperature is used to determine the phonon distribution, here only the Fermi-Dirac statistics are needed. These rates were found to be most suitably approximated using a power fit

$$W = A\Delta E^b \quad (3.4.13)$$

These fits are compared to the calculated data at $T_e=25, 77$, and $300K$ in Figure 3.4.27.

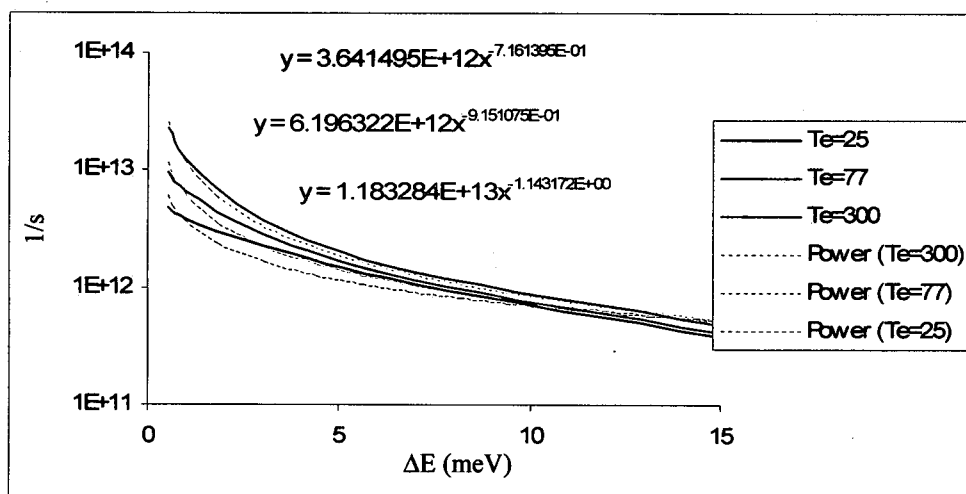


Figure 3.4.27: The gg-gg mean electron-electron basis rates at $T_e=25K, 77K$, and $300K$ along with the corresponding power fitting functions.

These coefficients are then fit linearly with the electron temperature

$$A, b = y + xT_e \quad (3.4.14)$$

to arrive at the necessary fitting values shown in Table 3.4.5.

	A	b
y	3.412127E+12	-7.378787E-01
x	2.844347E+10	-1.394982E-03

Table 3.4.5: Coefficients required for determining the basis electron-electron rates.

Now that all the fits for these “localized basis rates” are tabulated the reproduction of coupled well scattering rates can be revisited to truly prove the sufficiency of these methods. For this consider the previous example system evaluated in Section 3.3., containing two 155Å GaAs wells separated by a 50Å $\text{Al}_{0.15}\text{Ga}_{0.85}\text{As}$ barrier. A plot of the two pictures (Localized and Delocalized States) is shown in Figure 3.4.28 as a reminder. As witnessed in Section 3.3 the delocalized states are always designated in the order of their respective eigenvalues (energies) while the localized states maintain a fixed order at all biases.

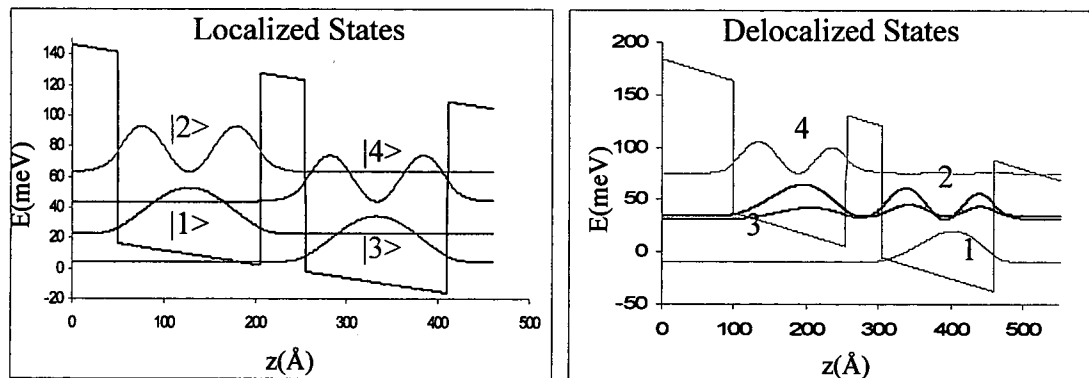


Figure 3.4.28: Localized (left) and delocalized (right) state for a system containing two 155Å GaAs wells separated by a 50Å $\text{Al}_{0.15}\text{Ga}_{0.85}\text{As}$ barrier.

The comparison between the LCIS method using the complete and general empirical fitting functions to the full numerical calculation can be started by considering the intradoublet LO-emission scattering. This rate, again, describes the transition between the ground state in the left well and the excited state in the right well. The results of using the empirical fitting functions outlined above combined with the LCIS procedure of Section 3.3 is then compared for these transitions to the full calculation in Figure 3.4.29. This plot shows that the scattering rate is very well represented not only in the behavior vs. the field but also very closely matches the crossing(anticrossing) peak rate.

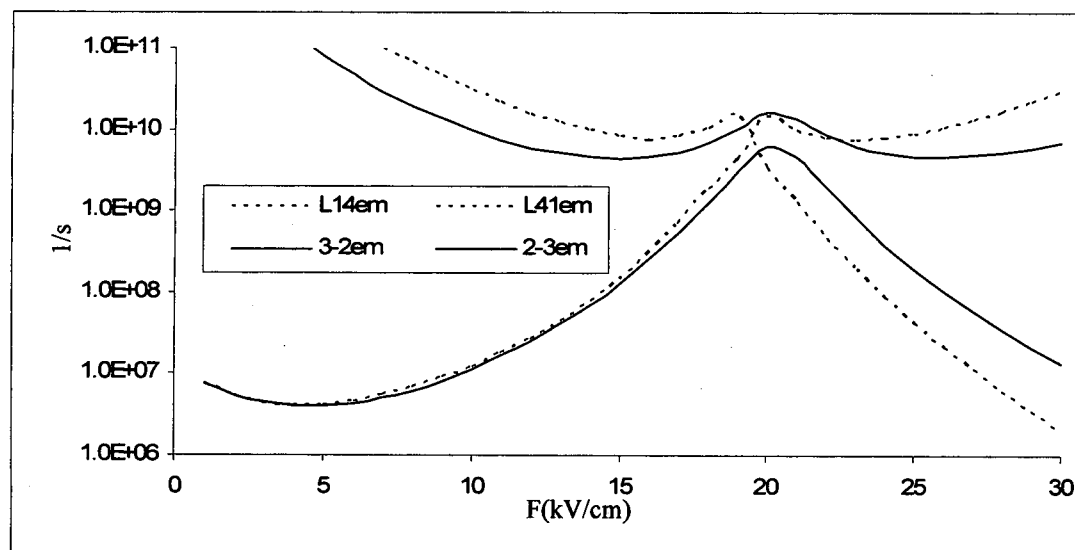


Figure 3.4.29: Comparison of the empirical LCIS predicted intradoublet emission rates (dotted lines) and the full numerical calculation (solid lines).

The comparison for the indirect LO-emission is then shown in Figure 3.4.30. Here there is again very good agreement between the empirical LCIS rates and the full calculation. It is also worthwhile to point out that the rates calculated in Figure (3.4.29) for the intradoublet scattering was between two states separated in energy, near the

crossing(anticrossing) point, by approximately 2.6meV which is well below the phonon resonance energy of 36meV. In this second comparison (Figure 3.4.30) the separation between the excited state and the ground in the right well, and the left ground to right ground near the crossing, is approximately 40meV which is slightly above the phonon resonance. It is also observed that the LCIS rate labeled L13 is also well represented out to the $F=30\text{kV/cm}$ bias where its energy separation is approximately 60meV. Therefore there can be confidence that these rates are suitably approximated on both sides of the phonon resonance.

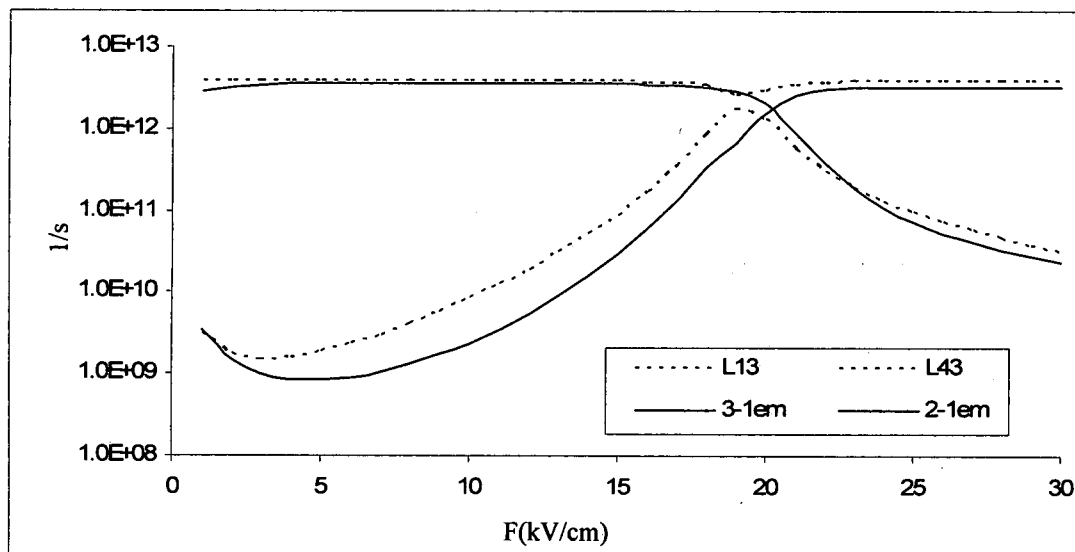


Figure 3.4.30: Comparison of the empirical LCIS predicted indirect emission rates (dotted lines) and the full numerical calculation (solid lines).

The absorption rates, which were calculated using the empirical LCIS technique using the simple emission-to-absorption ratio approach, are also compared to the full calculation for both transition types in Figures 3.4.31 & 3.4.32.

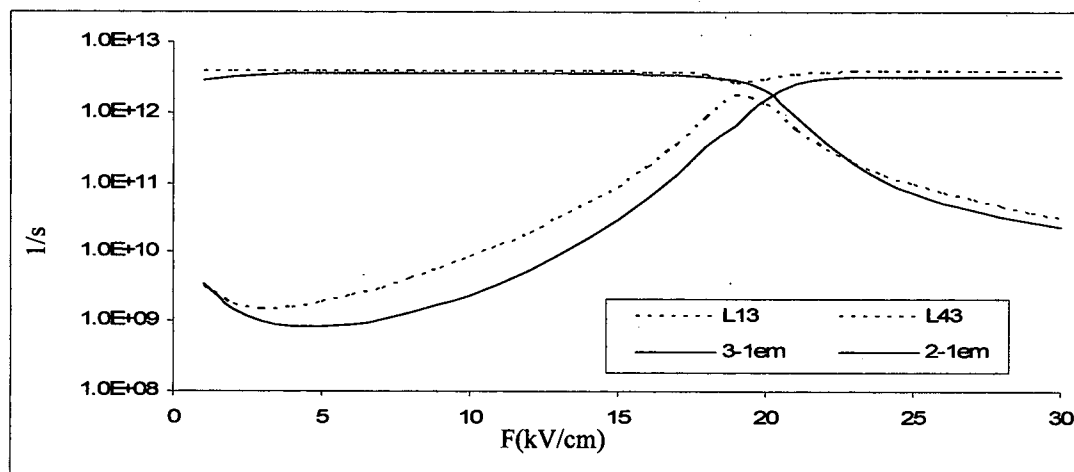


Figure 3.4.31: Comparison of the empirical LCIS predicted intradoublet absorption rates (dotted lines) and the full numerical calculation (solid lines).

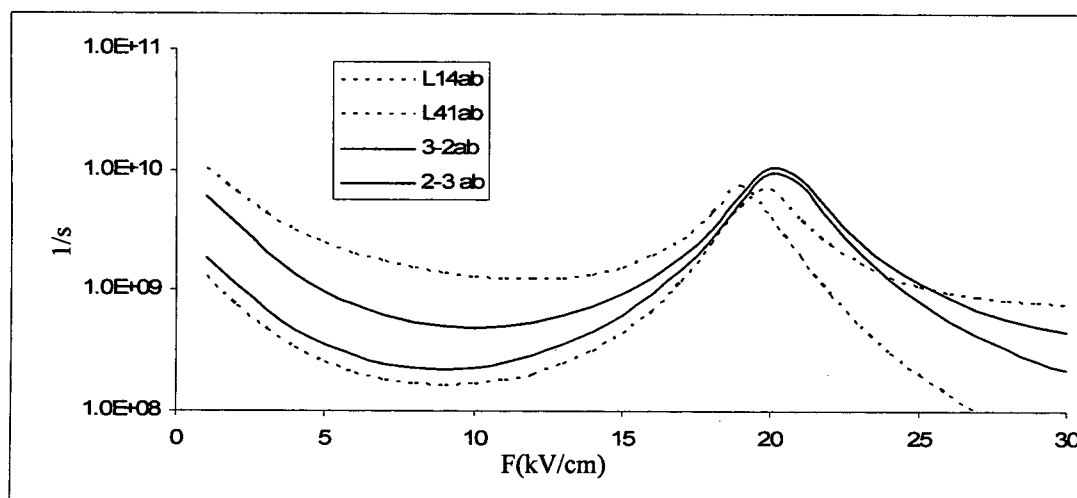


Figure 3.4.32: Comparison of the empirical LCIS predicted indirect absorption rates (dotted lines) and the full numerical calculation (solid lines).

These comparisons again show that the absorption rates are represented quite well using the simple LCIS method and the empirical fitting functions.

For the electron-electron rates the empirical LCIS method, using only the ii-ff, ii-fi, and if-ff rates, are compared to the full calculation where all rates of the form ij-fg (where $E_i > E_f$ and $E_j > E_g$) are used. This comparison is shown in Figure 3.4.33.

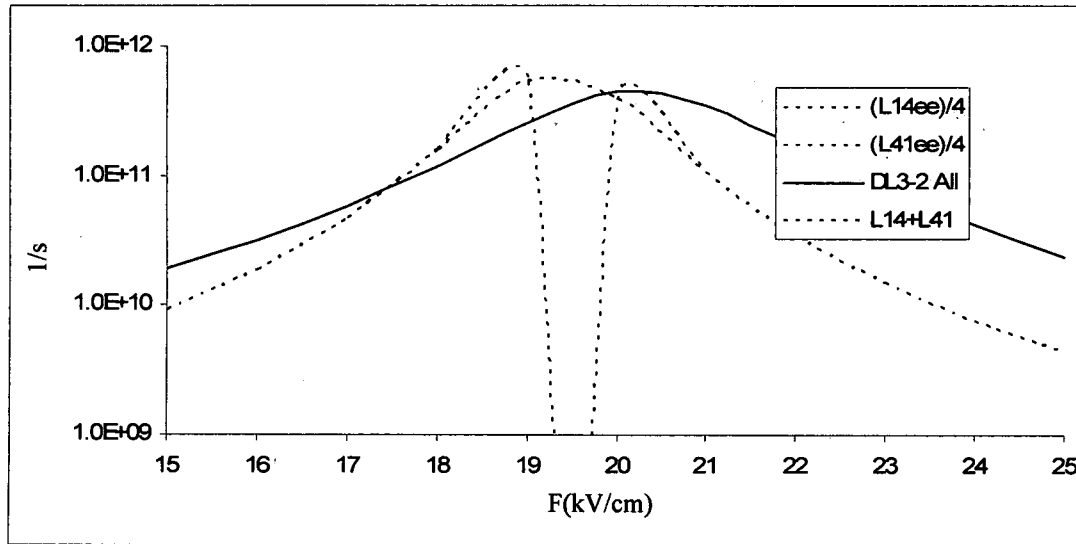


Figure 3.3.33: Comparison of the electron-electron rates calculated using the full numerical technique (solid line) and the empirical LCIS method (dotted lines). The combined 1-4 and 4-1 LCIS rates are also shown (dotted black line) for clarity.

In this plot the empirical LCIS rates are found to have the most accurate fit to the full calculation when weighted by a factor of $1/4$. While this factor has arisen before in the calculation of electron-electron scattering rates (see Refs [50, 160]), there is not a concern with justifying the origin, especially in light of all the approximations made for these empirical e-e LCIS rates. The choice is then made to write the e-e rates as

$$W_{ee} = \frac{1}{4} (2W_{iif} + W_{iif} + W_{iif}) \quad (3.4.15)$$

simply as a fitting parameter. Using this approach the magnitude and shape of the electron-electron rates vs. the field between the intradoublet states are again, represented reasonably well.

While the rates for this specific example appear to be sufficiently approximated by the simplified empirical LCIS procedure the plots above only represented an example of a single system. As mentioned previously in Section 3.3 this technique of expressing the mean scattering rates between delocalized states as a linear combination of localized mean scattering rates cannot be expected to exactly reproduce the full calculation. Instead, its accuracy should be dependent on the internal form factors and how well these are reproduced by the LCIS form factor envelope. Since it was previously demonstrated that these functions are highly dependent on the wavefunction separation it is important to also check the above simulations in a different system. In particular, since the previous examples were between wells separated by a 50\AA barrier (which is towards the upper boundary of most THz-QCL's) a reexamination of this system is carried out using a 20\AA barrier (which is near the lower end of the typical barrier widths).

The first thing to compare is the localized vs. delocalized energies over the electric field range, shown in Figure 3.4.34. In this plot the energies are again approximately well by the expansion in the local basis. The energy separation of the $|1\rangle$ to $|4\rangle$ doublet can be seen to deviate slightly more in this system than in the previous (Figure 3.3.5) due to the thin barrier. Specifically, the abrupt jump in the energy separation on each side of the crossing does not follow the smooth behavior of the full simulation. This abnormality is likely due to the increased coupling with the other states (besides $|1\rangle$ and $|4\rangle$) which produces some additional perturbing effects even at larger energy separations due to the much larger \tilde{V} terms. While the overall magnitude of this

energy separation is not significantly changed this could have the effect of altering the symmetry of calculated properties on each side of the crossing field.

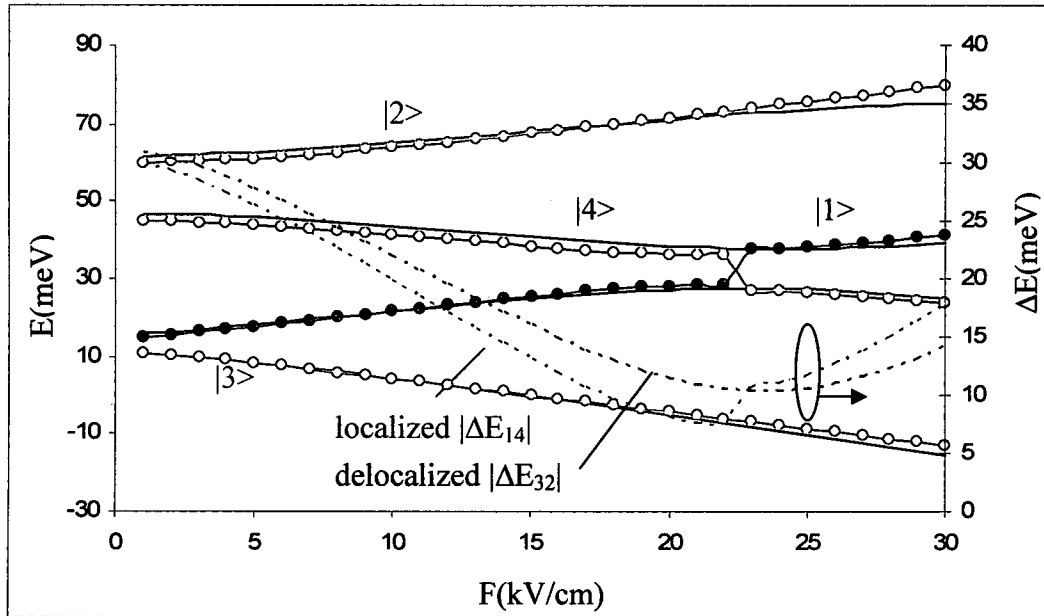


Figure 3.3.34: Comparison of the energies vs. the bias for two 155Å GaAs wells separated by a 20Å $\text{Al}_{0.15}\text{Ga}_{0.85}\text{As}$ barrier calculated using the full numerical approach (black lines) and the localized expansion (colored lines with circles). The energy separation for the right-ground to left-excited states in each picture is also plotted as dotted lines.

This asymmetry caused by the miscalculation of the energy separation in this tightly-bound doublet can be observed by comparing the LO-emission rates for this transition (Figure 3.3.35). In this plot the asymmetry of the LCIS rates around the crossing point is evident and displays the same effect as witnessed for the energies in Figure 3.3.34. The behavior and magnitude of the rates, compared to the full calculation, is still observed to be sufficiently reproduced.

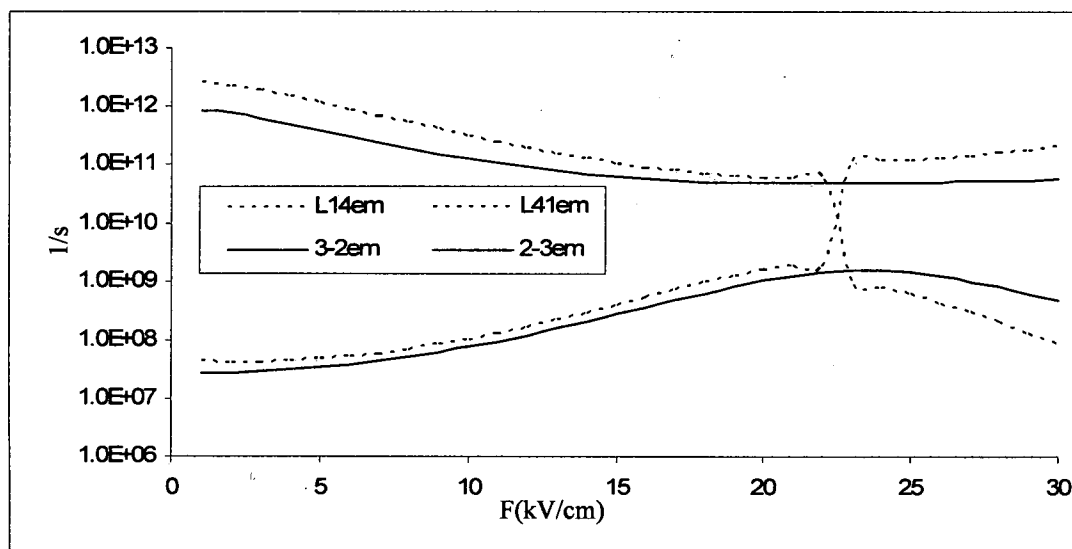


Figure 3.4.35: Comparison of the empirical LCIS predicted intradoublet emission rates (dotted lines) and the full numerical calculation (solid lines) for the 20Å barrier system.

This effect, presumably, should be most obvious for energy separations below the phonon resonance as this is the most highly energy dependent region. Consider the scattering rates from these doublet states to the ground state in the right well (Figure 3.4.36). For these transitions the asymmetry is not apparent as the energy separations are closer to a more stable rate vs. energy region. In this plot the rates vs. the field is again followed well by the LCIS method although there is a slightly more significant overestimation. The magnitude of the rates is still within a range which can be deemed as suitable, considering the computational simplifications permitted by this technique.

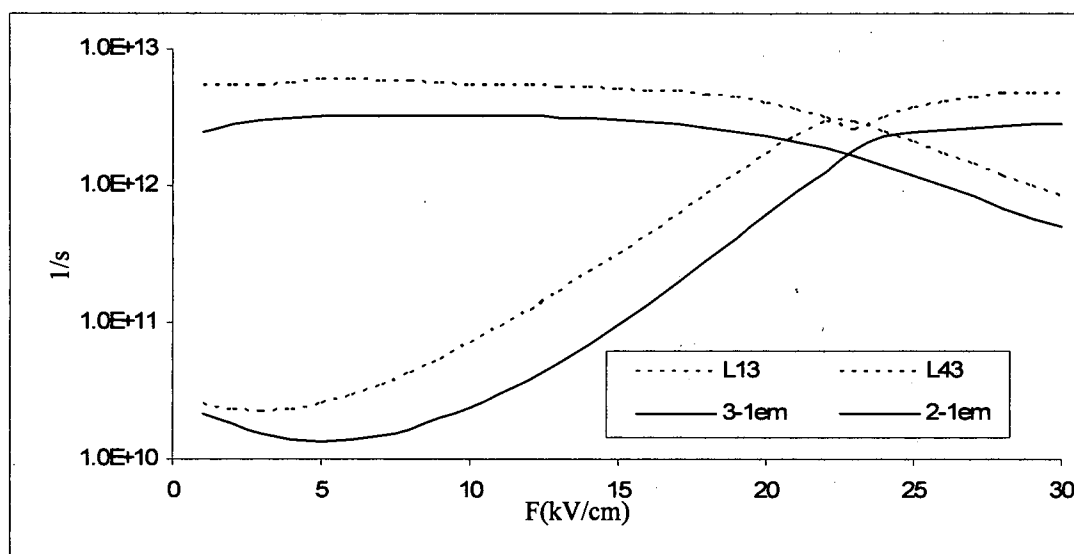


Figure 3.4.36: Comparison of the empirical LCIS predicted indirect emission rates (dotted lines) and the full numerical calculation (solid lines) for the 20Å barrier system.

The absorption rates for these two transitions are also plotted in Figures 3.4.37 and 3.4.38. In these figures the general behavior of the rates is again captured by the empirical LCIS method. Although there are more significant over (or under) estimations, compared to the 50Å barrier the predictions remain adequate. Comparison of the electron-electron rates for this system is also shown in Figure 3.4.39. Here the LCIS calculation shows some asymmetry and deviation from the full calculation in magnitude but not significantly more dramatic than in the larger barrier case.

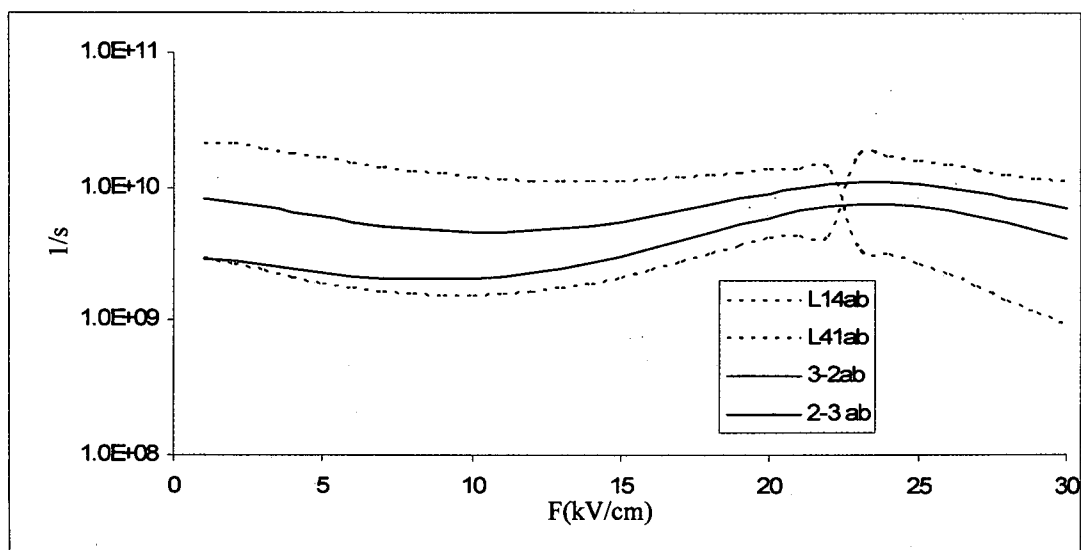


Figure 3.4.37: Comparison of the empirical LCIS predicted intradoublet absorption rates (dotted lines) and the full numerical calculation (solid lines) for the 20Å barrier system.

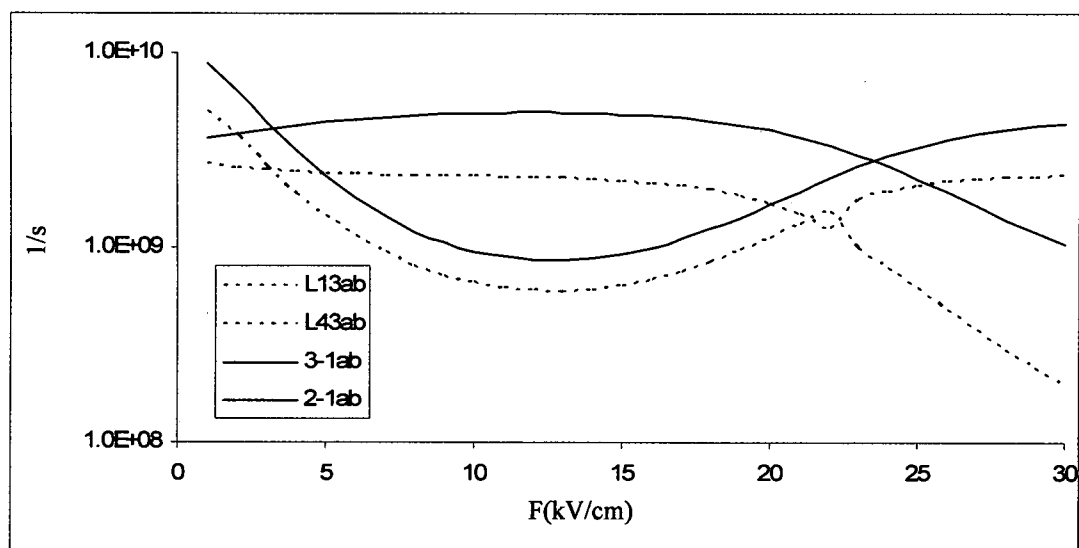


Figure 3.4.38: Comparison of the empirical LCIS predicted indirect absorption rates (dotted lines) and the full numerical calculation (solid lines) for the 20Å barrier system.

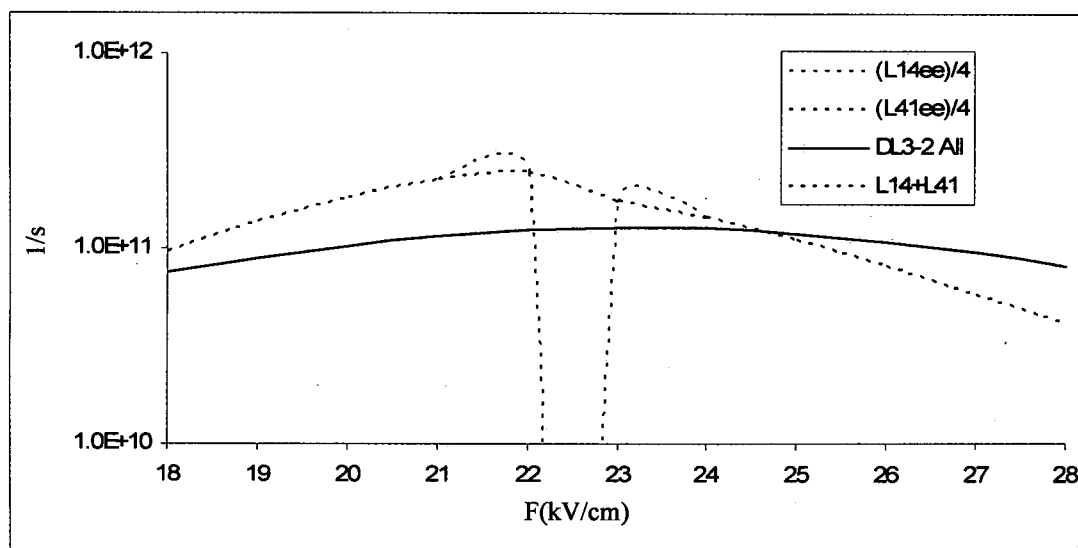


Figure 3.4.39: Comparison of the empirical LCIS predicted intradoublet electron-electron rates (dotted lines) and the full numerical calculation (solid lines) for the 20Å barrier system.

In this chapter the general methods for the calculation of electron-LO-phonon scattering and electron-scattering were introduced. The heterostructure effects on the phonon modes was investigated and determined to be of little importance for the low Al barrier compositions to be considered in later chapters. If higher Al composition systems needed to be modeled a simple technique using combinations of bulk-GaAs and bulk-AlAs modes was presented and demonstrated to be more suitable than the bulk-GaAs approximation without adding significant computational complexity.

Using the localized basis functions and tight-binding coupling parameters from Chapter 2 a method was presented to expand Fermi's Golden Rule into this local basis. Additionally, the assumption that coupled-well wavefunction mean-scattering rates can be directly written in terms of intrawell basis scattering rates was shown to be a suitable approximation which very closely predicts the behavior of the fully calculated rates vs. a

bias. This approximation was then shown to permit the enormous computational advantage of having all scattering rates described by single-well transitions between basis wavefunctions which do not change with an externally applied field. To exploit this important fact empirical fitting functions were used to create simple tabulated coefficient values which permit these basis scattering rates to be quickly evaluated for any arbitrary energy separation, lattice temperature, and electron temperature. These fitting functions were then used to compare the general empirical LCIS technique to full numerical scattering calculations and were shown to predict the rates surprisingly well.

Most importantly, this empirical LCIS method of describing the scattering rates in arbitrary heterostructure, combined with the analytical single-well basis techniques outlined in Chapter 2, has created a computational procedure where all properties discussed to this point (energies, wavefunctions, scattering rates) can be determined nearly instantaneously using pre-simplified analytical tight-binding expressions, empirical fitting functions, and require only the designation of the interface locations for evaluation.

CHAPTER 4

TRANSPORT IN QUANTUM HETEROSTRUCTURES

4.1 Introduction

Accumulating the results from the previous chapters the primary objective of the calculation of transport can now be commenced. First, a description of semiclassical transport using the laser rate equations will be presented in the context of the full numerical simulation. Using the single well basis, the analytical tight-binding coupling parameters, the expansion of the scattering rates in the local basis, and the empirical scattering rate fitting functions, an analogous semiclassical simulation will be presented and compared to the full computation. The tremendous computational advantage of the methods outlined in the previous chapters is illustrated. Questions regarding the validity of these semiclassical models will be introduced and treated in detail with the time-dependent Density Matrix Formalism. A simplification of this model will then be presented where the steady-state density matrix elements can be reformulated from an $N^2 \times N^2$ system back to an $N \times N$ problem resembling the laser rate equations while maintaining a description of coherence and dephasing. Aspects concerning the most suitable implementation of this simplified model to the simulation of transport and gain in THz-QCLs are analyzed. A description of gain is then given where, unlike the semiclassical models, dephasing plays a critical role in higher temperature operation. The

simplified treatment of transport outlined in this chapter permits accessible and analytical solutions for subband populations, current densities, and gain with all necessary elements needed for evaluation presented as empirical multi-parameter fitting functions or pre-evaluated integrals requiring only the description of the heterostructure and the designation of the temperature.

4.2 Semiclassical Transport

Semiclassical descriptions of transport imply static, time-independent, states. An example of this portrayal of transport is the familiar laser rate equations. Consider a generic system of N states (Figure 4.2.1).

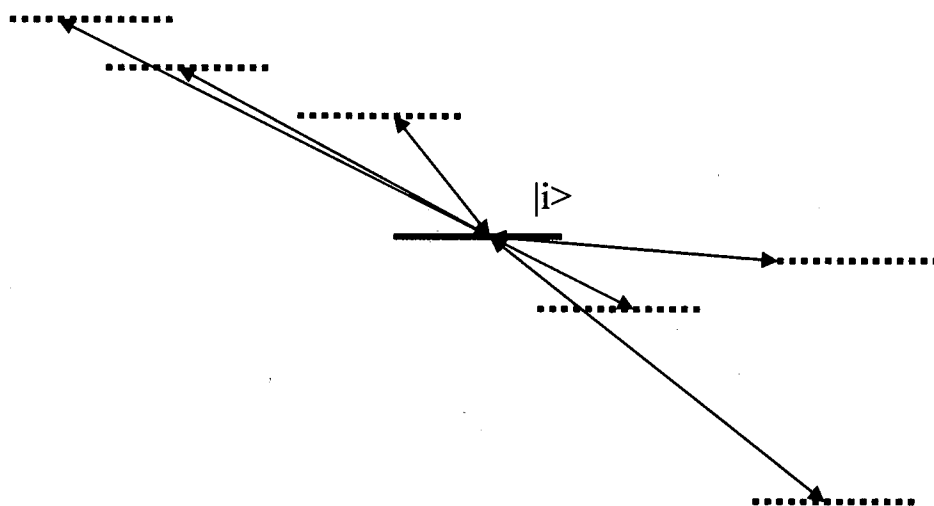


Figure 4.2.1: A generic collection of states depicting the standard rate equation model.

The rate of change of the population in a state $|i\rangle$ is simply

$$\frac{\partial}{\partial t} n_i = \sum_{f=1}^N (n_f W_{fi} - n_i W_{if}) \quad (4.2.1)$$

In the steady-state the population is then

$$n_i = \frac{\sum_{f=1}^N (n_f W_{fi})}{\sum_{f=1}^N (W_{if})} \quad (4.2.2)$$

As discussed in previous chapters, the true nature of the one-dimensionally confined subbands allows for in-plane dispersion and thus a full treatment of semiclassical transport would involve the treatment of all transitions between states $|i, k_i\rangle$ and $|f, k_f\rangle$ (Figure 4.2.2).

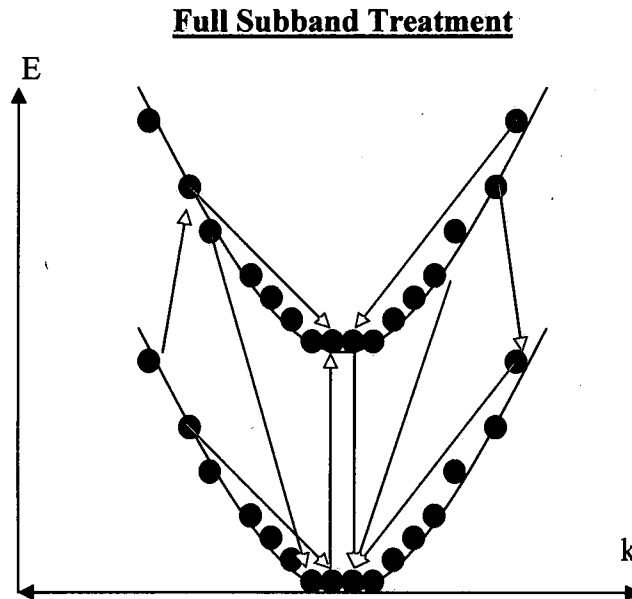


Figure 4.2.2: Full 2-dimensional nature of the subbands and the transport.

This full 2D nature of the subbands is treated using the semiclassical Monte-Carlo methods [93-101]. Clearly any manner of discretization of the k-space ensures an enormous computational burden. Fortunately, the definition of mean subband scattering rates, such as used in the QCL rate equation models [80-88], allows for the treatment of

the subbands as singular objects as represented in Figure 4.2.1. Within this framework the remainder of this discussion will be carried out.

First, consider a 150Å well/50Å barrier GaAs/Al_{0.15}Ga_{0.85}As superlattice shown in Figure 4.2.3. at F=6kV/cm. The states in this figure are numerically calculated using the full system Hamiltonian and are therefore unconstrained in the amount of delocalization of the wavefunctions.

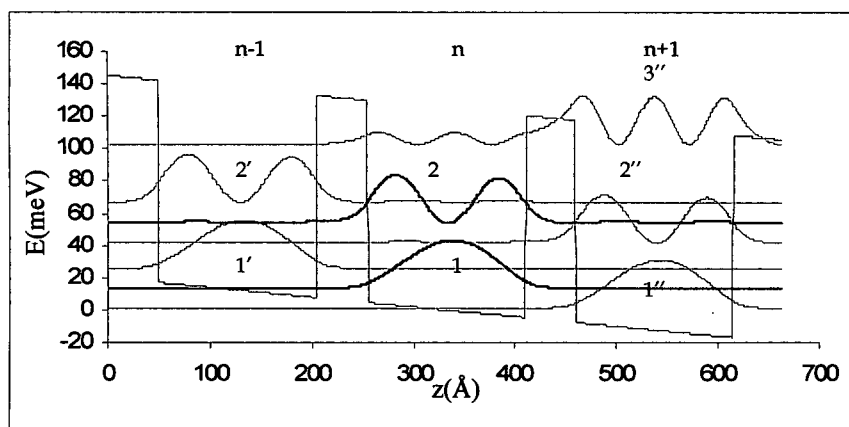


Figure 4.2.3: 3-periods of a 150Å well/50Å barrier GaAs/Al_{0.15}Ga_{0.85}As superlattice calculated using the full numerical simulation at F=6kV/cm.

To evaluate a repeating system such as the described superlattice only evaluation of the scattering rates for a single well is necessary, due to its duplicate nature. To accomplish this, the system is limited to three periods of an assumed infinitely repeating structure with the assumption that a calculation of the central period (well) is sufficient. A potential difficulty which arises for implementing this approach in the full numerical simulation occurs due to the ordering of the eigenvalues. Due to the anticrossing nature of the delocalized states the designation of which eigenstate “belongs” to which well changes with the bias. While numerical procedures, such as a well by well integration,

could be implemented to establish the location of the dominant portion of the wavefunction, a visual inspection at each bias will suffice.

Consider first the energies vs. the electric field bias shown in Figure 4.2.4. In this plot the normal ordered designation of the energies is depicted using full black lines. It is clear that these lines portray the anticrossing of energies. Using a visual inspection of the wavefunctions a designation of which energy corresponds to which well is made (depicted using the open and closed points). Here the full blue and red circles correspond to the ground and excited states in the central well, respectively. The open blue and open red circles correspond also to the neighboring ground and first excited states. The green points represent the 3rd excited state (3'').

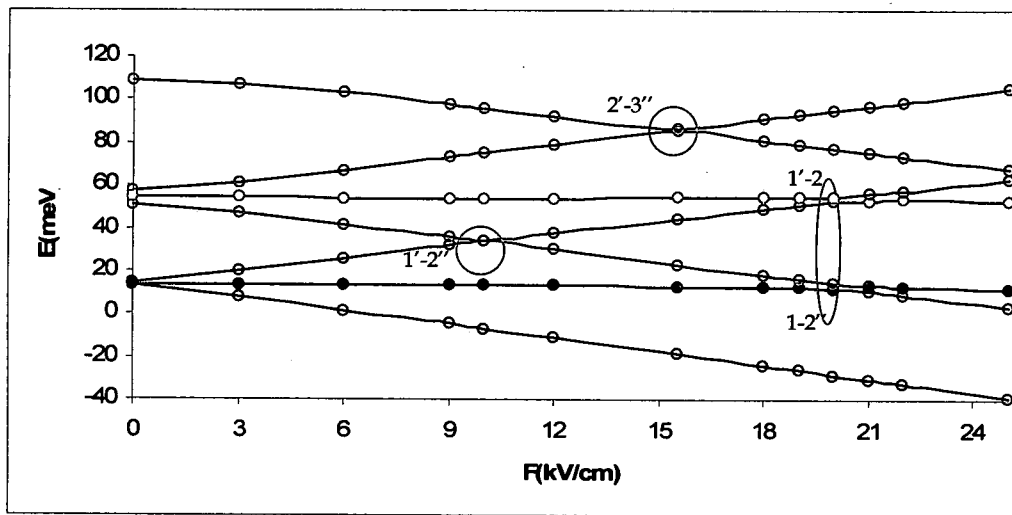


Figure 4.2.4: Energies vs. electric field bias for the full numerical simulation of the 150/50 GaAs/Al_{0.15}Ga_{0.85}As superlattice.

The grey circles in figure 4.2.4 point out some relevant anticrossings that need further consideration. The first point of interest occurs at approximately 10kV/cm where the state with the fixed label (1') crosses/anticrosses with state (2'') as shown in

Figure 4.2.5. At this bias it appears as though the ground state ($1'$) couples to state ($2''$). The assumption then must be made that if more than a 3 period system was chosen that couplings from a state 1 to another well state $2'''$ in well ($n+2$) is possible.

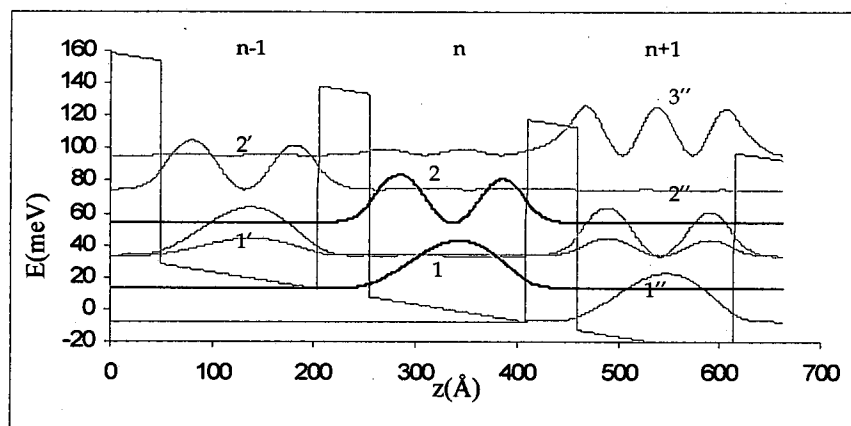


Figure 4.2.5: 3-periods of a 150Å well/50Å barrier GaAs/ $\text{Al}_{0.15}\text{Ga}_{0.85}\text{As}$ superlattice calculated using the full numerical simulation at $F=10\text{kV/cm}$.

This observation suggests that calculating rates from/to only the central well will be inadequate. The three period system can still be used it just requires that the lifetime of state states in the central well (n) also includes well ($n-1$) to well ($n+1$) transitions. A similar situation occurs at $\sim 15.5\text{kV/cm}$ (shown in Figure 4.2.6). In this another coupling from well ($n-1$) to well ($n+1$) is observed. This time the excited state ($2'$) couples with a state ($3''$) which is visibly above the barrier to its immediate right. This state can therefore be considered a “quasi-continuum” state. Again, due to the repeating nature of the system, if state ($2'$) in well ($n-1$) experiences this type of a coupling then so must state (2) in well (n) and all other identical excited states throughout the structure.

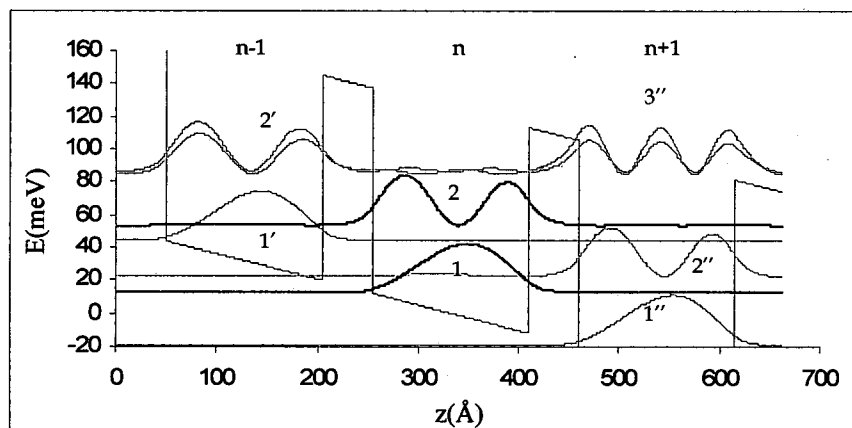


Figure 4.2.6: 3-periods of a 150Å well/50Å barrier GaAs/Al_{0.15}Ga_{0.85}As superlattice calculated using the full numerical simulation at $F=15.5\text{kV/cm}$.

The last, and primary, resonance to consider is the alignment of the nearest neighbor ground-to-excited states. This is the 1' to 2 or redundantly, the 1 to 2'' coupling shown below in Figure 4.2.7 at a field of 21kV/cm

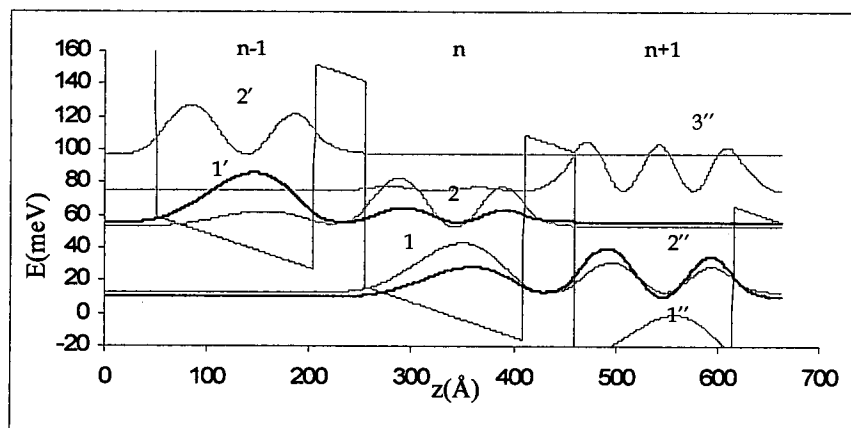


Figure 4.2.7: 3-periods of a 150Å well/50Å barrier GaAs/Al_{0.15}Ga_{0.85}As superlattice calculated using the full numerical simulation at $F=15.5\text{kV/cm}$.

Calculation of the scattering rates based on these full wavefunctions can now be carried out. As noticed above, it is necessary to include the 2nd nearest neighbor rates. To execute this the lifetimes of the ground and excited states can be written as

$$(\tau_s^n)^{-1} = \sum_{m=n-1}^{m=n+1} \sum_j W_{sj}^{nm} + \sum_a W_{sa}^{n-1n+1} + \sum_b W_{sb}^{n+1n-1} \quad (4.2.3)$$

To calculate the current flow the insertion of an arbitrary interface, naturally chosen as the barrier between well (n-1) and well (n), is used as shown in Figure 4.2.8.

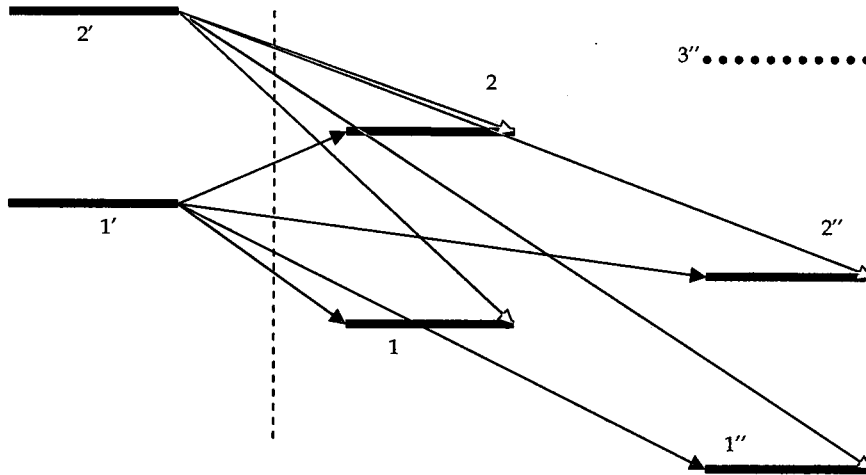


Figure 4.2.8: Figure displaying the interface and forward current flow for the superlattice calculation.

The “quasi-continuum” state (3'') in this treatment will not be given the same status as the ground and excited states in each well. In the full numerical calculation its potential to interfere with the other states cannot be avoided but at the same time it should not be considered as a bound state as it is clearly above the confining wells at the bias shown in Figure 4.2.6. Since any electron transferring into this state is certainly coupled to the

continuum it is assumed, in an ad hoc manner, that the population does not rest in these states and is thus recycled back into the confined states in later periods. This is assumed to keep the total population fixed in the bound states and, as a consequence, no description of parasitic current through the continuum is considered.

The current is then calculated using the expression

$$J = q \sum_i \sum_{w=n}^{n+1} \sum_s (n_i^{n-1} W_{is}^{n-1w} - n_s^w W_{si}^{wn-1}) \quad (4.2.3)$$

which simply states the flow from well (n-1) in the right direction minus the backwards flow.

$$\begin{aligned} n_1 (W_{1'2''} + W_{1'2'} + W_{12} + W_{1''2} + W_{1''2'}) - n_2 (W_{2''1'} + W_{2'1'} + W_{21} + W_{21''} + W_{21''}) &= 0 \\ n_2 (W_{2'1''} + W_{2'1'} + W_{21} + W_{2''1} + W_{2''1'}) - n_1 (W_{1''2'} + W_{12'} + W_{12} + W_{12''} + W_{1'2''}) &= 0 \end{aligned} \quad (4.2.4)$$

This can be presented in a matrix form including the condition that these two states must contain the per-period sheet density

$$\begin{bmatrix} -(W_{1''2'} + W_{12'} + W_{12} + W_{12''} + W_{1'2''}) & (W_{2'1''} + W_{2'1'} + W_{21} + W_{2''1} + W_{2''1'}) & 0 \\ (W_{1'2''} + W_{1''2'} + W_{12} + W_{12'} + W_{1''2}) & -(W_{2''1'} + W_{2''1} + W_{21} + W_{2'1'} + W_{2'1''}) & 0 \\ 1 & 1 & N_s \end{bmatrix} \quad (4.2.5)$$

The solutions for this system are

$$\begin{aligned} n_1 &= N_s \frac{W_{2'1''} + W_{2'1'} + W_{21} + W_{2''1} + W_{2''1'}}{(W_{2'1''} + W_{2'1'} + W_{21} + W_{2''1} + W_{2''1'}) + (W_{1''2'} + W_{12'} + W_{12} + W_{12''} + W_{1'2''})} \\ n_2 &= N_s \frac{W_{1''2'} + W_{12'} + W_{12} + W_{12''} + W_{1'2''}}{(W_{2'1''} + W_{2'1'} + W_{21} + W_{2''1} + W_{2''1'}) + (W_{1''2'} + W_{12'} + W_{12} + W_{12''} + W_{1'2''})} \end{aligned} \quad (4.2.6)$$

The numerical implementation of these equations can be simplified considerably by recognizing that many of the transitions are identical due to the repetition of the system. Even after identifying many identical rates, such as $W_{2'1''} = W_{2'1'}$, this simulation requires the calculation of 18 emission, 18 absorption, and 189 electron-electron transitions taking approximately 20 minutes per bias point to evaluate on a standard

personal computer. In the following calculation 11 bias points were chosen resulting in a computational time of approximately 4 hours. The results, using $T_e = T = 77\text{K}$ and a sheet density of $1 \times 10^{10} \text{cm}^{-2}$ are displayed in Figure 4.2.9.

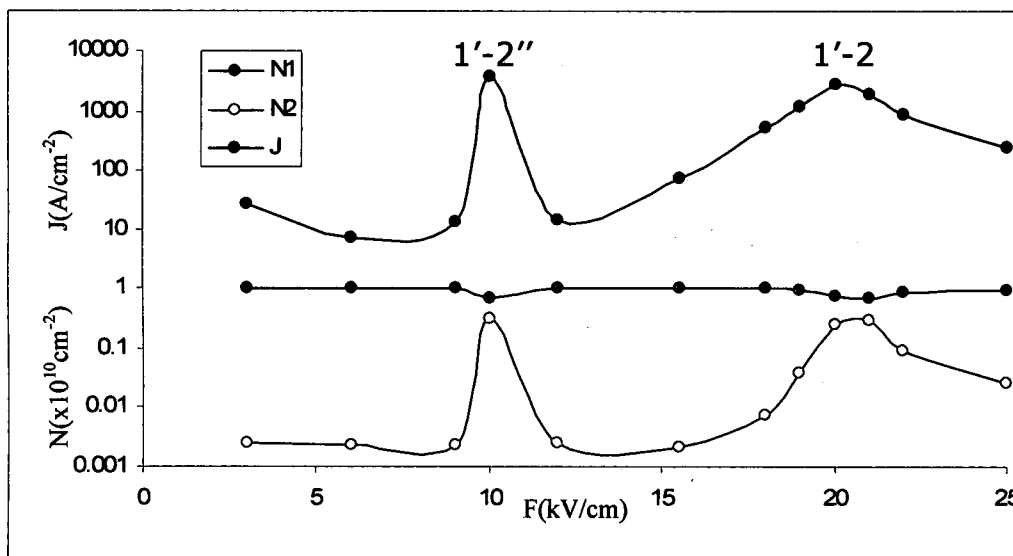


Figure 4.2.9: Current density and subband populations vs. the bias for the 150/50 GaAs/ $\text{Al}_{0.15}\text{Ga}_{0.85}\text{As}$ superlattice calculated at $T_e = T = 77\text{K}$ and assuming a total sheet density of $1 \times 10^{10} \text{cm}^{-2}$.

In this simulation the 2nd nearest neighbor coupling from $1' \rightarrow 2''$ is shown to display a very large current spike at approximately 10kV/cm. While these types of transitions are not outright forbidden, the magnitude of this predicted current being larger than the primary $1'-2$ resonances is highly questionable and is not observed at these magnitudes in experimental results [117]. This unrealistic spike is not witnessed at the other debatable crossing ($2'-3''$) at 15.5kV/cm. This can be explained by observing the subband populations. Examination of the populations near the $1'-2''$ current spike at

10kV/cm shows a slight reduction of the ground state yet there remains a significant concentration which results in the large current density (i.e. $J \propto nW$). At 15.5kV/cm, where $2'$ crossed with $3''$ the population of the excited state is near zero and thus no large current spike is observed even if an unrealistic scattering channel is permitted. The solution to deal with these spikes is often to observe the results, declare them improbable, and remove them from the plot. If the biases near 10kV/cm are ignored the resulting current is observed to rise in a fairly smooth manner to the $1'-2$ resonance where it reaches a peak and then is reduced. This post-resonance reduction is the negative differential resistance (NDR) region of the device.

The removal of suspected unlikely features in the predicted current, while satisfactory for producing results which appear more like those observed experimentally, is inadequate for inclusion in optimization or solution seeking algorithms which require a more "hands off" approach. A potential automatic correction could be implemented by realizing that the anti-crossing gaps are very small, and narrow vs. the field, for these "unrealistic couplings" and insertion of some threshold "energy gap" could be employed to ignore certain transitions. Consider the system at the 10 kV bias (Figure 4.2.5). If $1'$ and $2''$ were below some threshold energy gap we could ignore scattering from $1'-2''$ and even make some automatic decision to ignore $1'$ to the $1''$ or other extended interactions. This delocalization though also effects the more local scattering ($2'$ to $1'$) due to the change in the wavefunction normalization. The only solution for the full numerical simulation, if certain wavefunction delocalization is declared unreasonable, is to entirely skip over these troublesome biases.

This problem is easily corrected using the localized single-well basis (Chapter 2) and the LCIS method (Chapter 3). In this procedure the wavefunction delocalization is entirely controlled by the coupling coefficients. The previous discussions of this approach assumed nearest neighbor wavefunction coupling which, in turn, permits 2nd nearest neighbor scattering, although only through an intermediate well. In this description the states of the previously simulated 150/50 GaAs/Al_{0.15}Ga_{0.85}As superlattice are designated as shown in Figure 4.2.10. The energies vs. the bias are shown in Figure 4.2.11.

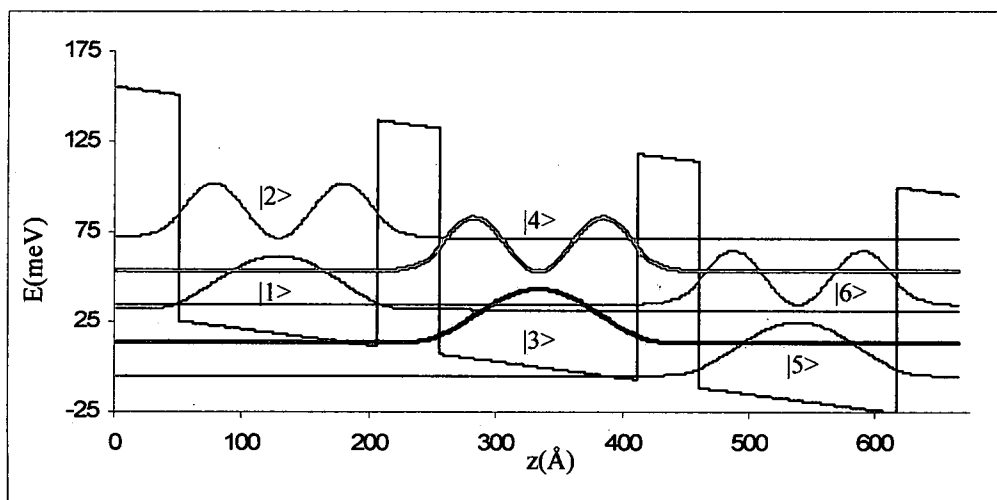


Figure 4.2.10: 3-periods of a 150Å well/50Å barrier GaAs/Al_{0.15}Ga_{0.85}As superlattice calculated using the localized basis.

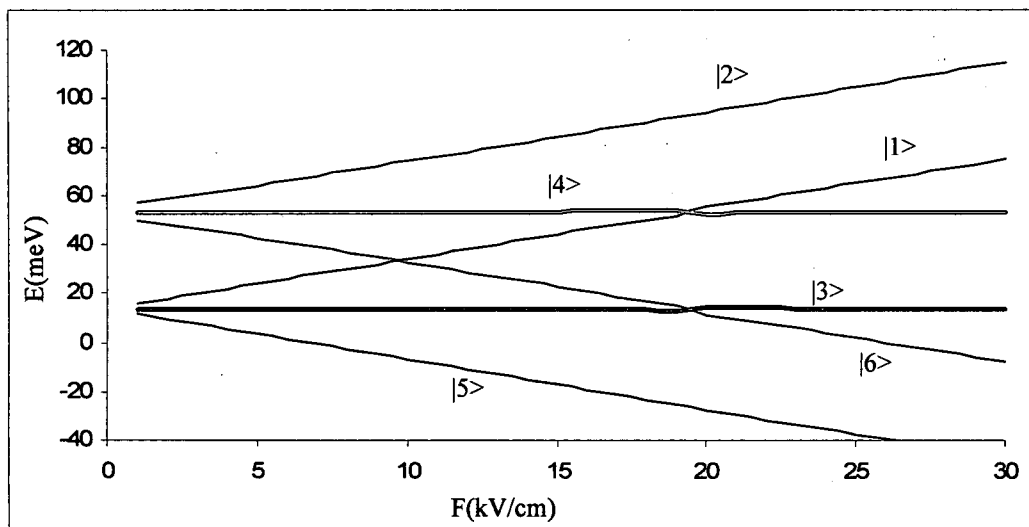


Figure 4.2.11: Energies vs. the field for a 150/50 barrier GaAs/ $\text{Al}_{0.15}\text{Ga}_{0.85}\text{As}$ superlattice calculated using the tight-binding expansion of the localized basis.

Before moving on to transport simulations consider first another key advantage of the localized basis expansion which can be exploited for a general repeating period system. In Figure 4.2.11 and in the full simulation Figure 4.2.4 it can be noticed that while the central period states display crossing/anticrossing behavior the states in the outer periods are unaffected. The lowest energy state in each of these plots can be observed to move linearly with the field while its central period counterpart is shifted near the 20kV/cm bias. In the traditional numerical simulation the choice is often made to analyze 3-periods of a given system and assume that the central period is the most accurate representation of the repeating system. This procedure is used because the full Hamiltonian of the given system is bounded on both ends and thus a state near either end (left-or-right) will not experience the exact same couplings compared to its alleged identical state in a more central period. In the LCIS method, since scattering is at most 2nd nearest neighbor, the addition of two additional wells on each end of the defined

system can be implemented. While these additional wells are truly only needed on one side, again due to the repetition, including them on both sides is more intuitive (Figure 4.2.12).

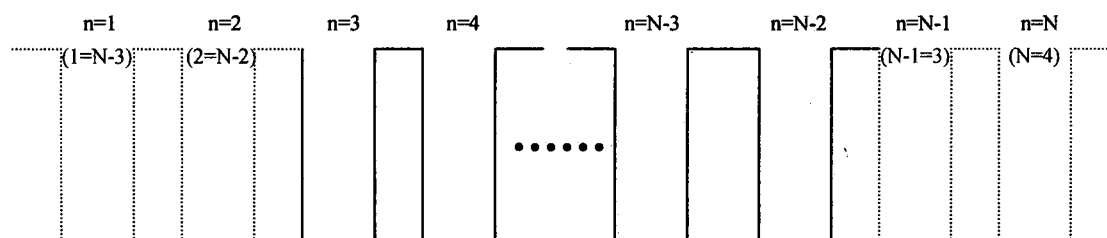


Figure 4.2.12: Diagram showing the simple implementation of repeating boundary conditions using the LCIS technique.

In this Figure the system is presented for a general repeating device containing $N-4$ wells per period. In this procedure the last two wells of the defined period are copied to the front, and the first two at the end. Perturbing interactions (i.e. \tilde{V} terms) can then be calculated for the central period and applied consistently to the outer states ensuring actual repetition of the system. For example, consider the repeating superlattice structure previously evaluated. Applying the repeating conditions for all properties produces the consistent behavior shown in Figure 4.2.13

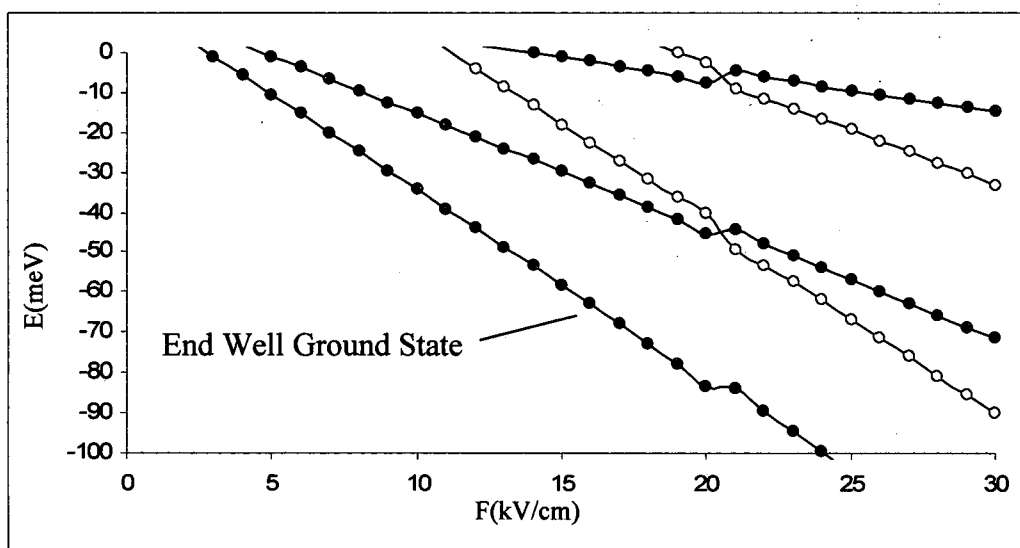


Figure 4.2.13: 150/30 barrier GaAs/ $\text{Al}_{0.15}\text{Ga}_{0.85}\text{As}$ superlattice calculated using the localized basis expansion with the application of the repeating period conditions.

In this example a 30\AA barrier was chosen to make the repelling effect more obvious. In this figure the end well ground state, which has no apparent coupling to another excited state on its right, is given the proper repelling perturbation automatically. Beyond just creating the proper and consistent energies the wavefunctions and hence, the scattering rates can also be made to ensure actual repetition. In this example, near the crossing bias, the end well ground state would have non-normalized wavefunction coefficients because a portion of it is assumed to be coupled to other states not depicted by the truncated system. These true repeating effects cannot be readily implemented in the standard full numerical evaluations of Schrödinger's equation.

For the calculation of transport using this LCIS method, with the fixed state designation as shown in Figure 4.2.10, the steady-state populations for the states in the middle well are

$$n_3 = N_s \frac{W_{25} + W_{23} + W_{43} + W_{63} + W_{61}}{(W_{25} + W_{23} + W_{43} + W_{63} + W_{61}) + (W_{52} + W_{32} + W_{34} + W_{36} + W_{16})} \quad (4.2.7)$$

$$n_4 = N_s \frac{W_{52} + W_{32} + W_{34} + W_{36} + W_{16}}{(W_{25} + W_{23} + W_{43} + W_{63} + W_{61}) + (W_{52} + W_{32} + W_{34} + W_{36} + W_{16})}$$

The current, as defined previously Equation 4.2.3, is

$$J = qN_s n_3 (W_{13} + W_{14} + W_{15} + W_{16}) + n_4 (W_{23} + W_{24} + W_{25} + W_{26}) - n_3 (W_{31} + W_{32} + W_{51} + W_{52}) - n_4 (W_{41} + W_{42} + W_{61} + W_{62}) \quad (4.2.8)$$

This method is then directly compared to the full numerical simulation in Figure 4.2.14.

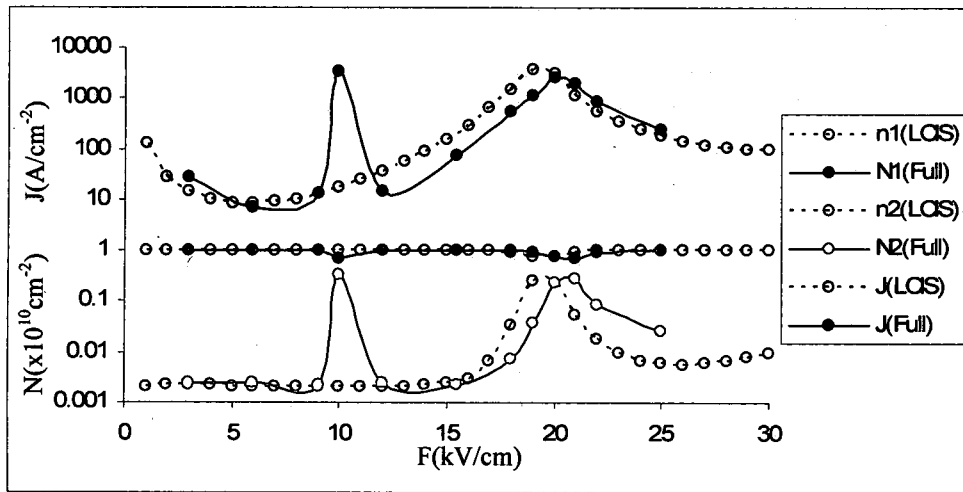


Figure 4.2.14: Current density and subband populations vs. the bias for the 150/50 GaAs/Al_{0.15}Ga_{0.85}As superlattice calculated at $T_e = T = 77K$ and assuming a total sheet density of $1 \times 10^{10} \text{ cm}^{-2}$ using both the full simulation (solid lines and points) and the LCIS method (dotted lines with open points).

The agreement between the two simulations is quite remarkable considering the full calculation took approximately 4 hours to evaluate while the LCIS took less than 1 second. To put this into perspective the full simulation calculated 36 electron-phonon rates and 189 electron-electron rates at each bias point for a total of 2275 different rates.

In the LCIS technique 48 coefficients were previously found (Table 3.4.1 and Table 3.4.2) for the calculation of LO phonon emission rates for any lattice and electron temperature. Once the temperatures are input and combined with the nearly instantaneously generated energies and coupling coefficient values, the emission rates are immediately produced through the fitting functions of Section 3.4. The absorption rates are then generated using the 4 coefficients of Table 3.4.4 and the emission-to-absorption ratio fitting function. The LCIS electron-electron rates are also fit using 4 coefficients (table 3.4.5) and calculated for only 3 types of interactions (ii-ff, ii-fi, and if-ff) compared to the 189 permutations in the full simulation. In addition, since there is control over the amount of wavefunction delocalization, in this case nearest neighbor, there is no need to worry about potential unrealistic current spikes. This demonstration of the LCIS technique being able to represent the full numerical, semiclassical, simulation with excellent agreement and virtually zero computational time is extraordinary. While this capability to simulate structures in a nearly real-time manner using the rate equation model is significant, the actual predictive value of this type of semiclassical approach needs to be further scrutinized.

Now that the ability of the LCIS technique to reproduce the full numerical simulation is established this procedure can be used to quickly examine varying multiple design aspects of a structure without the need of waiting several days or employing supercomputer and/or parallel computing systems. Take the previous 155Å superlattice as an example. Using the LCIS procedure the current can be simulated for a variety of barrier widths as shown in Figure 4.2.15:

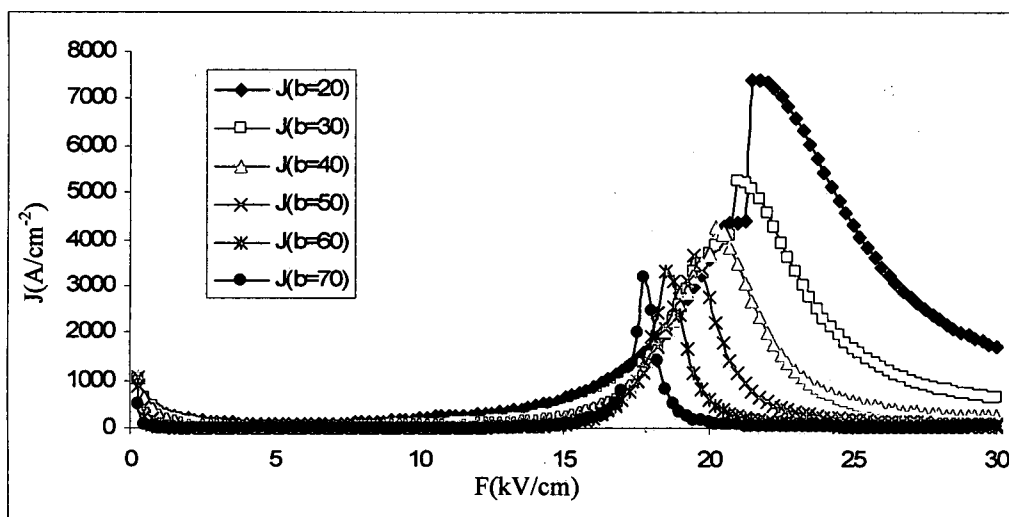


Figure 4.2.15: LCIS current density calculations for a 150/b GaAs/Al_{0.15}Ga_{0.85}As superlattice system with various barrier widths.

Here, as noticed in the previous chapter (Figure 3.4.35) there is a significant asymmetry around the resonance peak for the thinner barriers. This effect is likely exaggerated for this chosen well width as the intrawell energy separation is close to the phonon resonance. As a result the strong delocalization of the ground state to the excited state in the next well may experience scattering below the phonon peak on one side of the resonance and above on the other. This asymmetry is less noticeable at the thicker barriers as the delocalization is narrow with the field and has a much smaller repelling gap. Consider the peak current density on the low side of this asymmetry, where the NDR is first observed. This comparison is shown in Figure 4.2.16

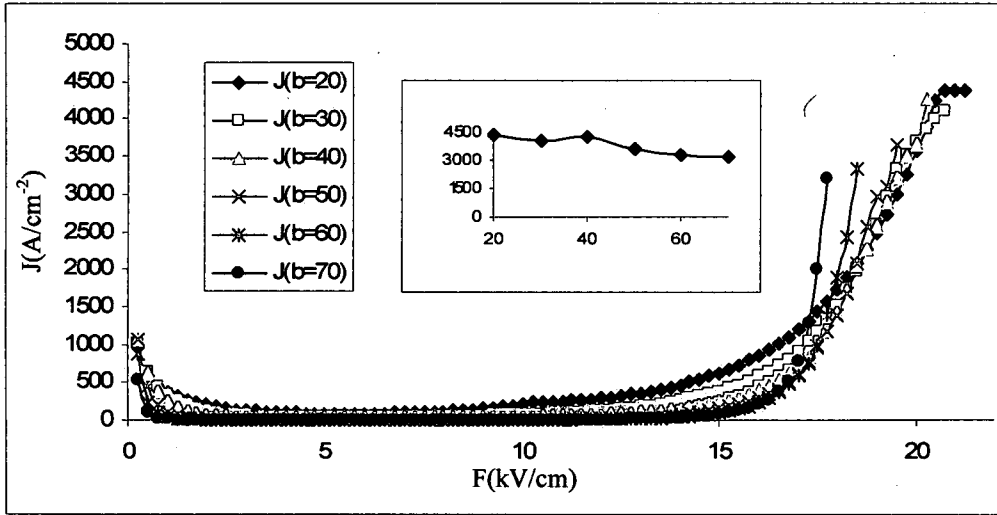


Figure 4.2.16: LCIS current density calculations for a 150/b GaAs/Al_{0.15}Ga_{0.85}As superlattice system with various barrier widths stopped at the resonance peak (the start of the NDR region). In the inset is this peak current density vs. the barrier width.

In this plot, and in the inset which shows this peak current density vs. the barrier width it is observed that, although there appears to be some decay, there is not a dramatic reduction of the current with the increasing barrier width.

Returning to a discussion first mentioned in Chapter 1, there will always be a bias that will couple the 2-states on each side of the barrier. Thus in the full calculation or in the LCIS method this will produce the maximum coupling of the two states. If all couplings except for the states which produce the “doublet” are neglected this would result in there always being an applied field such that

$$\begin{aligned}
 |\psi_A|^2 &= \frac{1}{2}|\Psi_A|^2 + \frac{1}{2}|\Psi_B|^2 \\
 |\psi_B|^2 &= \frac{1}{2}|\Psi_A|^2 + \frac{1}{2}|\Psi_B|^2
 \end{aligned}
 \tag{4.2.9}$$

where A and B are the two states on either side of the barrier. Of course, in the full treatment of all scattering events the change in the barrier produces a change in energy and thus some change in the current flow. In Figure 4.2.16 there does seem to be a drop as the barrier is changed from 20Å to 70Å from about 4000A/cm² to 3000 A/cm² yet, as will be discussed in the next section, this is much less than is considered reasonable.

The numerical simulations, using either the full approach or the LCIS method, have several complicating factors to consider in studying the varying barrier problem: energy dependent intradoublet scattering, energy dependent indirect scattering, and a difficulty in numerically locating the peak resonance at larger barrier widths. To make things easier consider a simple analytical approach for a two state per well superlattice biased at the ground-to-excited resonance (Figure 4.2.17).

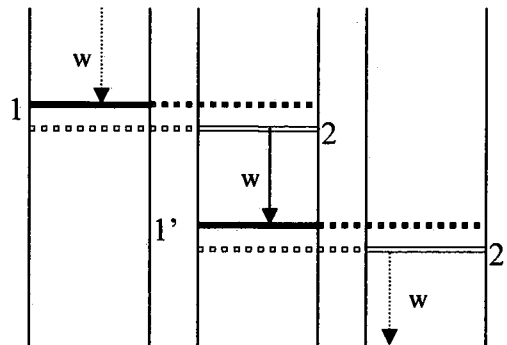


Figure 4.2.17: Diagram of a generic superlattice system biased at resonance.

Although any number of periods of the superlattice could be used it is truly only necessary to consider two consecutive doublets. Obviously in the superlattice pictured above $|1'\rangle = |1\rangle$ and $|2'\rangle = |2\rangle$. In the LCIS picture, assuming that the only relevant scattering rate (w) is between the excited and ground states in each well, the localized localized scattering can be written as

$$w = \begin{bmatrix} 0 & 0 \\ w & 0 \end{bmatrix} \quad (4.2.10)$$

where of course the only rate is the $|2\rangle$ to $|1'\rangle$. As was shown before in Chapter 3 the assumption is made that the local mean rate matrix elements are

$$m = \begin{bmatrix} 0 & 0 \\ \sqrt{w} & 0 \end{bmatrix} \quad (4.2.11)$$

At resonance the new, delocalized, wavefunctions are equally spread across the two wells thus the coefficients are

$$|b| = \begin{bmatrix} \frac{1}{\sqrt{2}} & \frac{1}{\sqrt{2}} \\ \frac{1}{\sqrt{2}} & \frac{1}{\sqrt{2}} \end{bmatrix} \quad (4.2.12)$$

The new matrix elements for the coupled well system can be found from

$$M = bmb^T \quad (4.2.13)$$

The delocalized scattering is then the square of each element

$$W = M^2 = \begin{bmatrix} \frac{w}{4} & \frac{w}{4} \\ \frac{w}{4} & \frac{w}{4} \end{bmatrix} \quad (4.2.14)$$

Now these values of $1/4w$ for the component rates make perfect sense by inspecting the two doublets in the delocalized scattering picture (Figure 4.2.18).

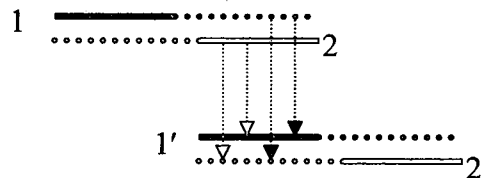


Figure 4.2.18: Delocalized scattering components in a resonantly biased superlattice.

In this case the doublet state (1) now is $\frac{1}{2}$ like the localized state $|1\rangle$ and $\frac{1}{2}$ like the localized state $|2\rangle$. The lower doublet expands in the same manner. The rate then from state (1) to state (1') is then $\frac{1}{4}$ the value of the localized $|2\rangle$ to $|1'\rangle$ rate. Of course now, there are 4 components to the total interdoublet current flow

$$\begin{aligned}
 J &= q(n_1 W_{11'} + n_1 W_{12'} + n_2 W_{21'} + n_2 W_{22'}) \\
 &= q\left(n_1 \frac{w}{4} + n_1 \frac{w}{4} + n_2 \frac{w}{4} + n_2 \frac{w}{4}\right) \\
 &= q2(n_1 + n_2) \frac{w}{4}
 \end{aligned} \tag{4.3.15}$$

Since the populations of n_1 and n_2 combine to give the per period sheet density N_s the current is then

$$J = \frac{qN_s}{2} w \tag{4.2.16}$$

It then becomes obvious in this simplified scenario, if the states are biased to a resonance condition, the resulting current will always be the same regardless of the barrier width. Additionally, due to the symmetry of the scattering rates and the fact that the $W_{11'}$ and $W_{22'}$ do not contribute to the change in population, the steady state rate equation matrix is simply

$$N = \begin{bmatrix} -\frac{w}{4} & \frac{w}{4} & 0 \\ \frac{w}{4} & -\frac{w}{4} & 0 \\ 1 & 1 & N_s \end{bmatrix} \tag{4.2.17}$$

which gives the obvious solution

$$N = \begin{bmatrix} 1 & 0 & \frac{1}{2}N_s \\ 0 & 1 & \frac{1}{2}N_s \\ 0 & 0 & 0 \end{bmatrix} \quad (4.2.18)$$

The population at resonance in this case is equally distributed in the two doublet states. This will be referred to throughout the remainder of this discussion as a "pure doublet".

In the above definition of the current it was taken to be everything flowing from the upper to the lower doublet. In the earlier examples the current flow was defined as electrons crossing an artificial interface. It can easily be shown that the current defined in either manner is equivalent. This is easily illustrated in Figure 4.2.19.

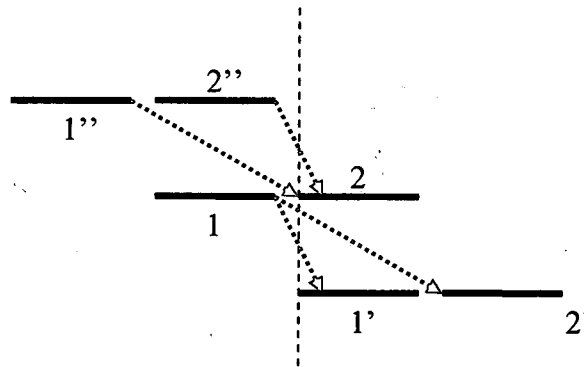


Figure 4.2.19: Description of current flow across an arbitrary interface for a superlattice system.

Here it is fairly obvious that the same 4 scattering components as derived previously will define the current flow. In the interface picture however, the nature of the current flow is not as intuitive. Consider again the interdouplet current picture (shown again in Figure 4.2.20)

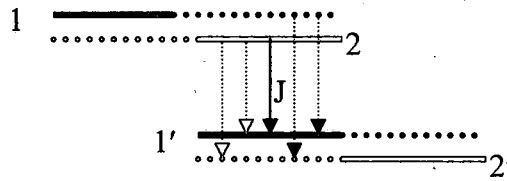


Figure 4.2.20: Description of current flow as interdoublet for a superlattice system.

Using this picture, combined with the LCIS representation, it is evident that the nature of the current flow is entirely due to the intrawell scattering between the localized excited and ground states. As the states couple with each other the scattering breaks into components but still actually occurs within the single well. This is essentially what was demonstrated by Wacker et. al. [124,125] using their Non-Equilibrium Green's Function NEGF model. In their fully quantum mechanical model they concluded that the nature of the interwell transport was fully coherent while incoherent scattering was a purely local phenomenon. In Figure 4.2.20 this is exactly what is depicted. The scattering is actually local and the delocalization of the coupled well states is what actually carries the current.

The insufficiency of the semiclassical models, and in fact the time independent Schrödinger's equation, is that the coupled well states are static. In fact, this static delocalization of the states is essentially a statement of full coherency. In this representation an electron placed into $|1\rangle$ is immediately permitted to scatter in the next well due to the coupling of the states. Consider then a more localized picture (Figure 4.2.21). In this figure the states are depicted as entirely localized in their respective wells. The term R represents an intrawell transition rate and Y is a currently undefined interwell transfer rate, presumably due to coherent tunneling.

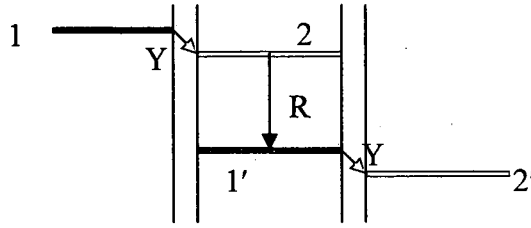


Figure 4.2.21: Localized state description of superlattice transport. R is an intrawell transition rate and Y is an undefined interwell tunneling rate.

It can be logically reasoned that in the steady-state any electron scattering out of $|2\rangle$ must be replaced by the tunneling phenomena from $|1\rangle$. Since the limited paths R and Y must carry the same amount of current we could write

$$J = qn_2 R \quad (4.2.19)$$

Using this expression it becomes apparent that if states $|1\rangle$ and $|2\rangle$ form a "pure doublet" this expression can be written as

$$J = \frac{qN_s}{2} R \quad (4.2.20)$$

Clearly if $R=w$ then the result is the same as derived previously for the semiclassical transport description. In this case however, the value of R was written as the current may be mediated by the presently unknown value of the tunneling rate Y . To determine this relationship the discussion must be expanded to account for time-dependent effects.

4.3. Density Matrix Formalism

Treatment of time-dependent phenomena will be carried out using the Density Matrix Formalism. Unlike the previous time-independent methods the Density Matrix approach assumes that our information regarding the actual states of the system is incomplete. Due to this lack of knowledge the entire system is considered to be in some "state"

$$\bar{\Psi}_{\text{state}}(\mathbf{r}, t) = \sum_n c_n(t) u_n(\mathbf{r}) \quad (4.3.1)$$

where $u_n(\mathbf{r})$ describes an arbitrary complete orthonormal set of functions and $c_n(t)$ describes the time-dependent coefficients of the overall state of the system with time. Physical observables are represented by Hermitian operators on the system, i.e. the expectation value of an operator A is

$$\begin{aligned} \langle A \rangle &= \langle \bar{\Psi}(\mathbf{r}, t) | A \bar{\Psi}(\mathbf{r}, t) \rangle \\ &= \left\langle \sum_m c_m(t) u_m(\mathbf{r}) \left| A \sum_n c_n(t) u_n(\mathbf{r}) \right. \right\rangle \\ &= \sum_m \sum_n c_m^*(t) \langle u_m(\mathbf{r}) | A u_n(\mathbf{r}) \rangle c_n(t) \end{aligned} \quad (4.3.2)$$

Assuming that a system can be prepared repeatedly a statistical sampling of measurements would result in the ensemble average of an operator as

$$\overline{\langle A \rangle} = \sum_m \sum_n \overline{c_m^* c_n} A_{mn} \quad (4.3.3)$$

A density matrix ρ_{mn} is then defined by

$$\rho_{mn} = \overline{c_n^* c_m} \quad (4.3.4)$$

Using this description of the ensemble average of an operator A can be rewritten as

$$\begin{aligned}
\overline{\langle A \rangle} &= \sum_m \sum_n \rho_{nm} A_{mn} \\
&= \sum_n \sum_m \rho_{nm} A_{mn} \\
&= \sum_n (\rho A)_{nn} \\
&= \text{tr}(\rho A)
\end{aligned} \tag{4.3.5}$$

The matrix ρ is Hermitian (i.e. $\rho_{mn} = \rho_{nm}^*$) and from the normalization condition of the wavefunction,

$$\text{tr}(\rho) = \sum_m \overline{c_m^* c_m} = 1 \tag{4.3.6}$$

These diagonal elements of the density matrix represent the distribution of the overall state in the basis functions $u_n(r)$. With the normalization condition given above it is then clear that determination of the electron population distributed through a set of basis states could be found from $N \rho$ where N is the total electrons in the system. The off-diagonal elements of the density matrix represent the coherence or polarization of the electronic system. From one statistical viewpoint an off-diagonal element ρ_{ij} would represent the probability of an electron being simultaneously in the states i and j . In a sense, the difference between classical physics, or semiclassical approximations, and quantum mechanics is in these off-diagonal elements.

The time evolution of Schrödinger's equation is

$$H\psi(r, t) = i\hbar \frac{\partial \psi(r, t)}{\partial t} \tag{4.3.7}$$

Inserting the density matrix into this expression gives

$$\frac{\partial \rho}{\partial t} = \frac{i}{\hbar} [\rho, H] = -\frac{i}{\hbar} [H, \rho] \tag{4.3.8}$$

where

$$[\rho, H] = \rho H - H\rho \text{ or } [H, \rho] = H\rho - \rho H \quad (4.3.9)$$

Using this approach consider a simple 2-state system. The Hamiltonian can be written as the unperturbed and perturbed parts.

$$H = H_0 + H' = \begin{bmatrix} \epsilon_1 & 0 \\ 0 & \epsilon_2 \end{bmatrix} + \begin{bmatrix} 0 & H'_{12} \\ H'_{21} & 0 \end{bmatrix} = \begin{bmatrix} E1 & H'_{12} \\ H'_{21} & E2 \end{bmatrix} \quad (4.3.10)$$

For the quantum heterostructure case consider two states in separate quantum wells separated by a barrier (Figure 4.3.1)

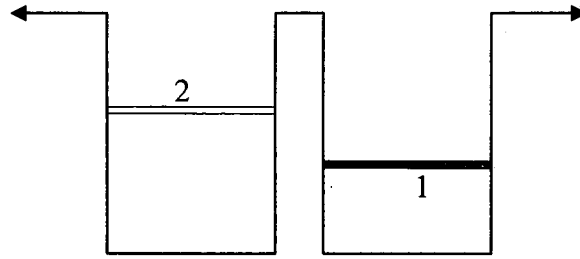


Figure 4.3.1: Two isolated quantum well states separated by a barrier.

Based on the coupled well interactions described in previous chapters, the coupling perturbation between these states, due to the additional well potentials, is \tilde{V} . Using this in the time evolution gives

$$\frac{\partial}{\partial t} \rho = -\frac{i}{\hbar} \begin{bmatrix} \tilde{V}_{12}\rho_{21} - \tilde{V}_{21}\rho_{12} & \tilde{V}_{12}(\rho_{22} - \rho_{11}) + (\epsilon_1 - \epsilon_2)\rho_{12} \\ \tilde{V}_{21}(\rho_{11} - \rho_{22}) + (\epsilon_2 - \epsilon_1)\rho_{21} & \tilde{V}_{21}\rho_{12} - \tilde{V}_{12}\rho_{21} \end{bmatrix} \quad (4.3.11)$$

Using the Hermiticity of ρ and assuming $\tilde{V}_{12} = \tilde{V}_{21} = \tilde{V}$ gives the following differential equations

$$\begin{aligned} \frac{\partial}{\partial t} \rho_{11} &= -\frac{i}{\hbar} \tilde{V}(\rho_{21} - \rho_{21}^*) & \frac{\partial}{\partial t} \rho_{12} &= i\omega_{21}\rho_{12} - \frac{i}{\hbar} \tilde{V}(\rho_{22} - \rho_{11}) \\ \frac{\partial}{\partial t} \rho_{21} &= -i\omega_{21}\rho_{21} + \frac{i}{\hbar} \tilde{V}(\rho_{22} - \rho_{11}) & \frac{\partial}{\partial t} \rho_{22} &= \frac{i}{\hbar} \tilde{V}(\rho_{21} - \rho_{21}^*) \end{aligned} \quad (4.3.12)$$

where $\omega_{ij} = \frac{\Delta\epsilon_{ij}}{\hbar}$. This system of equations of equations can then be solved producing

the following solutions, where R designates the real and M the imaginary part,

$$\rho_{11}(t) = \frac{2(\hbar\omega)^2 \rho_{11}(0) + 4\tilde{V}^2 \Sigma\rho_o}{2(\hbar\Omega)^2} - \frac{4\tilde{V}^2 \Delta\rho_o}{2(\hbar\Omega)^2} \cos\Omega t \quad (4.3.13)$$

$$R\rho_{12}(t) = \frac{\tilde{V}\Delta\rho_o}{2(\hbar\Omega)^2} [2\hbar\omega(1 - \cos\Omega t)] \quad (4.3.14)$$

$$M\rho_{12}(t) = \frac{\tilde{V}\Delta\rho_o}{2(\hbar\Omega)^2} [2\hbar(\omega - \Omega \sin\Omega t)] \quad (4.3.15)$$

$$R\rho_{21}(t) = \frac{\tilde{V}\Delta\rho_o}{2(\hbar\Omega)^2} [2\hbar\omega(1 - \cos\Omega t)] \quad (4.3.16)$$

$$M\rho_{21}(t) = \frac{\tilde{V}\Delta\rho_o}{2(\hbar\Omega)^2} [2\hbar(\omega + \Omega \sin\Omega t)] \quad (4.3.17)$$

$$\rho_{22}(t) = \frac{2(\hbar\omega)^2 \rho_{22}(0) + 4\tilde{V}^2 \Sigma\rho_o}{2(\hbar\Omega)^2} + \frac{4\tilde{V}^2 \Delta\rho_o}{2(\hbar\Omega)^2} \cos\Omega t \quad (4.3.18)$$

Here $\Delta\rho_o = \rho_{22}(0) - \rho_{11}(0)$, $\Sigma\rho_o = \rho_{22}(0) + \rho_{11}(0)$, and $\Omega = \frac{\sqrt{(\hbar\omega)^2 + (2\tilde{V})^2}}{\hbar}$.

Consider first the diagonal expressions, since they represent, in the quantum well system, the normalized electron population in states 1 and 2. To start, assume that the states are at resonance, i.e., $\omega = 0$. The diagonal components can then reduce to

$$\rho_{11}(t) = \frac{\Sigma\rho_o}{2} - \frac{\Delta\rho_o}{2} \cos\Omega t \quad \text{and} \quad \rho_{22}(t) = \frac{\Sigma\rho_o}{2} + \frac{\Delta\rho_o}{2} \cos\Omega t \quad (4.3.19)$$

where $\Omega(\omega = 0) = \frac{2\tilde{V}}{\hbar}$. Assume the initial distribution (sheet density of $1 \times 10^{10} \text{ cm}^{-2}$) is all

located in the left well in state 2. The value of \tilde{V} is calculated for a simple 2-well

GaAs/Al_{0.15}Ga_{0.85}As system with layers starting at the left well of 80/50/60 (barrier in bold face) giving $\tilde{V} \sim 2.84\text{meV}$. A plot of the diagonal coefficients vs. time as well as the system wavefunction $\bar{\Psi}_{\text{system}}(z, t)$ is shown in Figure 4.3.2.

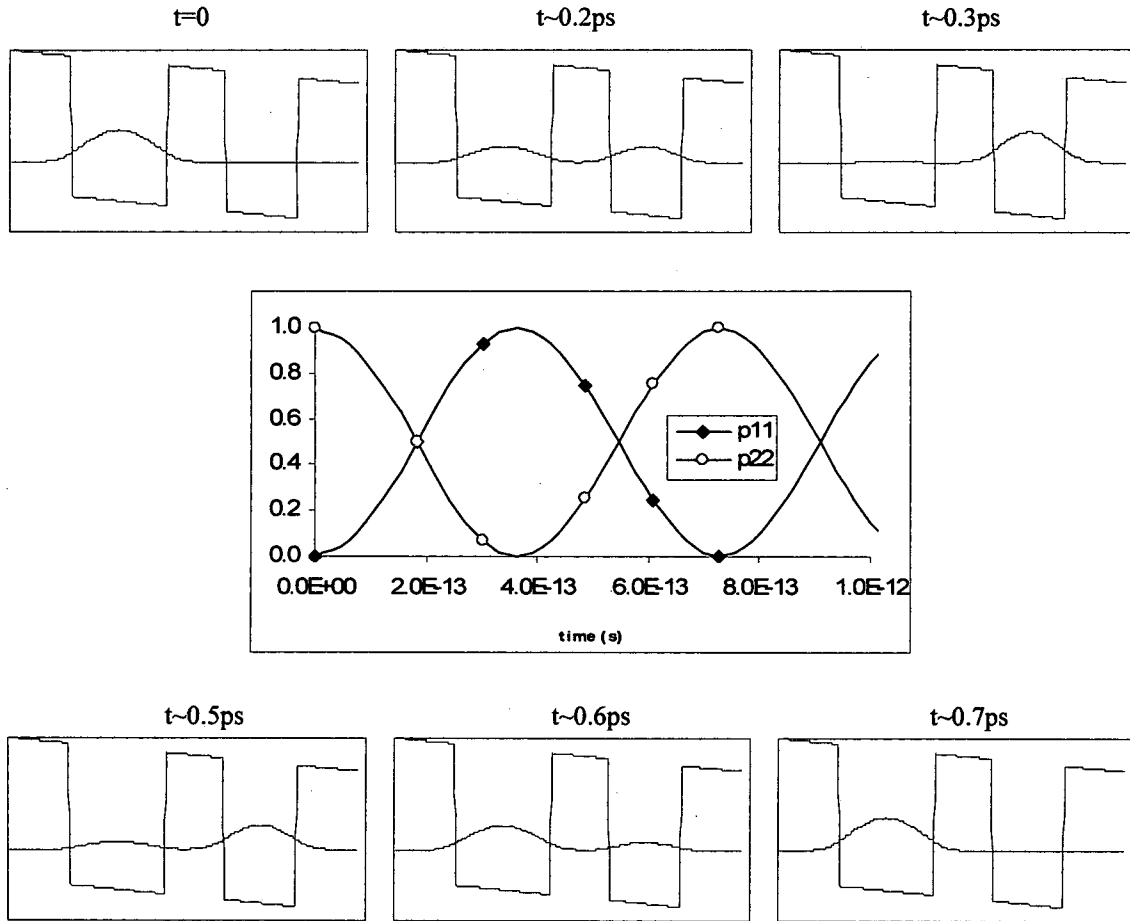


Figure 4.3.2. Time evolution of the system wavefunction for a 80/50/60 GaAs/Al_{0.15}Ga_{0.85}As system with the initial population at $t=0$ located in the left well.

In the center plot a simple oscillation of the diagonal matrix elements is shown. Recalling the differential equations for the diagonals

$$\frac{\partial}{\partial t} \rho_{11} = -\frac{i}{\hbar} \tilde{V} (\rho_{21} - \rho_{21}^*) \quad \frac{\partial}{\partial t} \rho_{22} = \frac{i}{\hbar} \tilde{V} (\rho_{21} - \rho_{21}^*) \quad (4.3.20)$$

it becomes clear that the driving force for the oscillation of these diagonal elements is the off-diagonal coherences induced by the coupling term \tilde{V} . The figures on the top of the central diagram show the system wavefunction $\bar{\Psi}_{\text{system}}(z, t)$ which describes the overall probability of finding the electron in a location z at a time t . The time evolution of the initial distribution in the left well is observed to tunnel entirely to the right well. In this simulation this transfer occurs at subpicosecond timeframes. Once the distribution is in the right well the same driving mechanism pulls the electron distribution back into the left well (figures on the bottom). This entire oscillation takes place, of course, at a frequency of $\Omega(\omega = 0) = \frac{2\tilde{V}}{\hbar}$. This oscillation demonstrates the fundamental flaw of considering states as delocalized across an entire system. For very narrow barriers, producing large \tilde{V} interactions, this oscillation speeds up and a picture of a state as being localized across 2-wells is reasonable. However, as shown in the previous chapters, electron lifetimes can be in the picosecond range which will produce difficulties in trying to describe a system using delocalized wavefunctions.

To illustrate this error of assuming static delocalized wavefunctions consider the same double well system simulated above at a range of barrier widths. In Figure 4.3.3 a plot of the $2\tilde{V}$ values over the range of barrier widths from 20\AA to 1000\AA is shown (black line) along with the $\frac{1}{2}$ period of oscillation (red line) which represents the time for the distribution to oscillate from the left to the right well.

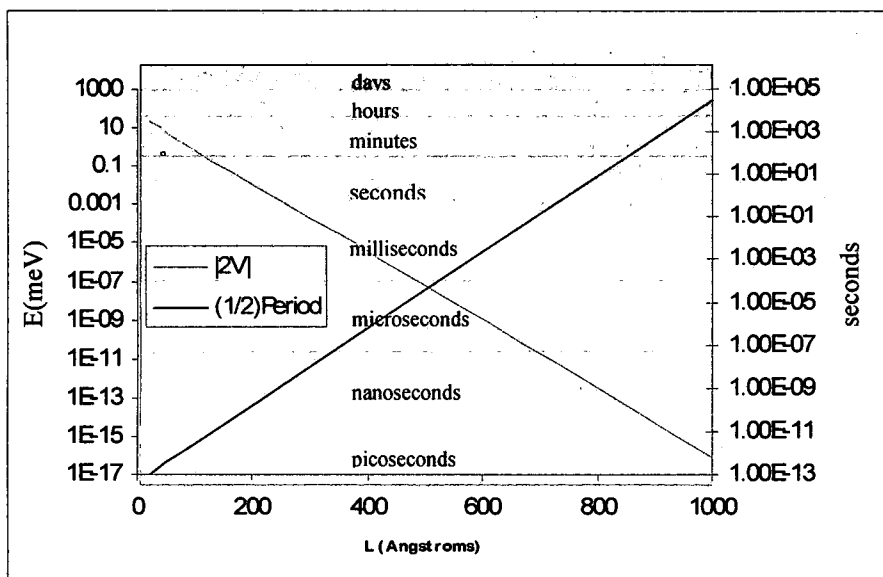


Figure 4.3.3: A plot of the coupling magnitude $2\tilde{V}$ and the $\frac{1}{2}$ period of oscillation for a $80/L/60 \text{ GaAs}/\text{Al}_{0.15}\text{Ga}_{0.85}\text{As}$ double well system.

In this plot the exponential decay of the interwell coupling term \tilde{V} as well as the exponential rise of the oscillation period with increasing barrier width is observed. Clearly, for barrier widths approaching 1000\AA the calculated $\frac{1}{2}$ period of oscillation is shown to take hours to days to tunnel through the barrier. Realistically, in this timeframe, the electron would never tunnel as interaction with the surrounding environment would surely interrupt this coherent process. In the QCL systems to be investigated, with scattering rates in these devices due to LO-phonon and electron-electron interactions in the picosecond range, it becomes necessary to consider that even relatively thin barriers $<100\text{\AA}$ might require reconsideration in assuming electronic states can be represented accurately using delocalized, static, wavefunctions.

Preparation of a truly isolated two state system, as shown in Figure 4.3.1, is only possible in introductory physics textbooks. In a realistic system the electrons interaction with the surrounding environment (phonons, other electrons, etc.) cannot be ignored. Both coherent (tunneling) effects and incoherent scattering must contribute to the time-dependent evolution of electron distributions. Notice that in the absence of any perturbation $\Delta V = 0$ that

$$\frac{\partial}{\partial t} \rho_{11} = \frac{\partial}{\partial t} \rho_{22} = 0 \quad (4.3.21)$$

meaning that the probability of finding the system in a particular state (Ψ_1 or Ψ_2) does not change, as expected. The off diagonal components, which describe the coherence between the states, in the absence of any perturbation, are

$$\begin{aligned} \frac{\partial}{\partial t} \rho_{12} &= i\omega_{21} \rho_{12} \\ \frac{\partial}{\partial t} \rho_{21} &= -i\omega_{21} \rho_{21} \end{aligned} \quad (4.3.22)$$

which have the solutions

$$\begin{aligned} \rho_{12}(t) &= \rho_{12}(0)e^{i\omega_{21}t} \\ \rho_{21}(t) &= \rho_{21}(0)e^{-i\omega_{21}t} \end{aligned} \quad (4.3.23)$$

This describes harmonically oscillating functions with frequency ω_{21} . Recall that this describes a system without a perturbation. If initially there is no coherence (i.e., $\rho_{12}(0) = \rho_{21}(0) = 0$) then obviously nothing changes. However, the same expressions could be arrived at if there was a perturbation which induced a nonzero coherence ($\rho_{12}, \rho_{21} \neq 0$) and it is turned off at a time $t=0$. The above equations would then indicate that the coherence between the states (if once created) would oscillate indefinitely. Since it was already reasoned that the interaction with the environment will not permit this,

due to a variety of elastic and inelastic "collisions", the original equations are noticeably incomplete.

Elastic collisions conserve energy, thus induce no change in level occupation, but can destroy the phase of the wavefunction. To describe this purely phase destroying phenomena without explicitly treating the multitude of events that could produce it, a commonly employed relaxation time T_2 is used. This is often referred to as the "pure dephasing" or decoherence time. This phenomenological term can be inserted into the off-diagonal components by writing

$$\begin{aligned}\frac{\partial}{\partial t} \rho_{12} &= i\omega_{21}\rho_{12} - \frac{i}{\hbar} \Delta V(\rho_{22} - \rho_{11}) - \frac{\rho_{12}}{T_2} \\ \frac{\partial}{\partial t} \rho_{21} &= -i\omega_{21}\rho_{21} + \frac{i}{\hbar} \Delta V(\rho_{22} - \rho_{11}) - \frac{\rho_{21}}{T_2}\end{aligned}\quad (4.3.24)$$

Evaluation now of the off-diagonal ρ_{21} , in the absence of a perturbation, produces

$$\begin{aligned}\frac{\partial}{\partial t} \rho_{21} &= -i\omega_{21}\rho_{21} - \frac{\rho_{21}}{T_2} \\ &= -\left(i\omega_{21} + \frac{1}{T_2}\right)\rho_{21}\end{aligned}\quad (4.3.25)$$

the solution is then

$$\rho_{21}(t) = \rho_{21}(0) \exp\left(\left[-i\omega_{21} - \frac{1}{T_2}\right]t\right) \quad (4.3.26)$$

which demonstrates the decay of the polarization due to the T_2 dephasing processes.

Inelastic collisions (scattering events), those which cause a change in level occupation, such as electron-phonon, electron-electron and other mechanisms, also contribute to dephasing. To incorporate these scattering rates a dephasing time τ_d is substituted in place of T_2 where

$$\frac{1}{\tau_{\text{deph}}} = \frac{1}{2T_1} + \frac{1}{T_2} \quad (4.3.27)$$

The T_2 term describes the rate of decay of the polarization ρ_{ij} , proportional to the amplitude of oscillation $\rho_{ij} \propto e^{-t/T_2}$. T_1 describes the probability decay rate of the energy density $\rho_{ii} \propto e^{-t/T_1}$. Since the decay of $\rho_{ii} \propto |p_{ij}|^2$ this must be written as $\rho_{ij} \propto e^{-t/2T_1}$.

The new unperturbed solution for the coherence is then

$$\rho_{21}(t) = \rho_{21}(0) \exp \left(\left[-i\omega_{21} - \frac{1}{\tau_{\text{deph}}} \right] t \right) \quad (4.3.28)$$

To easily implement these scattering and dephasing mechanisms into the density matrix expressions for a general system it is helpful to reformulate the expressions from the commutator form to a single operator acting on the density matrix. Since the time evolution is

$$\frac{\partial \rho}{\partial t} = -\frac{i}{\hbar} [H, \rho] \quad (4.3.29)$$

the elements of ρ undergo a linear transformation. This can then be rewritten as

$$\frac{\partial \rho}{\partial t} = -\frac{i}{\hbar} L \rho \quad (4.3.30)$$

where L is an $N^2 \times N^2$ matrix known as the Liouville operator, or superoperator. In this form, ρ takes the form of an N^2 -dimensional vector. The operator L can be expressed as

$$L_{ij,mn} = H_{im} \delta_{jn} - H_{jn}^* \delta_{im} \quad (4.3.31)$$

which, for the treatment of real-valued perturbation elements can be written as

$$L_{ij,mn} = H_{im} \delta_{jn} - H_{nj} \delta_{im} \quad (4.3.32)$$

Constructing the Liouville superoperator in the form

$$L = \begin{bmatrix} L_{1111} & L_{1112} & L_{1121} & L_{1122} \\ L_{1211} & L_{1212} & L_{1221} & L_{1222} \\ L_{2111} & L_{2112} & L_{2121} & L_{2122} \\ L_{2211} & L_{2212} & L_{2221} & L_{2222} \end{bmatrix} \quad (4.3.33)$$

and using the Hamiltonian

$$H = \begin{bmatrix} E_1 & H'_{12} \\ H'_{21} & E_2 \end{bmatrix} \quad (4.3.34)$$

allows this matrix to be written as

$$L = \begin{bmatrix} 0 & -H'_{21} & H'_{12} & 0 \\ -H'_{12} & E_1 - E_2 & 0 & H'_{12} \\ H'_{21} & 0 & E_2 - E_1 & -H'_{21} \\ 0 & H'_{21} & -H'_{12} & 0 \end{bmatrix} \quad (4.3.35)$$

The previous density matrix now becomes a vector

$$\rho = \begin{bmatrix} \rho_{11} \\ \rho_{12} \\ \rho_{21} \\ \rho_{22} \end{bmatrix} \quad (4.3.36)$$

The operation on the density vector is then

$$L\rho = \begin{bmatrix} 0 & -H'_{21} & H'_{12} & 0 \\ -H'_{12} & E_1 - E_2 & 0 & H'_{12} \\ H'_{21} & 0 & E_2 - E_1 & -H'_{21} \\ 0 & H'_{21} & -H'_{12} & 0 \end{bmatrix} \begin{bmatrix} \rho_{11} \\ \rho_{12} \\ \rho_{21} \\ \rho_{22} \end{bmatrix} = \begin{bmatrix} H'_{12}\rho_{21} - H'_{21}\rho_{12} \\ H'_{12}(\rho_{22} - \rho_{11}) + (E_1 - E_2)\rho_{12} \\ H'_{21}(\rho_{11} - \rho_{22}) + (E_2 - E_1)\rho_{21} \\ H'_{21}\rho_{12} - H'_{12}\rho_{21} \end{bmatrix} \quad (4.3.37)$$

In this manner $\frac{\partial \rho}{\partial t} = -\frac{i}{\hbar} L\rho$ produces the same result as $\frac{\partial \rho}{\partial t} = -\frac{i}{\hbar} [H, \rho]$.

Continuing with this approach the dephasing mechanisms can then be more generally introduced using another superoperator F where

$$\begin{aligned} F_{ij,mn} &= -\frac{1}{2}(W_i + W_j)\delta_{im}\delta_{jn} - \Gamma_{ij}^{\text{pure}}\delta_{im}\delta_{jn} \quad i \neq j \\ F_{ii,jj} &= W_{ji}(1 - \delta_{ij}) - W_i\delta_{ij} \end{aligned} \quad (4.3.38)$$

Here W_i and W_j are the total scattering rates out of the i and j levels, W_{ji} is the total scattering rate from j to i , and $\Gamma_{ij}^{\text{pure}} = 1/T_2$. The F matrix then takes the following form

$$F = \begin{bmatrix} -W_1 & 0 & 0 & W_{21} \\ 0 & -\frac{1}{2}(W_1 + W_2) - \Gamma_{12}^{\text{pure}} & 0 & 0 \\ 0 & 0 & -\frac{1}{2}(W_1 + W_2) - \Gamma_{21}^{\text{pure}} & 0 \\ W_{12} & 0 & 0 & -W_2 \end{bmatrix} \quad (4.3.39)$$

Now the time evolution can be written as

$$\frac{\partial \rho}{\partial t} = \left[-\frac{i}{\hbar} L + F \right] \rho \quad (4.3.40)$$

giving the differential system as

$$\frac{\partial \rho}{\partial t} = -\frac{i}{\hbar} \begin{bmatrix} H'_{12}\rho_{21} - H'_{21}\rho_{12} \\ H'_{12}(\rho_{22} - \rho_{11}) + (E_1 - E_2)\rho_{12} \\ H'_{21}(\rho_{11} - \rho_{22}) + (E_2 - E_1)\rho_{21} \\ H'_{21}\rho_{12} - H'_{12}\rho_{21} \end{bmatrix} + \begin{bmatrix} -W_1\rho_{11} + W_{21}\rho_{22} \\ -\frac{1}{2}(W_1 + W_2)\rho_{12} - \Gamma_{12}^{\text{pure}}\rho_{12} \\ -\frac{1}{2}(W_1 + W_2)\rho_{21} - \Gamma_{21}^{\text{pure}}\rho_{21} \\ -W_2\rho_{22} + W_{12}\rho_{11} \end{bmatrix} \quad (4.3.41)$$

This system then produces the following equations

$$\frac{\partial}{\partial t} \rho_{11} = -\frac{i}{\hbar} [H'_{12}\rho_{21} - H'_{21}\rho_{12}] - W_1\rho_{11} + W_{21}\rho_{22} \quad (4.3.42)$$

$$\frac{\partial}{\partial t} \rho_{12} = -\frac{i}{\hbar} [H'_{12}(\rho_{22} - \rho_{11}) + (E_1 - E_2)\rho_{12}] - \frac{1}{2}(W_1 + W_2)\rho_{12} - \Gamma_{12}^{\text{pure}}\rho_{12} \quad (4.3.43)$$

$$\frac{\partial}{\partial t} \rho_{21} = -\frac{i}{\hbar} [H'_{21}(\rho_{11} - \rho_{22}) + (E_2 - E_1)\rho_{21}] - \frac{1}{2}(W_1 + W_2)\rho_{21} - \Gamma_{21}^{\text{pure}}\rho_{21} \quad (4.3.44)$$

$$\frac{\partial}{\partial t} \rho_{22} = -\frac{i}{\hbar} [H'_{21} \rho_{12} - H'_{12} \rho_{21}] - W_2 \rho_{22} + W_{12} \rho_{11} \quad (4.3.45)$$

Returning to the coupled well perturbation terms $H'_{12} = H'_{21} = \tilde{V}$ gives

$$\frac{\partial}{\partial t} \rho_{11} = -\frac{i}{\hbar} \tilde{V} (\rho_{21} - \rho_{21}^*) - W_1 \rho_{11} + W_{21} \rho_{22} \quad (4.3.46)$$

$$\frac{\partial}{\partial t} \rho_{12} = i\omega_{21} \rho_{12} - \frac{i}{\hbar} \tilde{V} (\rho_{22} - \rho_{11}) - \Gamma \rho_{12} \quad (4.3.47)$$

$$\frac{\partial}{\partial t} \rho_{21} = -i\omega_{21} \rho_{21} + \frac{i}{\hbar} \tilde{V} (\rho_{22} - \rho_{11}) - \Gamma \rho_{21} \quad (4.3.48)$$

$$\frac{\partial}{\partial t} \rho_{22} = \frac{i}{\hbar} \tilde{V} (\rho_{21} - \rho_{21}^*) - W_2 \rho_{22} + W_{12} \rho_{11} \quad (4.3.49)$$

where $\Gamma_{12} = \Gamma_{21} = \Gamma = \left(\frac{1}{2} W_1 + \frac{1}{2} W_2 + \Gamma^{\text{pure}} \right)$.

To examine these new expressions consider first only the pure dephasing induced by the elastic Γ^{pure} (or T_2) effects. In this first example there are thus no inelastic scattering events which transfer electrons between or out of the two states but simply mechanisms destroying the coherence. Choosing a generic system where $\tilde{V} = 4\text{meV}$ and then assuming the states are at resonance $\omega=0$ the effects of this purely phase destroying phenomena is plotted in figure 4.3.4. In this plot the inclusion of a pure dephasing rate causes a decay of the off-diagonal terms representing the coherence which in turn produces a decay of the oscillation between the states. As expected, for faster dephasing rates the population relaxes much quicker to a steady-state value.

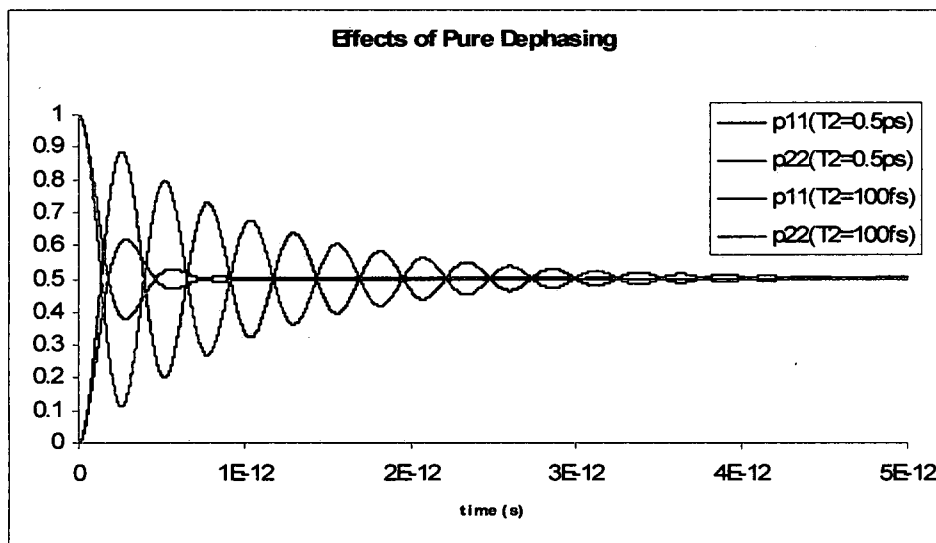


Figure 4.3.4: The effects of pure dephasing in a generic $\tilde{V} = 4\text{meV}$ 2-state coupled well system at $T_2=0.5$ and 100ps.

Now assume the states in the system are not entirely isolated but instead have finite lifetimes permitting the population to transfer out to other, undefined, states (Figure 4.3.5).

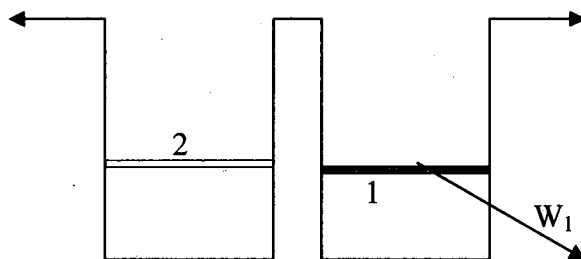


Figure 4.3.5: Generic 2-state system where state $|1\rangle$ is permitted to scatter to undefined states.

In this assume that the population again starts entirely in state $|2\rangle$ and only state $|1\rangle$ has a total scattering rate of $W_1=1\times 10^{12}\text{s}^{-1}$. This simulation is shown in Figure 4.3.6.

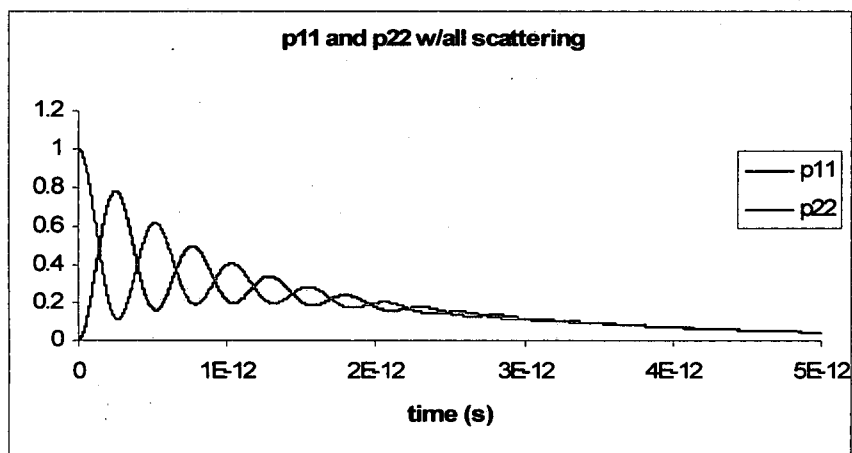


Figure 4.3.6: Time-dependent evolution of the distribution where state $|1\rangle$ has a finite incoherent lifetime.

In this simulation the population which starts in $|2\rangle$ begins to oscillate across the barrier with state $|1\rangle$. With the inclusion of a finite lifetime for state $|1\rangle$ the oscillation not only decays but the entire population begins to drain from the system. Since state $|1\rangle$ drains to undefined locations, the overall population disappears and the $\text{Trace}(\rho)$ is no longer unity.

In quantum cascade lasers, or a multi-well superlattice, a system continually repeats itself over many identical periods. Thus the scattering out from one period pumps the subsequent period. Consider a simple repeating 2-state superlattice shown in Figure 4.3.7. Since the states in each period are assumed to be identical the periods can be folded back into a general 2-state system (Figure 4.3.8).

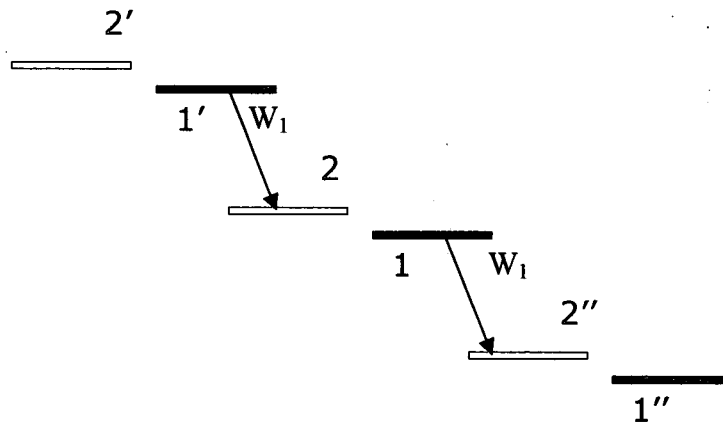


Figure 4.3.7: Multiple periods of a general 2-state superlattice.

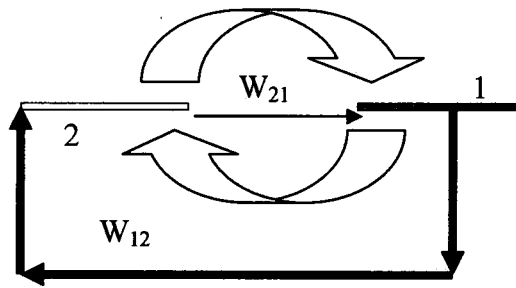


Figure 4.3.8: Folding the repeating 2-state superlattice back into a 2-state system. The curved arrows represent the coherent oscillation between states $|2\rangle$ and $|1\rangle$ and the black lines represent incoherent scattering.

In Figure 4.3.8 the curved arrows represent the coherent oscillation between states $|2\rangle$ and $|1\rangle$ and the black line represent incoherent scattering. Since the state $|1\rangle$ scattering is directed into state $|2\rangle$ in the next period the system is easily cast back into a 2-state problem. Assuming this system repeats indefinitely a simulation can then be made for a system at resonance where $W_{21} = W_{12} = 1 \times 10^{10} \text{ s}^{-1}$, $W_{12} = 1 \times 10^{12} \text{ s}^{-1}$, and $\Gamma_{21}^{\text{pure}} = 2 \times 10^{12} \text{ s}^{-1}$. This simulation is shown in Figure 4.3.9

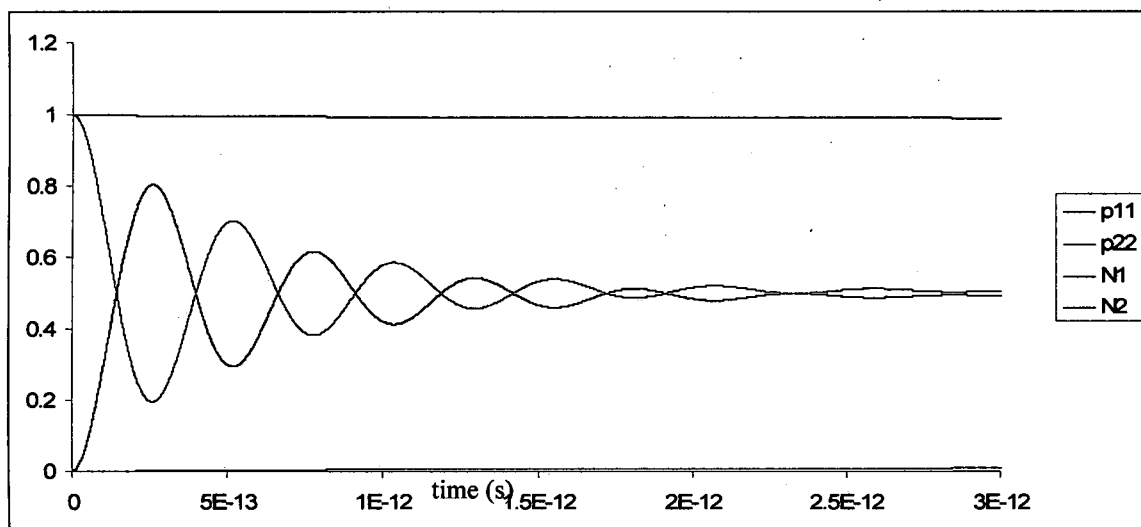


Figure 4.3.9: Time-dependent evolution of the distribution in a repeating period 2-state superlattice.

In this simulation, since each stage in the repeating system replenishes itself, the population remains constant and the $\text{Trace}(\rho)=1$. Here it is important to note that although the scattering rate from the $|1\rangle$ states to the $|2\rangle$ states is much larger than the $|2\rangle$ to $|1\rangle$, the oscillation has intervened to produce only a slight inversion between these states. For reference, also plotted are the semiclassical solutions using the simple rate equations

$$\begin{aligned}\frac{\partial n_1}{\partial t} &= n_2 W_{21} - n_1 W_{12} \\ \frac{\partial n_2}{\partial t} &= n_1 W_{12} - n_2 W_{21}\end{aligned}\tag{4.3.50}$$

The results for these expressions are labeled N1, and N2 in the Figure 4.3.9. Undoubtedly the inclusion of the coherent oscillation has a dramatic effect on the steady state values which is drastically different from the semiclassical description. Adjustment of the rates to $W_2 = 1 \times 10^{12} \text{ s}^{-1}$ and $W_{12} = 2 \times 10^{12} \text{ s}^{-1}$ produces the result shown in

4.3.10. In this simulation, where state $|2\rangle$ now has significant scattering into state $|1\rangle$, there is more agreement between the semiclassical and Density Matrix (DM) convergence to the steady-state. The semiclassical rate equations are still observed though to overestimate the steady state inversion between the states.

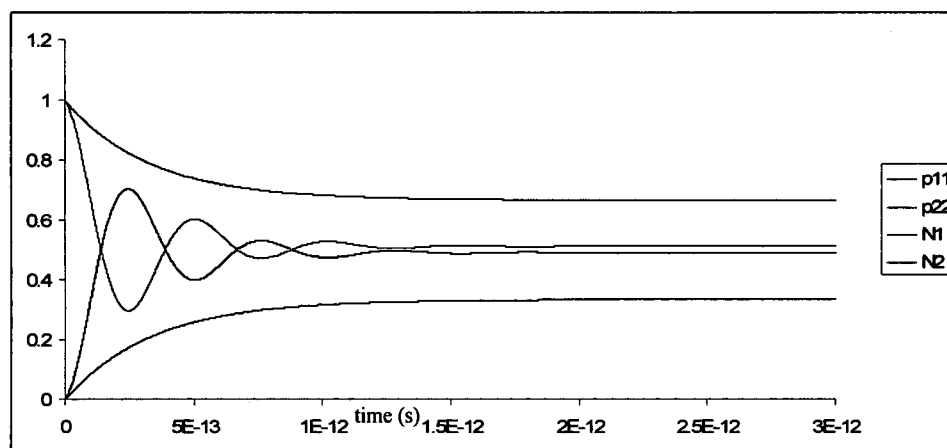


Figure 4.3.10: Time-dependent evolution of the distribution in a repeating period 2-state superlattice with the $|2\rangle$ to $|1\rangle$ rate increased.

To further investigate this relationship between the semiclassical rate equation description and the DM approach, analytical arguments can again be presented. Assume a superlattice structure where each well contains 2-states (Figure 4.3.11).

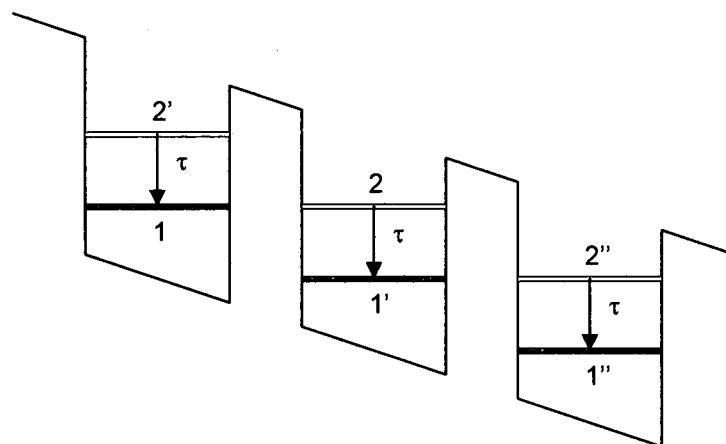


Figure 4.3.11: 2-state superlattice structure.

In this example assume that the states in each well are separated in energy enough such that the interwell (1-2) coupling is undisturbed by any other states, i.e. there is a two state system which repeats itself. Assume that scattering is restricted to the intrawell transition from the excited state to the ground and this is described by a rate of $W=\tau^{-1}$. The time evolution of the density matrix in this case would be

$$\frac{\partial \rho}{\partial t} = \left[-\frac{i}{\hbar} L + F \right] \rho = \begin{bmatrix} 0 & \frac{i}{\hbar} \tilde{V} & -\frac{i}{\hbar} \tilde{V} & \tau^{-1} \\ \frac{i}{\hbar} \tilde{V} & i\omega_{21} - \tau_d^{-1} & 0 & -\frac{i}{\hbar} \tilde{V} \\ -\frac{i}{\hbar} \tilde{V} & 0 & -i\omega_{21} - \tau_d^{-1} & \frac{i}{\hbar} \tilde{V} \\ 0 & -\frac{i}{\hbar} \tilde{V} & \frac{i}{\hbar} \tilde{V} & -\tau^{-1} \end{bmatrix} \begin{bmatrix} \rho_{11} \\ \rho_{12} \\ \rho_{21} \\ \rho_{22} \end{bmatrix} \quad (4.3.51)$$

where the dephasing lifetime $\tau_d^{-1} = \frac{1}{2\tau} + \Gamma^{\text{pure}}$. In the steady-state this system can be

written as an augmented matrix

$$\bar{A} = \begin{bmatrix} 0 & \frac{i}{\hbar} \tilde{V} & -\frac{i}{\hbar} \tilde{V} & \tau^{-1} & 0 \\ \frac{i}{\hbar} \tilde{V} & i\omega_{21} - \tau_d^{-1} & 0 & -\frac{i}{\hbar} \tilde{V} & 0 \\ -\frac{i}{\hbar} \tilde{V} & 0 & -i\omega_{21} - \tau_d^{-1} & \frac{i}{\hbar} \tilde{V} & 0 \\ 0 & -\frac{i}{\hbar} \tilde{V} & \frac{i}{\hbar} \tilde{V} & -\tau^{-1} & 0 \end{bmatrix} \quad (4.3.52)$$

which reduces to

$$\bar{A} = \begin{bmatrix} 1 & 0 & 0 & -\frac{2\tilde{V}^2\tau_d\tau + \hbar^2 + \hbar^2\omega_{21}^2\tau_d^2}{2\tilde{V}^2\tau\tau_d} & 0 \\ 0 & 1 & 0 & \frac{-i\hbar(i\omega_{21}\tau_d + 1)}{2\tilde{V}\tau} & 0 \\ 0 & 0 & 1 & \frac{-i\hbar(i\omega_{21}\tau_d - 1)}{2\tilde{V}\tau} & 0 \\ 0 & 0 & 0 & 0 & 0 \end{bmatrix} \quad (4.3.53)$$

Using $\Omega = \frac{2\tilde{V}}{\hbar}$ allows for the solution to be written as

$$\rho_{22} = \frac{\frac{1}{2}\Omega^2\tau\tau_d}{1 + (\Delta E_{21}/\hbar)^2\tau_d^2 + \frac{1}{2}\Omega^2\tau\tau_d}\rho_{11} \quad (4.3.54)$$

Since the trace of the density matrix must be unity $\rho_{22} + \rho_{11} = 1$ is used to write

$$\rho_{22} = \frac{1}{2} \frac{\Omega^2\tau\tau_d}{1 + (\Delta E_{21}/\hbar)^2\tau_d^2 + \Omega^2\tau\tau_d} \quad (4.3.55)$$

In this stated system the excited state $|2\rangle$ is drained to the ground state $|1\rangle$ while oscillating with the ground state $|1\rangle$ in the well to its left. In the steady state the continuity of current flow would require that electrons scattering out of state $|2\rangle$ be replenished with electrons from state $|1\rangle$. Writing the total electrons in state $|2\rangle$ as $N_2 = N_s\rho_{22}$ allows the current density across the barrier to be written as

$$J = \frac{qN_s\rho_{22}}{\tau} = \frac{qN_s}{2} \frac{\Omega^2\tau_d}{1 + (\Delta E_{21}/\hbar)^2\tau_d^2 + \Omega^2\tau\tau_d} \quad (4.3.56)$$

Assuming the resonance condition $\Delta E_{21} = 0$ gives

$$J = \frac{qN_s}{2} \frac{\Omega^2\tau_d}{1 + \Omega^2\tau\tau_d} \quad (4.3.57)$$

Here two limiting cases can be considered. The first case is when $\Omega^2\tau\tau_d \ll 1$. In this situation the current density reduces to

$$J = \frac{qN_s}{2} \Omega^2\tau_d \quad (4.3.58)$$

and thus is driven by both the oscillation and the dephasing rate. The physical meaning of this limit can be explained in terms of frequency as $\Omega^2 \ll W\Gamma$ which implies that the oscillation of the interwell states is much slower than the scattering and dephasing. It is therefore expected that decoherence dominates and not many oscillations, if any, occur

before the electron dephases and scatters from the states. Under these conditions it is expected that the two states are essentially localized in their respective wells and the transport due to tunneling is one-way as the oscillation is overdamped. In terms of energy this limit is $(2\tilde{V})^2 \ll \hbar^2 \tau^{-1} \tau_d^{-1}$. As discussed in previous chapters the term $2\tilde{V}$ represents the anti-crossing gap of two coupled interwell states. This limit therefore represents the level broadening of the states being much larger than the anticrossing gap.

In the other limit $\Omega^2 \tau \tau_d \gg 1$ the current density reduces to

$$J = \frac{qN_s}{2} \frac{1}{\tau} = \frac{qN_s}{2} W \quad (4.3.59)$$

which is the result obtained in chapter 4.2.2 by considering the interwell resonant states as a delocalized doublet. In this case the frequency $\Omega^2 \gg W\Gamma$ meaning that the oscillation is much faster than the scattering/dephasing. The electron distribution is then permitted to oscillate back and forth across the barrier many times before the coherence is destroyed. It is therefore not surprising to assume that the system in this limit would appear to behave as a delocalized "doublet" where the states are considered to extend equally into both wells. In the energy picture this limit also represents $(2\tilde{V})^2 \gg \hbar^2 \tau^{-1} \tau_d^{-1}$ where the anticrossing gap is much larger than the broadening.

To further understand these limits application of the same type of analysis to a system which may be more familiar, i.e., a radiation field interacting with a 2-state system (Figure 4.3.12) can be carried out. A thorough analysis of this type of system can be found in Yariv [161].

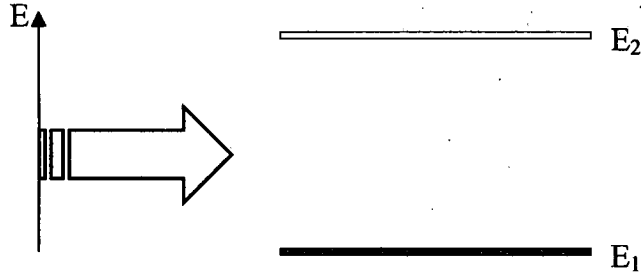


Figure 4.3.12: Interaction of a radiation field with a two-state system.

For this system the perturbation is the electric field and can be written as

$$H' = -\mu E(t) \quad (4.3.60)$$

where μ is the dipole operator. Assuming only the off-diagonal terms of this operator are nonzero the Hamiltonian is

$$H = H_0 + H' = \begin{bmatrix} E_1 & 0 \\ 0 & E_2 \end{bmatrix} + \begin{bmatrix} 0 & \mu \\ \mu & 0 \end{bmatrix} = \begin{bmatrix} E_1 & \mu \\ \mu & E_2 \end{bmatrix} \quad (4.3.61)$$

Using this operator in the density matrix the following coupled differential equations can be arrived at

$$\frac{\partial \rho_{21}}{\partial t} = -i\omega_0 \rho_{21} + i\frac{\mu}{\hbar}(\rho_{11} - \rho_{22})E(t) - \frac{\rho_{21}}{T_2} \quad (4.3.62)$$

$$\frac{\partial}{\partial t}(\rho_{11} - \rho_{22}) = \frac{2i\mu E(t)}{\hbar}(\rho_{21} - \rho_{21}^*) - \frac{(\rho_{11} - \rho_{22}) - (\rho_{11} - \rho_{22})_0}{\tau} \quad (4.3.63)$$

where $\omega_0 = (E_2 - E_1)/\hbar$, T_2 describes the decay of the coherence, and τ represents the time for the system to return to its equilibrium population difference $(\rho_{11} - \rho_{22})_0$ in the absence of a field. Using the usual description of a harmonic field

$$E(t) = \frac{E_0}{2}(e^{i\omega t} + e^{-i\omega t}) \quad (4.3.64)$$

the ensemble average of the induced dipole moment becomes

$$\langle \mu(t) \rangle = 2\mu [\text{Re} \sigma_{21}(t) \cos \omega t + \text{Im} \sigma_{21}(t) \sin \omega t] \quad (4.3.65)$$

where $\sigma_{21}(t)$ is the slowly varying portion of $\rho_{21}(t)$. Using the macroscopic polarization $P = N\langle \mu \rangle$ and then defining the atomic susceptibility $\chi = \chi' - i\chi''$, gives the steady-state solutions of

$$\chi'(\omega) = \frac{\mu^2 T_2 \Delta N_0}{\epsilon_0 \hbar} \frac{(\omega - \omega_0) T_2}{1 + (\omega - \omega_0)^2 T_2^2 + 4\Omega^2 T_2 \tau} \quad (4.3.66)$$

$$\chi''(\omega) = \frac{\mu^2 T_2 \Delta N_0}{\epsilon_0 \hbar} \frac{1}{1 + (\omega - \omega_0)^2 T_2^2 + 4\Omega^2 T_2 \tau} \quad (4.3.67)$$

where $\Delta N_0 = N(\rho_{11} - \rho_{22})_0$ and $\Omega = \mu E_0 / 2\hbar$. In this example Ω is referred to as the Rabi oscillation frequency. A plot of these expressions, in units of T_2 , for the limiting case of $4\Omega^2 \tau T_2 \ll 1$, is shown below in Figure 4.3.13. Here it is recognized that χ' and χ'' are related to the index of refraction and the absorption (or gain), respectively.

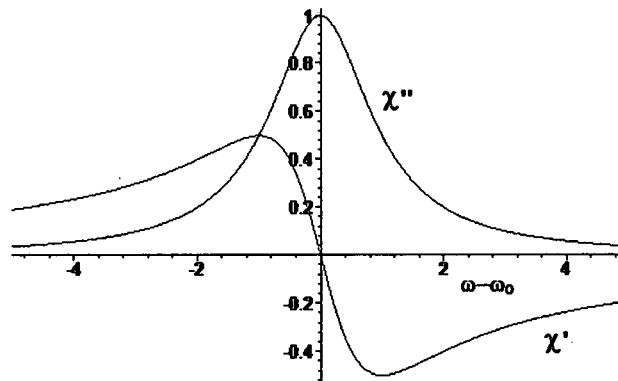


Figure 4.3.13: A plot of the susceptibilities vs. $\omega - \omega_0$, in units of T_2 , for the limiting case of $4\Omega^2 \tau T_2 \ll 1$.

Continuing now the previous discussion of the limiting cases, first consider $4\Omega^2\tau T_2 \ll 1$. In this picture of 2 states interacting with a radiation field this is the "small signal" limit. Here the perturbation is small and has little effect on the states it is interacting with. In the other limit, $4\Omega^2\tau T_2 \gg 1$, this is commonly referred to as "saturation". This implies the perturbation is large and has a significant effect on the interacting states. For the analogous coupled well system then, the "small signal" limit, implying thicker barriers, produces a case where the current flow is driven by the slow oscillation and the dephasing (Equation 4.3.58). The semiclassical picture of scattering between delocalized states is thus inappropriate to describe the current in this situation. In the "saturation" limit, implying a thin barrier, the current (Equation 4.3.59) is driven by the incoherent scattering as is predicted by the semiclassical rates of the delocalized states yet the strong coupling "saturation" has the capability to significantly effect the population in the states. Before elucidating further on this comparative discussion some significant simplifications can be made to the density matrix description permitting easier implementation and integration with the methods outlined in Chapter 2 and Chapter 1.

4.4 Diagonal Density Matrix

In Section 4.3 it was observed that the method for calculating the time evolution, or steady-state solutions, of the density matrix requires evaluation of a matrix system with $N^2 \times N^2$ elements, where N is the number of states in the system. For realistic quantum cascade laser structures the size of this matrix becomes very large, very quickly. Simplifications can be made based on a description of the basis states as localized and assuming nearest-neighbor only interactions.

Consider a multi-quantum well system containing any arbitrary number of wells (Figure 4.4.1), each with at most a ground and excited state. Assuming that interactions will occur between nearest neighbor wells the analysis of any state can be limited to interactions over any three wells.

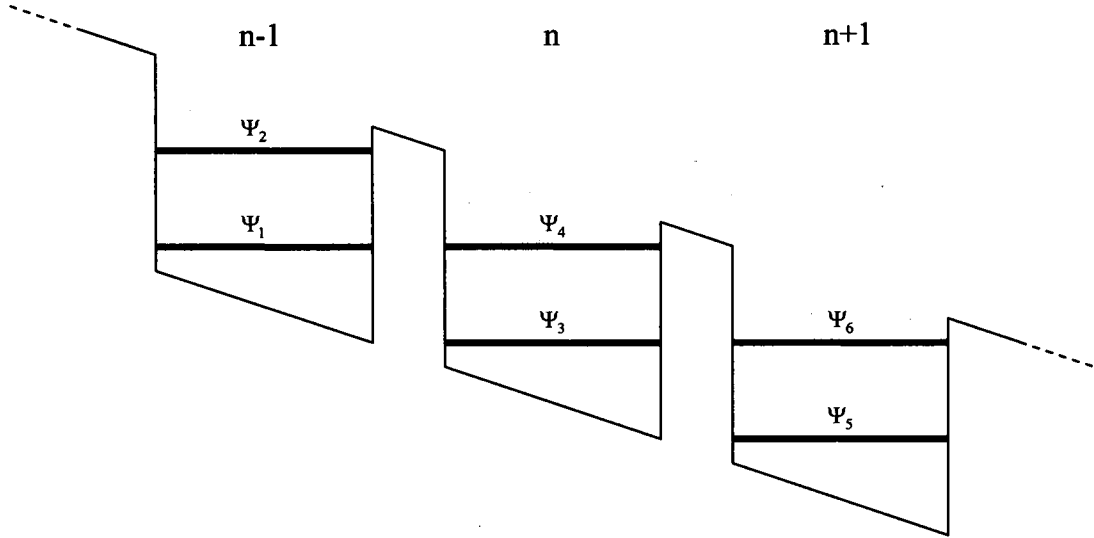


Figure 4.4.1: General multi-well system with 2-states per well.

In this three well portion of an arbitrary extended system 6 states can be used to describe the density matrix elements corresponding to the states in the central well, labeled here as $|3\rangle$ and $|4\rangle$. To evaluate the necessary terms for the ground state in this central well a full density matrix system over these 6 states and is constructed resulting in the following expressions

$$\begin{aligned}
 \frac{\partial \rho_{31}}{\partial t} = & -\frac{i}{2} [\Omega_{31} \rho_{11} + \Omega_{32} \rho_{21}] \\
 & + \left[\frac{i}{2} (\Omega_{31} \rho_{33} + \Omega_{41} \rho_{34}) - (i\omega_{31} + \tau_{d,31}^{-1}) \rho_{31} \right] \\
 & - \frac{i}{2} [\Omega_{35} \rho_{51} + \Omega_{36} \rho_{61}]
 \end{aligned} \tag{4.4.1}$$

$$\begin{aligned}
\frac{\partial \rho_{32}}{\partial t} = & -\frac{i}{2} [\Omega_{31} \rho_{12} + \Omega_{32} \rho_{22}] \\
& + \left[\frac{i}{2} (\Omega_{32} \rho_{33} + \Omega_{42} \rho_{34}) - (i\omega_{32} + \tau_{d,32}^{-1}) \rho_{32} \right] \\
& - \frac{i}{2} [\Omega_{35} \rho_{52} + \Omega_{36} \rho_{62}]
\end{aligned} \tag{4.4.2}$$

$$\begin{aligned}
\frac{\partial \rho_{33}}{\partial t} = & \frac{i}{2} [\Omega_{31} (\rho_{31} - \rho_{13}) + \Omega_{32} (\rho_{32} - \rho_{23})] \\
& + \left[\sum_{\substack{i=1 \\ i \neq 3}}^6 W_{i3} \rho_{ii} - W_3 \rho_{33} \right] \\
& + \frac{i}{2} [\Omega_{35} (\rho_{35} - \rho_{53}) + \Omega_{36} (\rho_{36} - \rho_{63})]
\end{aligned} \tag{4.4.3}$$

$$\begin{aligned}
\frac{\partial \rho_{34}}{\partial t} = & \frac{i}{2} [\Omega_{41} \rho_{31} + \Omega_{42} \rho_{32} - \Omega_{31} \rho_{14} - \Omega_{32} \rho_{24}] \\
& - [i\omega_{34} \rho_{34} + \tau_{d,34}^{-1} \rho_{34}] \\
& + \frac{i}{2} [\Omega_{45} \rho_{35} + \Omega_{46} \rho_{36} - \Omega_{35} \rho_{54} - \Omega_{36} \rho_{64}]
\end{aligned} \tag{4.4.4}$$

$$\begin{aligned}
\frac{\partial \rho_{35}}{\partial t} = & -\frac{i}{2} [\Omega_{31} \rho_{15} + \Omega_{32} \rho_{25}] \\
& + \left[\frac{i}{2} (\Omega_{35} \rho_{33} + \Omega_{45} \rho_{34}) - (i\omega_{35} + \tau_{d,35}^{-1}) \rho_{35} \right] \\
& - \frac{i}{2} [\Omega_{35} \rho_{55} + \Omega_{36} \rho_{65}]
\end{aligned} \tag{4.4.5}$$

$$\begin{aligned}
\frac{\partial \rho_{36}}{\partial t} = & -\frac{i}{2} [\Omega_{31} \rho_{16} + \Omega_{32} \rho_{26}] \\
& + \left[\frac{i}{2} (\Omega_{36} \rho_{33} + \Omega_{46} \rho_{34}) - (i\omega_{36} + \tau_{d,36}^{-1}) \rho_{36} \right] \\
& - \frac{i}{2} [\Omega_{35} \rho_{56} + \Omega_{36} \rho_{66}]
\end{aligned} \tag{4.4.6}$$

Assuming that only nearest neighbor elements are nonzero terms such as ρ_{51} , ρ_{61} , etc. will vanish leaving

$$\begin{aligned}\frac{\partial \rho_{31}}{\partial t} = & -\frac{i}{2}[\Omega_{31}\rho_{11} + \Omega_{32}\rho_{21}] \\ & + \left[\frac{i}{2}(\Omega_{31}\rho_{33} + \Omega_{41}\rho_{34}) - (i\omega_{31} + \tau_{d,31}^{-1})\rho_{31} \right]\end{aligned}\quad (4.4.7)$$

$$\begin{aligned}\frac{\partial \rho_{32}}{\partial t} = & -\frac{i}{2}[\Omega_{31}\rho_{12} + \Omega_{32}\rho_{22}] \\ & + \left[\frac{i}{2}(\Omega_{32}\rho_{33} + \Omega_{42}\rho_{34}) - (i\omega_{32} + \tau_{d,32}^{-1})\rho_{32} \right]\end{aligned}\quad (4.4.8)$$

$$\begin{aligned}\frac{\partial \rho_{33}}{\partial t} = & \frac{i}{2}[\Omega_{31}(\rho_{31} - \rho_{13}) + \Omega_{32}(\rho_{32} - \rho_{23})] \\ & + \left[\sum_{\substack{i=1 \\ i \neq 3}}^6 W_{i3}\rho_{ii} - W_3\rho_{33} \right] \\ & + \frac{i}{2}[\Omega_{35}(\rho_{35} - \rho_{53}) + \Omega_{36}(\rho_{36} - \rho_{63})]\end{aligned}\quad (4.4.9)$$

$$\begin{aligned}\frac{\partial \rho_{34}}{\partial t} = & \frac{i}{2}[\Omega_{41}\rho_{31} + \Omega_{42}\rho_{32} - \Omega_{31}\rho_{14} - \Omega_{32}\rho_{24}] \\ & - [i\omega_{34}\rho_{34} + \tau_{d,34}^{-1}\rho_{34}] \\ & + \frac{i}{2}[\Omega_{45}\rho_{35} + \Omega_{46}\rho_{36} - \Omega_{35}\rho_{54} - \Omega_{36}\rho_{64}]\end{aligned}\quad (4.4.10)$$

$$\begin{aligned}\frac{\partial \rho_{35}}{\partial t} = & \left[\frac{i}{2}(\Omega_{35}\rho_{33} + \Omega_{45}\rho_{34}) - (i\omega_{35} + \tau_{d,35}^{-1})\rho_{35} \right] \\ & - \frac{i}{2}[\Omega_{35}\rho_{55} + \Omega_{36}\rho_{65}]\end{aligned}\quad (4.4.11)$$

$$\begin{aligned}\frac{\partial \rho_{36}}{\partial t} = & \left[\frac{i}{2}(\Omega_{36}\rho_{33} + \Omega_{46}\rho_{34}) - (i\omega_{36} + \tau_{d,36}^{-1})\rho_{36} \right] \\ & - \frac{i}{2}[\Omega_{35}\rho_{56} + \Omega_{36}\rho_{66}]\end{aligned}\quad (4.4.12)$$

The real and imaginary parts can be separated by defining

$$\rho_{ij} = \rho'_{ij} + i\rho''_{ij} \quad (4.4.13)$$

This converts the previous expression to

$$\begin{aligned} \frac{\partial \rho_{31}}{\partial t} = & \left[\frac{(\Omega_{32}\rho''_{21} - \Omega_{41}\rho''_{34})}{2} + (\omega_{31}\rho''_{31} - \tau_{d,31}^{-1}\rho'_{31}) \right] \\ & + i \left[\frac{\Omega_{31}(\rho'_{33} - \rho'_{11}) + (\Omega_{41}\rho'_{34} - \Omega_{32}\rho'_{21})}{2} - (\omega_{31}\rho'_{31} + \tau_{d,31}^{-1}\rho''_{31}) \right] \end{aligned} \quad (4.4.14)$$

$$\begin{aligned} \frac{\partial \rho_{32}}{\partial t} = & \left[\frac{(\Omega_{31}\rho''_{12} - \Omega_{42}\rho''_{34})}{2} + (\omega_{32}\rho''_{32} - \tau_{d,32}^{-1}\rho'_{32}) \right] \\ & + i \left[\frac{\Omega_{32}(\rho'_{33} - \rho'_{22}) + (\Omega_{42}\rho'_{34} - \Omega_{31}\rho'_{12})}{2} - (\omega_{32}\rho'_{32} + \tau_{d,32}^{-1}\rho''_{32}) \right] \end{aligned} \quad (4.4.15)$$

$$\begin{aligned} \frac{\partial \rho_{33}}{\partial t} = & -(\Omega_{31}\rho''_{31} + \Omega_{32}\rho''_{32}) \\ & + \left(\sum_{i=1, i \neq 3}^6 W_{i3}\rho'_{ii} - W_3\rho'_{33} \right) \\ & - (\Omega_{35}\rho''_{35} + \Omega_{36}\rho''_{36}) \end{aligned} \quad (4.4.16)$$

$$\begin{aligned} \frac{\partial \rho_{34}}{\partial t} = & \left[\frac{\Omega_{31}\rho''_{14} + \Omega_{32}\rho''_{24} + \Omega_{35}\rho''_{54} + \Omega_{36}\rho''_{64} - \Omega_{41}\rho''_{31} - \Omega_{42}\rho''_{32} - \Omega_{45}\rho''_{35} - \Omega_{46}\rho''_{36}}{2} + (\omega_{34}\rho''_{34} - \tau_{d,34}^{-1}\rho'_{34}) \right] \\ & + i \left[\frac{\Omega_{41}\rho'_{31} + \Omega_{42}\rho'_{32} + \Omega_{45}\rho'_{35} + \Omega_{46}\rho'_{36} - \Omega_{31}\rho'_{14} - \Omega_{32}\rho'_{24} - \Omega_{35}\rho'_{54} - \Omega_{36}\rho'_{64}}{2} - (\omega_{34}\rho'_{34} + \tau_{d,34}^{-1}\rho''_{34}) \right] \end{aligned} \quad (4.4.17)$$

$$\begin{aligned} \frac{\partial \rho_{35}}{\partial t} = & \left[\frac{(\Omega_{36}\rho''_{65} - \Omega_{45}\rho''_{34})}{2} + (\omega_{35}\rho''_{35} - \tau_{d,35}^{-1}\rho'_{35}) \right] \\ & + i \left[\frac{\Omega_{35}(\rho'_{33} - \rho'_{55}) + (\Omega_{45}\rho'_{34} - \Omega_{36}\rho'_{65})}{2} - (\omega_{35}\rho'_{35} + \tau_{d,35}^{-1}\rho''_{35}) \right] \end{aligned} \quad (4.4.18)$$

$$\begin{aligned} \frac{\partial \rho_{36}}{\partial t} = & \left[\frac{(\Omega_{35}\rho''_{56} - \Omega_{46}\rho''_{34})}{2} + (\omega_{36}\rho''_{36} - \tau_{d,36}^{-1}\rho'_{36}) \right] \\ & + i \left[\frac{\Omega_{36}(\rho'_{33} - \rho'_{66}) + (\Omega_{46}\rho'_{34} - \Omega_{35}\rho'_{56})}{2} - (\tau_{d,36}^{-1}\rho''_{36} + \omega_{36}\rho'_{36}) \right] \end{aligned} \quad (4.4.19)$$

By observing the common form of each equation the expressions can be rewritten for the interwell and intrawell elements in a general manner using generic indices as

Interwell

$$\begin{aligned} \frac{\partial \rho_{if}}{\partial t} = & \left[\frac{(\Omega_{ik}\rho''_{kf} - \Omega_{jf}\rho''_{ij})}{2} + (\omega_{if}\rho''_{if} - \tau_{d,if}^{-1}\rho'_{if}) \right] \\ & + i \left[\frac{\Omega_{if}(\rho'_{ii} - \rho'_{ff}) + (\Omega_{jf}\rho'_{ij} - \Omega_{ik}\rho'_{kf})}{2} - (\omega_{if}\rho'_{if} + \tau_{d,if}^{-1}\rho''_{if}) \right] \end{aligned} \quad (4.4.20)$$

Intrawell

$$\begin{aligned}
 \frac{\partial \rho_{ii}}{\partial t} &= \sum_{n=1}^{n+1} (W_{fi} \rho'_{ff} - W_{if} \rho'_{ii} - \Omega_{if} \rho''_{if}) \\
 \frac{\partial \rho_{if}}{\partial t} &= \left[\frac{1}{2} \sum_{s=1, s \neq i, f}^6 (\Omega_{is} \rho''_{sf} - \Omega_{fs} \rho''_{is}) + (\omega_{if} \rho''_{if} - \tau_{d,if}^{-1} \rho'_{if}) \right] \\
 &+ i \left[\frac{1}{2} \sum_{s=1, s \neq i, f}^6 (\Omega_{fs} \rho'_{is} - \Omega_{is} \rho'_{sf}) - (\omega_{if} \rho'_{if} + \tau_{d,if}^{-1} \rho''_{if}) \right]
 \end{aligned} \tag{4.4.21}$$

where (i) is the initial state in a central well, (f) is a final state in a neighboring well, (j) is the other state in the central well, and (k) is the other state in the neighboring well. The sum from (n-1) to (n+1) implies summing over the state in the central well and the neighboring wells on each side. The summation over the index (s) implies to sum over only the states in the neighboring wells.

A major simplification occurs if it is assumed that all off-diagonal coherences are interwell. This permits all ρ_{xy} terms that are not (i) or (f) to be omitted. Using this assumption these equations can be solved in the steady-state as

Interwell off-diagonals (steady-state)

$$\rho'_{ij} = \frac{\frac{1}{2} \Omega_{ij} (\rho'_{ii} - \rho'_{jj}) \omega_{ij}}{(\omega_{ij})^2 + (\tau_{d,ij}^{-1})^2} \quad \rho''_{ij} = \frac{\frac{1}{2} \Omega_{ij} (\rho'_{ii} - \rho'_{jj}) \tau_{d,ij}^{-1}}{(\omega_{ij})^2 + (\tau_{d,ij}^{-1})^2} \tag{4.4.22}$$

Intrawell Diagonals (steady-state)

$$\rho'_{ii} = \frac{\sum_{n=1}^{n+1} \left(W_{fi} \rho'_{ff} + \frac{\frac{1}{2} \Omega_{if}^2 \tau_{d,if}^{-1}}{(\omega_{if})^2 + (\tau_{d,if}^{-1})^2} \rho'_{ff} \right)}{\sum_{n=1}^{n+1} \left(W_{if} + \frac{\frac{1}{2} \Omega_{if}^2 \tau_{d,if}^{-1}}{(\omega_{if})^2 + (\tau_{d,if}^{-1})^2} \right)} \tag{4.4.23}$$

The dephasing is written as

$$\Gamma_{if}^{nm} = (\tau_{d,if}^{nm})^{-1} = \frac{1}{2\tau_i^n} + \frac{1}{2\tau_f^m} + \Gamma^{\text{pure}} \quad (4.4.24)$$

and defining a coherent tunneling term as

$$\Phi_{if}^{nm} = \frac{\Gamma_{if}^{nm} (\Omega_{if}^{nm})^2}{(\omega_{if}^{nm})^2 + (\Gamma_{if}^{nm})^2} \quad (4.4.25)$$

allows the diagonals to be written entirely in terms of the other diagonals

$$\rho'_{ii} = \frac{\sum_{n=1}^{n+1} \left[\left(W_{fi} + \frac{1}{2} \Phi_{fi} \right) \rho'_{ff} \right]}{\sum_{n=1}^{n+1} \left(W_{if} + \frac{1}{2} \Phi_{if} \right)} \quad (4.4.26)$$

In the above the indices in the Φ terms were flipped for clarity. This makes no difference as $\Phi_{if} = \Phi_{fi}$. In this expression the description of the diagonal elements now closely resembles the semi-classical steady-state rate equations with the inclusion of additional tunneling terms Φ . If Φ were set to zero in Equation 4.4.26 the expressions return to the semiclassical form. With the addition of these terms, however, both the contributions of incoherent scattering (the W 's) and the coherent tunneling (the Φ 's) can be treated simultaneously.

As an example consider the superlattice system (Figure 4.4.2) which was solved using the standard density matrix approach in Section 4.3. In this calculation again assume a 2-state single well system which repeats indefinitely. Also assume, as before, that the only relevant interwell coupling term is the 1' to 2, and equivalent, interactions. The only scattering rate in this simple system is considered to be the excited to ground transition.

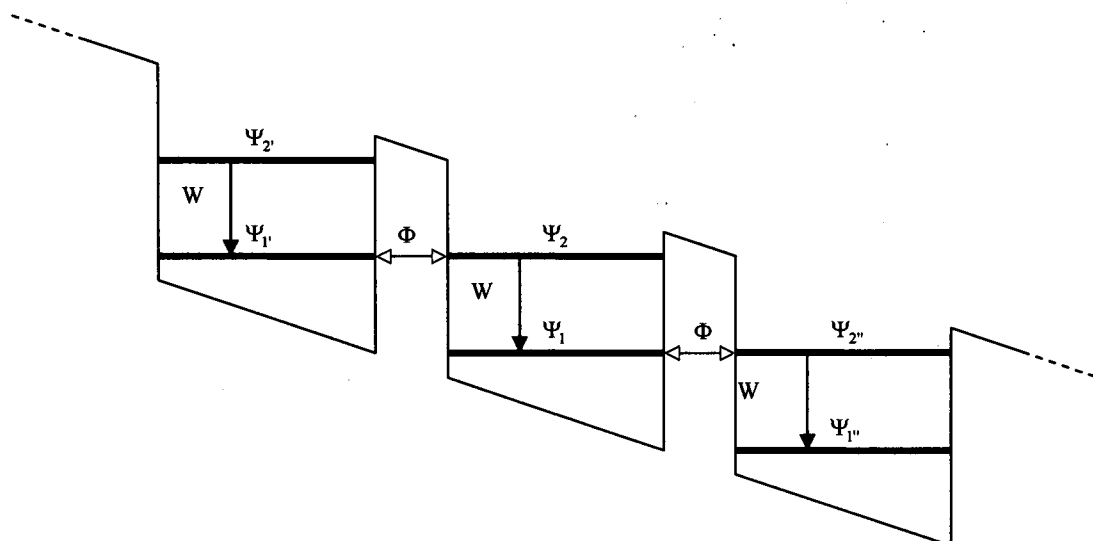


Figure 4.4.2: Simple repeating two state superlattice for the diagonal density matrix description.

Now, using the diagonal density matrix (DDM) description (Equation 4.4.26) the ground and excited steady-states equations are

$$\rho_{11} = \frac{\left(W + \frac{1}{2}\Phi\right)\rho_{22}}{\frac{1}{2}\Phi} \quad \rho_{22} = \frac{\frac{1}{2}\Phi\rho_{11}}{W + \frac{1}{2}\Phi} \quad (4.4.27)$$

In this picture the interaction between the coupled states on each side of the barrier is shown to be equivalent. There is essentially an oscillating loop between state 1' and 2 which is both pumped and drained by the intrawell scattering W . This system then could also, as previously shown in Section 4.2, be depicted as shown in Figure 4.4.3.

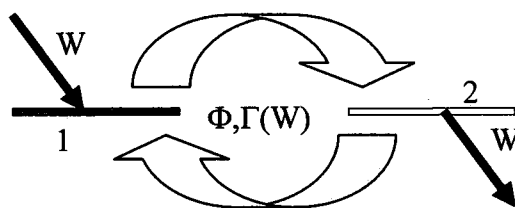


Figure 4.4.3: The repeating superlattice in the 2-state description.

In this picture the flow of electrons across the barrier is driven by both the scattering and the oscillation. In the steady state, any electron draining out of $|2\rangle$ due to scattering must be replaced by the tunneling of an electron from state $|1\rangle$. Since the system repeats itself the rate of scattering into state $|1\rangle$ is equivalent to the draining of state $|2\rangle$. Now it becomes more clear that the relationship between the oscillation rate, the scattering, and the dephasing will determine the population and current flow across the system.

To solve this system the previous expressions can be written into the augmented matrix

$$\begin{bmatrix} -\frac{1}{2}\Phi & W + \frac{1}{2}\Phi & 0 \\ \frac{1}{2}\Phi & -W - \frac{1}{2}\Phi & 0 \\ 1 & 1 & 1 \end{bmatrix} \quad (4.4.28)$$

where the last row ensures that the $\text{Trace}(\rho)=1$. The solution is

$$\rho_{11} = \frac{W + \frac{1}{2}\Phi}{W + \Phi} \quad \rho_{22} = \frac{\frac{1}{2}\Phi}{W + \Phi} \quad (4.4.29)$$

Using Figure 4.4.3 it can again be reasoned that any electron draining from $|2\rangle$ must be replaced through the tunneling term Φ pulling an electron across the barrier from state $|1\rangle$. Conversely, to maintain steady-state populations, any new electron injected into state $|1\rangle$ must tunnel across the barrier to state $|2\rangle$. Since the oscillation is a 2-way cyclical process the current can be written as

$$J = J_{12} - J_{21} = qN_s \frac{1}{2} \Phi (\rho_{11} - \rho_{22}) = \frac{qN_s}{2} \Phi (\Delta\rho_{12}) \quad (4.4.30)$$

In this expression the direction of the current flow will be, logically, from higher to lower electron concentration. Plugging in the solutions gives, for the normalized inversion and current density

$$\Delta\rho_{12} = \frac{W}{W + \Phi} \quad J = \frac{qN_s}{2} \frac{\Phi W}{W + \Phi} \quad (4.4.31)$$

Consider this expression for the current density. First, expanding the Φ terms using equation 4.4.25 gives

$$J = \frac{qN_s}{2} \frac{\frac{\Gamma\Omega^2}{\omega^2 + \Gamma^2} W}{W + \frac{\Gamma\Omega^2}{\omega^2 + \Gamma^2}} \quad (4.4.32)$$

This expression simplifies to

$$J = \frac{qN_s}{2} \frac{\Gamma\Omega^2 W}{\Gamma^2 W + \omega^2 W + \Gamma\Omega^2} \quad (4.4.33)$$

Multiply the numerator and denominator by $\tau_d^2 \tau = (\Gamma^2 W)^{-1}$ gives

$$J = \frac{qN_s}{2} \frac{\Omega^2 \tau_d}{1 + (\Delta E/\hbar)^2 \tau_d^2 + \Omega^2 \tau_d \tau} \quad (4.4.34)$$

which is identical to the expression derived in Section 4.3 using the standard density matrix approach. Similarly the inversion is

$$\Delta\rho_{12} = \frac{1 + (\Delta E/\hbar)^2 \tau_d^2}{1 + (\Delta E/\hbar)^2 \tau_d^2 + \Omega^2 \tau_d \tau} \quad (4.4.35)$$

As observed in the previous chapter if the oscillation is much faster than the scattering and dephasing (i.e. $\Omega^2 \tau_d \tau \gg 1$) and, assuming a resonance condition where $\Delta E = 0$, these expressions reduce to

$$J = \frac{qN_s}{2} W \quad \text{and} \quad \Delta\rho_{12} = 0 \quad (4.4.36)$$

Therefore if the oscillation dominates the states are equally populated and, as can be reasoned by observing Figure 4.4.3, the current flow is entirely due to the pumping/draining rate W . This case is, as pointed out previously, identical to the semiclassical description using the LCIS method with no intradoublet scattering (see Figure 4.4.4).

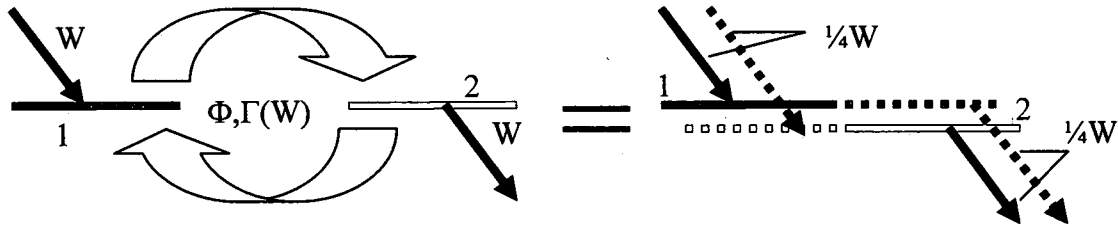


Figure 4.4.4: The equivalence of the DDM and LCIS method (w/o intradoublet scattering) for the limiting case of $\Omega^2 \tau_d \tau \gg 1$.

In the other limit, where the scattering/dephasing dominates, i.e. $\Omega^2 \tau_d \tau \ll 1$

$$J = \frac{qN_s}{2} \frac{\Omega^2}{\Gamma} \quad \text{and} \quad \Delta\rho_{12} = 1 \quad (4.4.37)$$

which signifies that electrons are built up in state 1, on the left side of the barrier, and the oscillation is a one-way tunneling process. This unity inversion does not imply the possibility of large gain rather it signifies that, due to the dominance of the scattering/dephasing, the states should actually be considered entirely localized. Further, it implies that the tunneling process is so slow that all electrons are essentially stuck behind the barrier in state 1. This situation is depicted in Figure 4.4.5. It is therefore important to note that this effect cannot be treated in the semiclassical description as the coupling-induced delocalization automatically implies coherency across the barrier.

$$\rho_{11} = \frac{W_{21}\rho_{22} + \frac{1}{2}(\Phi_{gg}\rho_{11} + \Phi_{eg}\rho_{22} + \Phi_{gg}\rho_{11} + \Phi_{ge}\rho_{22})}{W_{12} + \frac{1}{2}(\Phi_{gg} + \Phi_{eg} + \Phi_{gg} + \Phi_{ge})} \quad (4.4.38)$$

$$\rho_{22} = \frac{W_{12}\rho_{11} + \frac{1}{2}(\Phi_{ge}\rho_{11} + \Phi_{ee}\rho_{22} + \Phi_{ee}\rho_{22} + \Phi_{eg}\rho_{11})}{W_{21} + \frac{1}{2}(\Phi_{ge} + \Phi_{ee} + \Phi_{ee} + \Phi_{eg})} \quad (4.4.39)$$

The solutions for this system are

$$\rho_{11} = \frac{W_{21} + \frac{1}{2}(\Phi_{ge} + \Phi_{eg})}{W_{21} + W_{12} + (\Phi_{ge} + \Phi_{eg})} \quad \rho_{22} = \frac{W_{12} + \frac{1}{2}(\Phi_{ge} + \Phi_{eg})}{W_{21} + W_{12} + (\Phi_{ge} + \Phi_{eg})} \quad (4.4.40)$$

It is immediately noticed that the "self-tunneling" terms cancel from the expressions. This makes perfect sense in the repeating superlattice system as the ground(excited) states in each well have equal populations and equal tunneling terms Φ and therefore there would be no net transfer between these equivalent states.

The current flowing across the barrier is then the combined flow into states $|2\rangle$ and $|1\rangle$, minus the backflow

$$J = J_1 + J_2 = qN_s (\Phi_{eg} [\rho_{22} - \rho_{11}] + \Phi_{ge} [\rho_{11} - \rho_{22}]) \quad (4.4.41)$$

Here, if the $2' \rightarrow 1$ states are far from resonance the equation reduces to the previously derived simplified form. In this general case, however, substituting in ρ_{11} and ρ_{22} gives

$$J = qN_s \left(\frac{\Phi_{eg}(W_{12} - W_{21}) + \Phi_{ge}(W_{21} - W_{12})}{W_{21} + W_{12} + (\Phi_{ge} + \Phi_{eg})} \right) \quad (4.4.42)$$

Notice that the first term $\Phi_{eg}(W_{12} - W_{21})$ implies a negative current flow if $W_{21} > W_{12}$ which is usually the case. This is a result of the current being defined as moving from left

to right. In order to get a strong Φ_{eg} though, the system must be reverse biased (see Figure 4.4.7). In this case it is logical that the current flow would move right to left which would be the negative bias for the chosen directional designation.

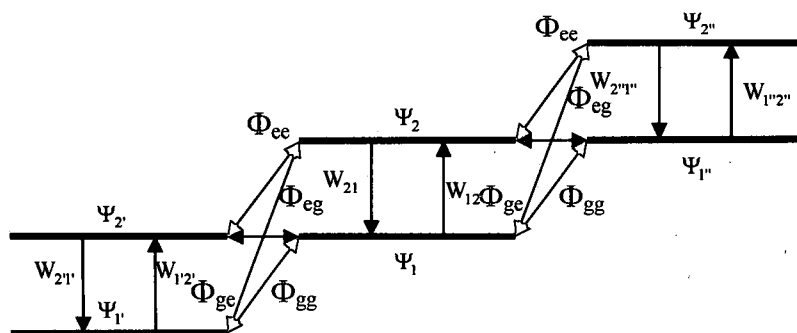


Figure 4.4.7: A more general treatment of the 2-state superlattice with numerous interwell tunneling terms.

4.5 Combining Coherent and Incoherent Transport

In Section 4.3. and Section 4.4. the application of the density matrix or the diagonal density matrix (DDM) to a 2-state per well system was shown to converge in the steady-state to the semiclassical LCIS description when the oscillation is very fast compared to the dephasing/scattering. To gain further insight into these equivalent pictures consider the diagram of Figure 4.5.1. In the semiclassical LCIS description of transport it was shown that starting with the localized single well basis, and assuming all scattering is intrawell, an expansion of Fermi's Golden Rule could be made using the tight-binding coupling coefficients where the current flows do to the delocalization of the wavefunctions.

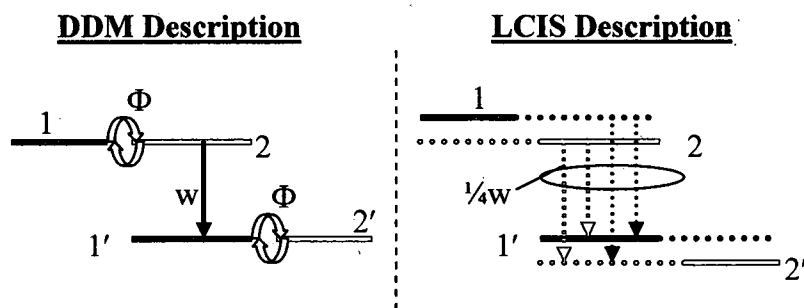


Figure 4.5.1: Comparison of the DDM and LCIS descriptions of transport.

As discussed in Section 4.2., the current flow could be explained as being a result of interwell scattering yet the more appropriate picture is to consider the scattering as simply being components of the local intrawell rate. As previously concluded, this semiclassical description is actually representing perfect coherency across the doublet states and thus the true nature of the interwell transport is a coherent phenomena. The scattering itself does not transfer electrons from one well to another, rather it serves to pump and drain the oscillating doublet on the local level. This is precisely the assumption that was made in the density matrix picture also shown in Figure 4.5.1. In this description the states are completely isolated in their respective wells. The intrawell scattering rate is the full basis rate (w) as there are no components, since there is no static coupling. In this situation the interwell transport is described by the coherent tunneling terms Φ . Analysis for both of these models established that in the limit where the oscillation dominates (i.e. $\Omega^2 \gg \Gamma W$) these pictures are exactly identical. This equivalency is again pictured below in Figure 4.5.2.

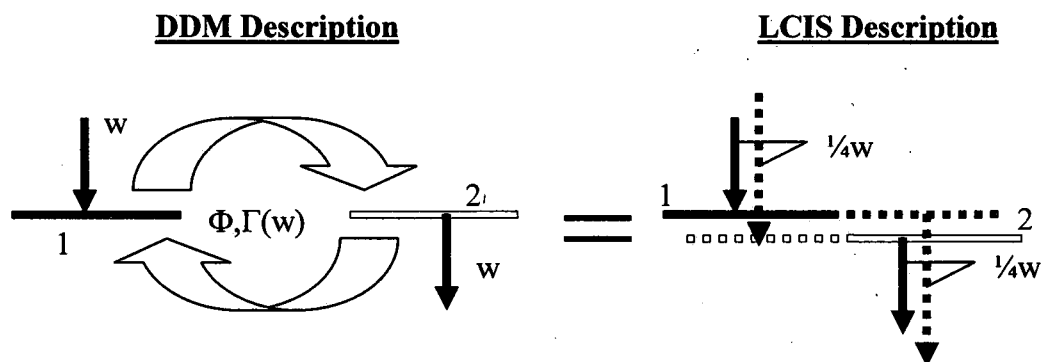


Figure 4.5.2: The equivalence of the DDM and LCIS method for the limiting case of $\Omega^2 \gg \Gamma W$.

This result was again logically reasoned as an electron in either state $|1\rangle$ or $|2\rangle$ are oscillating very quickly across the barrier. Since electrons have the ability to tunnel back and forth many times before scattering out of the doublet it is not unexpected that the static delocalized wavefunction, representing the probability of the electrons position, would be spread equally across both wells. In the opposite limit however, shown in Figure 4.5.3, where the scattering/dephasing dominates $\Omega^2 \ll W\Gamma$, there is significant disagreement between the descriptions.

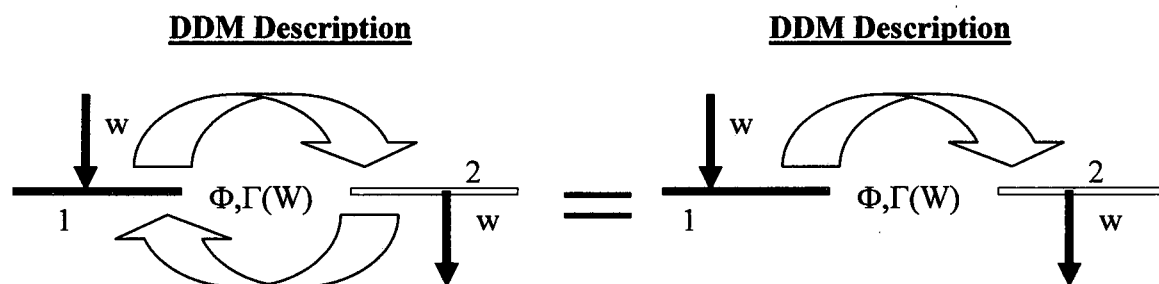


Figure 4.5.3: The non-equivalence of the DDM and LCIS method for the limiting case of $\Omega^2 \ll W\Gamma$.

In this case the dominance of the dephasing/scattering creates the scenario where any electron which tunnels from state $|1\rangle$ to $|2\rangle$ is drained from the doublet before it can ever tunnel back. The DDM description then suggests that there is not an equal probability of finding the electron in both states. In fact, since the system repeats itself the draining of the excited state $|2\rangle$ sends the population back into the next ground state $|1'\rangle$ and therefore, near this limit, practically the entire population resides in the ground state of each well. There is no semiclassical analogue for this situation. Applying the delocalized doublet picture to this result would suggest a large population inversion which could be exploited to produce lasing when in fact there is no doublet.

This realization is very important for the modeling of THz-QCL's as most of the successful designs achieve lasing between states which form a doublet. Consider a generic laser design for this type of intradoublet lasing (Figure 4.5.4). In this figure the common strategy for THz-QCL's is shown. Much like the traditional 4-level laser the upper state must be pumped by some mechanism and the lower state drained. As previously discussed and established, the full use of a semiclassical description is not appropriate for the modeling of these devices. It is then important to determine how the density matrix description, or specifically the simplified DDM, can be implemented.

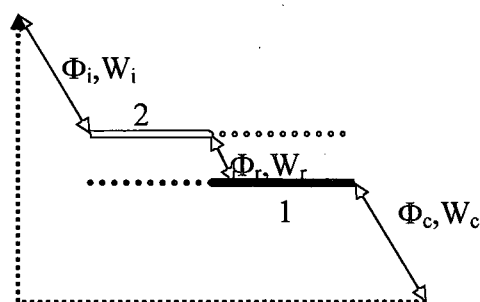


Figure 4.5.4: General strategy for an intradoublet lasing THz-QCL.

There are some fundamental questions that must be answered with regards to the density matrix description presented. The first is directly related to the use of the localized basis. Since the diagonal element ρ_{ii} of the density matrix represents the probability of finding the system in the basis state $|i\rangle$ a large inversion in the upper state of a doublet (as depicted in Figure 4.5.4), signifies only that the electrons reside in this local state (or well). In the standard use of extended wavefunctions a large delocalization is usually sought after to produce the appropriate wavefunction overlap needed for larger oscillator strengths to promote gain. While a treatment of gain will be given in the next Chapter the important aspect to consider is that without an obvious picture of delocalization it is unclear how radiative transitions can occur. This is also a question of localized scattering. If only intrawell scattering occurs within the localized basis where do the radiative transitions come from? Further, if the resonance condition for the localized basis is $\omega = 0$, and yet phonons are emitted, do they have zero energy $\hbar\omega = 0$?

The density matrix formalism itself should be, theoretically, independent of the choice of basis. An expansion could have been made, for instance, using the full eigenstates of the numerically calculated system. Either choice in this manner, localized or delocalized, is still an approximation. Neither choice is truly a complete set as they describe only the bound states and in their respective presentations in this work, treat the subband as a singular object. With these common deficiencies being stated the choice of the localized basis can be argued to be more suitable. Consider the overdamped case where $\Omega^2 \ll W\Gamma$. This represents a coherency between states which is destroyed due to fast dephasing/scattering. It is then assumed in the decoherence of the states that the system collapses down to the basis. Thus, if the delocalized basis was chosen this system would collapse, illogically, to a still delocalized state.

In keeping with the spirit of this research, the goal is not to develop a comprehensive and complete theory of everything. Instead, it is to determine what needs to be included and how can this be simplified to present an intuitive, accessible, and computationally efficient approach to modeling THz-QCL's. In light of this objective the choice of basics (delocalized vs. localized) can be examined. Consider that, as demonstrated in Section 4.2, the use of the local basis can be expanded using the LCIS method essentially reproducing the delocalized system. For a simplified analysis consider the system portrayed in Figure 4.5.5.

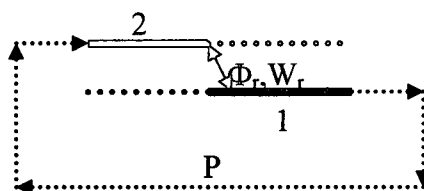


Figure 4.5.5: Simple picture of two states with a repeating pumping mechanism.

In this picture there are two states in separate wells and there is some undefined pumping mechanism which repeats the loop. Assuming the states are then coupled and delocalized the system, in a multiple period picture, can be presented as shown in Figure 4.5.6.

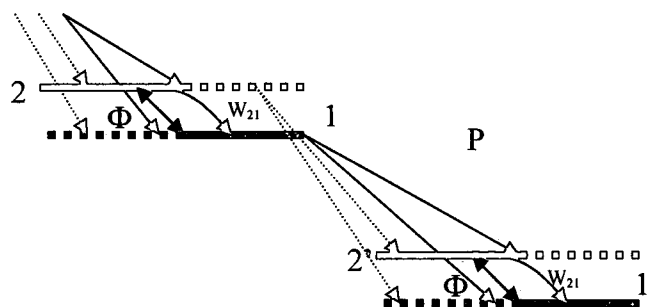


Figure 4.5.6: Repeating 2-state system connected by a pumping mechanism in the delocalized state representation.

In the DDM derivation of Section 4.4., the resulting description of the diagonal elements was

$$\rho'_{ii} = \frac{\sum_{n=1}^{n+1} \left[\left(W_{fi} + \frac{1}{2} \Phi_{fi} \right) \rho'_{ff} \right]}{\sum_{n=1}^{n+1} \left(W_{if} + \frac{1}{2} \Phi_{if} \right)} \quad (4.5.1)$$

which made no assumption as to the spatial extent of the scattering. As shown previously, if the states are considered equally delocalized the local pumping rate P can be broken into 4 equal components of $\frac{1}{4}P$. First, the semiclassical LCIS steady state matrix would be

$$\begin{bmatrix} -W_{12'} & W_{21} + W_{21'} & 0 \\ W_{12'} & -W_{21} - W_{21'} & 0 \\ 1 & 1 & 1 \end{bmatrix} = \begin{bmatrix} -\frac{1}{4}P & W_{21} + \frac{1}{4}P & 0 \\ \frac{1}{4}P & -W_{21} - \frac{1}{4}P & 0 \\ 1 & 1 & 1 \end{bmatrix} \quad (4.5.2)$$

which results in an inversion and current density of

$$\Delta\rho_{21,LCIS} = \frac{-2W_{21}}{2W_{21} + P} \quad \text{and} \quad J_{LCIS} = \frac{qN_s}{2} P \quad (4.5.3)$$

The difference between this result and the previous examples is that now an intradoublet scattering rate W_{21} is included. This additional scattering rate can be observed to not effect the calculation of the current. Only the inversion is effected and in the limit of a vanishing W_{21} rate returns to the "pure doublet" case. For the DDM description this fully delocalized system, using Equation 4.5.1, takes a similar form but now includes the tunneling terms

$$\begin{bmatrix} -\frac{1}{4}P - \frac{1}{2}\Phi & W_{21} + \frac{1}{4}P + \frac{1}{2}\Phi & 0 \\ \frac{1}{4}P + \frac{1}{2}\Phi & -W_{21} - \frac{1}{4}P - \frac{1}{2}\Phi & 0 \\ 1 & 1 & 1 \end{bmatrix} \quad (4.5.4)$$

For this case the current flowing across the barrier now has additional terms (Figure 4.5.7)

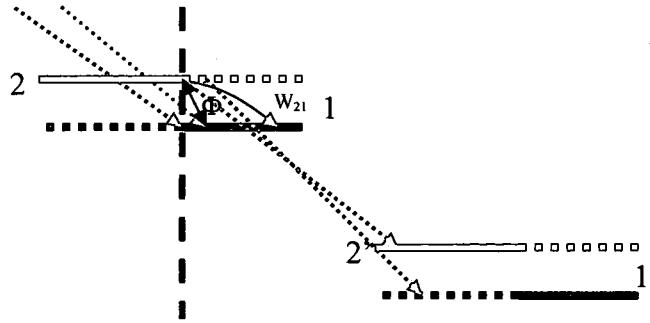


Figure 4.5.7: The inclusion of additional (Coherent + Incoherent) current.

Writing out both the scattering and tunneling components of the current across the barrier gives

$$J_{\text{DDM}} = qN_s \left(\frac{1}{4}P + W_{21}\rho_{22} + \frac{1}{2}P\rho_{22} \right) + qN_s \frac{1}{2}\Phi(\rho_{22} - \rho_{11}) \quad (4.5.5)$$

Solving the system in Equation 4.5.4 produces the solutions for the diagonal elements

$$\rho_{11} = \frac{2W_{21} + \frac{1}{2}P + \Phi}{2W_{21} + P + 2\Phi} \quad \rho_{22} = \frac{\frac{1}{2}P + \Phi}{2W_{21} + P + 2\Phi} \quad (4.5.6)$$

Inserted this into Equation 4.5.5., produces

$$J_{\text{DDM}} = qN_s \frac{1}{2}P \quad (4.5.7)$$

which is exactly the same as the semiclassical case. This result is at first surprising since the starting conditions assumed that both tunneling and delocalized scatter could

contribute to the current flow. In fact, now the tunnel contribution to the current flow has completely disappeared. The fundamental flaw in this picture is logically revealed as if the scattering is through delocalized states the system is already considered fully coherent. As previously mentioned, even if dephasing/scattering is overwhelming the system collapses to the delocalized starting condition.

The inversion calculated in this manner is different then the semiclassical case and can be written as

$$\Delta\rho_{21} = \frac{-2W_{21}}{2W_{21} + P + 2\Phi} \quad (4.5.8)$$

Here there is an additional term of 2Φ which is absent in the previous LCIS derivation. This expression then converges to the semiclassical case if $\Phi \rightarrow 0$. This limit represents a situation where

$$\Phi = \frac{\Gamma\Omega^2}{\omega^2 + \Gamma^2} \rightarrow 0 \quad (4.5.9)$$

which, at the standard resonance condition of $\omega = 0$ implies

$$\Phi(\omega = 0) = \frac{\Gamma\Omega^2}{\Gamma^2} = \frac{\Omega^2}{\Gamma} \rightarrow 0 \quad (4.5.10)$$

This means that the dephasing would need to be much larger than the oscillation. This again is an illogical conclusion as the density matrix description of coupled well interactions should converge to the semiclassical when there is coherence, not when the system collapses.

Clearly the combination of the DDM treatment combined with full delocalized scattering is not the correct method for treating both coherent and incoherent events. Assuming then that this description should limit the scattering to intrawell the problem

of radiative emission then appears. First, consider a typical doublet used for a THz-QCL (Figure 4.5.8).

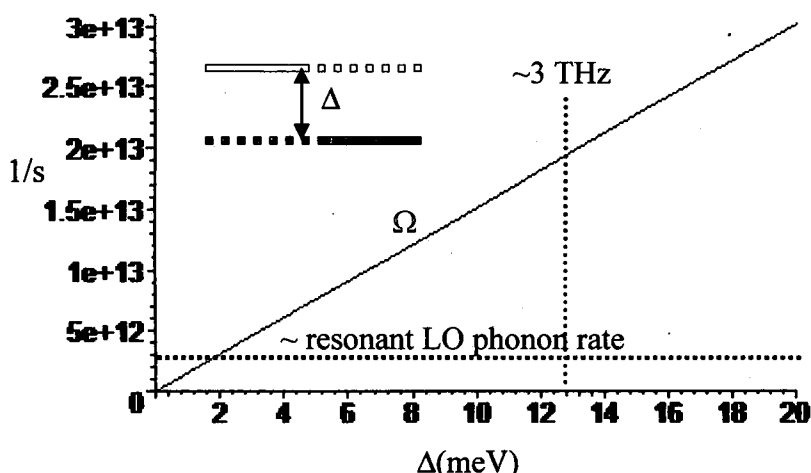


Figure 4.5.8: The oscillation frequency for a typical doublet in a THz-QCL.

In this figure the oscillation frequency Ω is plotted vs. the doublet splitting energy $\Delta = 2\tilde{V}$. For reference, a line at approximately 3THz is drawn as well as a typical resonant LO phonon scattering rate. Normally the doublet itself is pumped and drained through interwell transport and thus should not experience such a large scattering/dephasing rate since the upper and lower states are well below the phonon resonance. It is therefore safe to assume, in the typical THz-QCL system, that the oscillation between the lasing states is much faster than the scattering/dephasing and thus a doublet does exist, as designed. With this in mind, the resonance condition which produces the radiative doublet should not be considered as $\omega=0$. If this were the case there would be no energy of the photon emitted.

Since the energy of the photon emitted in the radiative transition is due to the energy splitting consider the resonance condition for this presupposed doublet to be $\omega = \Omega = 2\tilde{V}/\hbar$. To compare this to the $\omega=0$ condition as well as the semiclassical transport consider first a doublet system, such as shown in 4.5.5., with a very low pumping rate of $P=1 \times 10^{11} \text{ s}^{-1}$ and a constant $\Gamma^{\text{pure}}=1 \times 10^{12} \text{ s}^{-1}$. In this example (Figure 4.5.9) consider there to be no intradoublet scattering $W_{21}=0$ in either the DDM or LCIS descriptions, and assume a nominal sheet density of $N_s=2 \times 10^{10} \text{ cm}^{-2}$.

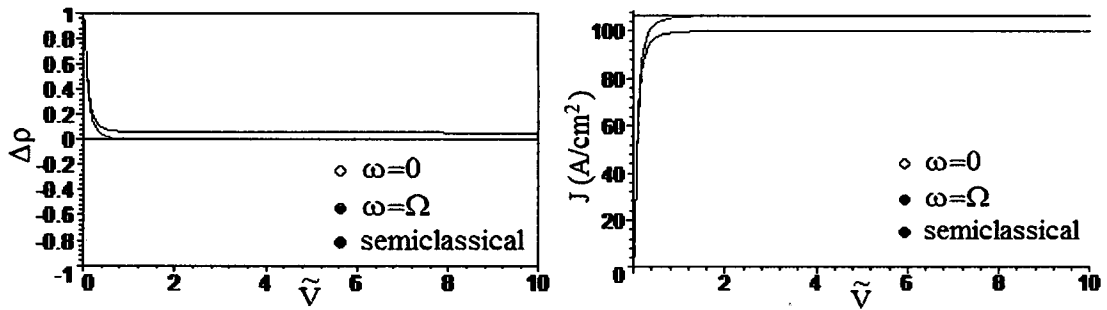


Figure 4.5.9: Comparison of the normalized inversion and current densities for a doublet pumped and drained at $P=1 \times 10^{11} \text{ s}^{-1}$.

The semiclassical case, which is independent of \tilde{V} (i.e. the barrier width), produces a constant “pure doublet” since the LCIS rates are assumed identical for each state. The difference between the $\omega=0$ and the $\omega=\Omega$ resonance descriptions are fairly small. Both inversion plots can be seen to decay very quickly from being stuck behind the barrier (very low \tilde{V} or large barrier) to becoming “pure doublets” with no inversion. While the zero energy resonance drops all the way to equal populations the $\omega=\Omega$ simulation seems to converge to a small but nonzero value. The same behavior is witnessed in the convergence towards the semiclassical current as the oscillation dominates over the dephasing/scattering.

Increasing the pumping rate to a fairly large $P=5 \times 10^{12} \text{s}^{-1}$ value gives the results shown in Figure 4.5.10.

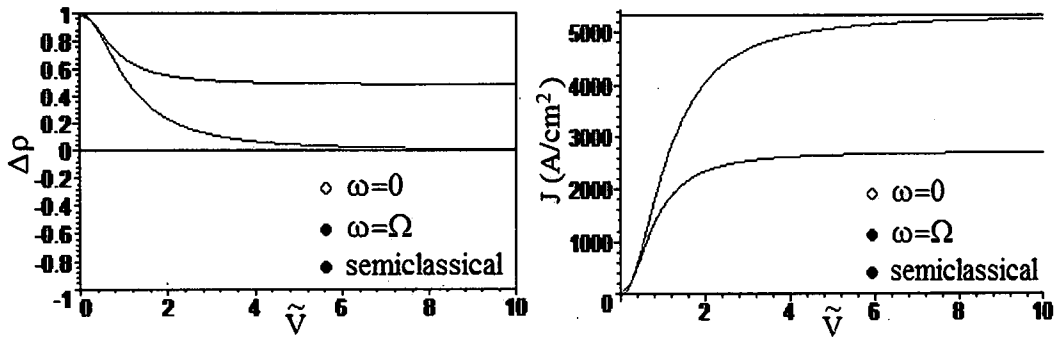


Figure 4.5.10: Comparison of the normalized inversion and current densities for a doublet pumped and drained at $P=5 \times 10^{12} \text{s}^{-1}$.

The semiclassical inversion of course is unchanged due to the symmetry of the rates. With this increased pumping rate though, there is a significant difference between the two resonant conditions. First, the $\omega=0$ case again drops very quickly to the pure doublet condition where it converges to the semiclassical current. The $\omega=\Omega$ case on the other hand decays and converges to a nonzero inversion and a current density close to $\frac{1}{2}$ that of the semiclassical case.

This disagreement can be further investigated by fixing \tilde{V} and varying the pumping rate. This fixed coupling (or barrier width) simulation is shown in Figure 4.5.11 for $\tilde{V} = 1 \text{meV}$ and in Figure 4.5.12 for $\tilde{V} = 10 \text{meV}$. At $\tilde{V} = 1 \text{meV}$, implying a thick barrier, both simulations are very similar. They both predict an inversion, although this is the case where the population is actually stuck behind the barrier and is not useful for gain.

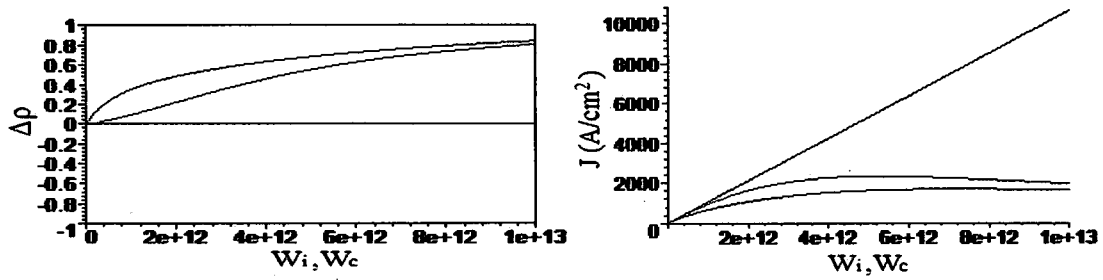


Figure 4.5.11: Comparison of the normalized inversion and current densities for a doublet with a constant $\tilde{V} = 1\text{meV}$ at various pumping rates.

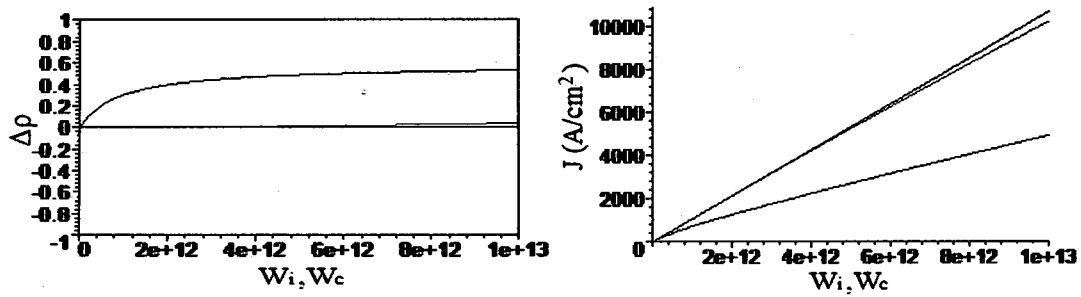


Figure 4.5.12: Comparison of the normalized inversion and current densities for a doublet with a constant $\tilde{V} = 10\text{meV}$ at various pumping rates.

For the thin barrier with $\tilde{V} = 10\text{meV}$ it is observed that the $\omega=\Omega$ predicts an increasing inversion with an increasing pumping rate. This is a logical result as the upper state is injected and the lower state drained at higher levels. In contrast, the $\omega=0$ resonance condition is overwhelmed by the large oscillations pull towards the zero inversion “pure doublet”. Since THz lasing in QCL’s has been in these intradoublet designs the inversion must exist. Clearly the splitting of the energy for the doublet system (i.e. $\omega=\Omega$) is the more suitable decision.

There still remains the problem of the interwell radiative emission. If the doublet is oscillating very fast compared to the dephasing/scattering the density matrix predicts a probability of the population to be distributed on each side of the barrier. If the hypothesis of local scattering is kept, much like the splitting of the LCIS rates into components (Figure 4.5.1), the assumption can then be made that the intradoublet transitions are also local in nature (Figure 4.5.13).

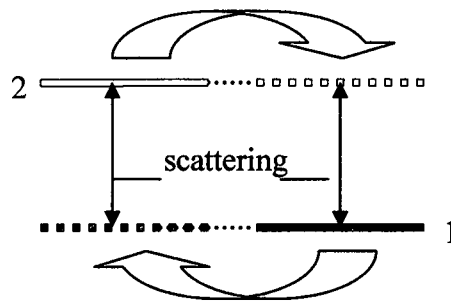


Figure 4.5.13: Locally expanded intradoublet scattering.

Using this picture the scattering will be described as being the LCIS components of the intrawell basis rates and the transport will still be considered as coherent through the DDM analysis using the doublet splitting condition $\omega = \Delta E/\hbar = 2\tilde{V}/\hbar = \Omega$. In this representation intradoublet scattering is not permitted to transfer electrons from one well to the other, and thus does not actually fit into the density matrix description of transfer from one diagonal element to another. Instead, intradoublet scattering, which may include electron-electron or higher electronic temperature LO-phonon transitions, will be inserted into the dephasing of the oscillation. In this depiction the population inversion would not be directly altered due to higher temperature permitted phonon

transitions but instead would be indirectly influenced by the dephasing rate Γ . To expand on this indirect influence further a proper description of the gain is required.

4.6 Gain in Terahertz Quantum Cascade Lasers

In Section 4.4 expressions were derived for a simplified density matrix (DDM) where all diagonal terms can be written in terms of the other diagonals in the system. This method can now be used to obtain an expression for the gain due to a two-state system interacting with a time harmonic electric field. In this representation the off-diagonal element ρ_{21} is

$$\rho_{21} = \frac{\frac{1}{2}\Omega_{21}(\rho_{22} - \rho_{11})\omega_{21}}{(\omega_{21})^2 + (\tau_{d,21}^{-1})^2} + i \frac{\frac{1}{2}\Omega_{21}(\rho_{22} - \rho_{11})\tau_{d,21}^{-1}}{(\omega_{21})^2 + (\tau_{d,21}^{-1})^2} \quad (4.6.1)$$

To implement the interaction with a radiation field $E(t)$ assume the steady state inversion $(\rho_{22} - \rho_{11})$ is entirely dependent on the coupled well transport mechanisms and not on the radiation field itself (small signal approximation). This inversion will be designated as the unperturbed inversion ΔQ_0 representing the states in the absence of the additional field. Now with the assumption that the coupled well perturbations have already reached this unperturbed steady-state, consider the new perturbation by switching the usual term

$$\frac{1}{2}\Omega_{21} = \frac{\tilde{V}}{\hbar} \rightarrow \frac{-\mu E(t)}{\hbar} \quad (4.6.2)$$

to one that now describes the interaction with the radiation field. Similarly, a switch can in the frequency term

$$\omega_{21} \rightarrow (\omega_0 - \omega) \quad (4.6.3)$$

where ω_0 is the frequency difference of the states due to the coupled well and static field interactions and ω is the frequency of the radiation field where

$$E(t) = \frac{E_0}{2} (e^{i\omega t} + e^{-i\omega t}) \quad (4.6.4)$$

Inserting this into Equation 4.6.1., gives

$$\rho_{21} = \frac{\frac{-\mu E_0}{2\hbar} \Delta\rho_0 (\omega_0 - \omega)}{(\omega_0 - \omega)^2 + (\tau_{d,21}^{-1})^2} (e^{i\omega t} + e^{-i\omega t}) + i \frac{\frac{-\mu E_0}{2\hbar} \Delta\rho_0 \tau_{d,21}^{-1}}{(\omega_0 - \omega)^2 + (\tau_{d,21}^{-1})^2} (e^{i\omega t} + e^{-i\omega t}) \quad (4.6.5)$$

Defining the slowly varying variables

$$\begin{aligned} \rho_{21}(t) &= \sigma_{21}(t) e^{-i\omega t} \\ \rho_{12}(t) &= \sigma_{12}(t) e^{i\omega t} \end{aligned} \quad (4.6.6)$$

gives

$$\sigma_{21} = \frac{\frac{-\mu E_0}{2\hbar} \Delta\rho_0 (\omega_0 - \omega)}{(\omega_0 - \omega)^2 + (\tau_{d,21}^{-1})^2} + i \frac{\frac{-\mu E_0}{2\hbar} \Delta\rho_0 \tau_{d,21}^{-1}}{(\omega_0 - \omega)^2 + (\tau_{d,21}^{-1})^2} \quad (4.6.7)$$

where higher order 2ω terms have been discarded. Separating this into real and imaginary parts produces

$$R\{\sigma_{21}\} = \frac{-\Omega_r \Delta\rho_0 (\omega_0 - \omega)}{(\omega_0 - \omega)^2 + (\tau_{d,21}^{-1})^2} \quad (4.6.8)$$

$$Im\{\sigma_{21}\} = \frac{-\Omega_r \Delta\rho_0 \tau_{d,21}^{-1}}{(\omega_0 - \omega)^2 + (\tau_{d,21}^{-1})^2} \quad (4.6.9)$$

where $\Omega_r = \frac{\mu E_0}{2\hbar}$. Using these expressions in the ensemble average of the induced

dipole moment from Section 4.3 gives

$$\langle \mu \rangle = 2\mu \left(\frac{-\Omega_r \Delta \rho_o (\omega_o - \omega)}{(\omega_o - \omega)^2 + (\tau_{d,21}^{-1})^2} \cos \omega t + \frac{-\Omega_r \Delta \rho_o \tau_{d,21}^{-1}}{(\omega_o - \omega)^2 + (\tau_{d,21}^{-1})^2} \sin \omega t \right) \quad (4.6.10)$$

Using the macroscopic polarization $P = N\langle \mu \rangle$ and

$$\begin{aligned} P(t) &= \text{Re} \{ \epsilon_o \chi E_o e^{i\omega t} \} \\ &= E_o \epsilon_o (\chi' \cos \omega t + \chi'' \sin \omega t) \end{aligned} \quad (4.6.11)$$

allows the polarization to be written as

$$P = \left(\frac{-\frac{\mu^2 E_o}{\hbar} \Delta N_o (\omega_o - \omega)}{(\omega_o - \omega)^2 + (\tau_{d,21}^{-1})^2} \cos \omega t + \frac{-\frac{\mu^2 E_o}{\hbar} \Delta N_o \tau_{d,21}^{-1}}{(\omega_o - \omega)^2 + (\tau_{d,21}^{-1})^2} \sin \omega t \right) \quad (4.6.12)$$

where $\Delta N_o = N\Delta \rho_o$ is the population inversion. Solving for the real and imaginary parts of the atomic susceptibility gives

$$\chi' = -\frac{\mu^2 \Delta N_o}{\epsilon_o \hbar} \frac{(\omega_o - \omega)}{(\omega_o - \omega)^2 + (\tau_{d,21}^{-1})^2} \quad (4.6.13)$$

$$\chi'' = -\frac{\mu^2 \Delta N_o}{\epsilon_o \hbar} \frac{\tau_{d,21}^{-1}}{(\omega_o - \omega)^2 + (\tau_{d,21}^{-1})^2} \quad (4.6.14)$$

Multiplying the top and bottom of each expression by $\tau_{d,21}^2$ gives

$$\chi' = -\frac{\mu^2 \Delta N_o \tau_{d,21}}{\epsilon_o \hbar} \left(\frac{(\omega_o - \omega) \tau_{d,21}}{1 + (\omega_o - \omega)^2 \tau_{d,21}^2} \right) \quad (4.6.15)$$

$$\chi'' = -\frac{\mu^2 \Delta N_o \tau_{d,21}}{\epsilon_o \hbar} \left(\frac{1}{1 + (\omega_o - \omega)^2 \tau_{d,21}^2} \right) \quad (4.6.16)$$

These expressions can be recognized as being in the traditional forms for the susceptibility (as shown in Section 4.3) in the “small signal” limit. The only difference is the use of the full dephasing time τ_d instead of T_2 .

The gain can then be written as

$$g(\omega) = -\frac{\omega}{c} \frac{\text{Im}\{\chi(\omega)\}}{n} \quad (4.6.17)$$

and at resonance $\omega = \omega_0$ the peak gain is

$$g_0 = \frac{\omega}{cn} \frac{\mu^2 \Delta N_0 \tau_d}{\epsilon_0 \hbar} \quad (4.6.18)$$

The inversion in this case is assumed to be in the form of the population density (cm^{-3}).

Dividing by the period length of the system produces the sheet density (cm^{-2}). Changing the frequency to energy and using $\mu = e z_{if}$ gives

$$g_{if} = \frac{e^2 \Delta E_{if} \tau_{d,if}}{cn L_p \epsilon_0 \hbar^2} \Delta N_{if} z_{if}^2 \quad (4.6.19)$$

The matrix elements z_{if} can then be evaluated using

$$z_{if} = \frac{C}{\Delta E(\text{meV})} \left\langle \psi_i \left| \frac{\partial \psi_f}{\partial z} \right. \right\rangle \quad (4.6.20)$$

where $C=113746$ which represents a group of constants for GaAs quantum wells. Since the wavefunctions in the local basis are described analytically these integrals, as was done in Section 2.4 for the \tilde{V} terms, can be evaluated using

$$\Psi_i^n = A_i^n e^{+\kappa_i^n z} \Big|_{-\infty}^{z_n} + \left[C_i^n \sin(k_i^n z) + D_i^n \cos(k_i^n z) \right] \Big|_{z_n}^{z_n+L_n} + G_i^n e^{-\kappa_i^n z} \Big|_{z_n+L_n}^{+\infty} \quad (4.6.21)$$

$$\Psi_j^m = A_j^m e^{+\kappa_j^m z} \Big|_{-\infty}^{z_m} + \left[C_j^m \sin(k_j^m z) + D_j^m \cos(k_j^m z) \right] \Big|_{z_m}^{z_m+L_m} + G_j^m e^{-\kappa_j^m z} \Big|_{z_m+L_m}^{+\infty} \quad (4.6.22)$$

Simplifying the notation to

$$\Psi_i^n = a_i^n \Big|_{-\infty}^{z_n} + c d_i^n \Big|_{z_n}^{z_n+L_n} + g_i^n \Big|_{z_n+L_n}^{+\infty} \quad (4.6.23)$$

$$\Psi_j^m = a_j^m \Big|_{-\infty}^{z_m} + cd_j^m \Big|_{z_m}^{z_m+L_m} + g_j^m \Big|_{z_m+L_m}^{+\infty} \quad (4.6.24)$$

allows first for the derivative of the final state to be written as

$$\frac{\partial}{\partial z} \Psi_j^m = \frac{\partial}{\partial z} a_j^m \Big|_{-\infty}^{z_m} + \frac{\partial}{\partial z} cd_j^m \Big|_{z_m}^{z_m+L_m} + \frac{\partial}{\partial z} g_j^m \Big|_{z_m+L_m}^{+\infty} \quad (4.6.25)$$

which evaluates to

$$\frac{\partial}{\partial z} \Psi_j^m = \kappa_j^m a_j^m \Big|_{-\infty}^{z_m} + \kappa_j^m [C_j^m \cos(\kappa_j^m z) - D_j^m \sin(\kappa_j^m z)] \Big|_{z_m}^{z_m+L_m} - \kappa_j^m g_j^m \Big|_{z_m+L_m}^{+\infty} \quad (4.6.26)$$

The integral is then

$$\begin{aligned} \left\langle \psi_i \left| \frac{\partial \psi_j}{\partial z} \right. \right\rangle &= \left\langle a_i^n \Big|_{-\infty}^{z_n} + cd_i^n \Big|_{z_n}^{z_n+L_n} + g_i^n \Big|_{z_n+L_n}^{+\infty} \left| \kappa_j^m a_j^m \Big|_{-\infty}^{z_m} + \kappa_j^m [C_j^m \cos(\kappa_j^m z) - D_j^m \sin(\kappa_j^m z)] \Big|_{z_m}^{z_m+L_m} - \kappa_j^m g_j^m \Big|_{z_m+L_m}^{+\infty} \right\rangle \\ &= \left\langle a_i^n \Big|_{-\infty}^{z_n} \left| \kappa_j^m a_j^m \Big|_{-\infty}^{z_m} \right\rangle + \left\langle a_i^n \Big|_{-\infty}^{z_n} \left| \kappa_j^m [C_j^m \cos(\kappa_j^m z) - D_j^m \sin(\kappa_j^m z)] \Big|_{z_m}^{z_m+L_m} \right\rangle + \left\langle a_i^n \Big|_{-\infty}^{z_n} \left| -\kappa_j^m g_j^m \Big|_{z_m+L_m}^{+\infty} \right\rangle \\ &+ \left\langle cd_i^n \Big|_{z_n}^{z_n+L_n} \left| \kappa_j^m a_j^m \Big|_{-\infty}^{z_m} \right\rangle + \left\langle cd_i^n \Big|_{z_n}^{z_n+L_n} \left| \kappa_j^m [C_j^m \cos(\kappa_j^m z) - D_j^m \sin(\kappa_j^m z)] \Big|_{z_m}^{z_m+L_m} \right\rangle + \left\langle cd_i^n \Big|_{z_n}^{z_n+L_n} \left| -\kappa_j^m g_j^m \Big|_{z_m+L_m}^{+\infty} \right\rangle \\ &+ \left\langle g_i^n \Big|_{z_n+L_n}^{+\infty} \left| \kappa_j^m a_j^m \Big|_{-\infty}^{z_m} \right\rangle + \left\langle g_i^n \Big|_{z_n+L_n}^{+\infty} \left| \kappa_j^m [C_j^m \cos(\kappa_j^m z) - D_j^m \sin(\kappa_j^m z)] \Big|_{z_m}^{z_m+L_m} \right\rangle + \left\langle g_i^n \Big|_{z_n+L_n}^{+\infty} \left| -\kappa_j^m g_j^m \Big|_{z_m+L_m}^{+\infty} \right\rangle \end{aligned} \quad (4.6.27)$$

Assuming the transition is to an adjacent well $(m)=n+1$ cancels many of these terms

leaving

$$\begin{aligned} \left\langle \psi_i \left| \frac{\partial \psi_j}{\partial z} \right. \right\rangle &= \left\langle a_i^n \Big|_{-\infty}^{z_n} \left| \kappa_j^m a_j^m \Big|_{-\infty}^{z_m} \right\rangle + \left\langle cd_i^n \Big|_{z_n}^{z_n+L_n} \left| \kappa_j^m a_j^m \Big|_{-\infty}^{z_m} \right\rangle \\ &+ \left\langle g_i^n \Big|_{z_n+L_n}^{+\infty} \left| \kappa_j^m a_j^m \Big|_{-\infty}^{z_m} \right\rangle + \left\langle g_i^n \Big|_{z_n+L_n}^{+\infty} \left| \kappa_j^m [C_j^m \cos(\kappa_j^m z) - D_j^m \sin(\kappa_j^m z)] \Big|_{z_m}^{z_m+L_m} \right\rangle \\ &+ \left\langle g_i^n \Big|_{z_n+L_n}^{+\infty} \left| -\kappa_j^m g_j^m \Big|_{z_m+L_m}^{+\infty} \right\rangle \end{aligned} \quad (4.6.28)$$

It is also reasonable to assume the identical decaying elements $\langle a|a \rangle$ and $\langle g|g \rangle$ will be very small. This simplifies the expression to

$$\begin{aligned} \left\langle \psi_i \left| \frac{\partial \psi_j}{\partial z} \right. \right\rangle &= \left\langle cd_i^n \Big|_{z_n}^{z_n+L_n} \left| \kappa_j^m a_j^m \Big|_{-\infty}^{z_m} \right\rangle + \left\langle g_i^n \Big|_{z_n+L_n}^{+\infty} \left| \kappa_j^m a_j^m \Big|_{-\infty}^{z_m} \right\rangle \\ &+ \left\langle g_i^n \Big|_{z_n+L_n}^{+\infty} \left| \kappa_j^m [C_j^m \cos(\kappa_j^m z) - D_j^m \sin(\kappa_j^m z)] \Big|_{z_m}^{z_m+L_m} \right\rangle \end{aligned} \quad (4.6.29)$$

The limits of integration can then be changed to

$$\begin{aligned} \left\langle \psi_i \left| \frac{\partial \psi_j}{\partial z} \right. \right\rangle &= \left\langle cd_i^n \left| \kappa_j^m a_j^m \right. \right\rangle_{z_n}^{z_n+L_n} + \left\langle g_i^n \left| \kappa_j^m a_j^m \right. \right\rangle_{z_n+L_n}^{z_m} \\ &+ \left\langle g_i^n \left| \kappa_j^m \left[C_j^m \cos(\kappa_j^m z) - D_j^m \sin(\kappa_j^m z) \right] \right. \right\rangle_{z_m}^{z_m+L_m} \end{aligned} \quad (4.6.30)$$

These three integrals can then be evaluated in their indefinite form

$$\begin{aligned} &\left\langle cd_i^n \left| \kappa_j^m a_j^m \right. \right\rangle_{z_n}^{z_n+L_n} \\ &= \frac{A_j^m \kappa_j^m e^{\kappa_j^m z}}{(\kappa_j^m)^2 + (k_i^n)^2} \left[C_i^n \left(\kappa_j^m \sin(k_i^n z) - k_i^n \cos(k_i^n z) \right) + D_i^n \left(k_i^n \sin(k_i^n z) + \kappa_j^m \cos(k_i^n z) \right) \right] \end{aligned} \quad (4.6.31)$$

$$\left\langle g_i^n \left| \kappa_j^m a_j^m \right. \right\rangle_{z_n+L_n}^{z_m} = \frac{G_i^n A_j^m \kappa_j^m}{\kappa_j^m - \kappa_i^n} e^{(\kappa_j^m - \kappa_i^n) z} \quad (4.6.32)$$

and

$$\begin{aligned} &\left\langle g_i^n \left| \kappa_j^m \left[C_j^m \cos(\kappa_j^m z) - D_j^m \sin(\kappa_j^m z) \right] \right. \right\rangle_{z_m}^{z_m+L_m} \\ &= \frac{G_i^n \kappa_j^m e^{-\kappa_i^n z}}{(k_j^m)^2 + (\kappa_i^n)^2} \left[C_j^m \left(k_j^m \sin(k_j^m z) - \kappa_i^n \cos(k_j^m z) \right) + D_j^m \left(\kappa_i^n \sin(k_j^m z) + k_j^m \cos(k_j^m z) \right) \right] \end{aligned} \quad (4.6.33)$$

These matrix elements, like the \tilde{V} terms, can then be easily computed using only the location of the heterostructure interfaces and the polynomial fit of the single well energies $\epsilon(L)$.

The gain in this derivation, given by

$$g_{if} = \frac{e^2 \Delta E_{if} \tau_{d,if}}{cnL_p \epsilon_0 \hbar^2} \Delta N_{if} Z_{if}^2 = \frac{e^2 \Delta E_{if}}{cnL_p \epsilon_0 \hbar^2 \Gamma_{if}} \Delta N_{if} Z_{if}^2 \quad (4.6.34)$$

is very similar to that used in the semiclassical descriptions [82,83,93,96,97]. The primary difference is that this expression contains the dephasing rate Γ_{if} in the denominator while the semiclassical models, which have no description of dephasing, typically insert an experimentally measured electroluminescence linewidth $\Delta\nu$. In the previous chapter a

discussion was presented where intradoublet scattering would contribute to transport only indirectly through these dephasing terms. Thus, in the typical THz-QCL doublet where lasing is to occur, the effect of higher temperatures results in previously forbidden ($<36\text{meV}$ subband separation) phonon scattering. In the model presented, this temperature induced scattering results not in a significant decay of the inversion but instead produces a temperature dependant dephasing term Γ which acts to destroys the gain (Equation 4.6.34). This temperature dependent line broadening is not treated with the constant Δv value used in the semiclassical models. Recent simulations [126] performed using the fully quantum-mechanical Non-Equilibrium Greens Function method demonstrated that this temperature dependent change in the lineshape is the leading cause of the gain reduction, and not the less significant decay of the population inversion. This observation gives further validation to the presented model where the intradoublet scattering will only effect the dephasing and not directly change the inversion.

In summary this chapter presented both semiclassical and quantum descriptions of transport in heterostructures. Building on the results on previous chapters it was shown that the combination of analytical expressions and empirical fitting functions permitted a semiclassical transport description which agreed very well with the full numerical simulation in an infinitesimally faster computational time. While this method is undeniably useful for near real-time modeling in the semiclassical picture it was demonstrated, using the Density Matrix Formalism, that this description itself is inadequate in many circumstances. In view of this revelation a simplified diagonal density matrix description was presented which was shown to converge to the semiclassical results only in certain limiting cases. Discussions concerning the most

suitable implementation of this method were carried out leading to the conclusion that all incoherent scattering should be considered as intrawell and a tightly-bound doublet (very thin barrier case) should include the energy splitting. Treatment of intradoublet scattering as only contributing to the dephasing lead to, after derivation of the gain, a description where temperature induced scattering within the coupled well laser states leads to a decay of the gain due to a change in the lineshape and not primarily a reduction of the inversion.

CHAPTER 5

SIMULATION OF TERAHERTZ QUANTUM CASCADE LASERS

5.1 Introduction

Simulation of THz-QCL's must begin with what is, perhaps, the most thoroughly investigated THz-QCL, namely the 4-well resonant phonon depopulation laser [28,30,31,33-43]. Due to the experimental successes of this design numerous modeling approaches have been conducted, primarily using either Monte Carlo (MC) techniques [92-95,97,98,100,102] or, more recently, the Non-Equilibrium Greens Function (NEGF) approach [118,123,124-126]. While the MC simulations are still actively being used for simulation and prediction of device optimization, their potential downside, due to the semiclassical nature, is recognized [93,94,102]. In many of these MC simulations [93,94,96,97] the manifestation of very large current spikes, attributed to unrealistic wavefunction delocalization, are omitted and the remaining data, where the I-V characteristics are more in tune with experimental results, is assumed reasonable and presented. While this selective omission of modeling results may be appropriate there cannot be inherent certainty in the remaining data with the realization that fundamental flaws are present in the models. The fully quantum-mechanical NEGF techniques, on the other hand, have been instrumental in the discovery of insufficiencies in the semiclassical models, specifically the lacking treatments of coherency and dephasing

processes. These more complete descriptions however, are inescapably accompanied by increased complexity and computational requirements.

The necessities for inclusion of potential wavefunction decoherence, and in turn localization, into accessible models and numerical procedures is preferred. Incorporating these coherent effects into traditional, and more efficient, procedures was demonstrated by Callebaut and Hu [102] where repeating periods of the 4-well resonant phonon QCL were separated and then linked together using a tight-binding and density matrix description. The intraperiod transport was treated using the MC simulation and resonant tunneling between the localized periods was calculated for the entire 2-D nature of the subbands under the assumption that coherent processes between states $|i, k_i\rangle$ and $|f, k_f\rangle$ occurs for $k_i = k_f$ only. (see Figure 5.2.1).

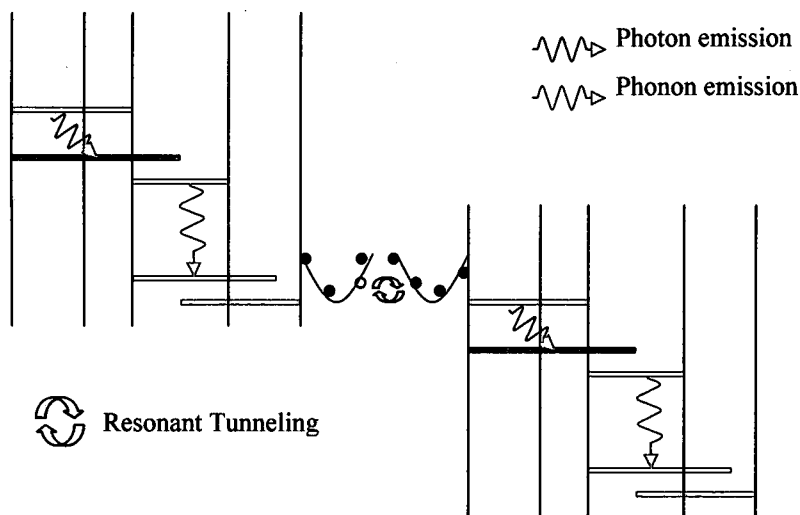


Figure 5.2.1: Picture of the Monte Carlo/Tight-Binding Density Matrix hybrid model of Callebaut and Hu [102].

In their simulation the authors concluded that breaking up the periods of the device and treating only the transport through the thicker ($\sim 45\text{-}55\text{\AA}$) injection barrier using a simple density matrix description produced improved agreement with experimental results without the additional complexity and time constraints of a fully quantum mechanical model. Recently, Terrazi et.al. [162], introduced a similar model where a QCL device is separated at the active region and both injection and depopulation was treated as sequential resonant tunneling using a tight-binding density matrix approach. In their simulation scattering within the injector/collector and active regions was calculated and the full 2D nature of the subbands was evaluated where tunneling between states $k_i \neq k_f$ was included. Results from their simulations showed excellent agreement with experimental I-V characteristics for a mid-infrared QCL's. These "hybrid" methods demonstrate the promise of incorporating coherent effects into simpler models, compared to the NEGF and other comprehensive techniques, but are still hindered by the 2D subband nature and the computational demands of calculating a multitude of scattering rates.

The hybrid model of Callebaut and Hu [102] combined with the semiclassical mean-scattering rate equation approach of Harrison [80-88] was the inspiration for the research undertaken in this thesis. If, as demonstrated, the interplay between coherent and incoherent processes could be treated by separating periods of a QCL and applying tight-binding density matrix procedures, why not break the entire system down to the single well basis? With the analogy of the quantum well as an "artificial atom" why not apply empirical pre-evaluated or fitting function techniques similar to the successful Linear Combination of Atomic Orbitals method [140-144] of solid-state theory?

In the spirit of these preceding theories and procedures the framework of the previous chapters was established. In Chapter 2 a technique was presented where single well eigenstates, in a arbitrary multi-well system, could be analytically described using only the interface locations and a predetermined knowledge of single-well energies for any well width $\epsilon(L)$. Tight-binding methods were then demonstrated to have the capability to accurately reconstruct delocalization and coupled well behavior over controlled distances. Due to a derived approximation to the full tight-binding matrix expansion, and using pre-evaluated indefinite forms for all integrals, all relevant coupled well parameters could be determined at practically zero computational expense.

In Chapter 3 the most significant advantage for the localized basis was demonstrated. Using the coupled well, tight-binding parameters, an expansion of Fermi's Golden Rule was derived where the insertion of mean intrawell subband rates was shown to be a reasonable approximation to full scattering calculations. After scrutinizing calculations of scattering rates over a range of parameters, empirical fitting functions were found to describe these basis rates. Within this construction, multi-well properties are fully described as "linear combinations of intrawell properties" and, due to the reduced analytical forms of the relevant expressions, can be immediately evaluated requiring only the location of the heterostructure interfaces.

In Chapter 4 treatment of semiclassical and quantum transport was investigated. A simplified "diagonal density matrix" was introduced and, correspondingly, an expression for gain in a coupled-well "doublet" was presented. In this chapter the merger of these simplified descriptions will be applied to actual terahertz quantum cascade laser designs and compared with reported experimental results and alternate simulations.

5.2 The 4-Well Resonant Phonon Depopulation Laser

While many variations of the 4-well resonant phonon depopulation QCL exist [28,30,31,33-43], most differ only by slight perturbations (a few monolayers) of the well and barrier widths. The basic premise for these devices depends slightly on the transport picture used to describe it. This is illustrated in Figure 5.2.1.

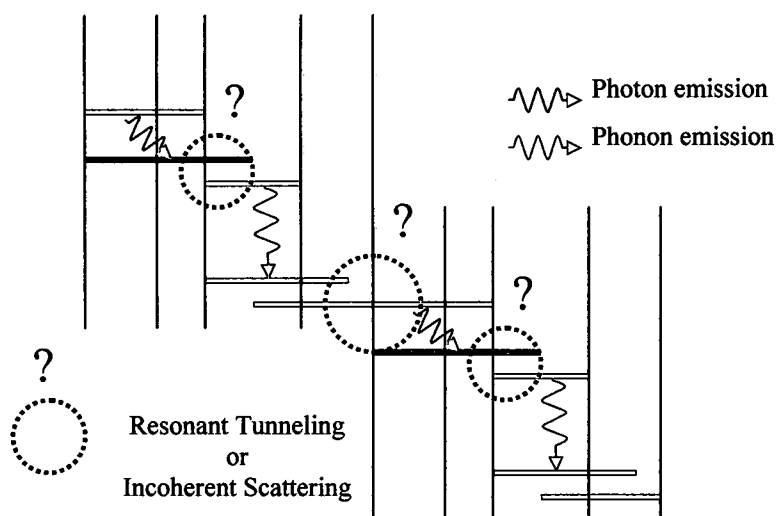


Figure 5.2.1: Diagram of the 4-well resonant phonon depopulation QCL.

In the delocalized wavefunction/incoherent scattering picture electrons are injected into the upper lasing level by closely separated states where electron-electron scattering would be assumed to play an important role due to the small energy gaps. The lower lasing state is closely positioned in energy to an excited state in the adjacent downstream well which has a near resonant phonon transition to the ground level in the same well. If the wavefunction of the lower lasing subband extends across this barrier a direct phonon scattering path to the ground state is available in addition to transfer into the excited state. In this semiclassical picture the design goals are clear and familiar to the laser engineering community. The injection should be designed such that “parasitic

scattering", i.e. injection transitions to states other than the upper lasing level, should be minimized. Likewise, scattering from the upper lasing level to the collection states should be as slow as possible.

In the resonant tunneling picture slightly different arguments for optimization can be made. Specifically, questions regarding under which limiting regime ($\Omega^2 \ll WT$ or $\Omega^2 \gg WT$) will performance be optimized has been previously discussed [79] in Mid-IR QCL's. If the oscillation dominates over the dephasing/scattering there is no "injection bottleneck" yet the creation of a doublet could interfere with the single upper-to-lower lasing state gain, essentially creating two separate upper lasing states. In this representation there is not a direct picture of "parasitic scattering" channels that should be minimized. Instead, as shown Chapter 4, interwell scattering processes can be considered as components of intrawell transitions which are mediated by the coherent tunneling interaction.

Before discussions regarding device operation can be made the very simplified models outlined in previous chapters must be validated using the realistic and more complex devices. Consider first the design of Williams et.al. [34]. This QCL is a GaAs/Al_{0.15}Ga_{0.85}As device with layer widths (starting with the upper lasing state well) in Å of 79/**25**/66/**41**/156/**33**/90/**49** (barriers in boldface). The 156Å phonon depletion well is doped at $1.9 \times 10^{16} \text{cm}^{-3}$ resulting in a per period sheet density of $3.0 \times 10^{10} \text{cm}^{-2}$. This device was reported to lase at approximately 3.0THz ($\sim 13 \text{meV}$) and demonstrated operation up to 164K in pulsed mode and 117K cw. 3-periods of this device calculated using the full numerical approach is displayed in Figure 5.2.2. In this numerical simulation the energy separation of the lasing states at 12kV/cm, for the central period,

is calculated at 12.92meV (~ 3.12 THz) and the phonon depletion mechanism at 35.6meV. Both are thus in very good agreement with the intended design.

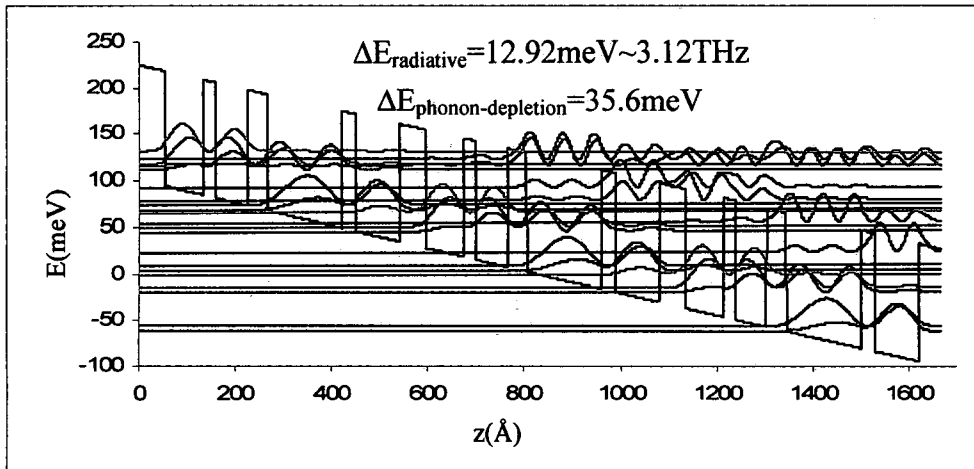


Figure 5.2.2: Full numerical simulation over 3-periods of the device from Reference [34]. The system is displayed at a bias of 12kV/cm.

While this full numerical simulation provides the reference that these devices can be very accurately modeled the objective of this work is to validate the simplified methods outlined in the previous chapters. To accomplish this, the localized basis system (shown in Figure 5.2.3), is then directly compared to the full calculation (Figure 5.2.4).

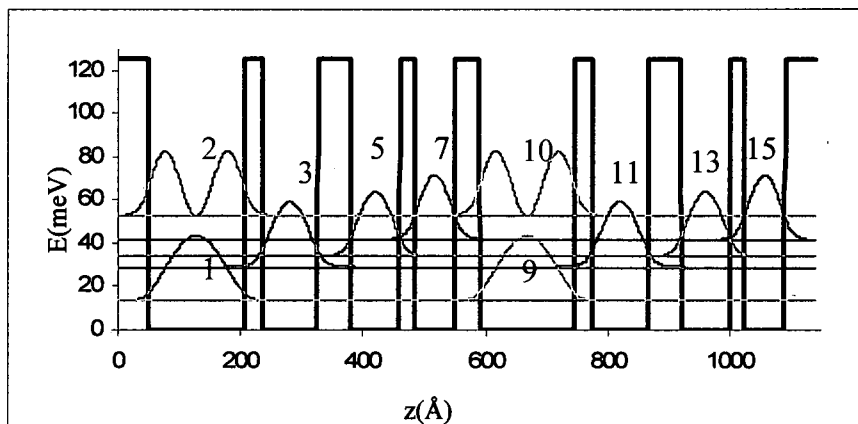


Figure 5.2.3: Localized basis for device from Reference [34].

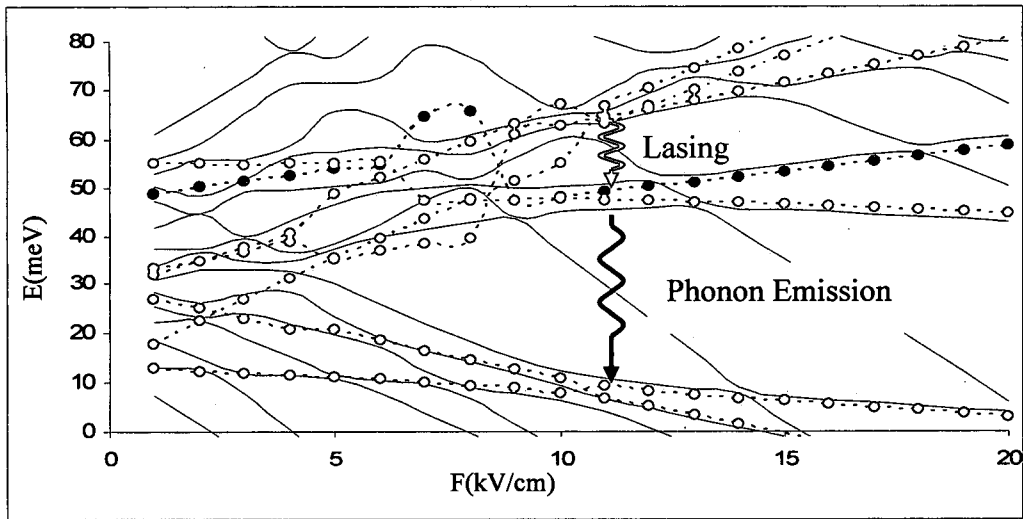


Figure 5.2.4: Comparison of the energies vs. the bias for the coupled-well expansion in the localized basis and the full numerical model.

In this plot the energies vs. the bias is shown for both the full numerical simulation (black lines) and the tight-binding expansion of the single well basis (colored lines). While a diagram such as this can be a bit overwhelming due to the numerous states involved consider just the two primary energies of interest (Figure 5.2.5).

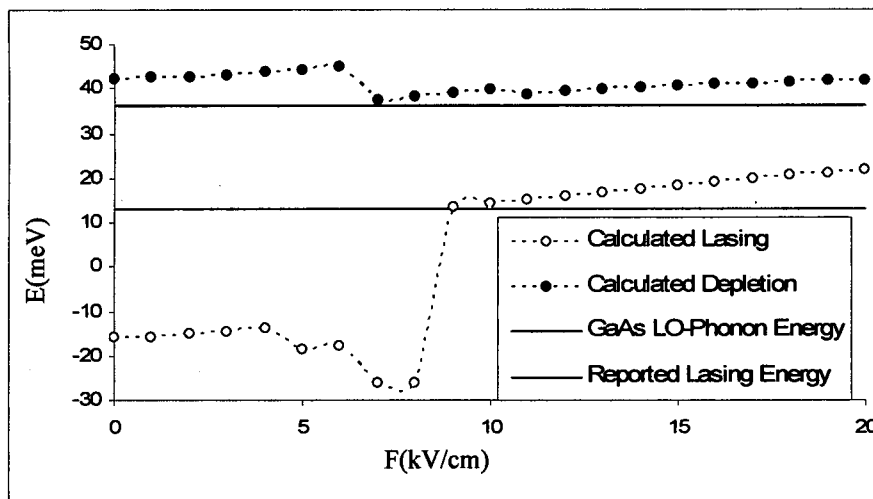


Figure 5.2.5: Localized basis calculation of the lasing state energy separation and the phonon depletion mechanism compared to reported results.

In this diagram the energy separation for the lasing states as well as the phonon depletion mechanism are plotted using the localized basis expansion and compared directly to the reported values. Here it can be observed that after the appropriate crossing point ($\sim 9\text{kV/cm}$) the tight-binding expansion of the single-well basis predicts quite accurately the 3THz (or 13meV) lasing, especially near the design bias range (10-12kV/cm). The calculated phonon depletion mechanism, while not a direct observable, is shown to follow very closely the intended goal of approximately 36meV near this design bias. The wavefunctions, expanded over nearest neighbors, is also compared to the full calculation at 12kV/cm in Figure 5.2.6.

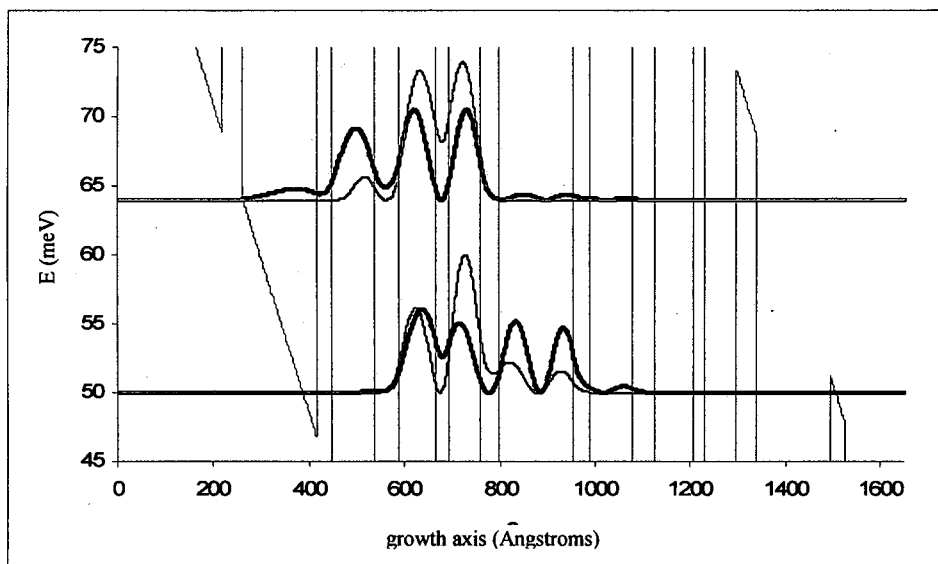


Figure 5.2.6: Localized basis calculation of wavefunctions compared to the full simulation at $F=12\text{kV/cm}$.

This comparison of the wavefunctions shows decent agreement over the nearest neighbor wells however, since the full simulation is unbounded, the potential for disagreement is much greater than in previous simulations restricted to doublet

calculations. This disagreement can lead to potential problems in the calculation of oscillator strengths (related to the gain) if this basis was to be used in a semiclassical simulation.

For example, consider the semiclassical rate equation approach to this system using the localized basis and the expanded mean rate (LCIS) analysis. Using the standard approach of Section 4.2., this system was calculated over a range of lattice temperatures. The I-V and V-I simulated curves are shown in Figure 5.2.7. In this simulation an electron-lattice coupling constant of $\alpha_{e-l}=0.05(\text{K}/\text{A} \cdot \text{cm}^2)$ was implemented. This value, suggested as a suitable parameter by Harrison et.al. [85] for THz-QCL's, is incorporated by setting the electron temperature to $T_e=T+\alpha_{e-l}J$, where J is the current density, and iterating until convergence is reached. Due to the extremely fast calculations of the empirical LCIS technique these iterations produce negligible increases in computational time and the I-V characteristic are still predicted in 1-2 seconds.

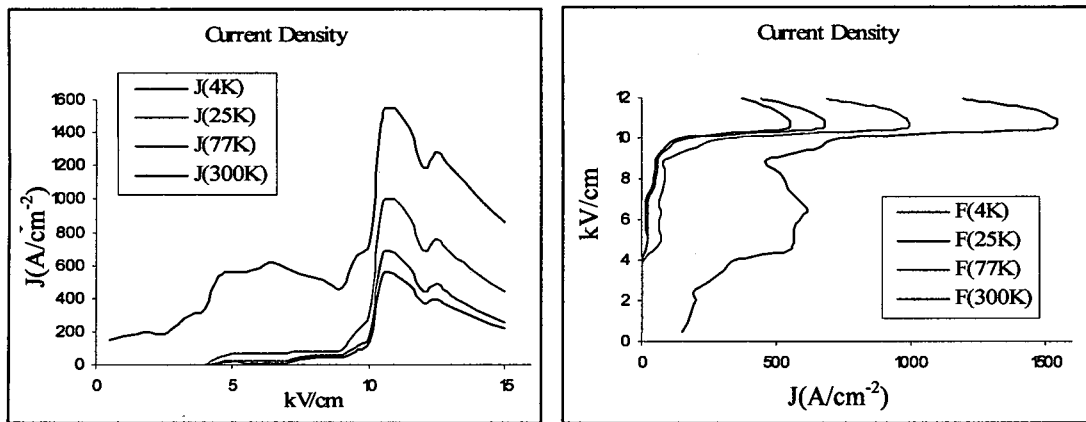


Figure 5.2.7: Empirical LCIS (I-V and V-I) calculations using a semiclassical rate equation model.

As discussed in Section 4.2, while the approach described in the LCIS technique allow for extremely fast calculation (seconds vs. hours), confidence in the results are not high. While the general behavior of the device is predicted, in that a peak occurs near the design bias at approximately 10-12kV/cm followed by NDR, this turn on current is much too sharp compared to experimental results which follow a smoother behavior. In addition, there is a large deviation in the peak current density at different lattice temperatures which is not observed in measurement. The calculated gain and electron temperature are also plotted in Figure 5.2.8.

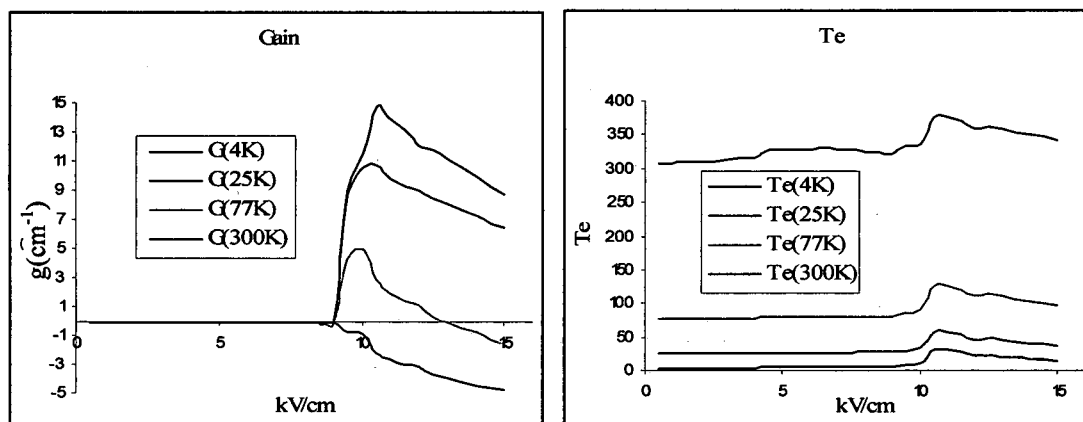


Figure 5.2.8: Empirical LCIS gain and electron temperature calculations using a semiclassical rate equation model.

For this calculation of gain an experimental value of broadening $\Delta\nu=1.5\text{THz}$ was used. These gain calculation are much lower than those typically simulated in Monte Carlo simulations [92-95,97,98,100,102], where values are usually 2-4 times greater than these calculated above. In fact, with the gain threshold for these devices considered to be approximately 40cm^{-1} [93,96,102], this simulation would predict no lasing at any

temperature. A large reason for this discrepancy is the limited delocalization used in the nearest neighbor expansion resulting in lower oscillator strengths ~ 0.5 compared to >1 for the full simulations. While corrections could be made to permit the use of more delocalized wavefunctions in the calculation of the gain, the limited promise of this basic semiclassical approach makes this unworthy of further consideration.

Consider now the diagonal density matrix (DDM) representation of transport outlined in Section 4.4. Assuming the localized basis and intrawell scattering only this system can be treated as illustrated in Figure 5.2.9.

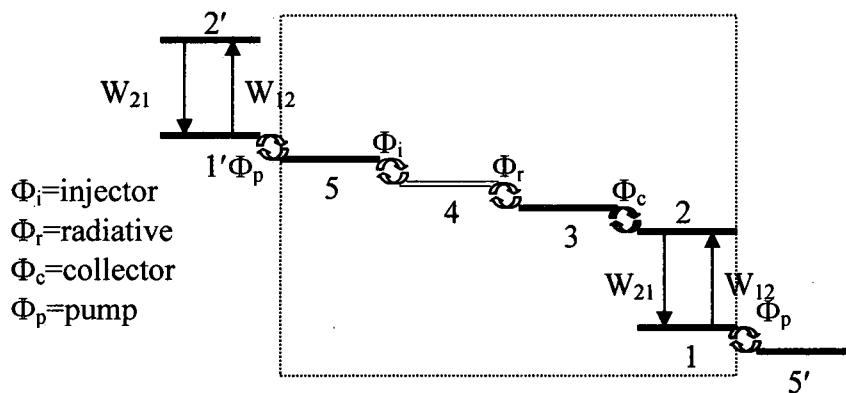


Figure 5.2.9: DDM picture of transport using the localized basis and assuming intrawell scattering only.

In this simplified picture the system reduces to a sequential resonant tunneling transport description where the various tunneling terms Φ combine to couple the isolated states and the entire system is driven by the intrawell scattering occurring only in a single well. In this representation the diagonal density matrix elements can be written as

$$\begin{aligned}
\rho_{11} &= \frac{W_{21}\rho_{22} + \frac{1}{2}\Phi_p\rho_{55}}{W_{12} + \frac{1}{2}\Phi_p} & \rho_{22} &= \frac{W_{12}\rho_{11} + \frac{1}{2}\Phi_c\rho_{33}}{W_{21} + \frac{1}{2}\Phi_c} \\
\rho_{33} &= \frac{\frac{1}{2}(\Phi_r\rho_{44} + \Phi_c\rho_{22})}{\frac{1}{2}(\Phi_r + \Phi_c)} & \rho_{44} &= \frac{\frac{1}{2}(\Phi_i\rho_{55} + \Phi_r\rho_{33})}{\frac{1}{2}(\Phi_i + \Phi_r)} & \rho_{55} &= \frac{\frac{1}{2}(\Phi_p\rho_{11} + \Phi_i\rho_{44})}{\frac{1}{2}(\Phi_p + \Phi_i)}
\end{aligned} \tag{5.2.1}$$

which can be cast into the augmented steady-state matrix system

$$\begin{bmatrix}
-\left(W_{12} + \frac{1}{2}\Phi_p\right) & W_{21} & 0 & 0 & \frac{1}{2}\Phi_p & 0 \\
W_{12} & -\left(W_{21} + \frac{1}{2}\Phi_c\right) & \left(\frac{1}{2}\Phi_c\right) & 0 & 0 & 0 \\
0 & \frac{1}{2}\Phi_c & -\frac{1}{2}(\Phi_r + \Phi_c) & \frac{1}{2}\Phi_r & 0 & 0 \\
0 & 0 & \frac{1}{2}\Phi_r & -\frac{1}{2}(\Phi_i + \Phi_r) & \frac{1}{2}\Phi_i & 0 \\
\frac{1}{2}\Phi_p & 0 & 0 & \frac{1}{2}\Phi_i & -\frac{1}{2}(\Phi_p + \Phi_i) & 0 \\
1 & 1 & 1 & 1 & 1 & 1
\end{bmatrix} \tag{5.2.2}$$

The system then can be solved resulting in analytical expression for the subband populations

$$n_1 = N_s\rho_{11} = N_s \frac{\Phi_{icrp} + 2W_{21}(\Phi_{icr} + \Phi_{crp} + \Phi_{icp} + \Phi_{irp})}{5\Phi_{icrp} + 2W_{21}(\Phi_{icr} + 2\Phi_{crp} + 3\Phi_{icp} + 4\Phi_{irp}) + 2W_{12}(4\Phi_{icr} + 3\Phi_{crp} + 2\Phi_{icp} + \Phi_{irp})} \tag{5.2.3}$$

$$n_2 = N_s\rho_{22} = N_s \frac{\Phi_{icrp} + 2W_{12}(\Phi_{icr} + \Phi_{crp} + \Phi_{icp} + \Phi_{irp})}{5\Phi_{icrp} + 2W_{21}(\Phi_{icr} + 2\Phi_{crp} + 3\Phi_{icp} + 4\Phi_{irp}) + 2W_{12}(4\Phi_{icr} + 3\Phi_{crp} + 2\Phi_{icp} + \Phi_{irp})} \tag{5.2.4}$$

$$n_3 = N_s\rho_{33} = N_s \frac{\Phi_{icrp} + 2W_{21}(\Phi_{irp}) + 2W_{12}(\Phi_{icr} + \Phi_{crp} + \Phi_{icp})}{5\Phi_{icrp} + 2W_{21}(\Phi_{icr} + 2\Phi_{crp} + 3\Phi_{icp} + 4\Phi_{irp}) + 2W_{12}(4\Phi_{icr} + 3\Phi_{crp} + 2\Phi_{icp} + \Phi_{irp})} \tag{5.2.5}$$

$$n_4 = N_s\rho_{44} = N_s \frac{\Phi_{icrp} + 2W_{21}(\Phi_{irp} + \Phi_{icp}) + 2W_{12}(\Phi_{icr} + \Phi_{crp})}{5\Phi_{icrp} + 2W_{21}(\Phi_{icr} + 2\Phi_{crp} + 3\Phi_{icp} + 4\Phi_{irp}) + 2W_{12}(4\Phi_{icr} + 3\Phi_{crp} + 2\Phi_{icp} + \Phi_{irp})} \tag{5.2.6}$$

$$n_s = N_s \rho_{ss} = N_s \frac{\Phi_{icrp} + 2W_{21}(\Phi_{irp} + \Phi_{icp} + \Phi_{crp}) + 2W_{12}(\Phi_{icr})}{5\Phi_{icrp} + 2W_{21}(\Phi_{icr} + 2\Phi_{crp} + 3\Phi_{icp} + 4\Phi_{irp}) + 2W_{12}(4\Phi_{icr} + 3\Phi_{crp} + 2\Phi_{icp} + \Phi_{irp})} \quad (5.2.7)$$

where the multiple subscript Φ terms

$$\Phi_{abc} = \Phi_a \Phi_b \Phi_c \quad (5.2.8)$$

represent the product of the designated tunneling expressions. The current density in the steady state can be taken over any barrier in the form

$$J_b = \frac{qN_s}{2} \Phi_b (\rho_{ii} - \rho_{ff}) \quad (5.2.9)$$

where Φ_b is the tunneling term across the designated barrier (b), as shown in Figure 5.2.9. ρ_{ii} and ρ_{ff} are the diagonal elements (or normalized populations) of the left and right state across the barrier, respectively. The resulting current density expression is

$$J = qN_s \frac{\Phi_{icrp}(W_{21} - W_{12})}{5\Phi_{icrp} + 2W_{21}(\Phi_{icr} + 2\Phi_{crp} + 3\Phi_{icp} + 4\Phi_{irp}) + 2W_{12}(4\Phi_{icr} + 3\Phi_{crp} + 2\Phi_{icp} + \Phi_{irp})} \quad (5.2.10)$$

This statement indicates that the current flow is a product of all the tunneling terms Φ as well as the difference between the downward W_{21} and upward W_{12} scattering rates. The population inversion reduces to

$$\Delta N_{43} = N_s \frac{2\Phi_{icrp}(W_{21} - W_{12})}{5\Phi_{icrp} + 2W_{21}(\Phi_{icr} + 2\Phi_{crp} + 3\Phi_{icp} + 4\Phi_{irp}) + 2W_{12}(4\Phi_{icr} + 3\Phi_{crp} + 2\Phi_{icp} + \Phi_{irp})} \quad (5.2.11)$$

or more simply

$$\Delta N_{43} = \frac{2J}{q\Phi_r} \quad (5.2.12)$$

This expression suggests that the inversion follows closely the current and is diminished by the value of the radiative tunneling term Φ_r .

To implement these expressions into a simulation of the specific device treated above the method described in Section 4.5 is used. In this treatment (Figure 5.2.10) the lasing states are considered as a pseudo or “hybrid-doublet” in that the repelling energy splitting is calculated yet the transport is still considered in the DDM picture with intradoublet scattering only contributing to transport through dephasing terms.

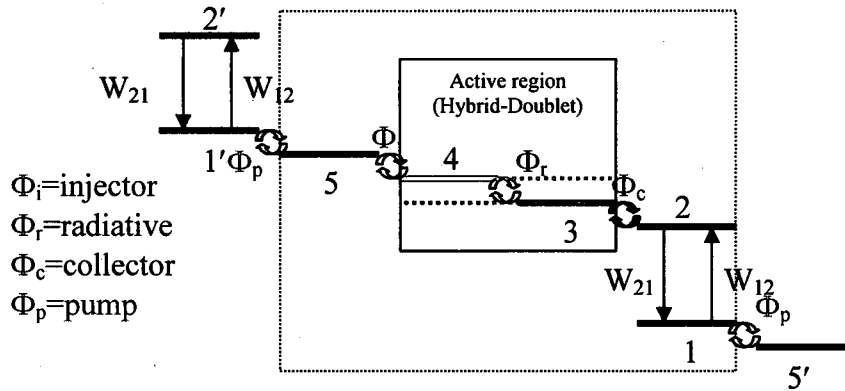


Figure 5.2.10: DDM picture of transport using the localized basis with a pseudo or “hybrid-doublet” used as the active region.

This picture then essentially represents a doublet which is pumped and drained on each side by tunneling mechanisms which, in turn, are driven by scattering in the phonon depopulation well.

Since only the active region doublet is treated using the repelling effect the other energies in the system are described by the perturbed basis energies $\tilde{\epsilon}$ (Equation 2.4.42). These energies vs. the bias are shown in Figure 5.2.11. In this plot the repelled “hybrid doublet” displays a nearly constant energy separation throughout the entire range of the bias. This is a result of the very strong coupling due to the narrow barrier (25Å). The remaining, unrepelled, states follow a simple linear path vs. the field.

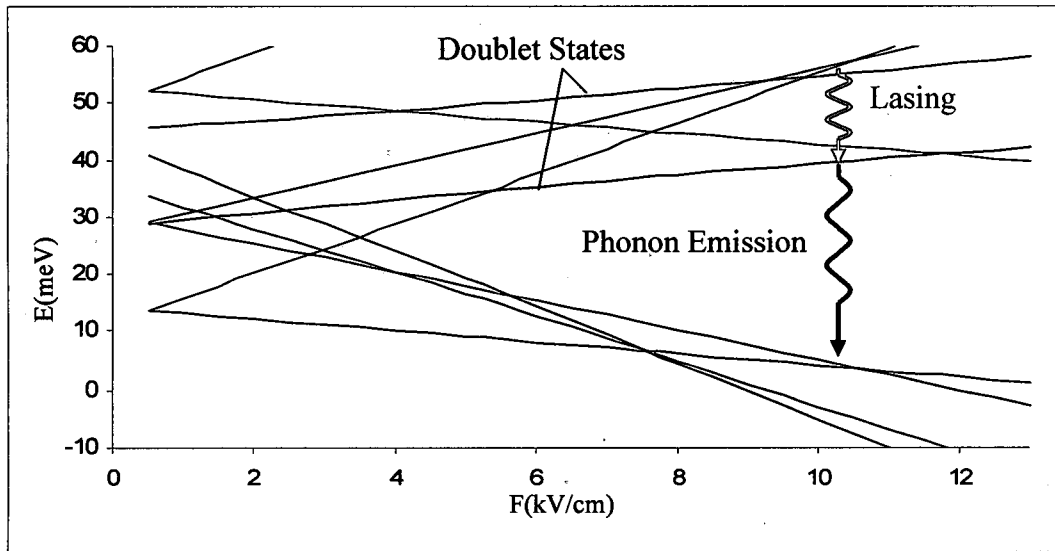


Figure 5.2.11: DDM picture of energies vs. bias with the “hybrid doublet”.

For these simulations, as well as the previous semiclassical LCIS calculation, the value of the electron temperature is not easily calculable. While Harrison et.al. [85-88] suggested a method for determining this non-equilibrium temperature using the mean subband rates and kinetic energy balance iteration, the results applied to a simple system as depicted above could lead to unreasonable conclusions. For instance, in this approach, electrons in subbands separated by greater than the LO-phonon resonance lead to an increase in kinetic energy as the phonon emission must redistribute carriers near the minima to higher values of $k_{||}$ (see Figure 5.2.12). If the subbands are separated by less than the LO-phonon energy higher $k_{||}$ carriers are scattered lower into the minima producing cooling. In the mean scattering rate method, and with the limited transitions occurring in the DDM picture (Figure 5.2.10) setting the ΔE_{21} just below the resonance (36meV) would permit current flow while suggesting an electron temperature below that of the lattice. Since a relationship of $T_e = T + \alpha_e J$ is demonstrated experimentally, this technique cannot be used to calculate logical results.

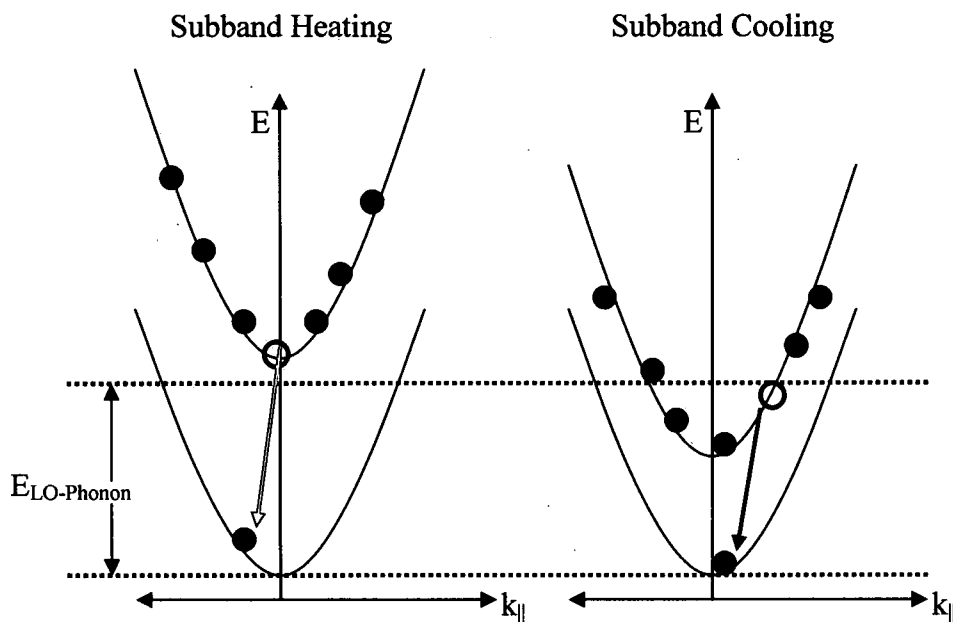


Figure 5.2.12: Depiction of subband heating and cooling due to kinetic energy redistributions for phonon emission.

Presumably, these kinetic energy balance considerations could be made if the 2D subband nature was treated. This however, would undo the computational simplicity of the previously established empirical mean intrawell rates. It is therefore appropriate to examine this electron temperature as an unknown parameter in the above model. The simplicity of the stated model and numerical procedures requires the input of the heterostructure interfaces, the lattice temperature, the electron temperature, and a pure (T_2) dephasing time. Setting $T_2=0.67\text{ps}$, and varying the electron temperature for the previously described 4-well device produces the current vs. bias plots shown in Figure 5.2.13.

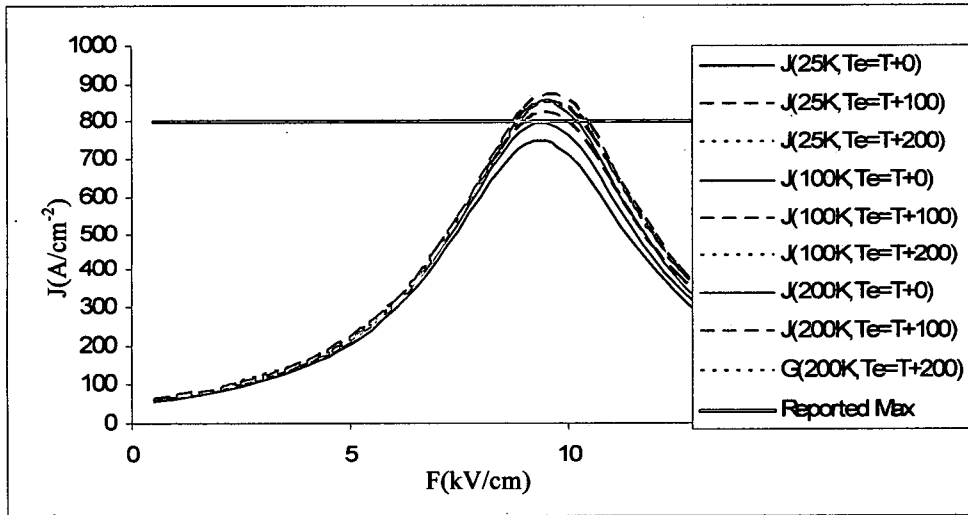


Figure 5.2.13: Current-Voltage curves for the 4-well QCL of Reference [34] calculated using the simple DDM technique at various lattice and electron temperatures.

In these current-voltage plots, which are generated nearly instantaneously using the given method, it is observed that the peak current densities are altered only slightly by both the lattice and electron temperatures in the range of $T=25\text{K}$ to 200K . The reported max current density of approximately $800\text{A}/\text{cm}^2$ is also plotted as a reference. This nearly stable current with temperature, which was not predicted in the semiclassical approach, is observed experimentally for these devices. Observing equation 5.2.10 shows that the current, at the maximum product of the tunneling terms Φ , has a temperature dependence on the difference between W_{21} and W_{12} . Higher temperature increases of W_{21} will be mediated by a simultaneous increase in W_{12} and thus the difference is observed to be rather stable with temperature.

Since the current densities are minimally affected by the electron temperature the calculation of gain can then be examined. This is shown in Figure 5.2.14. In this figure a more dramatic variation is observed with both the lattice and electron temperatures.

Comparison of these calculations to the assumed threshold value of 40cm^{-1} [93,96,102], shows that all temperature values predict lasing at low lattice temperatures of 25K and none of the simulations predict 200K operation.

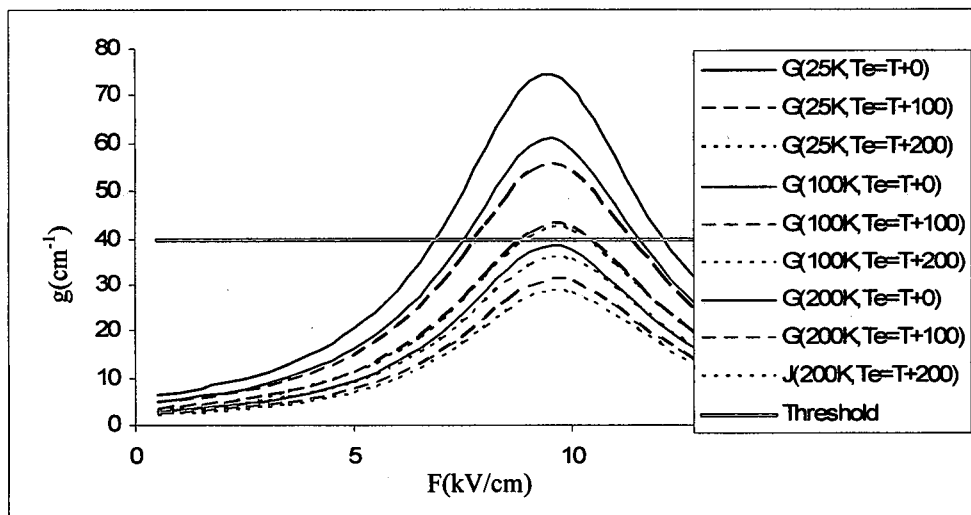


Figure 5.2.14: Gain vs. bias curves for the 4-well QCL of Reference [34] calculated using the simple DDM technique at various lattice and electron temperatures.

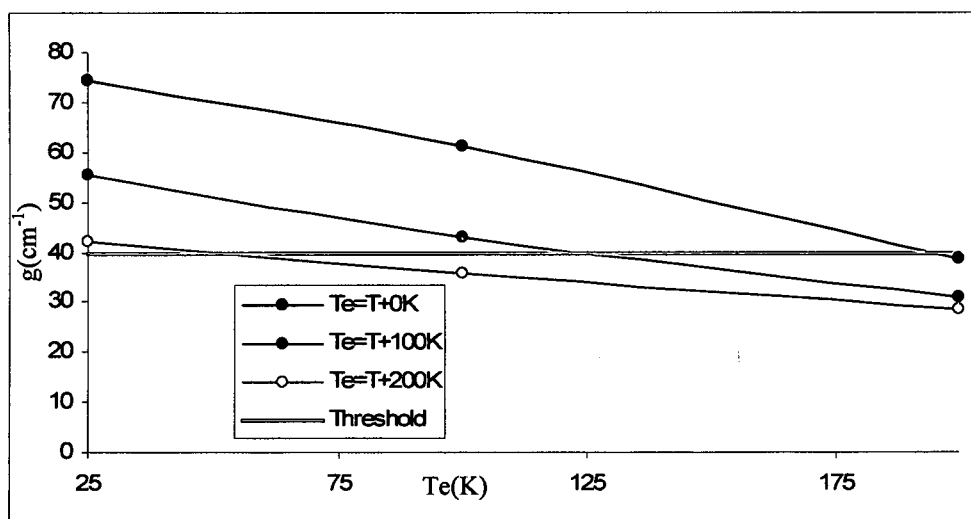


Figure 5.2.15: Peak gain vs. lattice temperature curves for the 4-well QCL Reference [34] calculated using the simple DDM technique at various electron temperatures.

A more direct comparison of the peak gains vs. the lattice temperature is shown in Figure 5.2.15. In this plot it can be seen that the $T_e = T + 0K$ peak gain is, as assumed, an overestimation as this device was demonstrated up to 164K pulsed and 117K cw. Likewise, the $T_e = T + 200K$ line is an underestimation of performance as this suggests a cutoff near 50K. Monte Carlo simulations, which treat fully the 2D subband distributions, have shown calculated electron temperatures at $T = 25K$ in the range slightly above $T_e = 100K$ [93,94,102]. These results, which imply an electron lattice coupling constant in the range of $\alpha_{e-l} = 0.1(K/A \cdot cm^2)$, due to the peak currents of $800A/cm^2$, would fall practically in the middle of the upper and lower limits shown in Figure 5.2.15. This value would agree well with the experimentally demonstrated operational limits and will be used in subsequent calculations for these devices.

The other uncalculated parameter in these simulations is Γ^{pure} (or T_2). This value, although uncertain, has been suggested to be in the $T_2 = 0.33..0.5ps$ range by observing electroluminescence linewidths [102]. A plot of the current densities for various T_2 values is shown in Figure 5.2.16.

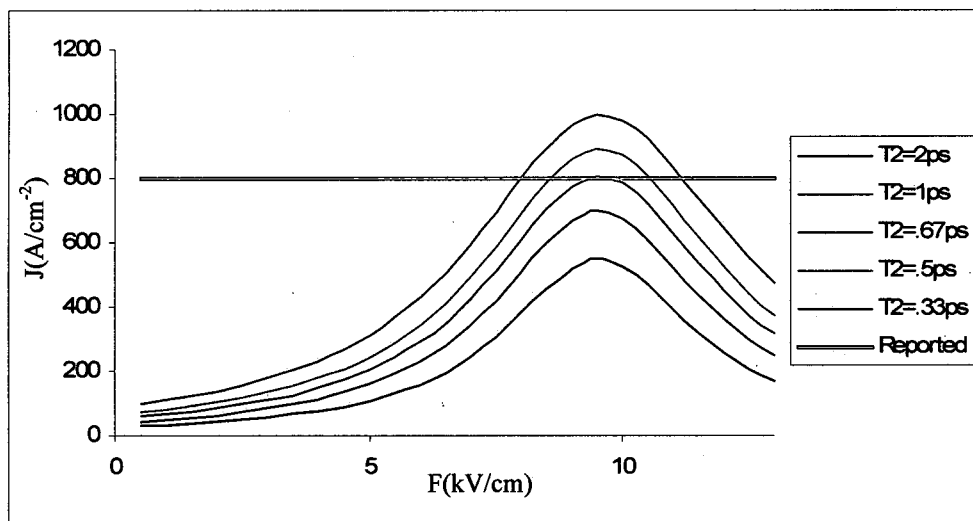


Figure 5.2.16: Current-Voltage for the 4-well QCL Reference [34] for various T_2 values.

Here it can be seen that this phenomenological, pure dephasing, term has a slightly more dramatic effect on the peak current density. A value near $T_2=0.67\text{ps}$ corresponding to $\Gamma^{\text{pure}}=1.5\times 10^{12}\text{s}^{-1}$ seems to have the most agreement with the experimentally observed current density. The gain, calculated at $T=150\text{K}$, is also plotted for various T_2 times in Figure 5.2.17. In this plot the use of longer times ($T_2 > 1\text{ps}$) clearly shows substantial above threshold gain at $T=25\text{K}$. Similarly, the very fast ($T_2 < 0.5\text{ps}$) times likely underestimate the gain, as noted by Callebaut and Hu in their hybrid density matrix simulation [102]. For this reason a value of $T_2 < 0.67\text{ps}$ will be used for modeling this and similar devices. While both this pure dephasing time and the electron-lattice coupling constant is likely a result of the specific system involved these values are quite reasonable as shown in the plots and in their use for prior simulations [85,93,94,102]. While these parameters are likely not applicable to superlattice/miniband mid-IR QCL's their values in the resonant phonon THz-QCL's can be assumed to have little variance.

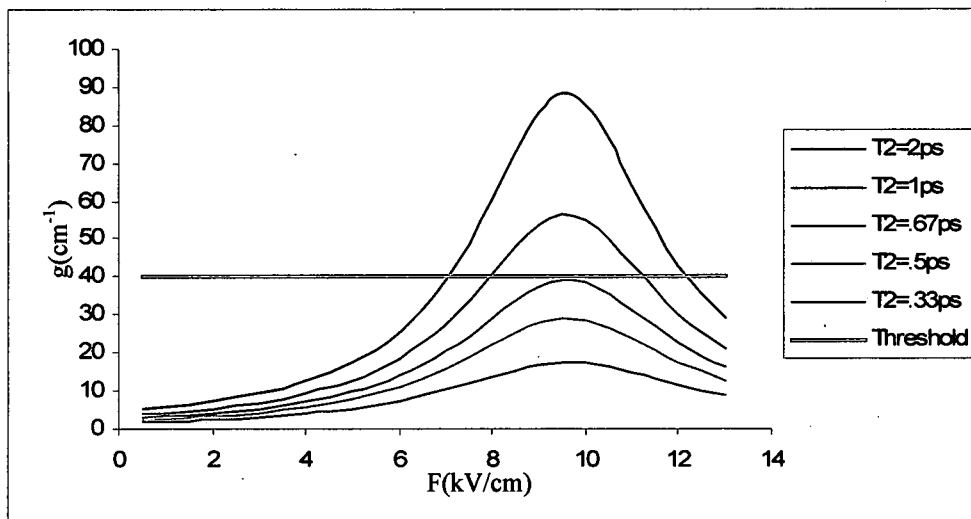


Figure 5.2.17: Gain vs. the bias for the 4-well QCL Reference [34] for various T_2 values.

Using these parameters a further analysis of this model, and its suitability for fast and intuitive calculation of THz-QCL operation, can be carried out. Using the simple picture of Figure 5.2.10, where the isolated wells are linked together by the coherent effects of the Φ terms, a normalized plot of these expressions (Figure 5.2.18), as well as the current density and the gain, can be observed for further insight into the transport processes.

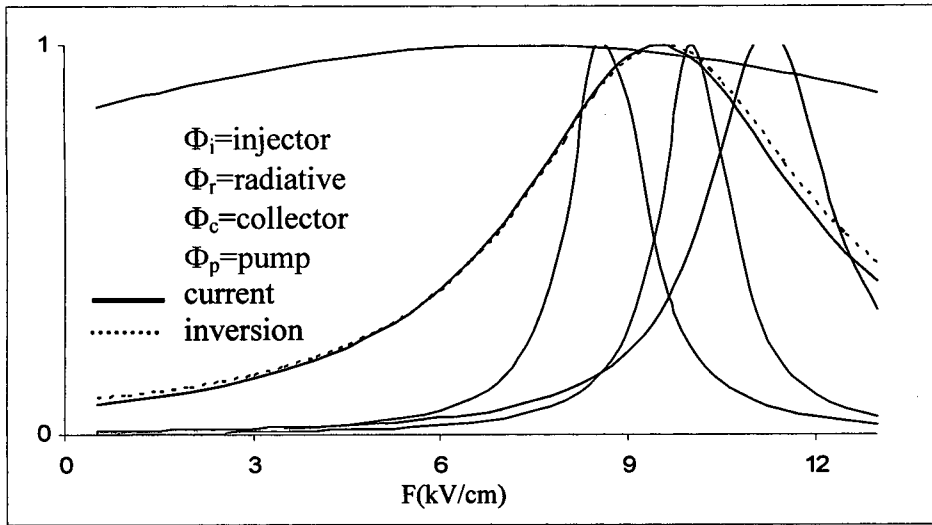


Figure 5.2.18: Normalized plots of the tunneling terms Φ as well as the current density and inversion vs. the bias.

In this plot it can be observed that the calculated resonances are slightly misaligned vs. the field. The current density, which according to Equation 5.2.10 is a function of the product of each of these terms, is shown to peak between the injector and pump alignments. The actual magnitude of the Φ terms is shown in Figure 5.2.19. In this plot the dominance of the collector resonance is observed due to the larger \tilde{V} coupling between the lower lasing state and the excited state of the phonon depletion well. The lineshape vs. the field (proportional to ΔE) for this resonance is also observed to have a

broader width due to its direct proximity to the scattering (lifetime broadening) in the phonon depletion well. The radiative resonance is observed to be very small due to its definition as a “hybrid doublet”. The energy splitting of this doublet makes the resonance condition

$$\Phi_r(\text{resonance}) = \frac{\Gamma \Omega^2}{\omega_{\text{resonance}}^2 + \Gamma^2} = \frac{\Gamma \Omega^2}{\Omega^2 + \Gamma^2} \quad (5.2.13)$$

instead of the usual

$$\Phi(\text{resonance}) = \frac{\Gamma \Omega^2}{\omega_{\text{resonance}}^2 + \Gamma^2} = \frac{\Omega^2}{\Gamma} \quad (5.2.14)$$

If this case was not implemented, as discussed in Section 4.5, the population inversion (Equation 5.2.12) which is proportional to Φ_r^{-1} would vanish due to the dominant coupling of the radiative states. This overwhelming pull towards the “pure doublet” condition cannot predict realistic gain if the active region is not permitted to be a delocalized system.

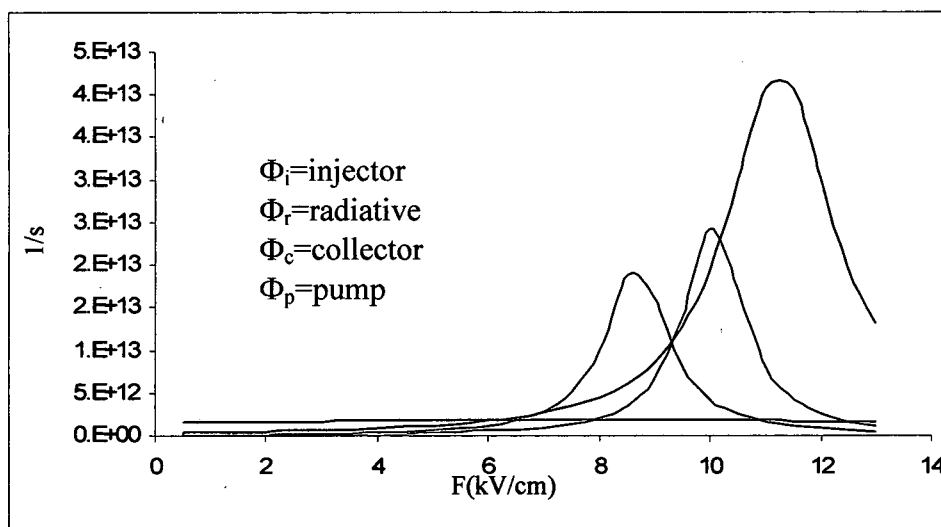


Figure 5.2.19: The tunneling terms Φ vs. the bias.

Simulation of the current density and gain for this system is plotted at various lattice temperatures in Figure 5.2.20. This simulated data, plotted in the usually displayed manner of most experimental reports, clearly indicates the nice smooth curve which peaks at nearly all temperatures in the reported range of approximately $800\text{A}/\text{cm}^2$. The threshold line at 40cm^{-1} indicates a temperature cutoff for this device at over 125K agreeing well with the experimental results of 164pulsed and 117cw. The predicted threshold current at 5K is approximately $460\text{A}/\text{cm}^2$ which again shows excellent agreement with the measured value of $435\text{A}/\text{cm}^2$. The simulated threshold vs. the lattice temperature follows a nearly linear behavior while the experimental results [34] show a significant nonlinearity at low temperatures. As a result, the predicted threshold currents at intermediate temperatures are slightly overestimated.

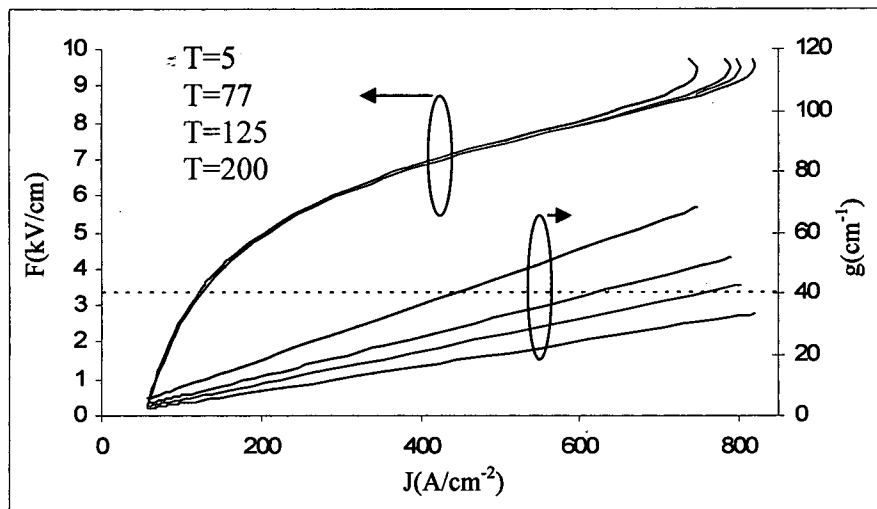


Figure 5.2.20: Simulated Voltage and gain vs. Current and at various lattice temperatures for the device of Reference [34].

Studying the precise alignment of the resonances can also be accomplished nearly instantaneously using this simple method. It was observed in Figures 5.2.18 and 5.2.19 that the tunneling events linking the wells peaked at different biases. These slight

misalignments are potentially the results of small errors made in the energy perturbation calculations and not in the intended design. To examine the effect of these alignments this first case, the original "recipe", can be altered by leaving the doublet fixed and making small changes to the injector and phonon depletion wells (Figure 5.2.21). The first adjustment aligns the injector and collector while the second aligns the injector, collector, and the pump. A comparison of the threshold current and the peak gain for each variation is shown in Figure 5.2.22.

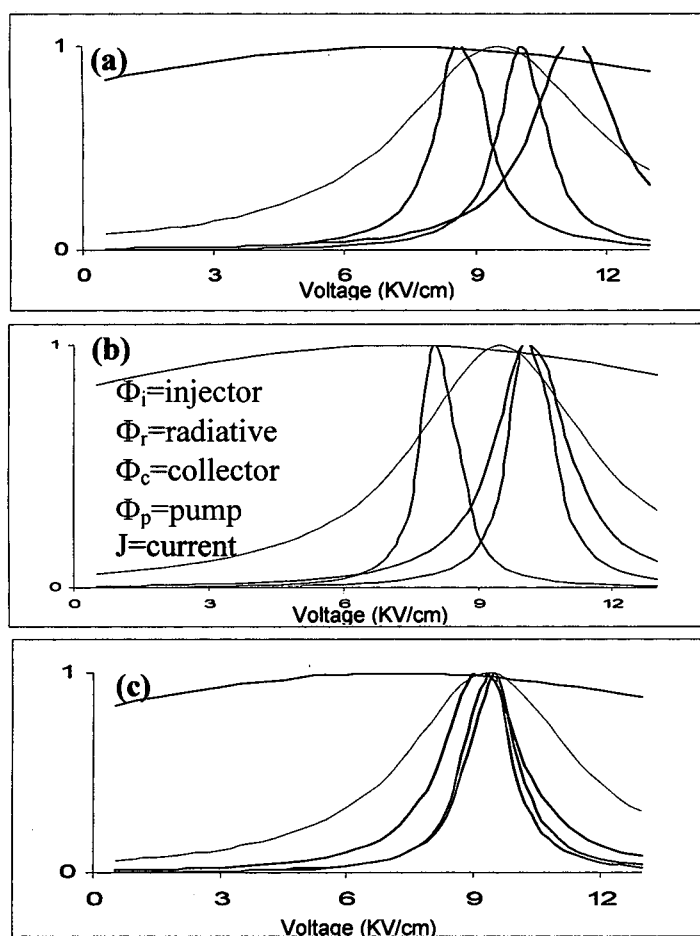


Figure 5.2.21: Normalized tunneling terms and current for the three variations of the 4-well QCL described in the text.

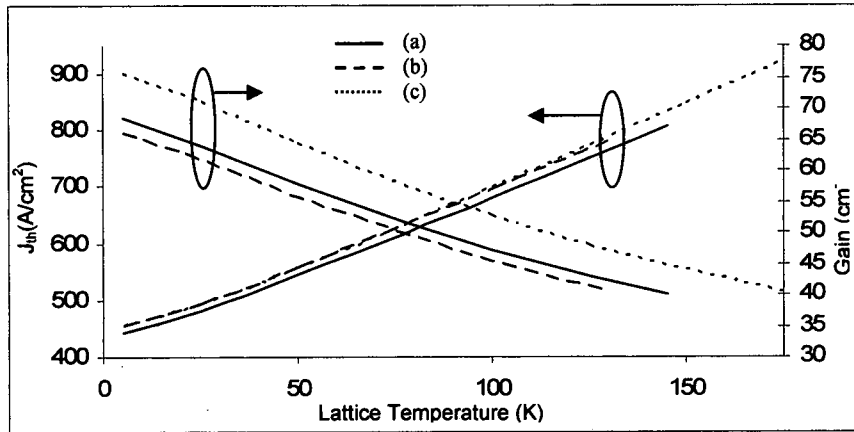


Figure 5.2.22: Threshold current densities and peak gain vs. lattice temperature for the three variations of the 3-well resonant phonon design.

Observation of Figure 5.2.22 shows that the first adjustment, which aligned the injection and collection mechanisms, produced only a slight upward shift of the threshold current density while slightly reducing the peak gain. In the second adjustment the simultaneous alignment of the pump, injector, and collector, produced a near negligible increase of the threshold, compared to the first adjustment, while the peak gain is notably increased. Observing the maximum operating temperatures, where the gain reduces to 40cm^{-1} , shows the cutoffs at approximately 145K, 130K, and 175K, respectively, for systems (a), (b), and (c). These predicted values fall near the experimentally demonstrated range for these types of lasers and the comparison of the alignment variations leads to the logical conclusion that each transport mechanism should align at the same bias for optimal performance.

Further, as pointed out in Section 4.6, the mechanism for the decay of the gain is quite different than in the semiclassical models. To illustrate this, a plot of both the peak inversion and peak gain is shown in Figure 5.2.23. From this plot it is immediately

recognized that the inversion is predicted to still exist at the higher temperatures. It also appears that the reduction in the inversion is practically linear with vs. the lattice temperature. The gain on the other hand drops in a more rapid and slightly nonlinear manner. This effect was recently pointed out by Nelander and Wacker [126] using the NEGF simulation for a similar four-well THz-QCL. Results of their simulation showed an inversion falling in a linear manner from low to high temperature operation while the gain displayed a more dramatic nonlinear decay. Their conclusion was that broadening effects played a significant role in the gain reduction and that the reliance on calculating population inversion, which the semiclassical models are restricted to, is insufficient for predicting higher temperature operation.

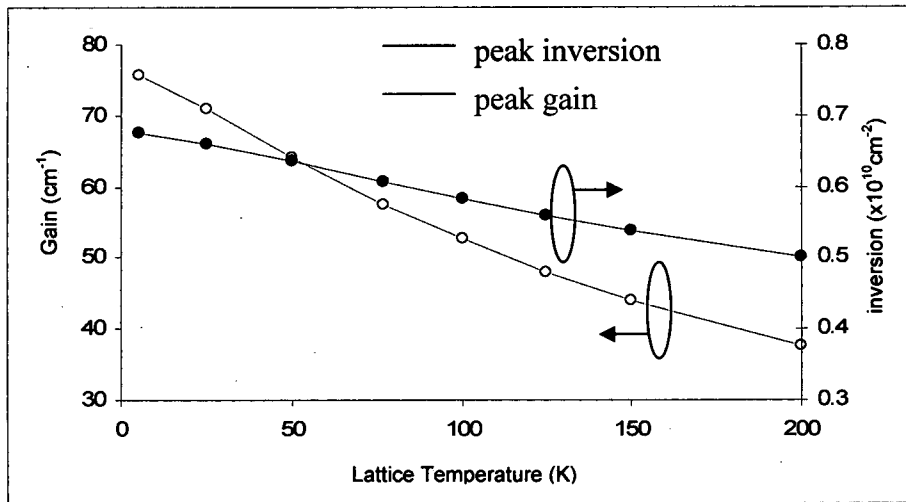


Figure 5.2.23: Peak gain and peak inversion vs. the lattice temperature.

The explanation for the gain decay, beyond that of the reduction in the inversion, is directly due to the use of the dephasing rate in the description of the gain. This expression, given by equation 4.6.34, shows the gain as being proportional to $\Delta N/\Gamma$, where Γ is the intradoublet dephasing. To observe this a plot of $\Delta N/\Gamma$, normalized to

the $T=5\text{K}$ value, is presented along with the simulated peak gain vs. the lattice temperature in Figure 5.2.24. From this figure it is clearly seen that the decay of the gain is a direct result of both the decrease of the inversion and the increase of the intradoublet dephasing. This very simple simulation, which requires practically zero computational time, captures this result as demonstrated in the fully quantum mechanical NEGF models. The semiclassical simulations (Monte Carlo and Rate Equations) have no description for this dephasing induced gain reduction and are limited to analysis of gain entirely dependent on the population inversion.

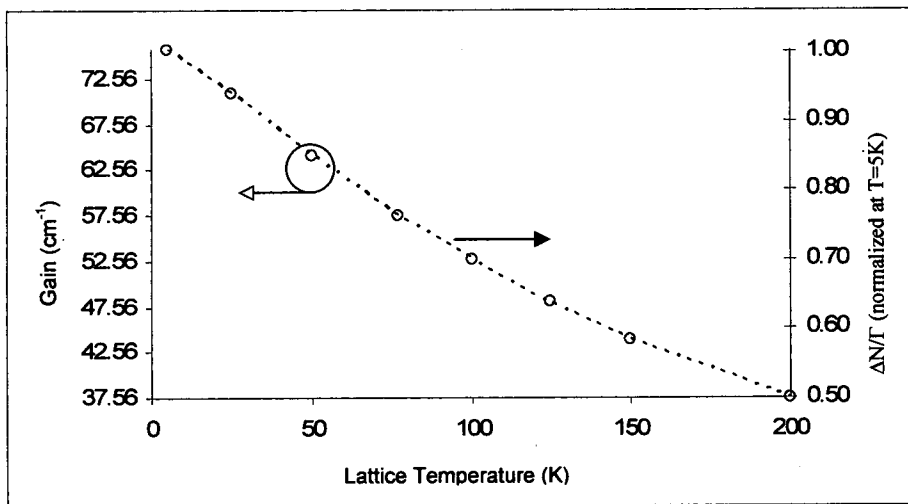


Figure 5.2.24: Peak gain (red dots) vs. temperature and the value $\Delta N/\Gamma$ (black dotted line) normalized at $T=5\text{K}$.

5.3 The 3-Well Resonant Phonon Depopulation Laser

Recently (2007), a three-well per period resonant phonon QCL was demonstrated [42]. This device simply removes one of the injector wells in the 4-well design (see Figure 5.3.1). Possible benefits of removing potentially unnecessary wells (states) in these devices include higher current flow and less photon absorption in

injector states separated by energies close the desired emission. This three well device presently holds the THz high temperature operation record of 178K in pulsed mode at 3 THz [43]. Similar to the 4-well QCL this device has typically been modeled using the Monte Carlo simulations [96,101].

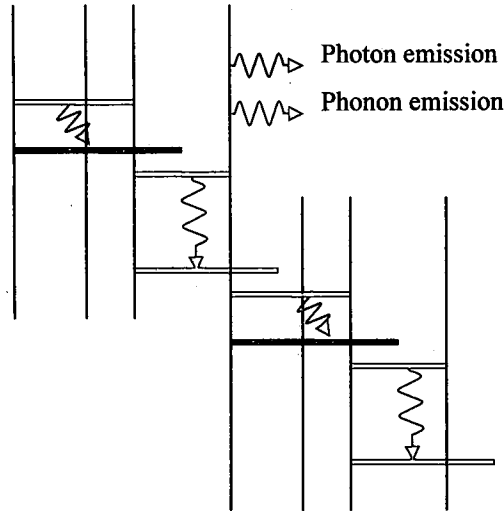


Figure 5.3.1: Diagram of the 3-well resonant phonon depopulation THz-QCL.

The device to be simulated is a GaAs/ $\text{Al}_{0.15}\text{Ga}_{0.85}\text{As}$ system [42,43] with layer widths in Å, starting at the upper lasing state well, of 96/**20**/74/**42**/161/**48** (barriers in bold). The phonon well is doped resulting in a sheet density of $3.6 \times 10^{10} \text{ cm}^{-2}$. Similar to the 4-well QCL the first step is to check that the expansion in the localized basis can accurately predict the lasing energy (of $\sim 13 \text{ meV}$ or 3THz) and the desired resonant phonon depopulation mechanism (near 36meV). A plot of the tight-binding energies (with repelling effects) vs. the bias is shown in Figure 5.3.2., and the comparison with the reported values is shown in Figure 5.3.3. The predicted energy separations for the lasing energy and the phonon depopulation are shown to agree very well with the reported data

and the intended design. With this verified the calculation of transport in the DDM representation can be carried out.

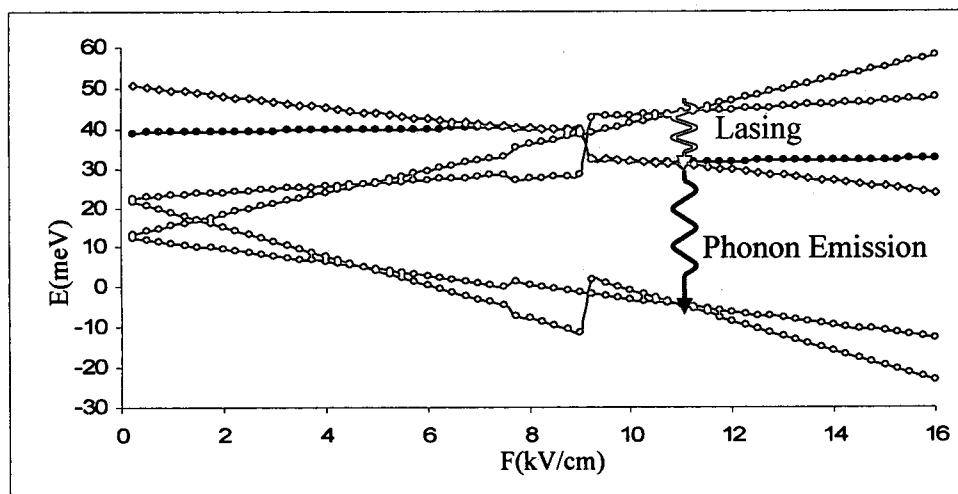


Figure 5.3.2: Comparison of the energies vs. the bias for the coupled-well expansion in the localized basis and the full numerical model.

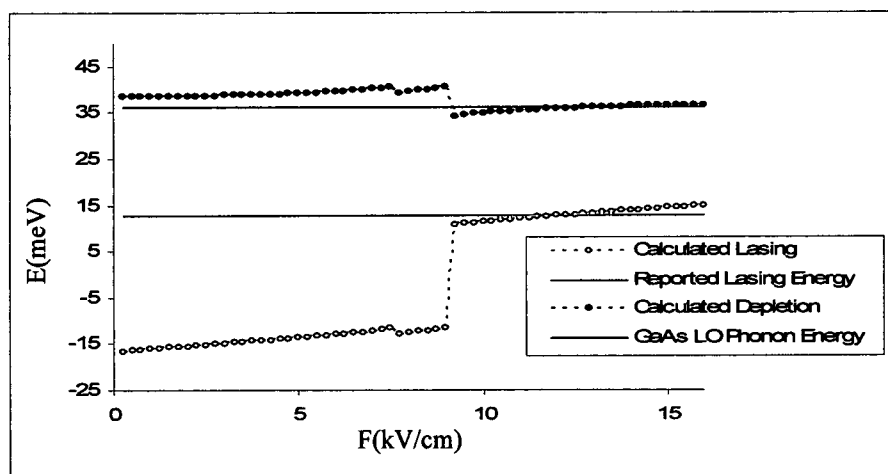


Figure 5.3.3: Localized basis calculation of the lasing state energy separation and the phonon depletion mechanism compared to reported results.

The simple DDM description of transport for this QCL design follows the same procedure as implemented in Section 5.2. The scattering is assumed to be intrawell only and the active region is split into a “hybrid doublet” (Figure 5.3.4).

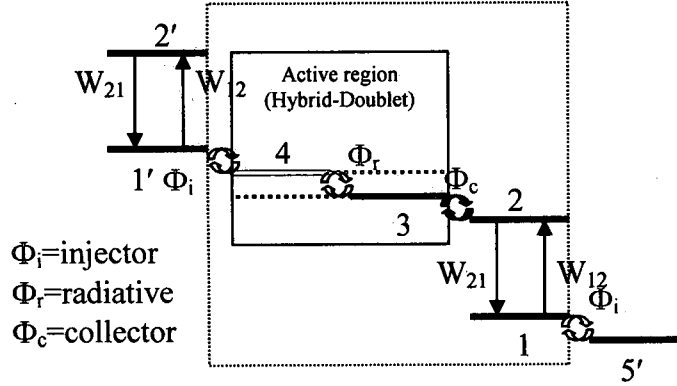


Figure 5.3.4: DDM picture of transport using the localized basis with a pseudo or “hybrid-doublet” used as the active region.

The steady-state diagonal elements of the density matrix can then be written as

$$\begin{aligned} \rho_{11} &= \frac{W_{21}\rho_{22} + \frac{1}{2}\Phi_i\rho_{44}}{W_{12} + \frac{1}{2}\Phi_i} & \rho_{22} &= \frac{W_{12}\rho_{11} + \frac{1}{2}\Phi_c\rho_{33}}{W_{21} + \frac{1}{2}\Phi_c} \\ \rho_{33} &= \frac{\frac{1}{2}(\Phi_r\rho_{44} + \Phi_c\rho_{22})}{\frac{1}{2}(\Phi_r + \Phi_c)} & \rho_{44} &= \frac{\frac{1}{2}(\Phi_i\rho_{11} + \Phi_r\rho_{33})}{\frac{1}{2}(\Phi_i + \Phi_r)} \end{aligned} \quad (5.3.1)$$

Solving this system produces the following results for the populations

$$N_1 = N_s \rho_{11} = N_s \frac{\Phi_{irc} + 2W_{21}(\Phi_{ir} + \Phi_{ic} + \Phi_{rc})}{4\Phi_{irc} + 2W_{21}(\Phi_{rc} + 2\Phi_{ic} + 3\Phi_{ir}) + 2W_{12}(\Phi_{ir} + 2\Phi_{ic} + 3\Phi_{rc})} \quad (5.3.2)$$

$$N_2 = N_s \rho_{22} = N_s \frac{\Phi_{irc} + 2W_{12}(\Phi_{ir} + \Phi_{ic} + \Phi_{rc})}{4\Phi_{irc} + 2W_{21}(\Phi_{rc} + 2\Phi_{ic} + 3\Phi_{ir}) + 2W_{12}(\Phi_{ir} + 2\Phi_{ic} + 3\Phi_{rc})} \quad (5.3.3)$$

$$N_3 = N_s \rho_{33} = N_s \frac{\Phi_{irc} + 2W_{21}\Phi_{ir} + 2W_{12}(\Phi_{ic} + \Phi_{rc})}{4\Phi_{irc} + 2W_{21}(\Phi_{rc} + 2\Phi_{ic} + 3\Phi_{ir}) + 2W_{12}(\Phi_{ir} + 2\Phi_{ic} + 3\Phi_{rc})} \quad (5.3.4)$$

$$N_4 = N_s \rho_{44} = N_s \frac{\Phi_{irc} + 2W_{21}(\Phi_{ir} + \Phi_{ic}) + 2W_{12}\Phi_{rc}}{4\Phi_{irc} + 2W_{21}(\Phi_{rc} + 2\Phi_{ic} + 3\Phi_{ir}) + 2W_{12}(\Phi_{ir} + 2\Phi_{ic} + 3\Phi_{rc})} \quad (5.3.5)$$

The current density is then

$$J = qN_s \frac{\Phi_{irc}(W_{21} - W_{12})}{4\Phi_{irc} + 2W_{21}(\Phi_{rc} + 2\Phi_{ic} + 3\Phi_{ir}) + 2W_{12}(\Phi_{ir} + 2\Phi_{ic} + 3\Phi_{rc})} \quad (5.3.6)$$

which is very similar to the previous 4-well structure. The inversion takes the same form as before

$$\Delta N_{43} = \frac{2J}{q\Phi_r} \quad (5.3.7)$$

Using these expressions and the α_{e1} and T_2 parameters established for the 4-well design, the voltage-current and peak gain simulation results for the exact recipe given by References 42 and 43, are shown in Figure 5.3.5 at various lattice temperatures. The calculated current density, at all temperatures in the range of $T=5K$ to $T=200K$ are observed to peak at approximately $1300A/cm^2$. While experimental results have shown the maximum obtainable current at larger values approaching $1600A/cm^2$ [42,43], a very clear and abrupt shoulder at $1350A/cm^2$ is attributed to the NDR point resulting from the misalignment of the injector and the upper lasing state [43]. The results of this

simulation are then shown to be in excellent agreement with the experimental results regarding the peak current density.

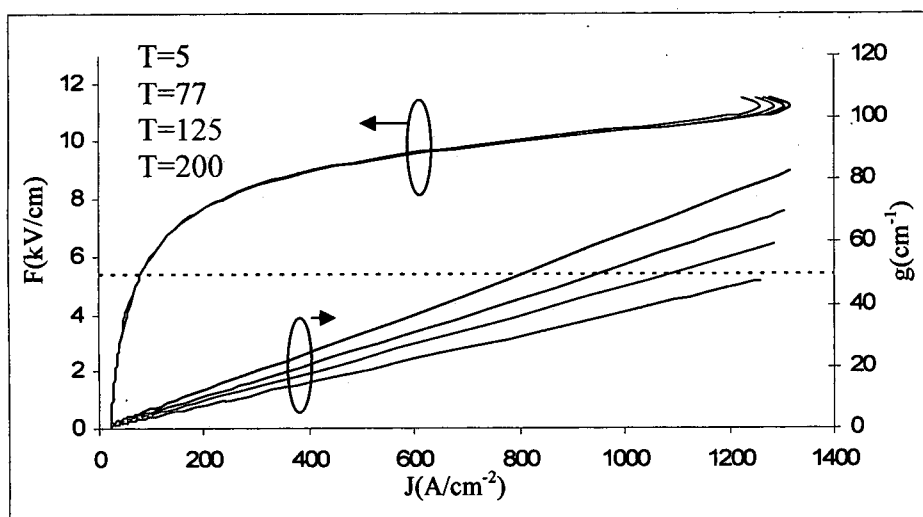


Figure 5.3.5: Figure 5.2.18: Simulated voltage and gain vs. current at various lattice temperatures for the device of References [42,43].

The gain predicted by the simple DDM simulation is also compared to the reference threshold, assumed to be 50cm^{-1} [96] for this device. As is illustrated by the plot, this simulation predicts the maximum operating temperature just under $T=200\text{K}$. Further simulations refined this value to 185K . This again displays exceptional agreement with the confirmed maximum pulsed operating temperature of 178K [43]. Similar to the 4-well simulation the calculated slope of the gain vs. the current is somewhat different than observed experimentally for intermediate temperatures. For instance, the measured threshold current at 78K is just over $700\text{A}/\text{cm}^2$ while the prediction is slightly higher at just over $900\text{A}/\text{cm}^2$. Nonetheless, simulated results agree very well with experimental data concerning both the peak current and the maximum operating temperature.

The normalized tunneling terms Φ for this device are plotted in Figure 5.3.6a. The slight misalignment of the resonances, as was observed previously for the 4-well QCL, is seen for this simulation using the exact recipe from the reported device [42,43]. Slight adjustments were then made, to the well widths only, to realign the injector and collector at the same bias (Figure 5.3.6b).

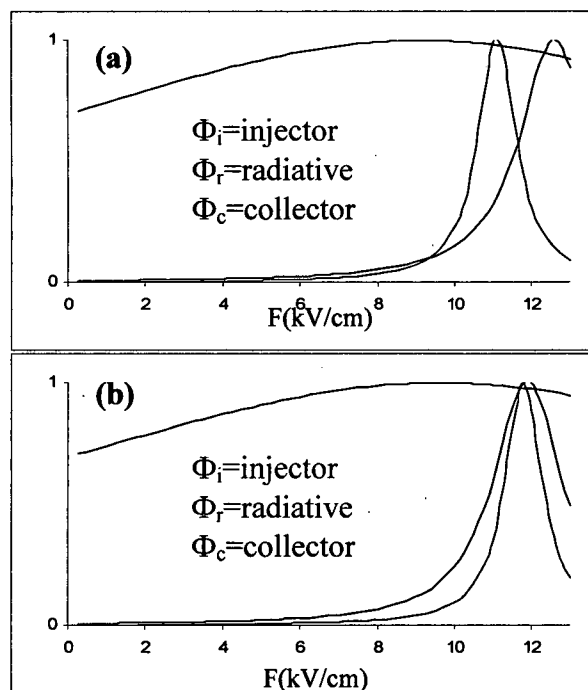


Figure 5.3.6: Normalized tunneling terms for the two variations of the 4-well QCL described in the text.

The comparison of the threshold currents and the peak gain vs. the lattice temperature for these two variations of the 3-well resonant phonon QCL is shown in Figure 5.3.7. In this plot the readjustment of the injection and collection resonances is shown to produce a negligible increase in the threshold current while displaying a significant increase in the peak gain. With the system perfectly aligned the predicted maximum operating

temperature is calculated to be approximately $T=225\text{K}$. While this temperature has yet to be demonstrated these 3-well resonant phonon QCL's are relatively new (2007) compared to the extensive optimization (since 2003) which has been carried out for the 4-well designs.

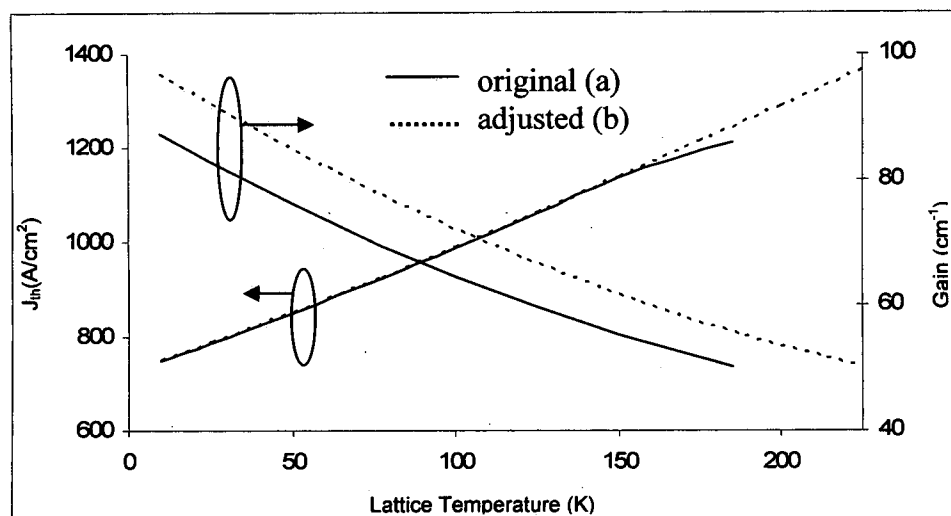


Figure 5.3.7: Threshold current densities and peak gain vs. lattice temperature for the two variations of the 3-well resonant phonon design.

5.4 Intrawell Lasing and Potential Problems with the Simplified Model

In their demonstration of the importance for including coherent and dephasing effects Callebaut and Hu [102] applied a tight-binding density matrix technique to join isolated periods of a QCL. Combined with an intraperiod treatment using a Monte Carlo simulation the conclusion was made that the semiclassical models, which do not account for these effects, have the potential to predict inversion and gain in designs not observed experimentally. Specifically, a two well system was analyzed where lasing was to occur between an excited and ground state in a single well. Their hybrid model approach,

which incorporated coherent effects, resulted in no prediction of inversion while the full semiclassical Monte Carlo calculation showed significant inversion capable of producing gain. Since no gain was observed experimentally it was concluded that the semiclassical result was incorrect.

Examination of this simple 2-well design using the simple DDM procedure is accomplished in the same manner as the prior examples. The primary difference between this device and the previous designs is the noticeable absence of a doublet (Figure 5.4.1)

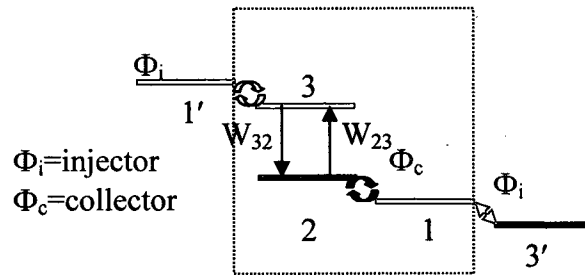


Figure 5.4.1: 2-well QCL laser design.

In this system lasing is to occur between states $|3\rangle$ and $|2\rangle$ and thus represents an intrawell process. This system, treated using the simple DDM method, produces the following steady-state augmented matrix for the diagonal elements

$$\begin{bmatrix} -\frac{1}{2}(\Phi_c + \Phi_i) & \frac{1}{2}\Phi_c & \frac{1}{2}\Phi_i & 0 \\ \frac{1}{2}\Phi_c & -\left(W_{23} + \frac{1}{2}\Phi_c\right) & W_{32} & 0 \\ \frac{1}{2}\Phi_i & W_{23} & -\left(W_{32} + \frac{1}{2}\Phi_i\right) & 0 \\ 1 & 1 & 1 & 1 \end{bmatrix} \quad (5.4.1)$$

which results in the solutions

$$N_1 = N_s \rho_{11} = N_s \frac{\Phi_{ic} + 2(W_{32}\Phi_c + W_{23}\Phi_i)}{3\Phi_{ic} + 4W_{32}\Phi_c + 2W_{32}\Phi_i + 4W_{23}\Phi_i + 2W_{23}\Phi_c} \quad (5.4.2)$$

$$N_2 = N_s \rho_{22} = N_s \frac{\Phi_{ic} + 2W_{32}(\Phi_c + \Phi_i)}{3\Phi_{ic} + 4W_{32}\Phi_c + 2W_{32}\Phi_i + 4W_{23}\Phi_i + 2W_{23}\Phi_c} \quad (5.4.3)$$

$$N_3 = N_s \rho_{33} = N_s \frac{\Phi_{ic} + 2W_{23}(\Phi_c + \Phi_i)}{3\Phi_{ic} + 4W_{32}\Phi_c + 2W_{32}\Phi_i + 4W_{23}\Phi_i + 2W_{23}\Phi_c} \quad (5.4.4)$$

The inversion in this case is

$$\Delta N_{32} = N_s \frac{2(\Phi_c + \Phi_i)(W_{23} - W_{32})}{3\Phi_{ic} + 4W_{32}\Phi_c + 2W_{32}\Phi_i + 4W_{23}\Phi_i + 2W_{23}\Phi_c} \quad (5.4.5)$$

resulting in the obvious conclusion that in order to achieve inversion the upward rate W_{23} must be greater than the downward rate W_{32} . This situation will not occur for any mean subband scattering rates treated in this work. While this analytical result may present an argument supporting the conclusion that gain is not possible in this type of device, recent experimental observation of lasing action in a single well has been demonstrated [163]. This result leads to some fundamental problems associated with the presented modeling approach.

In the simple model of sequential tunneling transport described in this research the current density is assumed to flow through localized states where the subband is treated as a singular object. Incoherent scattering is calculated only for intrawell/intersubband transitions. In the treatment of a system such as the 4-well resonant phonon QCL (Figure 5.4.2) there are multiple states (3, 4, & 5) which are considered to be the only, singular, paths through this region of the device. Since there is no account for any internal current driving mechanism within these single state wells, the entire current flow is essentially pulled by the phonon scattering well. In a sense, if the

coupling between the wells was more uniform, the entire series of states (2,3,4,5, & 1') could be considered as a type of "quintuplet" as is shown in Figure 5.4.3.

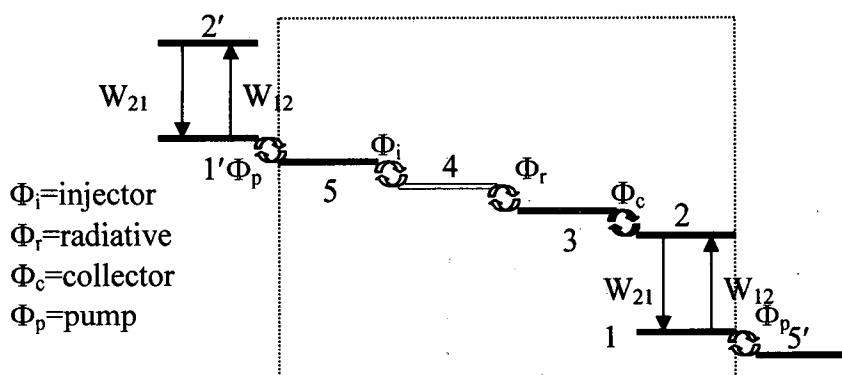


Figure 5.4.2: 4-well resonant phonon laser design.

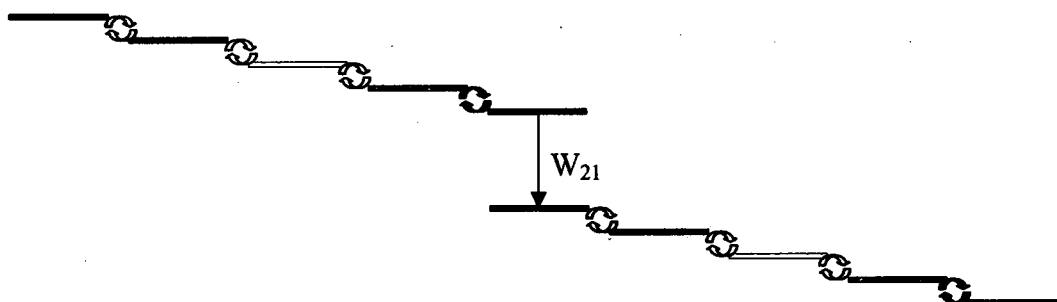


Figure 5.4.3: The 4-well resonant phonon design depicted as repeating "quintuplets".

This picture allows for the return of arguments originally introduced in Chapter 4 regarding the differences between the localized basis density matrix and the semiclassical picture. In treating a doublet system where only a single, intrawell, scattering rate was present it was argued that in the limit of a dominant coupling (oscillation) that the population converges to equal (pure doublet) and the semiclassical, delocalized, picture could be applied. The same arguments are applicable to the states shown in Figure 5.4.3, or any other "superlattice-type" of system. Thus, in the limit where all of the states are tightly bound the above picture represents two minibands, each containing 5 states, and

due to the symmetry at resonance, would all contain equal populations. At anything less than the “pure quintuplet” the population in the given model must be distributed from left-to-right in the above picture. This is a direct result of the singular subband DDM current expression

$$J = qN_s(\rho_{ii} - \rho_{ff}) \quad (5.4.6)$$

This equation implies that in order for the current to tunnel from left-to-right, the leftmost state must have the greater population since there is no other mechanism to redistribute the electrons or drive the current until the scattering well is reached. Since the last state in the upper “miniband” represents the upper state in the scattering well, and the first state in the lower “miniband” is the ground, the logical conclusion in this description is that the lower state always has a greater than or equal to population.

The proven lasing of the “superlattice-type” Mid-IR QCL’s are based upon a logical, but contradictory, argument. In this reasoning it is assumed that internal, intraminiband, processes carry the population quickly down to the lowest state in each band thus creating an inversion between the lowest state in the upper miniband and the highest state in the lower miniband. In fact, if a semiclassical simulation was performed where all intraminiband scattering was considered, this would be the result. Therefore, it is clear that the picture of indefinite sequential tunneling through many wells containing subbands treated as singular, isolated, entities has limitations.

In a recent model, Terrazi et. al. [162], presented a model of resonant tunneling which includes second-order effects. In this approach resonant tunneling between 2D subbands is treated in a manner which permits interaction between states $|E_i, k_i\rangle$ and $|E_o, k_o\rangle$ where $k_i \neq k_o$. In this picture (Figure 5.4.4) interwell tunneling occurs between states of equal energy and the internal, intrasubband processes, drive the current flow.

For equivalent subbands the distribution of electrons, and thus the direction of the tunneling transport, is dependant on the difference between the in-plane momentums k_i and k_f . If subband $|i\rangle$ is aligned below $|f\rangle$ then tunneling is occurring between states where $k_i > k_f$. In this case the current flows towards $|i\rangle$ due to the larger population in $|E_i, k_i\rangle$. Conversely, the same arguments can be applied to the case where subband $|i\rangle$ is aligned above $|f\rangle$ resulting in tunneling currents towards $|f\rangle$. Treatment of sequential tunneling in this manner, suggests that while the resonance condition between two equivalent subbands predicts a vanishing net current, transport in the desired direction can be optimized at slightly off-resonant positions.

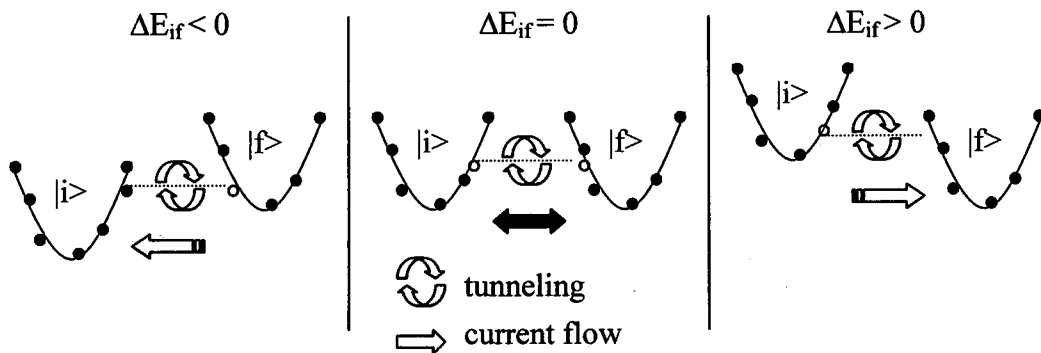


Figure 5.4.4: Diagram showing 2nd order tunneling effects.

The simplified treatment of tunneling using a mean intrawell scattering approach combined with a steady-state diagonal density matrix treatment does not have the capability to describe these 2nd order processes. Prediction of gain in a single well, lasing without inversion [164], and miniband transport as typically employed in the Mid-IR QCL's is not easily handled with this simplified model. As demonstrated in this chapter however, simulations of the limited state resonant phonon THz-QCL's are approximated quite accurately in an intuitive, analytically accessible, and nearly real-time manner.

CHAPTER 6

CONCLUSIONS

The objective of this thesis was not to further implement comprehensive theoretical quantum mechanics or to directly challenge the still, in many regards, applicable semiclassical models. Instead, a direction of simplicity and reduced computational complexity was sought. In recognition of the benefits of many previous models and procedures, an attempt was made to examine, simplify, and combine these techniques in a unique manner that is more accessible theoretically and efficient computationally.

The analogy of the quantum well as an "artificial atom" has the combined benefit of theoretical accessibility and the potential for efficient computation. Before the emergence of high speed computers, the technique of using Linear Combinations of Atomic Orbitals (LCAO) to describe molecules and solids was often utilized and proved successful in many circumstances for approximating properties in solid-state physics. In this method many quantities which regularly occur as matrix elements (or integrals) were pre-tabulated for easier implementation into more complex calculations. In the spirit of this technique, and with the observation of more recent models trending back towards localized eigenstates and tight-binding procedures, this research was an effort to create a method of calculating quantum cascade lasers using linear combinations of single well

properties. A chapter by chapter summary of this effort is given in the following discussion followed by recommendations for future improvements.

In Chapter 2 a method of calculating single well eigenstates was presented. While the calculation of energies and wavefunctions in general heterostructures is not computationally demanding, the construction of an analytical basis was required for further simplifications used in later calculations. With the general form of the single well wavefunction being well known, through the knowledge of the wavevectors $k(\epsilon)$ and $\kappa(\epsilon)$, it was recognized that a simple empirical fit of the single well energies $\epsilon(L)$ for a specific system could enable an automatic description over all space of the normalized wavefunction components. In this manner a wavefunction for a given well width could then be translated into a location in a multi-well structure without the need for any eigenvalue solution or renormalization procedure.

Using this analytical basis a simplified tight-binding approach was presented. Similar to the LCAO method, the main components of this procedure appear as matrix elements requiring integration. Since the single-well basis was described analytically, requiring only the designation of the interface locations to obtain the wavevectors, these tight-binding matrix element integrals were evaluated to an indefinite form again requiring only the interface locations for a nearly instantaneous determination of their values. By investigating the typical parameters used in THz-QCL's, such as well widths and the number of relevant states per well, an approximation to the full tight-binding matrix solution was developed. It was demonstrated in simple systems, and later in more complex QCL's, that this approximation to the full tight-binding eigenvalues showed very good agreement with both fully calculated energies and wavefunctions. At this point coupled-well effects such as repelling and wavefunction delocalization over a nearest

neighbor range can be described immediately by simply defining the interface locations of a given system.

Countless hours, and several overheated personal computers, were spent running scattering rate simulations on multiple computers leading to the realization that these were the major impediments to efficient computing. Potential complicating issues regarding the inclusion of heterostructure effects on phonon modes was investigated. Empirical fitting functions were found to sufficiently describe the numerous complex phonon modes using only combinations of GaAs-like and AlAs-like bulk phonons. The end result was the conclusion that in low AlAs composition barriers, which are used in most THz-QCL's, additional treatment beyond the GaAs-bulk phonon is not truly needed. If calculations are required for higher AlAs composition barriers the described technique was shown to be more accurate than the bulk-GaAs approximation with a negligible increase in computation.

The most significant computational benefit was found by combining mean subband rates, which average out the 2D nature of the confined electrons, with the localized analytical basis and the tight-binding method. Using an assumption of intrawell scattering only Fermi's Golden Rule was expanded in the localized single well basis. An assumption was then made that the mean scattering rates for single well transitions could be used for a direct linear combination of intrawell scattering (LCIS). Once this was proven reasonable the creation of a predetermined table or multi-parameter fitting functions was realized. A methodical investigation of the limited intrawell transitions for LO-phonon emission and absorption, as well as electron-electron scattering was carried out. Empirical fitting functions were then found to describe these "mean basis rates" for a wide range of energy separations, lattice temperatures, and electron temperatures.

Reconstruction of multi-well scattering events using this technique was compared to full numerical calculations demonstrating its suitability for extremely fast computation. With these fitting functions for the intrawell mean rates the constructed procedure enabled the description of all properties, including the subband lifetimes, requiring only the definitions of the interface locations and the lattice and electron temperatures.

In Chapter 4 the first demonstration of the benefits of the outlined procedure was shown. Using a semiclassical rate equation approach a calculation of transport properties in a repeating 2-state per well superlattice was conducted using both the full numerical simulation and the localized basis expansion with the empirical LCIS method. In this comparison the two techniques were shown to produce nearly identical results. The full simulation however, required 4 hours to calculate on a standard computer while the LCIS technique took less than 1 second. Additionally, it was shown that the full simulation has the tendency to predict unrealistic current spikes due to unphysical wavefunction delocalization while the LCIS technique, restricted to the nearest neighbor does not exhibit this error.

While this result showed impressive computational capabilities, compared to the rate equation approach, it was then determined that the semiclassical models have fundamental flaws and a further, time-dependant, description with the inclusion of dephasing was necessary. To treat this interplay between coherent and incoherent phenomena the density matrix formalism was investigated. Applying reasonable simplifications to the $N^2 \times N^2$ matrix expressions required for the full density matrix description allowed the steady-state expressions for the diagonal elements (the normalized subband populations) to be recast back into an $N \times N$ system while preserving a description of the coherent tunneling and dephasing processes. This simplified,

diagonal density matrix (DDM), was scrutinized and compared to semiclassical descriptions of transport. Taking into consideration the recent hybrid models of other authors, where QCL systems were artificially broken up into separate isolated regions, an assessment was made, based on simulated results and logical arguments, to treat the lasing doublet as a unique entity in an otherwise localized basis. In this treatment it was decided to maintain the designation of incoherent scattering transport as a local, intrawell process, and describe intradoublet scattering effects as indirectly contributing to transport through the dephasing terms. Based on this assumption a derivation of the gain was given using the simple density matrix description of a "small signal" radiation field interacting with a two-state system. The difference in the final gain description, compared to the semiclassical models, was the inclusion of the intradoublet dephasing instead of a constant linewidth value.

In Chapter 5 the notion of describing THz-QCL transport in the LCIS semiclassical representation was, not surprisingly, quickly dismissed. The implementation of the DDM technique though proved very useful. The ability to cast a system, regarding as very complex, into a simple analytical form for the populations, current density, and inversion was demonstrated. After determining reasonable values for the electron-lattice coupling parameter and the pure dephasing rate near real-time simulation of current-voltage characteristic and gain was performed. With the use of the analytical basis, the simplified tight-binding matrix elements, the empirical LCIS scattering technique, and the analytical form of the DDM expressions, the entire calculations of transport and gain required only the designation of the interface locations and the specification of the lattice temperature. As a result entire I-V and gain calculations took approximately 1 second to evaluate.

Comparison of the simulations with reported results for the 4-well resonant phonon QCL showed very good agreement for predictions of the temperature stable peak current and the smooth I-V curve, two results not typically achieved with the semiclassical models. Further, predictions of threshold currents and maximum operating temperatures showed excellent agreement with experimental results. In addition to the near-real computation and the demonstrated accuracy the presented technique was shown to provide insight not available with the semiclassical approaches. In particular, examination of the interwell resonance terms Φ was shown to be useful in that aspects of both the energy alignment as well as the scattering induced broadening can be investigated in a very intuitive manner. Similarly, the broadening of the radiative transition due to the intradoublet dephasing at higher temperatures was shown to contribute significantly to the reduction of gain. The semiclassical models, which have no description of temperature dependent dephasing, rely only on calculations of the inversion decay. This effect, which has recently been pointed out using results of the fully quantum-mechanical, Non-Equilibrium Greens Function models, was shown to contribute to significant gain depletion even in the presence of a considerable population inversion.

Further validity of the prescribed technique was demonstrated by evaluating the 3-well resonant phonon THz-QCL. This simulation also showed excellent agreement between the predicted and experimental results for the direct input of the device layer widths. After realigning the injection and collection resonances the potential for greater than 200K operation was predicted for these devices. While these temperatures have yet to be demonstrated the relative immaturity of this design, first demonstrated in 2007 and

now holding the THz high temperature record of 178K, makes this prediction seem reasonable.

The simplified DDM analysis, applied to a two-well/intrawell QCL design suggested that inversion cannot be achieved in this configuration. While this result agreed with experimental observations, where the semiclassical models fail by predicting gain, potential problems with the simplified model must be addressed. Specifically, the model cannot predict intrawell gain for any conceivable configuration even though recent reports suggest this occurrence. Accepted behavior of intraminiband transport, as typically found in the mid-IR QCL's, is not easily treatable with the presented approach. Nonetheless, the demonstrations of a modeling technique capable of near-zero computational time which can accurately portray transport and gain in the resonant phonon THz-QCL's while maintaining an accessible analytical form is certainly valuable as a simulation tool.

The basic approach to this research, as with any model, will require further iteration. The techniques towards simplification, presented in this work, could be reapplied to other phenomena. A systematic investigation of ionized-impurity scattering, interface disorder and other potential scattering mechanisms could be carried out and included in the same manner as the phonon and simple electron-electron rates. Examination of the starting eigenstates could be undertaken as this simplification process is not basis specific. A method for including intrasubband processes (the 2D nature) should be researched as this would help solve the "miniband" problem of many consecutive states without a scattering rate driving mechanism. Finally, the results of the full quantum mechanical models should continually be examined and techniques for incorporating their subtleties into simplified models should be attempted.

REFERENCES

- [1] Z. I. Alferov, *Rev. Mod. Phys.*, 73, 2001.
- [2] L. Esaki and R. Tsu, *IBM J. Res. Devel.*, 14:61, 1970.
- [3] R. F. Kazarinov and R. A. Suris, *Soviet Physics-Semiconductors*, 5:707, 1971.
- [4] R. Dingle, W. Wiegman, and C.H. Henry, *Phys. Rev. Lett.*, 33:827, 1974.
- [5] F. Capasso, *Science*, 235:172, 1987.
- [6] J. Faist, F. Capasso, C. Sirtori, D.L. Sivco, and A.Y. Cho, *Intersubband Transitions in Quantum Wells: Physics and Device Applications*, number 2, chapter VIII. Academic Press, N.Y. 2000.
- [7] F. Capasso, R. Paiella, R. Martini, R. Colombelli, C. Gmachl, T. L. Myers, M. S. Taubman, R. M. Williams, C. G. Bethea, K. Unterrainer, H. Y. Hwang, D. L. Sivco, A. Y. Cho, A. M. Sergent, H. C. Liu, and E. A. Whittaker, *IEEE J. Quant. Elec.*, 38:6, 2002.
- [8] C. Gmachl, F. Capasso, D. L. Sivco, and A. Y. Cho, *Rep. Prog. Phys.*, 64:1533, 2001.
- [9] Faist J, Capasso F, Sivco D L, Sirtori C, Hutchinson A H and Cho A Y, *Science*, 264:553, 1994.
- [10] Beck M, Hofstetter D, Aellen T, Faist J, Osterle U, Illegems M, Gini E and Melchior H, *Science* 295:301, 2002.
- [11] Evans A, Yu J S, David J, Doris L, Mi K, Slivken S and Razeghi M, *Appl. Phys. Lett.*, 84: 314 2004.
- [12] P.F. Yuh and K.L. Wang, *Appl. Phys. Lett.*, 51:1404, 1987.

- [13] S.I. Borenstain and J. Katz, *Appl. Phys. Lett.*, 55:654, 1989.
- [14] Q. Hu and S. Feng. *Appl. Phys. Lett.*, 59:2923, 1991.
- [15] A. N. Korotkoz, D.V. Averin, and K.K. Likharev. *Appl. Phys. Lett.*, 65:1865, 1994.
- [16] Rochat M, Faist J, Beck M, Oesterle U and Ilegems M, *Appl. Phys. Lett.*, 73:3724, 1998.
- [17] Williams B S, Xu B, Hu Q and Melloch M R, *Appl. Phys. Lett.*, 75:2927, 1999.
- [18] Ulrich J, Zobl R, Schrenk W, Strasser G, Unterrainer K and Gornik E, *Appl. Phys. Lett.*, 77 :928, 2000.
- [19] Sirtori C, Gmachl C, Capasso F, Faist J, Sivco D L, Hutchinson A L and Cho A Y, *Opt. Lett.*, 23:1366, 1998.
- [20] J. Ulrich, R. Zobl, N. Finger, K. Unterrainer, G. Strasser, and E. Gornik, *Physica B*, 272:216, 1999.
- [21] B. Xu, Q. Hu, and M.R. Melloch. *Appl. Phys. Lett.*, 71, 1997.
- [22] B.S. Williams, B. Xu, Q. Hu, and M.R. Melloch. *Appl. Phys. Lett.*, 75, 1999.
- [23] Kohler R, Tredicucci A, Beltram F, Beere H E, Linfield E H, Davies A G, Ritchie D A, Iotti R C and Rossi F, *Nature* 417:156, 2002.
- [24] M. Rochat, L. Ajili, H. Willenberg, J. Faist, H. Beere, G. Davies, E. Linfield, and D. Ritchie, *Appl. Phys. Lett.*, 81, 2002.
- [25] L. Ajili, G. Scalari, D. Hofsetter, M. Beck, J. Faist, H. Beere, G. Davies, E. Linfield, and D. Ritchie, *Electron. Lett.*, 38, 2002.
- [26] R. Kohler, A. Tredicucci, F. Beltram, H. E. Beere, E.H. Linfield, A.G. Davies, D.A. Ritchie, S.S. Dhillon, and C. Sirtori, *Appl. Phys. Lett.*, 82,2003.
- [27] G. Scalari, L. Ajili, J. Faist, H. Beere, E. Linfield, D. Ritchie, and G. Davies. *Appl. Phys. Lett.*, 82, 2003.

- [28] B.S. Williams, H. Callebaut, S. Kumar, Q. Hu, and J.L. Reno, *Appl. Phys. Lett.*, 82, 2003.
- [29] A. Tredicucci, R. Kohler, L. Mahler, H. E. Beere, E. H. Linfield and D. A. Ritchie, *Semicond. Sci. Tech.*, 20:S222, 2005.
- [30] B. S. Williams, S. Kumar, H. Callebaut, Q. Hu, and J. L. Reno, *Appl. Phys. Lett.*, 83:11, 2003.
- [31] B. S. Williams, S. Kumar, H. Callebaut, Q. Hu, and J. L. Reno, *Appl. Phys. Lett.*, 83:25, 2003.
- [32] R. Kohler, A. Tredicucci, C. Mauro, F. Beltram, H. E. Beere, E. H. Linfield, A. G. Davies, and D. A. Ritchie, *Appl. Phys. Lett.*, 84:8, 2004.
- [33] S. Kumar, B. S. Williams, S. Kohen, Q. Hu, and J. L. Reno, *Appl. Phys. Lett.*, 84:14, 2004.
- [34] B. S. Williams, S. Kumar, Q. Hu, and J. L. Reno, *Optics Express*, 13:9, 2005.
- [35] H.C. Liu, M. Wachter, D. Ban, Z. R. Wasilewski, M. Buchanan, G.C. Aers, J.C. Cao, S.L. Feng, B.S. Williams, and Q. Hu, *Appl. Phys. Lett.*, 87:141102, 2005.
- [36] D. Ban, M. Wachter, H.C. Liu, Z. R. Wasilewski, M. Buchanan, and G.C. Aers, J, *Vac. Sci. Technol.*, A24:3, 2006.
- [37] A. Benz, G. Fasching, A.M. Andrews, M. Martl, K. Unterrainer, T. Roch, W. Schrenk, S. Golka, and G. Strasser, *Appl. Phys. Lett.*, 90:101107 2007.
- [38] H. Luo, S.R. Laframboise, Z.R. Wasilewski, and H.C. Liu, *Elec. Lett.*, 43:11, 2007.
- [39] H. Luo, S.R. Laframboise, Z.R. Wasilewski, H.C. Liu, and J.C. Cao, *Elec. Lett.*, 44:10, 2008.
- [40] B.S. Williams, S. Kumar, Q. Hu and J.L. Reno, *Elec. Lett.*, 42:2, 2006.

- [41] S. Kumar, B. S. Williams, Qing Hu, and J. L. Reno, *Appl. Phys. Lett.*, 88:121123, 2006.
- [42] H. Luo, S.R. Laframboise, Z.R. Wasilewski, G.C. Aers, H.C. Liu, and J.C. Cao, *Appl. Phys. Lett.*, 90:041112, 2007.
- [43] M.A. Belkin, J. A. Fan, S. Hormoz, F. Capasso, S.P. Khanna, M. Lachab, A. G. Davies, and E.H. Linfield, *Optics Express*, 16:3242, 2008.
- [44] T. Ando, A.B. Fowler, and F. Stern, *Rev. Mod. Phys.*, 54:2, 1982.
- [45] Y.C. Chang and J.N. Schulman, *J. Vac. Sci. Technol.*, 21:540, 1982.
- [46] J.N. Schulman and Y.C. Chang, *Phys. Rev. B.*, 31:2056, 1986
- [47] A. D. Carlo, *Semicond. Sci. Technol.*, 18:R1, 2003.
- [48] T. B. Boykin, J. P. A. Van Der Wagt, and J. S. Harris, Jr., *Phys. Rev. B.*, 43:6, 1991.
- [49] T. B. Boykin, *Phys. Rev. B.*, 54:11, 1996.
- [50] P. Harrison, *Quantum Wells, Wires, and Dots*, John Wiley & Sons, Inc., Chichester, 2005.
- [51] F. Long, W.E. Hagston, and P. Harrison, *Proc. 23rd Int. Conf. Phys. Semicond.*, World Scientific, 1996.
- [52] G. Bastard and J.A. Brum, *IEEE J. Quant. El.*, QE-22:9, 1986.
- [53] G. Bastard, *Phys. Rev. B.*, 24:5693, 1981.
- [54] G. Bastard, *Phys. Rev. B.*, 25:7584, 1982.
- [55] M.F.H. Schuurmans and G.W. Hooft, *Phys. Rev. B.*, 31:8041, 1985.
- [56] G. Bastard, *Wave Mechanics Applied to Semiconductor Heterostructures*, Les Editions de Physique, Paris, 1988.
- [57] M.G. Burt, *J. Phys.: Condens. Matt.*, 4:6651, 1992.
- [58] M.G. Burt, *J. Phys.: Condens. Matt.*, 9:R53, 1999.

- [59] W. L. Bloss, *J. Appl. Phys.*, 65:12, 1989.
- [60] W. L. Bloss, *J. Appl. Phys.*, 67:3, 1990.
- [61] G. Bastard, R. Ferreira, S. Chelles, and P. Voisin, *Phys. Rev. B.*, 50:7, 1994.
- [62] M. Wagner and H. Mizuta, *Phys. Rev. B.*, 48:19, 1993.
- [63] B. Olejnikova, *Semicond. Sci. Technol.*, 8:525, 1993.
- [64] B.K. Ridley, *J. Phys. C.* 15:5899, 1982.
- [65] D. Calecki, J.F. Palmier, and A. Chromette, *J. Phys. C.*, 17:5017, 1984.
- [66] P.K. Baser and S. Kunder, *Appl. Phys. Lett.*, 47:264, 1985.
- [67] R. Ferreira and G. Bastard, *Phys. Rev. B.*, 40:2, 1989.
- [68] E. Molinari, C. Bungaro, M. Gulia, P. Lugli, and H. Rucker, *Semicond. Sci. Technol.*, 7:B67, 1992.
- [69] H. Rucker, E. Molinari, and P. Lugli, *Phys. Rev. B.*, 39:6747, 1992.
- [70] T. Unuma, M. Yoshita, T. Noda, H. Sakaki, and H. Akiyama, *J. Appl. Phys.*, 93:3, 2003.
- [71] J.H. Smet, C. G. Fonstad, and Q. Hu, *J. Appl. Phys.*, 79:9305, 1996.
- [72] S. Borenstain and J. Katz, *Phys. Rev. B.*, 39:10852, 1989.
- [73] P. Kinsler, P. Harrison, and R.W. Kelsall, *Phys. Rev. B.*, 58:8, 1998.
- [74] S.C. Lee and I. Galbraith, *Phys. Rev. B.*, 55:24, 1997.
- [75] S.C. Lee and I. Galbraith, *Phys. Rev. B.*, 59:24, 1999.
- [76] W.T. Masseling, *Phys. Rev. Lett.*, 66:11, 1991.
- [77] J.R. Meyer, D.J. Arnold, C.A. Hoffman, and F.J. Bartoli, *J. Appl. Phys.*, 74:11, 1993.
- [78] H. Sasaki, T. Noda, K. Hirakawa, M. Tanaka, and T. Matsusue, *Appl. Phys. Lett.*, 51:23, 1987.

- [79] C. Sirtori, F. Capasso, J. Faist, A. L. Hutchinson, D. L. Sivco, and A. Y. Cho, *IEEE J. Quant. El.*, 34:9, 1998.
- [80] K. Donovan, P. Harrison, and R.W. Kelsall, *J. Appl. Phys.*, 89:6, 2001.
- [81] P. Harrison, *Appl. Phys. Lett.*, 75:18, 1999.
- [82] D. Indjin, P. Harrison, R.W. Kelsall, and Z. Ikonic, *Appl. Phys. Lett.*, 81:3, 2002.
- [83] D. Indjin, S. Tomic, Z. Ikonic, P. Harrison, R.W. Kelsall, V. Milanovic, S. Kocinac, *Appl. Phys. Lett.*, 81:12, 2002.
- [84] D. Indjin, P. Harrison, R. W. Kelsall, and Z. Ikonic, *J. Appl. Phys.*, 91:11, 2002.
- [85] P. Harrison, D. Indjin, and R. W. Kelsall, *J. Appl. Phys.*, 92:11, 2002.
- [86] D. Indjin, P. Harrison, R. W. Kelsall, and Z. Ikonic, *Phot. Tech. Lett.*, 15:1, 2003.
- [87] P. Harrison, D. Indjin, V.D. Jovanovic, A. Mircetic, Z. Ikonic, R.W. Kelsall, J. McTavish, I. Savic, N. Vukmirovic, and V. Milanovic, *Acta Physica Polonica*, 107:1, 2005.
- [88] D. Indjin, Z. Ikonic, V. D. Jovanovic, N. Vukmirovic, P. Harrison, and R. W. Kelsall, *Semi. Sci. Tech.*, 20:S237, 2005.
- [89] S.M. Goodnick and P. Lugli, *Appl. Phys. Lett.*, 51:8, 1987.
- [90] K. Yokoyama and K. Hess, *Phys. Rev. B.*, 33:8, 1986.
- [91] M. Dur, S.M. Goodnick, and P. Lugli, *Phys. Rev. B.*, 54:24, 1996.
- [92] O. Bonno, J.L. Thobel, and F. Dessenne, *J. Appl. Phys.*, 87:043701, 2005.
- [93] H. Callebaut, S. Kumar, B.S. Williams, Q. Hu, and J.L. Reno, *Appl. Phys. Lett.*, 83:2, 2003.
- [94] H. Callebaut, S. Kumar, B.S. Williams, Q. Hu, and J.L. Reno, *Appl. Phys. Lett.*, 84:5, 2004.
- [95] J.T. Lu and J.C. Cao, *Appl. Phys. Lett.*, 88:061119, 2006.
- [96] H.L. Li, J.C. Cao, J.T. Lu, and Y.J. Han, *Appl. Phys. Lett.*, 92:221105, 2008.

- [97] H.L. Li, J.C. Cao, and J.T. Lu, *J. Appl. Phys.*, 103:103113, 2008.
- [98] H. Li, J.C. Cao, Y.J. Han, X.G. Guo, Z.Y. Tan, J.T. Lu, H.Luo, S.R.Laramboise, and H.C. Liu, *J. Appl. Phys.*, 104:043101, 2008.
- [99] H. Li, J.C. Cao, Z.Y. Tan, and S.L. Feng *Appl. Phys. Lett.*, 104:103101, 2008.
- [100] J.C. Cao, J.T. Lu, and H. Li, *Physica E*, 41:282, 2008.
- [101] H.Li, J.C. Cao, and H.C. Liu, *Semicond. Sci. Technol.*, 23:125040, 2008.
- [102] H. Callebaut and Q. Hu, *J. Appl. Phys.*, 98:104505, 2005.
- [103] D. Calecki, J.F. Palmier, and A. Chomette, *J. Phys. C.*, 17, 1984.
- [104] R. Tsu, and G. Dohler, *Phys. Rev. B.*, 12:2, 1975.
- [105] Y. L. Geller and J.P. Leburton, *Semicond. Sci. Technol.*, 10:1463, 1995.
- [106] M.P. Telenkov and Y.A. Mityagin, *J. Exp. Theor. Phys.*, 99:3, 2004.
- [107] R.C. Iotti and F. Rossi, *Phys. Rev. Lett.*, 87:14, 2001.
- [108] R.C. Iotti and F. Rossi, *Rep. Prog. Phys.*, 68:2533, 2005.
- [109] F. Eickenmeyer, K. Reimann, M. Woerner, T. Elsaesser, S. Barbieri, C. Sirtori, G. Strasser, T. Muller, R. Bratschitsch, and K. Unterrainer, *Phys. Rev. Lett.*, 98:4, 2002.
- [110] J. Kastrup, R. Hey, K.H. Ploog, H.T. Grahn, L.L. Bonilla, M. Kindelan, M. Moscoso, A. Wacker, and J. Galan, *Phys. Rev. B.*, 55:4, 1997.
- [111] A.J. Leggett, S. Chakravarty, A.T. Dorsey, M.P.A. Fisher, A. Garg, and W. Zwerger, *Rev. Mod. Phys.*, 59:1, 1987.
- [112] K. Leo, J. Shah, J.P. Gordon, T.C. Damen, D.A.B. Miller, C.W. Tu, and J.E. Cunningham, *Phys. Rev. B.*, 42:11, 1990.
- [113] R. Ferreira and G. Bastard, *Rep. Prog. Phys.*, 60:345, 1997.
- [114] S.A. Gurvitz, I. Bar-Joseph, and B. Deveaud, *Phys. Rev. B.*, 43:18, 1991.

- [115] H. Vaupel, P. Thomas, O. Kuhn, V. May, and K. Maschke, *Phys. Rev. B.*, 53:16531, 1996.
- [116] R.C. Iotti, E. Ciancio, and F. Rossi, *Phys. Rev. B.*, 72:125347, 2005.
- [117] A. Wacker, *Phys. Rep.*, 357:1, 2002.
- [118] C. Weber, A. Wacker, and A. Knorr, *Preprint_Cond-mat.mes-hall arXiv_0811.3736v1*.
- [119] R. Lake, G. Klimeck, R. C. Bowen, and D. Jovanovic, *J. Appl. Phys.*, 81:12, 1997..
- [120] A. Wacker and S.C. Lee, *Physica B Cond. Matt.*, 314:1, 2002.
- [121] S.C. Lee and A. Wacker, *Phys. Rev. B.*, 66:245314, 2002.
- [122] M.F. Pereira, Jr., S.C. Lee, and A. Wacker, *Phys. Rev. B.* 69 205310 2004.
- [123] F. Banit, S.C. Lee, A. Knorr, and A. Wacker, *Appl. Phys. Lett.*, 86:041108, 2005.
- [124] S.C. Lee, F. Banit, M. Woerner, and A. Wacker, *Phys. Rev. B.*, 73:245320, 2006.
- [125] A. Wacker, *Phys. Stat. Sol. C.*, 5:1, 2007.
- [126] R. Nelander and A. Wacker, *Appl. Phys. Lett.*, 92:081101, 2008.
- [127] I. Waldmueller, W.W. Chow, E.W. Young, and M.C. Wanke, *IEEE J. Quant. El.*, 42:3, 2006.
- [128] D.J. BenDaniel and C.B. Duke, *Phys. Rev.*, 152:683, 1966.
- [129] G.T. Einevoll and L.J. Sham, *Phys. Rev. B.*, 49:10533, 1994.
- [130] I. Galbraith and G. Duggan, *Phys. Rev.*, 38:10057, 1998.
- [131] J.P. Killingbeck, *Microcomputer Algorithms*, Hilger, Bristol, 1992.
- [132] D.A.B. Miller, D.S. Chemla, T.C. Damen, A.C. Gossard, W. Weigmann, T.H. Wood, and C.A. Burrus, *Phys. Rev. Lett.*, 53:2173, 1984.
- [133] M. Morita, K. Goro, and T. Suzuki, *Jap. J. Appl. Phys.*, 29:L1663, 1990.
- [134] N. Susa and T. Nakahara, *Electron. Lett.*, 28:941, 1992.
- [135] P.N. Brounkov, T. Benyattou, and G. Guillot. *J. Appl. Phys.*, 80:864, 1996.

- [136] A. Trellakis, A.T. Galick, A. Pacelli, and U. Ravaioli, *J. Appl. Phys.*, 81:7880, 1997.
- [137] A. Pacelli, *Electron. Dev.*, 44:7 1997.
- [138] C. Sirtori, F. Capasso, J. faist, D.L. Sivco, A.L. Hutchinson, and A.Y. Cho, *Appl Phys. Lett.*, 66:4, 1995.
- [139] P. Kruck, H. Page, C. Sirtori, S. Barbieri, M. Stellmacher, and J. Nagle. *Appl. Phys. Lett.*, 76:3340, 2000.
- [140] J.C. Slater and G.F. Koster, *Phys. Rev.*, 94:1498, 1954.
- [141] C.C.J. Roothaan, *Rev. Mod. Phys.*, 23:69, 1951.
- [142] S. Foryen and W.A. Harrison, *Phys. Rev. B.*, 20:2420, 1979.
- [143] R.A. Evarestov, *Quantum Chemistry of Solids: The LCAO First Principle Treatments of Crystal*, Springer, 2007.
- [144] W.A. Harrison, *Electronic Structure and the Properties of Solids: The Physics of the Chemical Bond*. Dover Publications, 1989.
- [145] A.K. Chandra, *Introduction to Quantum Chemistry*, Tata McGraw-Hill, 1994.
- [146] B.K. Ridley, *Phys. Rev. B.*, 39:8, 1989.
- [147] V.M. Menon, W.D. Goodhue, A.S. Karakashian, and L.R. Ram-Mohan, *J. Appl. Phys.*, 88:9, 2000.
- [148] V.M. Menon, L.R. Ram-Mohan, W.D. Goodhue, A.S. Karahashian, A. Naweed, A. Gatesman, and J. Waldman, *Physica E*, 15:197, 2002.
- [149] V.M. Menon, L.R. Ram-Mohan, W.D. Goodhue, A.J. Gatesman, and A.S. Karahashian, *Physica B*, 316 2002.
- [150] H.B. Teng, J.P. Sun, G.I. Haddad, M.A. Stroscio, S.Yu, and K.W. Kim, *J. Appl. Phys.*, 84:4, 1998.
- [151] H. Rucker, E. Molinari, and P. Lugli, *Phys. Rev. B.*, 45:12, 1992.

- [152] B.S. Williams and Q. Hu, *J. Appl. Phys.*, 90:11, 2001.
- [153] H. Rucker, E. Molinari, and P. Lugli, *Phys. Rev. B.*, 44:7, 1991.
- [154] K. Huang and B. Zhu, *Phys. Rev. B.*, 38:18, 1988.
- [155] N. Mori and T. Ando, *Phys. Rev. B.*, 40:9, 1989.
- [156] S. Yu, K.W. Kim, M.A. Stroscio, G.J. Iafrate, J.P. Sun, and G.I. Haddad, *J. Appl. Phys.*, 82:7, 1997.
- [157] H. Rucker, E. Molinari, and P. Lugli, *J. Appl. Phys.*, 79:9305, 1996.
- [158] A.R. Bhatt, K.W. Kim, M.A. Stroscio, and J.M. Higman, *Phys. Rev. B.*, 48:19, 1993.
- [159] R.L. Liboff, *Introductory Quantum Mechanics*. Holden-Day, S.F. 1980.
- [160] M. Mosko, A. Moskova, and V. Cambel, *Phys. Rev. B.*, 16860 1995.
- [161] A. Yariv, *Quantum Electronics*, John Wiley & Sons, Inc., New York, 1967.
- [162] R. Terazzi, T. Gresch, A. Wittmann, and J. Faist, *Phys. Rev. B.*, 78, 155328, 2008.
- [163] G. Scalari, R. Terazzi, M. Giovannini, N. Hoyler, and J. Faist, *Appl. Phys. Lett.*, 91:032103, 2007.
- [164] J. Faist, F. Capasso, C. Sirtori, D.L. Sivco, A.L. Hitchinson, M. S. Hybertsen, and A.Y. Cho, *Phys. Rev. Lett.*, 76:3, 1996.

R 702035106